

EX 10453  
SW 9550

# Electrodynamics of Superconducting Cables in Accelerator Magnets

CERN LIBRARIES, GENEVA

CERN LIBRARIES, GENEVA



P00025312

Thesis-1995-Verweij

Arjan P. Verweij

**ELECTRODYNAMICS OF SUPERCONDUCTING CABLES  
IN ACCELERATOR MAGNETS**

CERN LIBRARIES, GENEVA



CM-P00081075

Publication of this thesis has been financially supported by Holec Ridderkerk,  
The Netherlands

CIP-GEGEVENS KONINKLIJKE BIBLIOTHEEK, DEN HAAG

Verweij, Arjan Peter

Electrodynamics of superconducting cables in accelerator magnets /

Arjan Peter Verweij. - [S.l. : s.n.]. - 111.

Proefschrift Universiteit Twente Enschede. - Met lit. opg.

- Met samenvatting in het Nederlands.

ISBN 90-9008555-6

Trefw.: supergeleiding / versnellers / electrodynamica.

Eerste Uitgave 1995

Druk: Universiteit Twente

© A.P. Verweij 1995

# **ELECTRODYNAMICS OF SUPERCONDUCTING CABLES IN ACCELERATOR MAGNETS**

**PROEFSCHRIFT**

ter verkrijging van  
de graad van doctor aan de Universiteit Twente,  
op gezag van de rector magnificus,  
prof. dr. Th.J.A. Popma,  
volgens besluit van het College voor Promoties  
in het openbaar te verdedigen  
op vrijdag 15 september 1995 te 15.00 uur.

door

Arjan Peter Verweij  
geboren op 7 januari 1968  
te Arnhem





Dit proefschrift is goedgekeurd door:

prof. dr. C. Daum (promotor) en  
dr. ir. H.H.J. ten Kate (assistent-promotor).



## Preface

The work described in this thesis has been carried out partially in the Low Temperature group at the University of Twente and partially in the AT-MA group at CERN, in the framework of a collaboration agreement between CERN, the University of Twente, STW and NIKHEF.

I would like to thank all members of both groups for their help and the pleasant atmosphere during the day. Also the support of those who took care of the helium and the cryogenics of the magnets, often in the evening and in the weekend, is acknowledged.

I appreciated the help of the following persons in particular:

Kees Daum and Herman ten Kate for their general support and many useful comments on the concept text,

Daniel Leroy, Luc Oberli, David Richter, Andrzej Siemko, Peter Sievers, Louis Walckiers and Rob Wolf for their interest, advice and many fruitful discussions,

Stephan Russenschuck, for providing various field maps,

Christian Giloux, Guillaume Gerin and Benoît Geroudet for measuring many magnets in Block 4 and SM18,

Lars Eriksson, Andy Hofstede, Marijn Oomen, Bart Sachse and Maarten Bouwhuis for performing many experiments at the university,

John Baxter and Joyce Moore for correcting my English language.

Finally, I would like to thank my family and friends for their interest and encouragement, our sporting activities on clay, grass and snow, and other distractions in the evenings and weekends.

Enschede, September 1995

Arjan Verweij



# Contents

<b>1. General introduction</b>	<b>11</b>
1.1 Introduction to the electrodynamic properties of superconducting cables and magnets	12
1.2 Superconducting magnets	15
1.3 Accelerator magnets	17
1.4 Scope of the thesis	20
<b>2. Multistrand cables and magnets</b>	<b>23</b>
2.1 Magnetic field in the aperture of a magnet	24
2.2 Magnet characteristics	25
2.2.1 Magnet designs	29
2.2.2 Cold mass	30
2.2.3 Pre-compression of the coils	31
2.2.4 Field and force distributions	31
2.2.5 Superconductor	33
2.2.6 Quenching and protection	33
2.2.7 Operating procedure	34
2.2.8 Beam losses	35
2.2.9 Survey of the model magnets	35
2.3 Strand and cable characteristics	36
2.4 The $I_C(B, T)$ relation	40
2.5 Conclusions	42
<b>3. Losses in strands</b>	<b>43</b>
3.1 Introduction	44
3.2 Hysteresis loss	44
3.3 The $J_C$ - $B$ relation	48
3.4 Interfilament coupling currents	51
3.5 Interfilament time constants	56
3.6 Conclusions	59
<b>4. Interstrand coupling currents</b>	<b>61</b>
4.1 Introduction	62
4.2 Network model of a Rutherford-type cable	64
4.3 Contact resistances $R_a$ and $R_c$	72
4.4 Weak excitation	74
4.4.1 Steady-state calculations	74
4.4.2 Step response calculations	77
4.5 Strong excitation	80

4.6	Cables with $R_c$ varying across the cable width	83
4.7	Cables with $\dot{B}_\perp$ varying across the cable width	85
4.8	Cables of finite length with constant $\dot{B}$	87
4.9	Stacked cables	89
4.10	Influence of transverse pressure on $R_c$	90
4.10.1	Introduction	90
4.10.2	Theoretical model for the calorimetric method	91
4.10.3	Theoretical model for the electrical method	92
4.10.4	Experimental set-up	94
4.10.5	Results and discussion	95
4.11	Conclusions	99
<b>5.</b>	<b>Boundary-induced coupling currents</b>	<b>101</b>
5.1	Introduction	102
5.2	Cables with insulated strands	105
5.3	Simulating BICCs	107
5.4	Cables exposed to a $\dot{B}_\perp$ -step	109
5.4.1	Characteristic BICC pattern	109
5.4.2	Magnitude and characteristic length of BICCs under steady-state conditions	116
5.4.3	Characteristic time of BICCs	119
5.4.4	Propagation velocity of BICCs	122
5.4.5	Arbitrary $\dot{B}_\perp$ -distributions	123
5.5	Cable that are partially exposed to $\dot{B}_\perp$	125
5.6	$\dot{B}_\perp$ -steps with $R_c \gg R_a$	128
5.7	Non-uniform $R_c$ -distributions	129
5.8	Experimental observation of BICCs in a 1.3 m long cable	131
5.8.1	Introduction	131
5.8.2	Experimental set-up	132
5.8.3	Results and discussion	135
5.10	Conclusions	140
<b>6.</b>	<b>Coupling-current losses in accelerator dipole magnets</b>	<b>143</b>
6.1	Introduction	144
6.2	Loss components in magnets	145
6.2.1	Hysteresis loss	145
6.2.2	Interfilament coupling loss	146
6.2.3	Interstrand coupling loss	148
6.2.4	Losses in the connections and the wedges	150
6.2.5	Total loss	151
6.3	Measuring losses of a magnet during ramping	154
6.4	Experimentally determined $R_c$ -values of LHC magnets	158
6.5	Conclusions	162

<b>7. Coupling-current induced field distortions</b>	<b>165</b>
7.1 Introduction	166
7.2 Calculating coupling-current induced field distortions	168
7.3 Field $B_{if}$ in dipole magnets	171
7.4 Field $B_{is}$ in dipole magnets	172
7.5 Field $B_{bi}$ in dipole magnets	176
7.6 Experimental methods to determine $B_{cc}$	177
7.7 Experimental results of field $B_{cc}$ in LHC dipole magnets	179
7.7.1 1 m long CE1 magnet	180
7.7.2 1 m long EL2 magnet	184
7.7.3 10 m long AN2 magnet	185
7.7.4 10 m long AN3 magnet	188
7.7.5 Evaluation of fields $B_{is}$ and $B_{bi}$	189
7.8 Conclusions	191
<b>8. Ramp-rate limitation of dipole magnets</b>	<b>193</b>
8.1 Introduction	194
8.2 Calculation of the RRL of magnets	195
8.2.1 Influence of IFCCs on the RRL	196
8.2.2 Influence of ISCCs on the RRL	197
8.2.3 Influence of BICCs on the RRL	199
8.2.4 Influence of the ISCL on the RRL	202
8.2.5 Discussion	205
8.3 Influence of BICCs on the RRL in LHC dipole magnets	208
8.4 Estimate of the temperature increase of the cable due to power losses in the coil	215
8.5 Negative field-sweep rates	218
8.6 Conclusions	221
<b>9. General conclusions and recommendations</b>	<b>223</b>
9.1 Modelling of coupling currents in multistrand cables	224
9.2 Restrictions of the contact resistances	227
9.3 Controlling and measuring contact resistances	229
9.4 Effect of coupling currents in other magnets	230
<b>References</b>	<b>231</b>
<b>Nomenclature</b>	<b>239</b>
<b>Summary (in Dutch)</b>	<b>245</b>



## Chapter 1

# General introduction

*Since the discovery of materials that remain superconductive up to high-magnetic fields, the number of successful applications has increased considerably, in particular in the field of superconducting magnets. Together with the increase of the stored energy of large magnet systems, the size of the conductor also increased from single wires to large cables. This thesis deals with the consequences of the multistrand configuration of the cables on the electrodynamic properties of magnets.*

*In this first chapter the main applications of superconducting magnets are presented and the relevance of this thesis for the various applications is demonstrated. The emphasis is on accelerator magnets made of multistrand cables since the electromagnetic stability and field homogeneity of this type of magnet are strongly influenced by the cable configuration.*

*An introduction to the main electrodynamic effects in cables is presented. A change in the external magnetic field acting on a superconductor causes several types of induced-current patterns. Important issues are persistent currents in the filaments, interfilament coupling currents, interstrand coupling currents and boundary-induced coupling currents. The influence of these currents on the performance of the magnet with respect to power loss, field distortions and electromagnetic stability is discussed.*



## 1.1 Introduction to the electrodynamic properties of superconducting cables and magnets

Superconducting magnets are often used to produce high-magnetic fields and fields in large volumes where the use of conventional magnets would result in a large consumption of electric power. In magnet systems with a large stored energy the electrical conductors, from which the coils of the magnets are made, usually consist of multifilamentary strands arranged in cables. The main reason for using cables is the need to limit the quench voltages (see section 2.2.6). The filaments are made of superconducting alloys, in particular NbTi and Nb<sub>3</sub>Sn, and are embedded in a normal conducting matrix thus forming strands. Usually, the strands as well as the filaments are transposed with certain twist lengths. The following two types of cables are the most commonly used:

- Rutherford-type cables (see Fig. 1.1a) are manufactured by flattening hollow tubular multistrand cables, which are compacted by rolling to packing factors of up to 90%. The large compaction not only increases the overall current density but also reduces the average contact resistance between the strands, which will be shown to be an important parameter in the magnitude of the coupling currents. In accelerator magnets the cables are electrically insulated and cooled by means of bath cooling. The characteristics of these cables are dealt with in more detail in section 2.3.

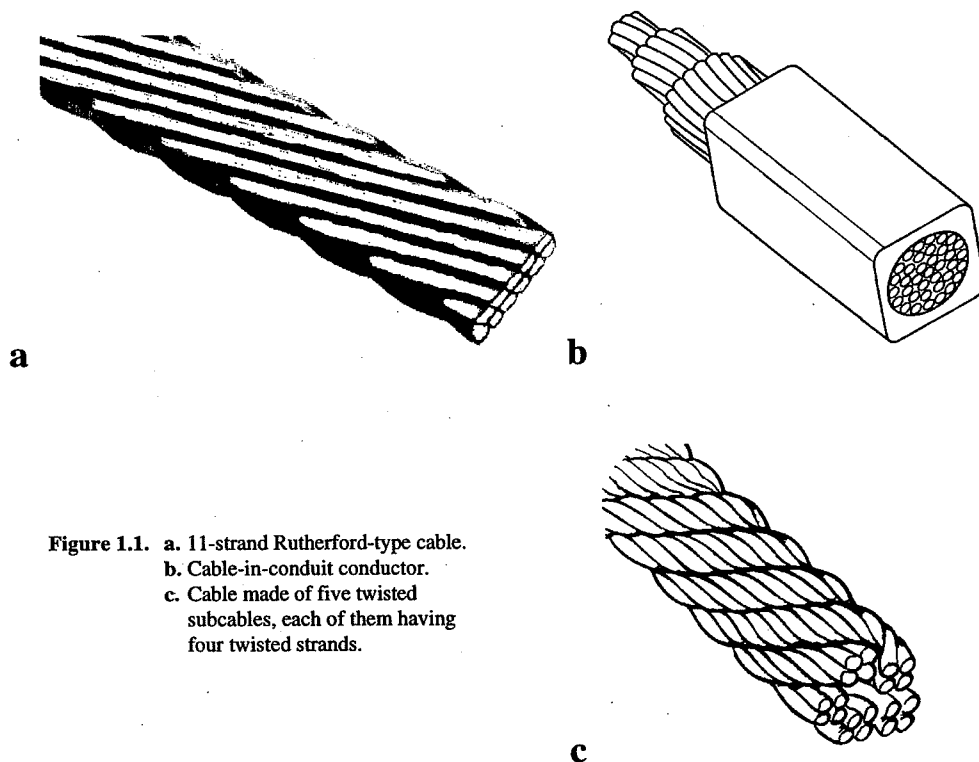


Figure 1.1. a. 11-strand Rutherford-type cable.  
b. Cable-in-conduit conductor.  
c. Cable made of five twisted subcables, each of them having four twisted strands.

- The cable-in-conduit conductor (see Fig. 1.1b) consists of a large number of strands or sub-cables which are wrapped inside a jacket (usually made of stainless steel) for mechanical reinforcement. The cable is often cooled by means of forced flow cooling, which implies that the helium is forced through the voids in the cable, which enhances the stability of the cable.

Various other types of cables exist, which differ mainly with respect to the number of subcables and strands, the amount of stabiliser, the type of cooling etc. As an example, a cable without a jacket, made of several subcables with twisted strands is shown in Fig. 1.1c. A general treatment of the design and fabrication of NbTi conductors can be found in the literature, for example in [Collings, '86].

If multistrand cables are exposed to a changing magnetic field, various currents are induced. These currents flow not only within the individual strands of the cable but also in and between the various strands of the cable. The latter increase considerably for an increasing size of the cable, similar to eddy currents in a normal conducting bar.

The main question to be clarified in this thesis is: *How do the induced currents, and in particular those currents flowing in and between the strands, affect the performance of superconducting magnets?* This influence is investigated with respect to:

- The energy loss inherent to the currents flowing through resistive parts of the strands or the cables. The energy loss leads to an additional heat load (at the operation temperature of the magnet) which has to be compensated by the cryogenic system. The effect is important for almost all magnets and in particular for those which are subject to large field variations.
- The field distortions caused by the currents. Especially in accelerator magnets, field distortions are a major concern since the particle motion becomes more unstable at larger field errors, which leads to enhanced beam losses and a reduced luminosity.
- The temperature margin and electromagnetic stability of the cable. Due to the energy dissipation, the cable warms up locally so that the difference between the transport current and the critical current decreases. The effect is especially important in magnets with poorly cooled cables. Additionally, the induced currents cause a non-uniform current distribution between strand sections in the cable so that some strand sections carry a total current which is larger than the transport current. This could directly lead to local saturation of a strand section and possibly a quench. Indirectly, a non-uniform current distribution locally limits the difference between the total strand current and the critical strand current and therefore reduces the electromagnetic stability of the cable.

Four types of induced currents can be distinguished which differ with respect to the part of the conductor through which they flow, the characteristic loop length and the characteristic time.

- Persistent currents (PCs) in the filaments (partially) shield the interior of the filaments against the external applied field. The magnitude of these currents depends on the field and the field history but, in first approximation, not on the field-sweep rate.
- Interfilament coupling currents (IFCCs) are induced by an external field variation and flow between and in the filaments of a strand. The magnitude of the IFCCs increases with increasing twist length of the filaments and decreasing resistivity of the matrix

material. The IFCCs have a characteristic loop length equal to the twist pitch of the filaments, exhibit time constants of typically 0.01 to 0.1 s and cause the interfilament coupling loss (IFCL).

- Interstrand coupling currents (ISCCs) are also induced by an external field variation and flow between and in the strands of the cable. The magnitude of the ISCCs increases with increasing twist length of the strands and decreasing electrical contact resistance between the strands. The ISCCs have a characteristic loop length equal to the twist pitch of the strands, exhibit time constants of typically 0.01 to 10 s and cause the interstrand coupling loss (ISCL).
- Boundary-induced coupling currents (BICCs) are mainly induced by variations of the field-sweep rate and the contact resistances along the length of the cable. BICCs can flow in and between the strands of a cable and also in and between the filaments of the strands. Only the former type of BICCs are dealt with in this thesis. The loop length and the characteristic time of the BICCs can be several orders of magnitude larger than those of the ISCCs. The additional power loss caused by the BICCs is dissipated in the contact resistances between the strands and is regarded in this thesis as an enhancement of the ISCL.

The characteristics of the currents are briefly surveyed in Table 1.1.

**Table 1.1.** Survey of the various currents and losses being present in a cable with non-insulated strands which is exposed to a varying field. The decay times represent characteristic times during which the currents decay once the driving force that has induced them becomes 0.

Currents	Loss	Location	Characteristic decay time
PCs	Filament magnetisation	In the filaments	$\rightarrow \infty$
IFCCs	Interfilament coupling loss (IFCL)	In and between filaments	0.01-0.1 s
ISCCs	Interstrand coupling loss (ISCL)	In and between strands	0.01-10 s
BICCs	(Included in the ISCL)	In and between strands	$> 10\text{-}10^5$ s

The persistent currents and interfilament coupling currents have been an important issue of research during the recent decades (and still are). Their properties are now well understood. The ISCCs have been investigated since the seventies and have become more and more important because the size of the cables has increased considerably. Qualitatively, the ISCCs are now more or less understood. Much research is still being carried out on the quantitative understanding of the ISCCs, which is a complicated matter since the value and the distribution of the contact resistances between strands, which determine the effective loop area's and the magnitude of the ISCCs, depend on many parameters (see section 4.2).

However, since the use of larger cables, anomalous time-dependent effects are often observed which could only be partially explained by the presence of ISCCs. In this thesis the existing models for the calculation of strand currents in superconducting cables are improved in order to investigate in more detail the time-dependent behaviour of cables in magnets. This has not only resulted in a realistic model of the ISCCs but has also led to the description of a new type of current, the so-called 'boundary-induced coupling current'. This name indicates that these currents, which are induced by a varying field, are created

due to boundaries especially those between local variations in the contact resistances and field change.

It is clear from the above that the influence of the coupling currents on the electrodynamic properties of a magnet is crucial for many magnets, made of multistrand conductors, if:

- the cables are exposed to large field changes,
- a homogeneous magnetic field in the aperture is required,
- the cables are poorly cooled.

In section 1.3 a brief survey of the main applications of magnets is given, showing for which magnets the performance is likely to be strongly affected by the coupling currents.

## 1.2 Superconducting magnets

In the late fifties, a new class of materials was discovered which exhibits superconducting properties up to high magnetic fields. The most important of this class are NbTi and Nb<sub>3</sub>Sn with critical fields of about 11 and 21-28 T respectively (at 4.2 K).

Small solenoid magnets were developed in the sixties. However, large fields could not be achieved due to the poor electromagnetic stability of the conductors. The development of the multifilamentary conductor in the seventies was an important step towards larger current densities at higher fields. These conductors, with diameters in the range of 0.1-1 mm, consist of superconducting filaments embedded in a normal conducting matrix. In large magnet systems many wires are bundled together to form multistrand cables, mainly in order to limit the inductance and the voltage levels. Nowadays, most applications of high-field magnets are based on coils wound from cabled superconductors.

The main applications of superconducting magnets are enumerated here. More detailed information can be found in the literature, for example in [Foner, '81], [Wilson, '83].

- **Solenoids.** These magnets are in use for general research at fields up to 20 T and bores up to 200 mm. The small solenoids are made of superconducting wire while the larger coils are wound from cables. High-field solenoids with a high field homogeneity are part of, for example, **NMR** (Nuclear Magnetic Resonance) spectrometers.
- **Magnets for nuclear fusion.** Power production on the basis of controlled thermonuclear fusion is feasible only by means of superconducting magnets since the use of conventional magnets is not economical. A magnet system of a tokamak mainly consists of DC toroidal field coils, enclosing a plasma ring, and pulsed transformer coils, for resistive heating of the plasma by inducing plasma currents. Both types of coils are made of large cable-in-conduit (CIC) conductors with forced-flow cooling. Although the toroidal coils carry a constant current during normal operation, which results in a constant self-field, they are also exposed to the changing field from the transformer coils. Not only the transformer coils but also the toroidal coils are therefore subject to large field-sweep rates of  $0.1 \text{ Ts}^{-1}$  (under normal operation) and up to  $10 \text{ Ts}^{-1}$  (in the case of plasma disruption).

- **Magnets for high-energy physics.** Superconducting magnets are part of the accelerator itself, for guiding the beam, as well as of the detectors of the physics experiments. In section 1.3 the beam-guiding magnets are discussed. Large detector magnets are applied to determine the momentum of charged particles from the curvature of the track. They often enclose a considerable part of the chamber volume of the detector and can therefore have diameters of several meters. The coils are made of Al-stabilised Rutherford-type conductors and are slowly ramped to the DC operating field of typically 1-4 T in the centre to 1-6 T in the windings.
- **Magnetic Resonance Imaging (MRI).** Superconducting MRI magnets are in use for medical diagnostics and were first developed in 1980. The higher image resolution due to the larger field, is the main reason that nowadays most MRI magnets are superconductive instead of normal-conductive. The magnets exhibit a high stability and field uniformity in time. MRI magnets are made of wires and are slowly ramped to nominal field.
- **Superconducting Magnet Energy Storage (SMES).** Superconducting coils can be applied as an inductive energy storage. Large SMES systems (with stored energies in the order of GWh's) are studied for load-balancing in existing power grids. The power oscillation in long power lines can be stabilised by means of pulsed SMES systems, while voltage failures in power lines are already made up with small SMES systems (with a stored energy of 1-10 MJ).
- **Magnetic levitation (MagLev).** Magnetically levitated transportation systems can be realised with superconducting coils, since light-weight high-field magnets are favourable. The levitation is achieved by the repelling force between the superconducting magnets in the vehicle/train and eddy currents on the track.
- **DC motors and AC generators.** The main characteristics of superconducting generators and motors are the high efficiency, high power rating and reduced size compared to conventional motors. Superconducting coils can be part of the field windings and the armature windings. The steady increase of the development of AC superconductors enables the manufacturing of fully superconducting machines.
- **Magnetic separation.** Ferromagnetic and paramagnetic particles can be separated from a large non-magnetic mass stream of material by a magnetic force. The field gradient and efficiency can be greatly improved using superconducting magnets.
- **Magnetohydrodynamic power generation (MHD).** An ionised hot gas is passed through a channel with a transversely applied magnetic field. The corresponding voltage on the wall of the channel causes a current through an external load.

The main applications of superconducting magnets are surveyed in Table 1.2 where the magnets are characterised with respect to the usual geometry of the conductor, maximum field in the windings, field accuracy and field-sweep rate. The geometry is represented by a W for a single wire, RC for a Rutherford-type cable, CIC for a cable-in-conduit conductor and C for a cable without jacket. Some magnets, of course, have been manufactured with different design fields or from other types of cable than those mentioned in the table.

**Table 1.2.** The main characteristics of superconducting magnets. W=wire, RC=Rutherford-type cable, CIC=cable-in-conduit, C=cable without jacket.

Application		Conductor	Max. field on cond. [T]	Field accuracy	Field-sweep rate [ $\text{Ts}^{-1}$ ]
Solenoids	Small bore	W	20	Medium	$10^{-2}$
	Large bore	C	15	Medium	Small
NMR		W	20	High	Small
Fusion	Toroidal coil	CIC	13	Low	0.1-10
	Transformer coil	CIC	13	Low	0.1-10
High-energy physics	Beam-guiding	RC	12	High	$10^{-2}$
	Detectors	C	6	Medium	Small
MRI		W	0.5-7	High	$10^{-3}$
SMES	Pulsed	C, RC	5-10	Low	$10^3$ - $10^4$
	Low frequency	C, RC	5-10	Low	Small
MagLev		RC	5	Low	Small
DC motors		RC	2-5	Low	Small
AC generators		RC	2-6	Low	10
Magnetic separation		C	8	Low	Small
MHD		RC	8	Low	Small

According to the conclusion at the end of section 1.1, coupling currents can especially affect the performance of fusion magnets, beam-guiding magnets for accelerators, pulsed SMES systems and AC generators. In this thesis the emphasis is on the electrodynamic properties of multistrand conductors in accelerator magnets, and especially in LHC dipole magnets because of the severe restrictions with respect to losses during ramping, stability and field homogeneity. A brief introduction to accelerator magnets is given in the next section.

### 1.3 Accelerator magnets

The desire for investigating matter and forces between elementary particles has encouraged physicists and engineers to construct devices for accelerating particles to higher and higher energies. This started around 1930 with small rectifier generators and cyclotrons and later with betatrons, linacs and synchrotrons.

Circular machines require mainly dipole magnetic fields to keep the beam of particles on the equilibrium orbit and quadrupole magnetic fields to focus and defocus the beam around the equilibrium orbit. Furthermore, there is a need for higher-order magnetic fields to correct field distortions and chromaticity. As the particle energy is proportional to the bending radius, the size of the accelerators has become larger and larger. In parallel, the linear dependence of the particle energy on the field strength of the dipole (bending) magnets has pushed the magnetic field to higher values.

For decades normal-conducting magnets have played an important role with fields up to 2 T, limited by the saturation of the iron. The breakthrough came with the construction of the Tevatron at Fermilab in 1983 [Cole, '79]. Here it was shown that a large number of dipole magnets (with a central field of 4.4 T) and quadrupole magnets (with a field gradient of  $75 \text{ Tm}^{-1}$ ) can be built, having a high quality and a good reproducibility.

After the Tevatron, other projects were approved, in which the design of the magnets was further improved. This has led to the construction of HERA in 1991 (with a dipole field of 4.7 T) [Wiik, '85], and the design of the Relativistic Heavy Ion Collider RHIC (3.5 T) [Ozaki, '90], the Accelerating and Storage Complex UNK (5 T) [Balbekov, '83], the Superconducting Super Collider SSC (6.6 T) [Edwards, '90] and the Large Hadron Collider LHC (8-10 T) [LHC, '91/'93].

In order to store an intense beam of particles, a high field quality is necessary. For normal conducting magnets this requirement can be quite easily attained since the field is determined by the shape of the iron yoke. In the case of superconducting magnets the field is governed by the geometry of the coils, a precise arrangement which is difficult to control, and by the persistent currents and coupling currents, as discussed in section 1.1.

The coils of all main accelerator magnets are made of Rutherford-type cables to enable an accurate coil winding and to have a high overall current density while keeping the inductance small. A survey of the geometry of the cables as used (or foreseen to be used) in various accelerator dipole magnets is given in Table 1.3.

**Table 1.3.** Survey of the geometry of the Rutherford-type cables (envisaged to be) used in several accelerator dipole magnets with a two-layer  $\cos(\theta)$  configuration (see section 2.2).

Institute	Accelerator	Central field [T]	Operating Temp. [K]	Coil	Nr. of strands	Width [mm]	Av. height [mm]
BNL	RHIC	3.5	4.6	<sup>a</sup>	30	9.7	1.17
Fermilab	Tevatron	4.4	4.6	inner	23	7.8	1.26
DESY	HERA	4.7	4.5	inner	24	10	1.48
				outer	24	10	1.48
IHEP	UNK	5.0	4.6	inner	19	8.7	1.63
				outer	19	8.7	1.63
SSCL	SSC	6.6	4.35	inner	30	12.3	1.46
				outer	36	11.7	1.16
CERN	LHC, 1 <sup>st</sup> design	10	1.9	inner	26	17	2.25
				outer	40	17	1.48
	LHC, 2 <sup>nd</sup> design	8.4	1.9	inner	28	15	1.89
				outer	36	15	1.47
<b>Nb<sub>3</sub>Sn model dipole magnets for the LHC, 1<sup>st</sup> design</b>							
CERN/ELIN [Asner, '90]		10	ca. 4.3	inner	24	16.8	2.44
				outer	36	16.8	1.63
CERN/UT [Ouden, den, '94]		11.1	ca. 4.3	inner	33	21.7	2.23
				outer	33	17.7	1.73

<sup>a</sup> This magnet has a single-layer  $\cos(\theta)$  geometry.

The increase in field is related to the cable dimensions as depicted in Fig. 1.2. It will be shown in chapters 4 and 5 that many effects related to the coupling between strands are strongly enhanced by an increase in the cable width. The figure shows therefore clearly that in circular accelerators the electrodynamic properties of the cable become more important with increasing field strength, i.e. usually increasing collision energy.

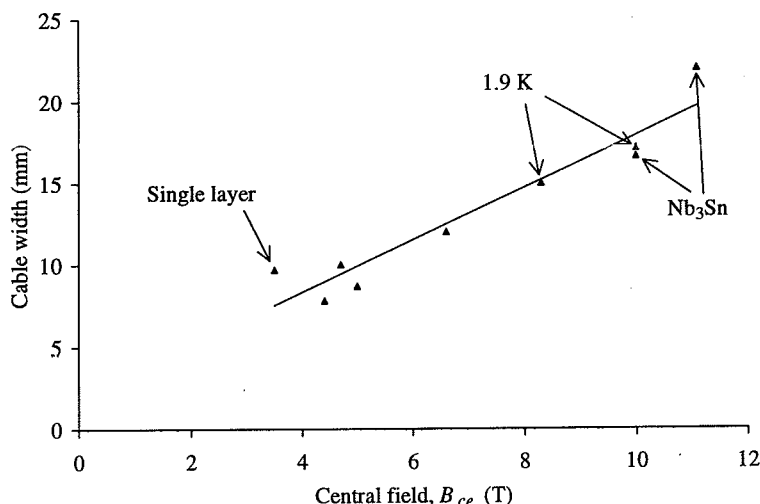


**Figure 1.2.** The width of Rutherford-type cables as a function of the design value of the central field of the dipole magnets (in which they are used). The operating temperature is about 4.3 K unless otherwise indicated.

On 16 December, 1994 the LHC was approved by the CERN member states to be the future accelerator to investigate mainly hadron physics, while also ion-ion and electron-proton collisions are envisaged. The LHC will be constructed in the same tunnel as the Large Electron Positron (LEP) machine, which came into operation in 1989. In LEP electrons and positrons are brought into collision whereas in LHC two proton beams will collide. The collision energy of LEP is limited to about 200 GeV caused by the synchrotron radiation that the particles emit as they are bent. In the case of protons the synchrotron radiation is much smaller and the collision energy is limited by the field produced by the bending magnets.

In two separate magnetic channels, two beams of particles with an equally signed charge and the same velocity, in the opposite direction, are brought into collision. This is accomplished by a novel design, that consists of two separate coil systems within the same mechanical structure (see section 2.2). The so-called 'twin-aperture structure' not only reduces the size of the magnets (compared to two single-aperture magnets) but probably results as well in a total cost savings of about 25%.

Superconducting dipole magnets with operation fields of about 8.4 T will be used in the LHC and result in a collision energy of about 14 TeV, about a factor 70 larger than in LEP. The maximum field of the magnets is about 10-20% larger to allow for adequate margins covering energy dissipation in the coils and production tolerances.



## 1.4 Scope of the thesis

This thesis consists of the following four parts which are illustrated in Fig. 1.3.

- In chapter 2 an introduction to accelerator dipole magnets is given. It is shown which aspects that are inherent to the cable and magnet design, influence the various currents as given in Table 1.1. A survey of the magnets, of which the electrodynamic properties are evaluated in chapters 6, 7 and 8, is presented. Also a survey of the main characteristics of the cables, from which the coils of these magnets are made, is given.
- In chapters 3, 4 and 5 the persistent currents and coupling currents in the strands and cables are dealt with as well as the loss related to these currents.
  - In chapter 3 an actual picture of the electrodynamic properties of single strands is presented in terms of filament magnetisation and interfilament coupling currents, which are both experimentally investigated on several LHC cables.
  - In chapter 4 the interstrand coupling is discussed. The network model, by which the ISCCs are calculated, is dealt with in detail. The contact resistances  $R_a$  and  $R_c$  between adjacent and crossing strands are introduced which will play a dominant role in all subsequent chapters. An important issue is the dependence of  $R_c$  on the transverse pressure on the cable.
  - In chapter 5 the influence of longitudinal variations in the contact resistance and the field-sweep rate are dealt with. These variations are, in particular, present near the cable-to-cable connections and in the coil ends and provoke a new type of current, the 'boundary-induced coupling current (BICC)'. The BICCs are described in terms of their magnitude, characteristic length, propagation velocity and characteristic time. The presence of BICCs in multistrand cables is demonstrated by analysis of the self-field of a 1.3 m long straight Rutherford-type cable.
- In chapters 6, 7 and 8 the effect of the coupling currents on the electrodynamic properties of accelerator magnets is investigated, in terms of:
  - the losses during ramping (chapter 6),
  - the field distortions (in the aperture of the magnets) caused by the coupling currents (chapter 7),
  - the ramp-rate limitation of the magnets, which is influenced by the coupling currents (chapter 8).
- In chapter 9 general conclusions are presented concerning the modelling of coupling currents and their impact on the performance of superconducting magnets. Recommendations are given for measuring and controlling the contact resistances in cables in the process from cable manufacturing to magnet operation.

Fig. 1.3 shows two dotted links. One of them concerns the field distortions due to the persistent currents which are not discussed in this thesis because it is a well-known phenomenon. The other one concerns the enhancement of the ISCL due to the BICCs which is dealt with in chapter 5 in the case of a single cable but is disregarded in chapter 6 in the case of a magnet. The increase is namely hard to assess and, where a dipole magnet is concerned, probably small compared to the coupling loss produced by the ISCCs.

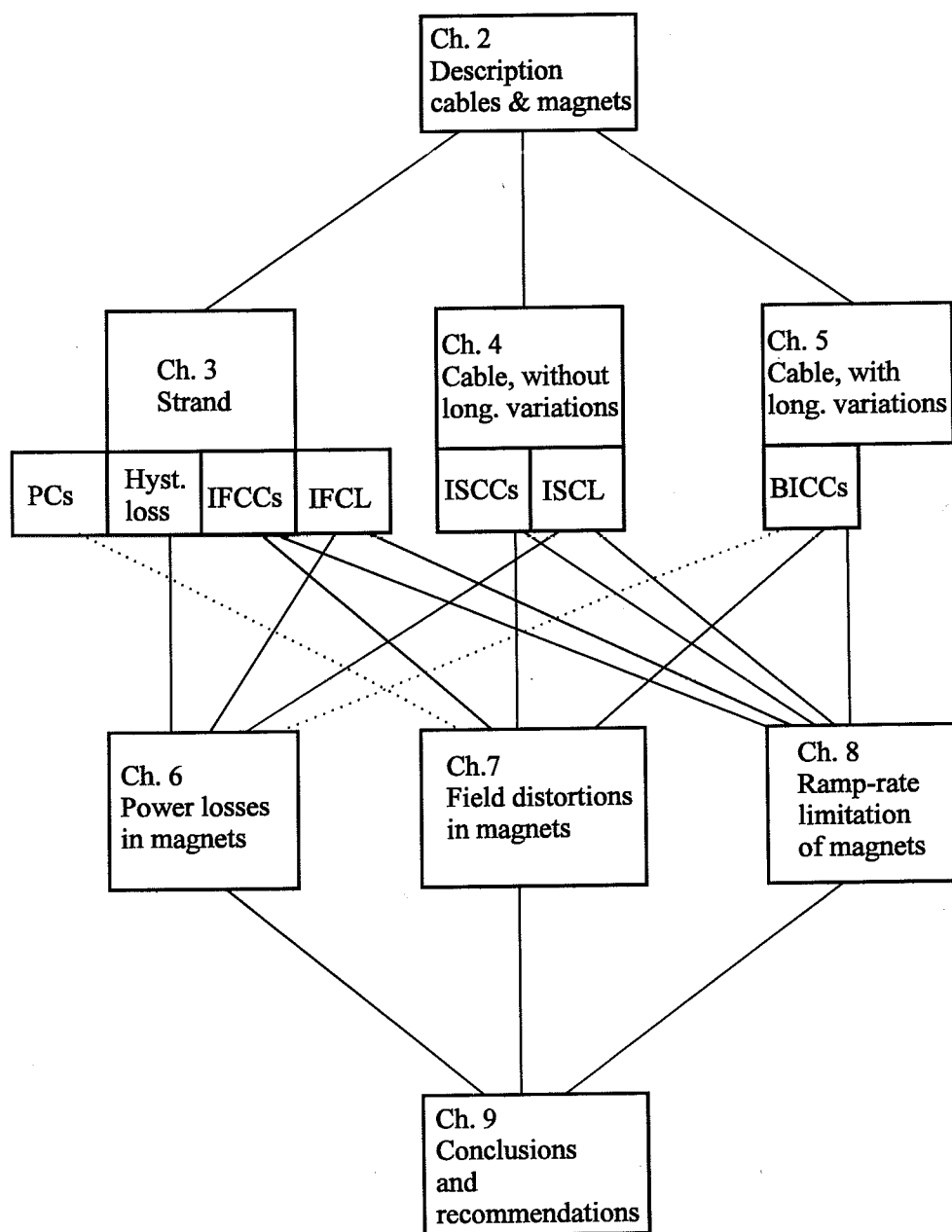


**Figure 1.3.** Schematic outline of the thesis, showing how the persistent currents, the coupling currents and the power losses at strand and cable levels affect the electrodynamic properties of superconducting magnets. The dotted lines are links that are present in a magnet but not discussed in the thesis.



## Chapter 2

# Multistrand cables and magnets

### **A survey of aspects affecting the electrodynamic properties of superconducting cables and magnets**

*The starting point of this chapter is the general expression for the magnetic field in the aperture of a magnet, which leads to the current distribution for generating a perfect multipole field of the order  $n$ . It is shown that, in particular, a perfect dipole field can be approximated by means of a 'shell-type' configuration of multistrand Rutherford-type cables.*

*The grading of the current density between the inner and outer coils and the structure enclosing the superconducting coils are discussed. Moreover, aspects concerning the operation of magnets such as quenching, training, quench protection, beam losses, operation procedure and operating temperature are dealt with. Those aspects of the cables and magnets that directly influence the electrodynamic behaviour of the magnets are explained in more detail. These are especially: the precompression of the coils, the cable-to-cable connections, the field and stress distribution in the straight part and in the coil ends, the cable geometry, the curing of the cable insulation, the matrix resistivity, the filament size and the twisting of the filaments and strands.*

*A survey of the dipole model magnets that are investigated at CERN is presented as well as a survey of the main characteristics of the cables from which the coils are wound.*

*Finally, a general relation between the critical current in a NbTi superconductor and the field and temperature is introduced which is required for the analysis of the ramp-rate induced quenches (chapter 8).*

## 2.1 Magnetic field in the aperture of a magnet

The magnetic field at position  $z=x+iy$  (see Fig. 2.2a) in the aperture of an accelerator magnet is usually expressed as a multipole expansion in two dimensions:

$$\mathbf{B} = B_y + iB_x = \sum_{n=1}^{\infty} (B_n + iA_n) \left( (x+iy)/r_0 \right)^{n-1} \quad [\text{T}], \quad (2.1)$$

with  $r_0$  the reference radius (normally  $r_0=10$  mm) and  $n$  the number of the harmonic component.  $B_n$  and  $A_n$  are called the normal- and skew-multipole coefficients respectively.

A coil, in which only  $B_1$  and  $A_1$  have finite values, while all the higher components ( $n>1$ ) are zero, is called a dipole coil and has a field:

$$\mathbf{B} = B_1 + iA_1 \quad [\text{T}]. \quad (2.2)$$

In a twin-aperture magnet the  $A_1$  component represents the misalignment between the dipole field of the two coil systems. In the case of single-aperture magnets the coordinate system is often defined in such a way that the average  $A_1$  (along the magnet axis) equals 0 so that  $\mathbf{B}$  corresponds to a normal-dipole field in the  $y$ -direction.

A coil in which all multipole fields are zero except for  $n=2$  is called a normal quadrupole coil and has a field:

$$\mathbf{B} = B_2 \left( \frac{x}{r_0} + i \frac{y}{r_0} \right) + A_2 \left( i \frac{x}{r_0} - \frac{y}{r_0} \right) \quad [\text{T}], \quad (2.3)$$

where the coordinate system is often defined in such a way that the average  $A_2$  is equal to 0. In a similar way sextupole ( $n=3$ ), octupole ( $n=4$ ), decapole ( $n=5$ ) and higher-order coils are defined (note that in the USA  $n=0$  is taken as the dipole,  $n=1$  the quadrupole and so on).

A perfect multipole field of order  $n$  is produced by a current density that varies as a function of the azimuthal angle  $\theta$  as:

$$J(\theta) = J_0 \cos(n\theta) \quad [\text{Am}^{-2}]. \quad (2.4)$$

The current distributions for a dipole, quadrupole and sextupole field of infinitely long coils are shown in Fig. 2.1.

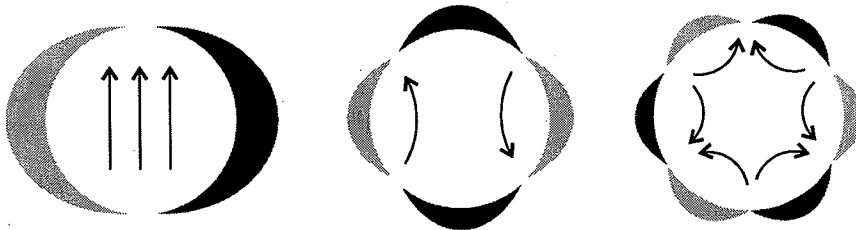


**Figure 2.1.** Current distributions for generating pure dipole, quadrupole and sextupole fields. The dark and light parts indicate positive and negative current densities respectively. The arrows denote the field direction. The direction of the currents is normal to that of the fields.

Dipole and quadrupole magnets are the main magnetic components of circular accelerators. The function of the main dipole magnets is to keep the beam of accelerated particles on the circular equilibrium orbit, perpendicular to the field direction. The main quadrupole magnets focus and defocus the beam around the equilibrium orbit.

Since a perfect  $\cos(n\theta)$  current distribution can never be technically achieved, other multipole components are present which are referred to as distortions or field errors. The distortions are corrected for by using tuning quadrupole-, sextupole- and other higher-order coils. Skew dipole magnets are required for correcting the beam in the vertical plane.

The main multipole is often referred to as the main component or fundamental, while the other multipoles are called harmonics. The harmonics are often normalised to the main component, so, for example, for a dipole coil:

$$\mathbf{B} = B_1 \sum_{n=1}^{\infty} (b_n + ia_n) \left( (x+iy)/r_0 \right)^{n-1} \quad [\text{T}], \quad (2.5)$$

with:

$$b_n = \frac{B_n}{B_1}, \quad a_n = \frac{A_n}{B_1}. \quad (2.6)$$

Design values of  $b_n$  and  $a_n$  for the lower harmonics of the LHC dipole magnets at injection field  $B_{inj}=0.58$  T (see section 2.2.7) are typically about  $10^{-4}$  at  $r_0=10$  mm. The relative multipole components  $b_n$  and  $a_n$  are therefore often expressed in units of  $10^{-4}$ .

## 2.2 Magnet characteristics

In section 2.1 it is shown that a perfectly homogeneous dipole field is generated by a  $\cos(\theta)$  current distribution, i.e. by a geometry of two intersecting circles or ellipses with their centres spaced apart, and with opposite current direction (see Fig. 2.2a). In practical high-field accelerator magnets such a current distribution can only be approximated since the coils are made from cables. Wide flattened cables carrying high currents are applied in order to limit the inductance and therefore enable a safe quench protection.

Usually, the so called 'shell-type' configuration is applied to approximate the ideal  $\cos(\theta)$  distribution. The cross-section of one quadrant of one aperture of a typical LHC dipole magnet is shown in Fig. 2.2b. Quadrants 1 and 2 are also referred to as pole 1 and quadrants 3 and 4 as pole 2. The main advantages of this configuration are that the conductor is put close to the aperture for an efficient use of the superconductor and that the coil ends are formed 'naturally' by the Roman-arc geometry. The blocks are separated by copper wedges to have enough design parameters to produce a high-quality dipole field and because the keystone angle of the cable (see eq. 2.14) is not sufficiently large to have radially orientated cables.

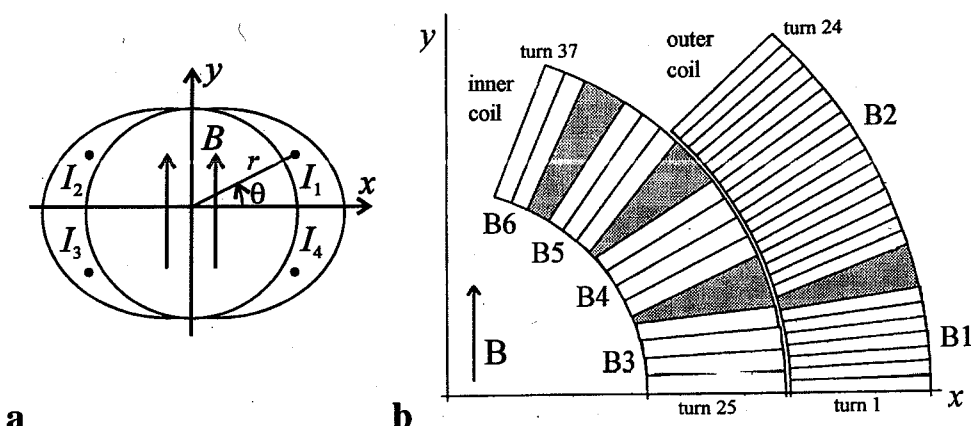


**Figure 2.2.** a: Generation of a perfect dipole field by two intersecting ellipses with their centres spaced apart.  $I_1$  (+),  $I_2$  (-),  $I_3$  (-) and  $I_4$  (+) indicate the currents in the four quadrants at positions  $(r, \theta)$ ,  $(r, \pi - \theta)$ ,  $(r, \pi + \theta)$  and  $(r, -\theta)$  respectively.  
 b: View of the cross-section of the turns of quadrant 1 of a two-shell dipole (here the design of the Pink Book Dipole magnet - see Table 2.1- is shown) and nomenclature of the blocks and turns (1-24 in the outer coil and 25-37 in the inner coil).

Since the currents in the inner and outer coils are equal while the peak field in the inner coil is larger than that in the outer coil (see also Fig. 2.6), a *grading of the current density* between the two coils is preferable. The grading is obtained by winding the inner and outer coils from cables with a different cross-section. Hence, three different *cable-to-cable connections* are present:

- Connections between the two coils of the same pole, also called splices. Each splice is located in a high-field region and is made by soldering the two cables over a length of about 15 cm (see Fig. 2.3). The resistance of the splice is typically 0.2-0.5 nΩ at zero field and increases due to the magnetoresistance with a factor of about 2-4 for a central field of 9 T.
- Connections between the coils of different poles. The connections are located in a low-field region and often shunted by a copper bar which results in a small resistance, normally about 0.2-0.5 nΩ.
- Connections between the current leads and the cables.

Fig. 2.3 shows a longitudinal view of the magnet with the positioning of the turns and the connections. The head of the magnet where the connections are located is referred to as the connection end whereas the opposite end is called the non-connection end.

The field distribution in the coil ends differs considerably from that in the straight part. Since the cable is bent over the beam pipe (see Fig. 2.4), the field  $B_1$  normal to the large face of the cable reduces to almost zero (see also section 2.2.4). As a result, the interstrand coupling power loss, which is proportional to  $\dot{B}_1^2$  (see chapter 4), is strongly reduced in the coil ends. However, the strong variations in  $\dot{B}_1$  along the cable also cause boundary-induced coupling currents (see chapter 5) which affect the electrodynamic properties of the magnet.

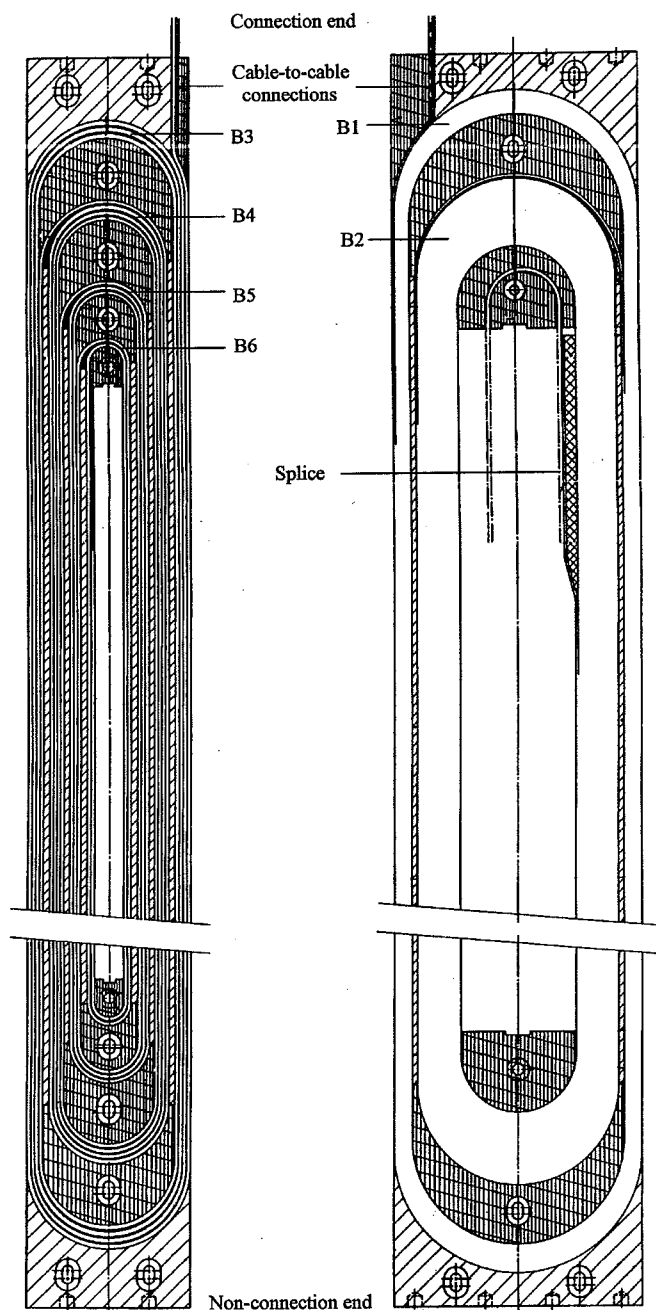


**Figure 2.3.** Longitudinal view of one pole of a dipole magnet showing the positioning of the turns, the splice between the inner and outer coils, and the connections to the other poles or the current leads. The turns of the outer coil are not drawn individually [LHC, '88].



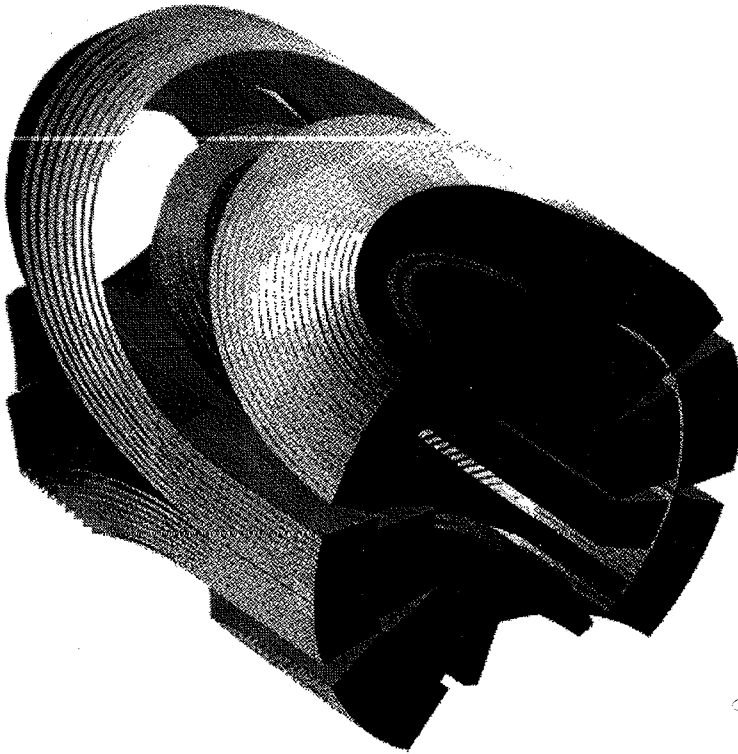


**Figure 2.4.** 3D view of the turns at the non-connection end of a six-block LHC-type dipole magnet [Russenschuck, '93].

The field at a position  $\mathbf{z}=x+iy$  caused by a current  $I$  at position  $\mathbf{r}=x_1+iy_1$  is, according to the law of Biot and Savart:

$$\mathbf{B} = \frac{\mu_0 I}{2\pi(\mathbf{z}-\mathbf{r})} \quad [\text{T}]. \quad (2.7)$$

A current distribution over the four quadrants in a magnet (see Fig. 2.2a), symbolically represented by:

$$\begin{bmatrix} I_2 & I_1 \\ I_3 & I_4 \end{bmatrix} \text{ at } \begin{bmatrix} r, \pi - \theta & r, \theta \\ r, \pi + \theta & r, -\theta \end{bmatrix}, \quad (2.8)$$

can be described by a linear combination of the currents  $I_A$ ,  $I_B$ ,  $I_C$  and  $I_D$ , corresponding to the different harmonic components of eq. 2.5:

$$\begin{bmatrix} -1 & +1 \\ -1 & +1 \end{bmatrix} I_A \quad \text{normal odd, } B_1, B_3, B_5 \dots, \quad (2.9)$$

$$\begin{bmatrix} +1 & +1 \\ +1 & +1 \end{bmatrix} I_B \quad \text{normal even, } B_2, B_4, B_6 \dots, \quad (2.10)$$

$$\begin{bmatrix} +1 & +1 \\ -1 & -1 \end{bmatrix} I_C \quad \text{skew odd, } A_1, A_3, A_5 \dots, \quad (2.11)$$

$$\begin{bmatrix} -1 & +1 \\ +1 & -1 \end{bmatrix} I_D \quad \text{skew even, } A_2, A_4, A_6 \dots \quad (2.12)$$

In practical dipole magnets all normal odd harmonics are present since the current distribution is slightly different from the ideal  $\cos(\theta)$  shape. Due to fabrication tolerances normal-even and skew harmonics can also arise. In twin-aperture magnets with a common mechanical structure additional field errors are introduced due to (non-symmetric) saturation effects of the iron yoke.

### 2.2.1 Magnet designs

Two designs of LHC-type dipole magnets are discussed in this thesis (see Table 2.1):

- The Pink Book Dipole magnet<sup>1</sup> -PBD- [LHC, '91]: the first official design of the bending magnets of the LHC. All experimental results described in chapters 6-8 are based on PBDs and the cables from which the coils are made.
- The White Book Dipole magnet -WBD- [LHC, '93]: the renewed design for the bending magnets as described in the second concept study for the LHC. The coils are made from smaller cables and operate at a lower field level in an effort to reduce the training as observed in the PBD models. The decrease in the field only slightly reduces the collision

**Table 2.1.** Survey of the design parameters of two LHC-type dipole magnets. The operating field and current correspond to the indicated collision energy.

		PBD <sup>a</sup>	WBD <sup>b</sup>
Maximum collision energy	TeV	15.4	14
Operating field	T	10	8.65 <sup>c</sup>
Operating current	A	15060	11470
Magnetic length	m	9	13.145
Number of turns of the inner coil per aperture	-	26	30
Number of turns of the outer coil per aperture	-	48	52
Cable width	mm	17	15
Diameter of the aperture	mm	50	56

<sup>a</sup> [LHC '91]

<sup>b</sup> [LHC '93]

<sup>c</sup> In 1994 the operating field was changed to 8.36 T [Perin, '95]

<sup>1</sup> The names 'Pink Book' and 'White Book' refer to the colour of the official CERN reports in which the designs of the magnets are described.

energy of the LHC since the effective magnetic length is increased. Results of calculations and simulations on the cables and coils of the WBD magnet are presented in chapters 6-8 in order to envisage the electrodynamic behaviour of the future LHC. Several aspects of the dipole magnets will be discussed in more detail in the following sections.

### 2.2.2 Cold mass

The cross-section of the twin-aperture LHC dipole magnet inside its cryostat is shown in Fig. 2.5. The so-called 'two-in-one' structure, in which the two beam channels (or apertures) are enclosed in a common structure, results in an economical and compact geometry.

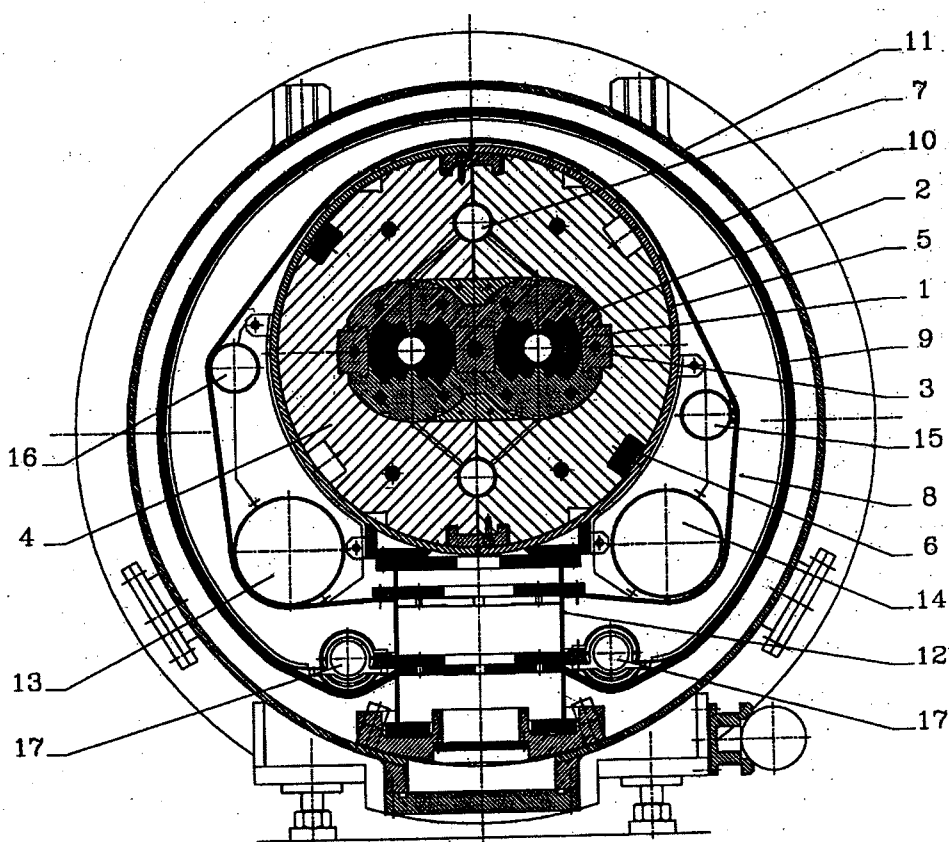


**Figure 2.5.** Cross-section of an LHC-type dipole magnet within its cryostat [LHC, '91].

- |                       |                               |                                |
|-----------------------|-------------------------------|--------------------------------|
| 1. Beam pipe          | 7. Heat exchanger             | 13. GHe pipe (5-10 K)          |
| 2. Coils              | 8. Radiative insulation (5 K) | 14. GHe pipe (1.8 K)           |
| 3. Collars            | 9. Thermal shield (50-70 K)   | 15. LHe pipe (2.2 K)           |
| 4. Yoke               | 10. Superinsulation           | 16. He pipe (5 K)              |
| 5. Shrinking cylinder | 11. Vacuum vessel             | 17. Cooling channels (50-70 K) |
| 6. Bus bars           | 12. Support post              |                                |

The part formed by the shrinking cylinder (nr. 5) and the interior are referred to as the cold mass, which is cooled down to a temperature of 1.9 K (or 4.3 K for some test measurements) before excitation. The main components of the cold mass are:

- The inner and outer coils (see Fig. 2.2b), made of superconducting NbTi cable. The characteristics of the cables are given in the section 2.3.
- The aluminium or stainless-steel collars, providing part of the prestress (see section 2.2.3) and defining the exact geometry of the coils.
- The iron yoke, shielding the exterior against the internal field and enhancing the central field in the aperture of the magnet by about 15%.
- The shrinking cylinder, providing part of the prestress and containing the Lorentz forces of about 600 tons/m maximum. It serves to contain the helium of the magnet cold mass and, at the same time, provides structural rigidity and longitudinal support.

### 2.2.3 Pre-compression of the coils

The support structure compresses the coils radially from the outside which results in an azimuthal compressive stress in the coils. The support has to counteract the Lorentz forces during excitation in order to avoid conductor displacements (i.e. to avoid premature quenching) and coil deformation (i.e. to reduce field errors). The value of the prestress is difficult to calculate due to fabrication tolerances, friction, possible plastic deformation and the different shrinkages of the magnet parts during cool-down. The required compression is about 60 MPa for the outer coil and 80 MPa for the inner coil. During the collaring process, the compressive stress in the coils can be 30-40% higher than the required value in order to obtain a small clearance which would permit the insertion of rods or keys to lock the collars together. Once the press force is released the stress in the coils decreases to a lower value.

The maximum compressive stress in the coils is an important parameter for the interstrand coupling loss since it can lead to deformation of the strand-to-strand contacts and can therefore decrease the contact resistance between strands (see section 4.3).

### 2.2.4 Field and force distributions

The field distribution over the cross-section of the straight part of the PBD magnet is depicted in Fig. 2.6 and the minimum and maximum values per block are given in Table 2.2. Note that the field varies strongly across the cable width and even reverses its sign in blocks 1 and 2. The consequences of such field variations with respect to the coupling currents are discussed in section 4.4 and chapter 5.

A survey of the minimum and maximum values of the azimuthal stress  $\sigma_\theta$  per block is given in Table 2.2. The values are indicative for the actual stress in a coil. During the collaring process the compressive stress in the coils is usually temporarily increased beyond the indicated values in order to lock the collars.

In a twin-aperture magnet the stress is larger in the quadrants near the centre and is slightly smaller in those quadrants near the shrinking cylinder. The compressive stress varies strongly across the cable width, with an average of about 40 MPa in the outer coil and 60 MPa in the inner coil.

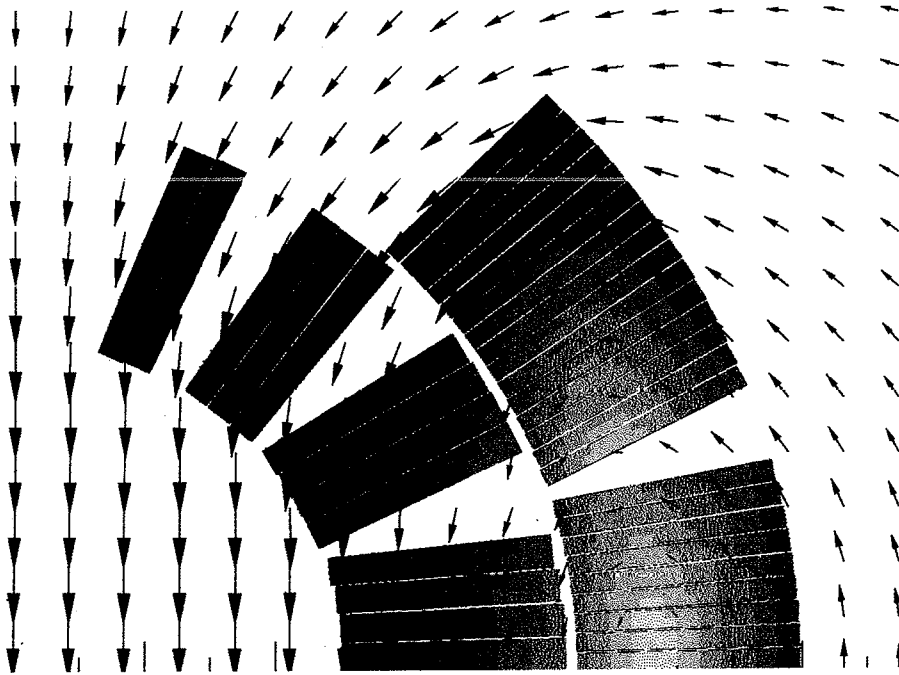


**Figure 2.6.** Field distribution in one quadrant of the straight part of a PBD magnet [Russenschuck, '93]. The arrows indicate the direction and the magnitude of the field.

The average values increase by about 20 MPa after cool-down. After excitation to 8-10 T the Lorentz force causes the average stress to vary between 105 MPa near the midplane to 50 MPa near the pole. The consequence of such stress variations across the cable width and over the cross-section of the coils on the contact resistance  $R_c$  between crossing strands are discussed in section 4.10 and chapter 5.

**Table 2.2.** Survey of the calculated magnetic field [Russenschuck, '93] and azimuthal stress [Spigo, '94] in each block of the PBD magnet. The minimum and maximum fields correspond to a central field of 10 T. The field  $B_{\perp}$  denotes the field component normal to the wide side of the cables in the block. The stress at 300 K, at 2 K, 0 T and at 2 K, 10 T are characteristic values before and after cool-down and excitation respectively.

Nr. of block	$B_x$ [T]	$B_y$ [T]	$B_{\perp}$ [T]	$\sigma_{\theta}$ (300 K) [MPa]	$\sigma_{\theta}$ (2 K, 0 T) [MPa]	$\sigma_{\theta}$ (2 K, 10 T) [MPa]
1	0-2.3	-3.1- 4.6	-3.1-4.5	40 (20- 70)	55 (50- 90)	90 ( 75-110)
2	0.5-5.8	-2.4- 7.6	-3.1-4.3	40 (20- 70)	55 (50- 70)	55 ( 20- 90)
3	0-1.3	4.5- 9.8	4.5-9.8	55 ( 0-110)	75 (60- 90)	105 (100-120)
4	-0.1-2.2	5.5- 9.9	4.6-8.7	55 (20- 90)	75 (50-100)	90 ( 70- 90)
5	0-3.7	7.3-10.1	1.3-6.1	60 (40- 90)	75 (70- 90)	70 ( 40- 90)
6	0-2.8	7.2-10.2	0.5-4.2	60 (20-140)	80 (70-130)	50 ( 20- 90)

## 2.2.5 Superconductor

High-field accelerator dipole magnets with a central field of 8-10 T have coils made of either NbTi or Nb<sub>3</sub>Sn superconductors.

### NbTi

Up to about 7.5 T, magnets are often cooled by liquid helium at 4.2 K. For higher fields superfluid helium below 2.17 K has to be used as a coolant which requires a more expensive and less efficient refrigeration system. Another drawback is the small heat capacity of all materials at 1.9 K which requires a very good heat exchange with the helium to avoid a temperature increase due to transient energy deposits. The heat capacity  $C$  (per unit volume of conductor) of NbTi with copper matrix [Lubell, '83] is:

$$C = (6.8 + 43.8\eta)T^3 + \eta(97.4 + 69.8B)T \quad [\text{Jm}^{-3}], \quad (2.13)$$

which is about 5 times larger at 4.3 K than at 1.9 K (for a NbTi volume fraction  $\eta=0.35$  and  $B=8$  T). The large heat capacity and heat conductivity of superfluid helium are important advantages for cryogenic stability of the superconductor.

### Nb<sub>3</sub>Sn

Fields beyond 8-10 T and up to about 18 T at 4.3 K can be attained with Nb<sub>3</sub>Sn conductors. One accelerator dipole model magnet with a design field of 11.5 T at 4.2 K [Ouden, den, '94] has been constructed and has reached 11.1 T. Another Nb<sub>3</sub>Sn dipole magnet with a design field of 13 T is still under construction [Dell'Orco, '93]. Due to the severe sensitivity of Nb<sub>3</sub>Sn to stress and strain [Haken, ten, '94], the coils are made using the 'wind and react process'. This implies that the conductor (with niobium and tin inside) is first wound and then heat-treated (at a temperature of about 700 °C for at least two days) to form the superconducting Nb<sub>3</sub>Sn. After the heat-treatment the coils are collared. Although the subsequent impregnation of the coils disables the helium to flow through the voids, the higher heat capacity of the material at 4.3 K could provide a safer operation than when using NbTi. The 'wind and react' process requires that the cable insulation and all other components in the collared coil withstand the reaction temperature.

In some Nb<sub>3</sub>Sn conductors 'bridging' occurs, which implies that during the chemical reaction between niobium and tin, filaments link together, thereby increasing the effective filament diameter. Bridging could be a drawback for some Nb<sub>3</sub>Sn conductors since it results in larger field distortions and a larger hysteresis loss (see chapter 3).

The formulas presented in this thesis will hold for NbTi as well as for Nb<sub>3</sub>Sn cables and magnets unless otherwise specified. However, all experimental results refer to NbTi cables and magnets.

## 2.2.6 Quenching and protection

The term 'quench' is generally used to denote the irreversible transition from the superconducting to the normal conducting state. A quench is often caused by a local transition of a strand section which generates heat and subsequently causes the other part of the strand and cable to quench. This 'avalanche' process propagates through the strand and

cable with a certain propagation velocity of which the value depends on several parameters such as the resistivity of the material, heat transfer, geometry, temperature, field and current. A typical propagation velocity is about  $10\text{--}50\text{ ms}^{-1}$  for NbTi superconductors.

Many magnets exhibit so-called 'training', a process characterised by a quench current that gradually increases with the increasing number of quenches. Training is present if the quenches are caused by displacements of strands or cables which locally heat up the cable (due to frictional energy) or by heat released in the cable surroundings such as epoxy cracking.

A thermal cycle of a (fully) trained magnet often reduces training since many displacements remain irreversible during warm-up and cool-down. Training can be improved by properly clamping the windings (so that the Lorentz force during excitation will not cause any displacement), by improvement of interfaces or impregnations and by enhancement of the cooling capacity of the windings.

When a superconducting magnet quenches, the stored magnetic energy is either dissipated outside the coil or distributed, as much as possible, within the coils to avoid overheating and possibly burning of part of the coil. In magnets with a large stored energy an active system of heaters is used to initiate multiple hot spots in the conductor as soon as a quench is detected, which results in a more global heating of the coils.

In an accelerator ring many magnets are connected in series. In case of a quench, the current is guided around the quenched magnet (by means of diodes) while the remaining series-connected magnets are de-excited [Coull, 94]. In this case, only the magnetic energy of the quenched magnet is dissipated as heat internally in the magnet. In order to avoid the quench spreading to the other magnets and the diode overheating, the chain of magnets has to be discharged rapidly if there is a quench in one of the magnets. The fast de-excitation is achieved by switching dump resistors in series with the magnets.

The LHC will be divided into 16 sub-units that are powered separately and are therefore electrically independent. The reduction of the coupling loss during de-excitation is, among other things, one of the advantages of such a subdivision. A de-excitation time constant of about 100 s is anticipated for the LHC, which corresponds to an initial field-sweep rate in the centre of the aperture of about  $-0.084\text{ Ts}^{-1}$ .

During the fast de-excitation, the coils of the series-connected magnets have to remain superconductive. This implies that the generated coupling currents and energy loss during the discharge should not cause the temperature in the cable to increase beyond the current-sharing temperature (see section 2.4).

### 2.2.7 Operating procedure

The beam is preaccelerated and then injected into the main accelerator at the injection field  $B_{inj}$  which is typically a factor of 10 to 20 smaller than the peak field (for LHC:  $B_{inj}=0.58\text{ T}$ ). The field sweep from 0 to  $B_{inj}$  can be freely defined since the beam has not yet been injected. A field precycle can be performed to verify the magnet's characteristics.

Once the beam is injected, which takes about 400 s, the dipole field is ramped up to the operation field. The excitation from injection field to nominal field (8.4 T) for LHC is foreseen to take about 1200 s which corresponds to an average central-field-sweep rate of

$0.0066 \text{ Ts}^{-1}$ . The field-sweep rate does not have to be constant but may vary during the sweep. At injection as well as at the operating field, the field homogeneity and the field stability in time should meet certain specifications in order to facilitate the field correction.

### 2.2.8 Beam losses

In high-luminosity colliders a continuous beam loss is present due to the emittance of particles. An actively cooled beam shield, placed inside the aperture, shields the coils from the particles. However, some particles still penetrate into the coils where the energy is absorbed by the conductor (see [Burnod, '89/'91] for a description of this process in LHC). The number of lost protons for LHC that is allowed to maintain the magnet at a sufficiently low temperature can be determined once the energy deposit per incident proton (inside the coil) and the thermal resistance between the coils and the coolant are known. In chapter 8 the latter effect is discussed in detail.

### 2.2.9 Survey of the model magnets

During the period 1990-1995 several dipole model magnets were constructed in industry and investigated at CERN. A survey of the models is presented in Table 2.3 and the characteristics of the cables are discussed in the next section. Besides the cables, the magnets are slightly different mainly with respect to the materials of the collars, end spacers and outer cylinder.

**Table 2.3.** Survey of the investigated NbTi dipole model magnets for the LHC (status of march '95). Three 10 m long models that are still under construction are included. The characteristics of the cables of the inner and outer coils of the magnets are presented in the next section (SA=single-aperture magnet, TA=twin-aperture magnet).

Magnet code	Manufacturer	SA/TA	Length [m]	Cable (see Table 2.4)		Date of first cool-down
				Inner coil	Outer coil	
AN1	Ansaldo	TA	1	I-1	O-4	05/91
AN2	Ansaldo	TA	10	I-2	O-3	03/94
AN3	Ansaldo	TA	10	I-6	O-6	07/94
AN4	Ansaldo	TA	10	I-6	O-6	03/95
CE1	CERN	TA	1	I-2	O-3	03/93
EL1	ELIN	TA	1	I-3	O-4	02/91
EL2	ELIN	SA	1	I-3	O-3	08/92
HO1	Holec	TA	1	I-3	O-1	08/91
JS1	Jeumont Schneider	TA	1	I-1	O-2	03/91
KE1 <sup>a</sup>	KEK	SA	1	I-5	O-5	05/92
KE2 <sup>a</sup>	KEK	TA	1	I-5	O-5	06/93
NO1	Noël	TA	10	I-7	O-7	11/94
AJS1	Alsthom/JS	TA	10			under construction
EH1	ELIN/Holec	TA	10			under construction
NO2	Noël	TA	10			under construction

<sup>a</sup> See [Yamamoto, '93] for more details on the slightly different design.



Either common or separate collars are applied for the two apertures which are assembled with rods and/or keys. These mechanical differences do not significantly contribute to different time-dependent electrodynamic properties of the magnets and are disregarded here but details are presented elsewhere [Bona, '92], [LHC, '93].

The coils of the two magnets manufactured by KEK are made of high keystoneed 15 mm wide cables and differ therefore from the other magnets. No wedges are present in these two magnets.

### 2.3 Strand and cable characteristics

The coils of high field accelerator magnets are often wound from high-current Rutherford-type cables (see Figs. 1.1a and 2.7), mainly to limit the inductance in order to obtain a safe quench protection. Such cables are formed by flattening a hollow tubular cable comprising between 20 and 40 strands. After cabling, the conductors are compacted by rolling in order to increase the overall current density in the coil. Flat NbTi cables can be compacted to filling factors of about 90% without significant damage. During the rolling the dimensional control is important in order to achieve the desired field uniformity.

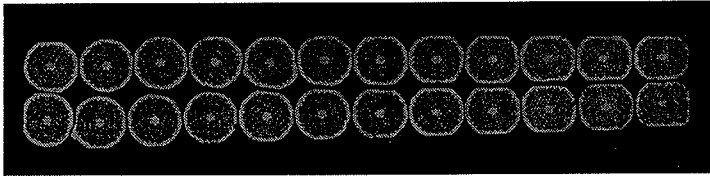


**Figure 2.7.** Cross-section of a 24-strand Rutherford-type cable with the thick edge on the left and the thin edge on the right. Note the severe deformation of the strands at the thin edge resulting in a large contact area between the strands of the two layers.

The strands are fully transposed with a transposition length (or cable pitch)  $L_{p,s}$  which is usually about 6-8 times the cable width  $w$ . The cable has a small keystone angle in order to have a more uniform structure of the coils and facilitate the winding of the magnet. The angle is defined as:

$$\alpha_k = \text{atan}((h_1 - h_2) / w) \quad [\text{deg}], \quad (2.14)$$

with  $h_1$  and  $h_2$  the thicknesses of the two small sides of the cable. Note the severe deformation of the strands in the cable, in particular at the thin edge, which leads to a large contact area between strands of the top and bottom layers. An increase of the contact area results in a decrease of the contact resistance  $R_c$  between the strands of both layers which is one of the key parameters concerning the interstrand coupling loss (see chapter 4).

Particular care is required to provide the cable with an insulation that not only withstands the voltage between turns but is also sufficiently porous to allow permeation of the helium. The insulation has to be strong enough to avoid breakage which could lead to short-circuits between the turns. The insulation is composed of a half-overlapped layer of kapton tape having a thickness of 25  $\mu\text{m}$  and one layer of 125  $\mu\text{m}$  thick glass-fibre tape,

pre-impregnated with epoxy resin with spaces of 2.5 mm between successive turns (Fig. 2.8). After winding, the coils are compressed and heat-treated for 2 hours at about 160 °C to cure the resin of the pre-impregnated glass-fibre tape so that adjacent turns adhere to each other. Such a heat treatment under pressure can strongly decrease  $R_a$  and  $R_c$ , due to plastic deformation of the strands (see section 4.3). The spacing between successive turns of the glass-fibre tape increases the porosity of the coil by forming helium flow channels without affecting the mechanical support between the turns. In and through the channels, the helium comes into direct contact with a large proportion of the cable surface and is likely to penetrate the interior of the cable, thereby providing additional stabilisation due to an increase of the enthalpy.

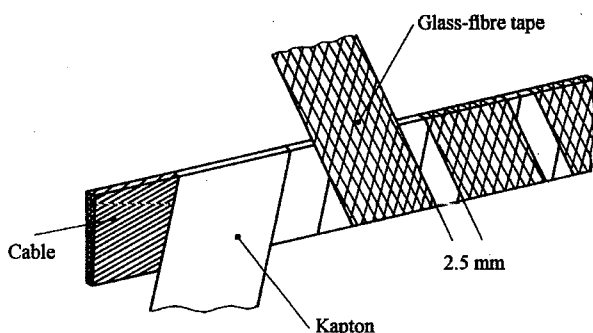


**Figure 2.8.** Insulation of the cable consisting of a half-overlapped layer of kapton tape with a thickness of 25  $\mu\text{m}$  and one layer of 125  $\mu\text{m}$  thick glass-fibre tape, pre-impregnated with epoxy resin with spaces of 2.5 mm between successive turns.

Due to the large azimuthal pressure on the turns in the coil, which reduces the size of the channels, it is uncertain whether the helium penetrates the channels and the interior of the cable. The maximum temperature of the helium in the interior of the cable should not exceed the transition temperature of 2.17 K, in order to benefit from its high thermal conductivity and low viscosity.

The main parameters of the cables of the LHC dipole model magnets (as specified in Table 2.3) are surveyed in Table 2.4. Note that the width of all the cables is 17 mm except for the cables I-5 and O-5 used in the two KEK dipole magnets. The strands in the cable differ mainly with respect to the filament diameter and the strand coating. The former influences the filament magnetisation (see section 3.2) while the latter affects the contact resistance between crossing strands and therefore the interstrand coupling currents (see section 4.4.1).

The multifilamentary strands consist of NbTi filaments embedded in a copper matrix (see Figs. 2.9a/b). The filaments in the strands are twisted in order to reduce the area enclosed by any two filaments and therefore the interfilament coupling loss in the case of a flux change (see section 3.4).

The main reason for the subdivision into small filaments is the reduction of the filament magnetisation (see section 3.2) which is the main cause of field distortions at weak excitation. Another advantage is the reduction of the energy loss during (de-)excitation.

**Table 2.4.** The main parameters of the inner (I-1 to I-7) and outer (O-1 to O-7) coil cables. All strands have Nb46.5%Ti filaments.

Name	I-1	I-2	I-3	I-4	I-5
Manufacturer	Alsthom	Alsthom	VAC	VAC	KEK
Dimensions (mm <sup>2</sup> )	17.0x2.04/2.50	17.0x2.04/2.50	17.0x2.04/2.50	17.0x2.04/2.50	15x1.88/3.09
Keystone angle (deg)	1.55	1.55	1.55	1.55	4.6
Number of strands	26	26	26	26	22
Ø strand (mm)	1.3	1.3	1.29	1.29	1.39
Cu/SC ratio	1.7	1.6	1.9	1.6	1.6
$L_{p,s}$ (mm)	130	130	130	117	110
Ø filament (µm)	14	5.4	25	4.8	6.0
Number of filaments	3060	21780	900	27954	ca. 21000
$L_{p,f}$ (mm)	25	25	25	25	25
$J_C$ at 8 T, 4.2 K (A/mm <sup>2</sup> )	1084	1087	986	938	910
$I_C$ (A) <sup>a</sup>	12350	13364	11288	ca. 12300	
Strand coating	zebra <sup>b</sup>	95%Sn/5%Ag	95%Sn/5%Ag	95%Sn/5%Ag	bare
Soldering	SnPb at one edge	no	no	no	no

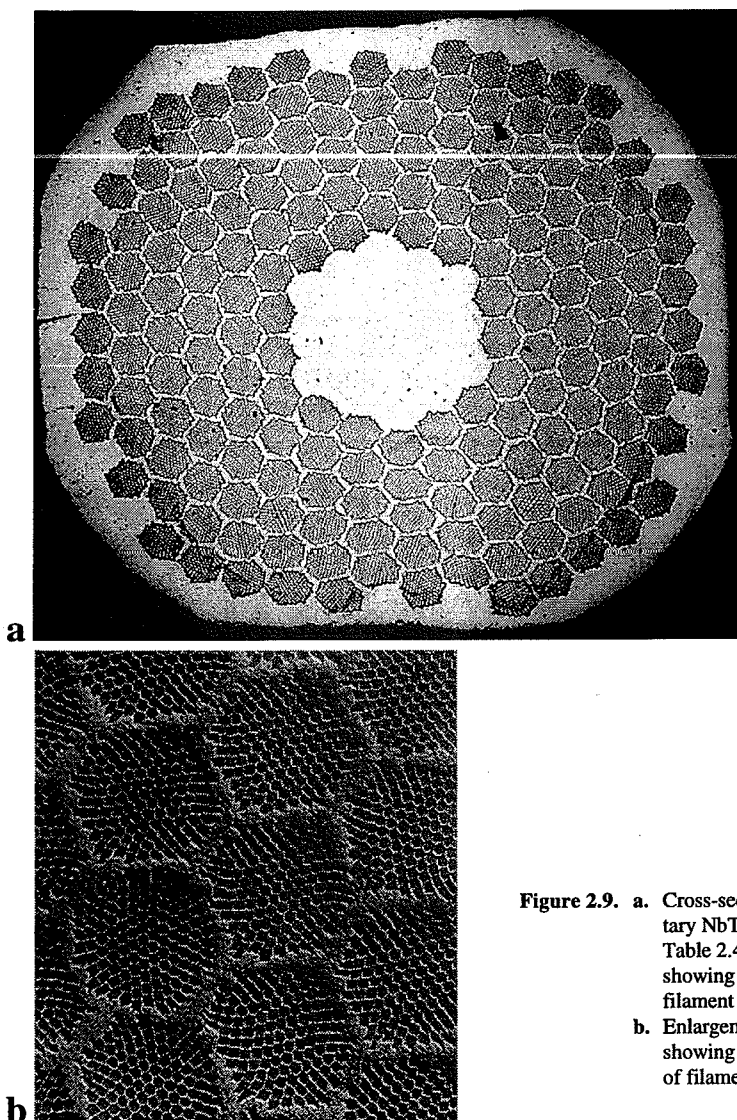
  

Name	I-6	I-7	O-1	O-2	O-3
Manufacturer	LMI	Alsthom	ABB	Alsthom	Alsthom
Dimensions (mm <sup>2</sup> )	17.0x2.04/2.50	17.0x2.04/2.50	17.0x1.32/1.67	17.0x1.30/1.65	17.0x1.30/1.65
Keystone angle (deg)	1.55	1.55	1.2	1.2	1.2
Number of strands	26	26	40	40	40
Ø strand (mm)	1.29	1.29	0.84	0.83	0.84
Cu/SC ratio		1.7	1.8	1.8	1.8
$L_{p,s}$ (mm)	120	130	132	95	100
Ø filament (µm)	7.8	4.8	14	9.5	5.1
Number of filaments	ca. 10500	26268	1230	2550	9438
$L_{p,f}$ (mm)	25	25	25	25	25
$J_C$ at 8 T, 4.2 K (A/mm <sup>2</sup> )				1136	
$I_C$ (A) <sup>a</sup>			16350	16040	16200
Strand coating	95%Sn/5%Ag	95%Sn/5%Ag	95%Sn/5%Ag		
Soldering	no	no			

Name	O-4	O-5	O-6	O-7
Manufacturer	LMI	KEK	LMI	VAC
Dimensions (mm <sup>2</sup> )	17.0x1.33/1.65	15.0x1.10/1.55	17.0x1.30/1.65	17.0x1.30/1.65
Keystone angle (deg)	1.1	1.7	1.2	1.2
Number of strands	40	37	40	40
Ø strand (mm)	0.84	0.79	0.84	0.84
Cu/SC ratio	1.8	1.8		1.75
$L_{p,s}$ (mm)	130	110	120	100
Ø filament (µm)	16	6.0	7.8	4.8
Number of filaments	ca. 1000	ca. 6000	ca. 4000	10164
$L_{p,f}$ (mm)	25	25	25	25
$J_C$ at 8 T, 4.2 K (A/mm <sup>2</sup> )		1040		
$I_C$ (A) <sup>a</sup>	17680	13766		
Strand coating		bare	95%Sn/5%Ag	95%Sn/5%Ag
Soldering	SnPb			

<sup>a</sup> at 8 T, 4.2 K for I-1 to I-7, and at 6 T, 4.2 K for O-1 to O-7<sup>b</sup> see section 4.6



**Figure 2.9. a.** Cross-section of a multifilamentary NbTi strand (number I-2, see Table 2.4) with 21780 filaments, showing the central core, the filament zone and the outer shell.

**b.** Enlargement of part of the strand showing the hexagonal bundles of filaments.

The stability of the strand in face of local thermal disturbances also benefits from the subdivision into small filaments. If a disturbance causes the temperature of a filament to rise locally beyond the critical temperature, the matrix can rapidly conduct the heat and transfer the current of the filament to adjacent filaments. The electrical resistivity of the matrix should therefore be small, especially in the longitudinal direction. The resistivity  $\rho_{mat}$  of the matrix at liquid-helium temperature can be expressed by:

$$\rho_{mat} = \rho_{mat,0} (1 + \alpha_m |B|) \quad [\Omega\text{m}], \quad (2.15)$$

in which  $\alpha_m|B|$  represents the increase of the resistivity by magnetoresistance which is inherent to metals. Technical values of  $\rho_{mat,0}$  and  $\alpha_m$  for copper are about  $1.2 \cdot 10^{-10} \Omega m$  and 0.5 respectively. The RRR-value (Residual Resistivity Ratio) gives the ratio between the resistivity at 300 K and at 4 K for zero field and is generally about 50-200 for practical NbTi superconductors.

A common lay-out of the cross-section of a NbTi strand consists of the following three concentric layers (see Fig. 2.9a):

- a central core of normal-conducting material,
- a ring filled with many thin filaments embedded in a matrix,
- an outer shell of normal-conducting material.

The outer shell is required to facilitate the wire production. The purpose of the normal-conducting core (and shell as well) is to maintain the required Cu/SC ratio for stability, since an empirical criterion for the filament spacing to filament diameter is about 0.15-0.20 [Green, '87].

The strands can be coated to increase  $R_a$  and  $R_c$  and therefore reduce the interstrand coupling currents and power loss (see chapter 4). Besides coatings, internal barriers in the strand or resistive barriers between the top and bottom layers of flat cables also enhance the contact resistances.

## 2.4 The $I_C(B, T)$ relation

The critical current  $I_C$  in a superconductor is a function of the field  $B$  and temperature  $T$ . The  $I_C(B, T)$  relation for NbTi can be described by the following formulas where the field direction is perpendicular to the current. At constant temperature the  $I_C$ - $B$  relation is expressed by means of the Kim relation [Kim, '62]:

$$J_C = J_0 B_0 / (B_0 + |B|) \quad [\text{Am}^{-2}] \quad \text{or:} \quad I_C = I_0 B_0 / (B_0 + |B|) \quad [\text{A}] \quad \text{for } |B| < B^*, \quad (2.16)$$

with  $J_0$ ,  $I_0$  and  $B_0$  temperature-dependent parameters. The Kim relation holds for most practical NbTi superconductors with  $B^*$  of about 3 T. The dependence of  $I_C$  on the field component parallel to the strand axis is not considered here since the relation is not well-known. A linear relationship for higher field is assumed (at constant temperature):

$$I_C = I_{C,0} (1 - C_0 |B|) \quad [\text{A}] \quad \text{for } |B| > B^*. \quad (2.17)$$

The temperature dependence of eq. 2.17 for NbTi with a volume fraction of about 45-50% Ti is expressed by the following empirical scaling law [Lubell, '83]:

$$I_C = (C_1 - C_2 |B|) \left( 1 - \frac{T}{T_C(B, I=0)} \right) \quad [\text{A}] \quad \text{for } |B| > B^*, \quad (2.18)$$

with the critical temperature or current-sharing temperature:

$$T_C(B, I=0) = 9.2 (1 - |B|/14.5)^{0.59} \quad [\text{K}]. \quad (2.19)$$

The linear relation between  $I_C$  and  $T$  is valid for temperatures higher than about 2-2.5 K. The constant 14.5 T (i.e. the critical field at 0 K and 0 A) has to be changed to about 14.8 T for fields larger than 10 T. In chapter 8 the linear relation is extended to temperatures of 1.9 K, which has no significant effect on the analysis of the ramp-rate limitation of magnets.

The  $I_C$ - $B$  relation at several temperatures is shown in Fig. 2.10. Also a characteristic 'load line' is included in the figure, which indicates the relation between the transport current in the cable and the peak field in the coil. In magnets with grading of the current density, each coil has a load line. The point of intersection of the load line and the  $I_C(B, T)$  relation indicates the maximum operating field and current at a temperature  $T$ . In magnets the operation field is about 20% lower than the critical field. The *temperature margin* is then defined as the difference between the operating temperature and the current sharing temperature.

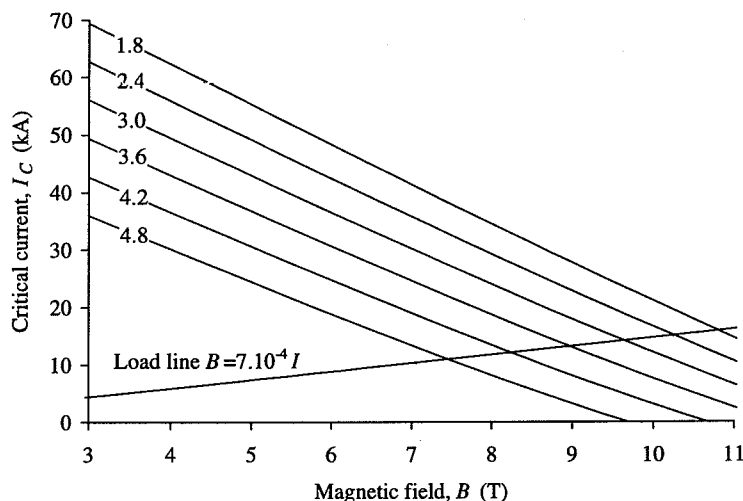


**Figure 2.10.** The  $I_C$ - $B$  relation of NbTi at several temperatures (1.8, 2.4, 3.0, 3.6, 4.2 and 4.8 K from top to bottom) according to eqs. 2.18 and 2.19 in the field range between 3 and 10 T. The constants  $C_1$  and  $C_2$  are taken to be  $11.3 \cdot 10^4$  A and  $7.8 \cdot 10^3$  AT<sup>-1</sup> respectively.

The unknown parameters  $I_0$  and  $B_0$  in the Kim relation are usually determined by means of a magnetisation measurement (see also section 3.3), while the temperature-dependent constants  $I_{C0}$  and  $C_0$  in eq. 2.17 are often extracted from a voltage-current measurement.

The current and field of a magnet cannot be varied independently, so that only one  $I_C(B)$ -value can be deduced at a certain temperature. The parameters  $C_1$  and  $C_2$  can then be deduced from the quench current (after training) at two different temperatures (e.g. 1.9 and 4.3 K). This is not possible if the training procedure is not completed or if the magnet is only operated at one temperature. In this case additional voltage-current measurements on a piece of cable, identical to the cable that is used in the coils, are required to estimate the parameters  $C_1$  and  $C_2$ .

## 2.5 Conclusions

Several aspects affecting the time-dependent electrodynamic behaviour of a coil are inherent to the design of the accelerator dipole magnet itself and are surveyed here.

- The need for a low inductance, in order to have a safe quench protection, requires a high-current cable. In order to increase the overall current density, coils are wound from multistrand Rutherford-type cables which are compacted to filling factors of about 90%. The combination of wide cables with a good contact between the strands enhances the coupling currents and power loss considerably (see chapter 4). In order to reduce the interstrand coupling currents, the strands are twisted. A further reduction of the coupling currents can be obtained by applying a coating on the strands, an internal resistive barrier in the strand or a resistive layer between the strands.
- The heat-treatment, in order to cure the resin of the pre-impregnated glass-fibre tape of the cable insulation, often results in a smaller  $R_c$  (see section 4.3), especially if the heat treatment is applied under pressure.
- A further reduction of  $R_c$  is inherent to the large stresses in the coils. These stresses are due to the Lorentz force during excitation as well as the large prestress that is required to avoid conductor displacements.
- The keystone of the cable results in a strong variation of  $R_c$  across the cable width.
- The performance of the magnet is improved by grading of the current density between the layers. This requires cable-to-cable connections with a small resistance to minimise the resistive loss. The local reduction of  $R_c$  introduces boundary-induced coupling currents during a field sweep (see chapter 5).
- The field perpendicular to the wide side of the cable decreases strongly in the coil ends where the cable bends around the beam pipe. These local variations in the field also provoke boundary-induced coupling currents during and after field sweeps.

The excitation of the LHC dipole magnets from the injection field (ca. 0.58 T) to the nominal field (ca. 8.4 T) is anticipated to take about 1200 s, which corresponds to an average central-field-sweep rate of about  $0.0066 \text{ Ts}^{-1}$ . In the case of a quench in a coil, the series-connected magnets have to be rapidly discharged. The time constant of the fast de-excitation is about 100 s which corresponds to an initial field-sweep rate of about  $-0.084 \text{ Ts}^{-1}$  maximum.

## Chapter 3

# Losses in strands

*The main objective of this chapter is to present a brief survey of the main loss components at strand level, namely the hysteresis loss in the filaments, the transport-current loss and the interfilament coupling loss.*

*The theory of the filament hysteresis and transport-current loss is discussed and general formulas are presented to describe the loss during a field change. The magnetisation due to the filament hysteresis in several LHC-type strands is experimentally determined.*

*The interfilament coupling loss is dealt with in detail and experimental results are given for several LHC-type strands in terms of the time constant  $\tau_{if}$  which quantifies the loss. The reduction of the maximum transport current in a strand, due to the additional interfilament coupling currents is discussed. The corresponding effect of the interfilament coupling currents on the ramp-rate limitation of dipole magnets is investigated.*

*The influence of the magnetisation of adjacent strands on the hysteresis loss and interfilament coupling loss is experimentally investigated, by evaluating the losses within the strand for a single strand as well as for a Rutherford-type cable.*



### 3.1 Introduction

In accelerator magnets, and especially at low excitation levels and small field-sweep rates, the energy loss and the field distortions are mainly determined by the filament hysteresis. The magnetisation or hysteresis loss is a well-understood phenomenon and it has already been shown in 1963 that the hysteresis can be reduced by the use of multifilamentary composite conductors with a small filament diameter [London, '63]. In order to provide stability and a good thermal conductivity the matrix of the conductors is generally a normal metal with a low electrical resistivity. This leads to the so-called interfilament coupling loss (IFCL) due to eddy currents in the normal matrix. The IFCL has been extensively treated by many authors and a useful publication is one by Campbell in which the IFCL and the time constant are discussed for various conductor geometries [Campbell, '82]. Detailed numerical solutions of the AC behaviour of superconducting wires have been presented during the last decade [Rem, '86], [Hartmann, '89]. Knowledge of the IFCL in the strands of a cable is necessary for separating the IFCL from the interstrand coupling loss in magnets. Only then can the origin of ramp-rate induced field-distortions and ramp-rate induced quenches in magnets be correctly evaluated.

In section 3.2 the hysteresis loss is discussed and illustrated by means of the current and field distribution over the cross-section of a filament exposed to a field cycle. It is shown that an additional transport current increases the total loss which is partially supplied by the external field and partially by the current supply.

Experimental results of the filament magnetisation are presented in section 3.3 for various cables from which the coils of the LHC dipole model magnets are wound. The analysis is made for filaments carrying no transport current exposed to field variations between -0.6 and 0.6 T at low frequency, so that the screening effect of the interfilament coupling currents (IFCCs) is small compared to the applied field. In chapter 6 the results are compared quantitatively to the hysteresis loss in entire coils.

The IFCCs are discussed in section 3.4 and it is shown that the loss can be represented by a mean time constant  $\tau_{ff}$ . The influence of the IFCCs, which saturate the outer layer(s) of filaments in a strand, on the maximum transport current is investigated. Experimental results are presented of  $\tau_{ff}$  of various cables as used in the LHC dipole model magnets and the corresponding decrease of the maximum transport current is estimated.

The influence of the neighbouring strands on the loss in a strand is discussed. This is achieved by determining not only the hysteresis loss and IFCL in a cable but also the losses in a single strand which is removed from the cable. The results and consequences for magnets are presented in section 3.5.

### 3.2 Hysteresis loss

If a superconducting filament without transport current is subjected to an increasing transverse magnetic field  $B_a$ , the field penetrates from the outside while the interior of the filament will remain field-free due to screening currents with density  $\pm J_C$  in the outer region (see Fig. 3.1a). The contour separating the screening currents region from the current-free region will penetrate the filament as the field increases because the critical current density is

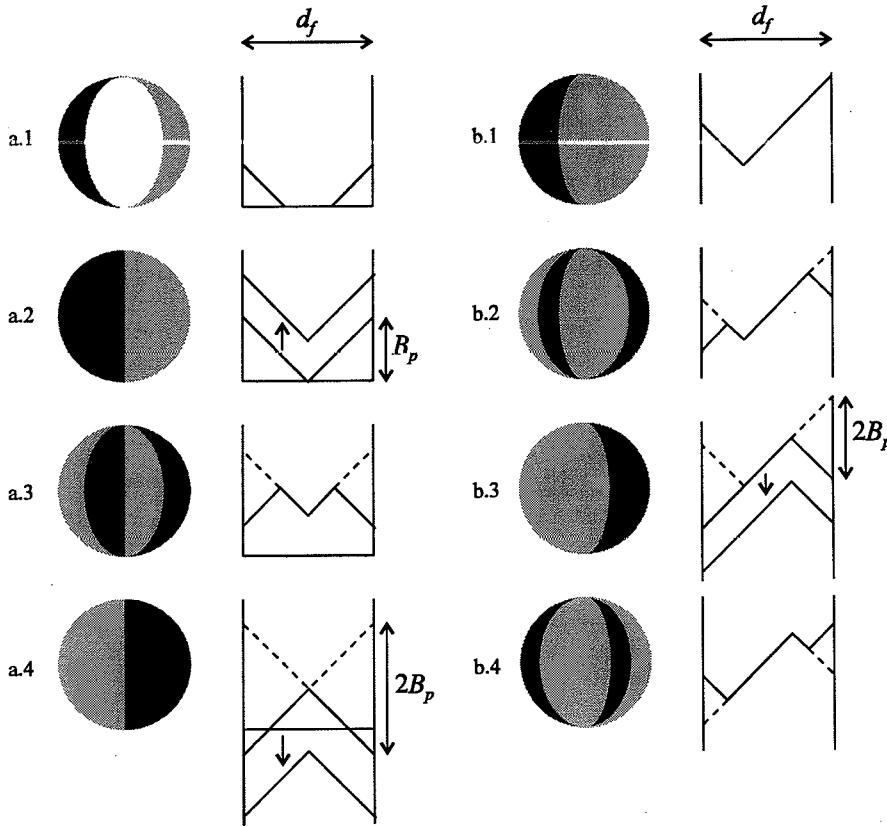


**Figure 3.1.** a. Current and field profiles of a superconducting filament without transport current in a varying external field: 1.  $B_{a,1} < B_p$ , 2.  $B_{a,2} = B_p$  and larger, 3.  $B_{a,2} - 2B_p < B_{a,3} < B_{a,2}$ , 4.  $B_{a,4} = B_{a,2} - 2B_p$  and smaller.  
b. Current and field profiles of a superconducting filament carrying a transport current in a varying external field: 1. field  $B_{a,1}$ , 2.  $B_{a,1} - 2B_p < B_{a,2} < B_{a,1}$ , 3.  $B_{a,3} = B_{a,1} - 2B_p$  and smaller, 4.  $B_{a,3} < B_{a,4} < B_{a,3} + 2B_p$ .

limited. The field at which the filament becomes completely penetrated is called the penetration field  $B_p$ , and is equal to:

$$B_p = \frac{\mu_0 J_C d_f}{\pi} \quad [\text{T}], \quad (3.1)$$

for round and isotropic filaments, with  $J_C$  the critical current density in the filament and  $d_f$  the filament diameter. The field  $B_p$  is therefore the maximum field produced by the screening currents. The magnetisation, defined as the magnetic moment per unit volume, of a fully penetrated round filament is:

$$M = -\frac{2}{3\pi} J_C d_f \operatorname{sgn}(\dot{B}_a) = -\frac{2}{3\mu_0} B_p \operatorname{sgn}(\dot{B}_a) \quad [\text{Am}^{-1}]. \quad (3.2)$$

When the applied-field change  $\vec{B}_a$  reverses its sign, the filament reacts again by screening the field, so that a new contour will appear in the outer region. A further change of the applied field will change the screening current density from  $+J_C$  to  $-J_C$  (and the other way around), so that the field is completely penetrated after a change of  $2B_p$  in the applied field (see Fig. 3.1a). A characteristic magnetisation loop is shown in Fig. 3.2 in the case of a filament with a penetration field of about 0.1 T at small fields and 0.05 T at  $B_a=0.5$  T.

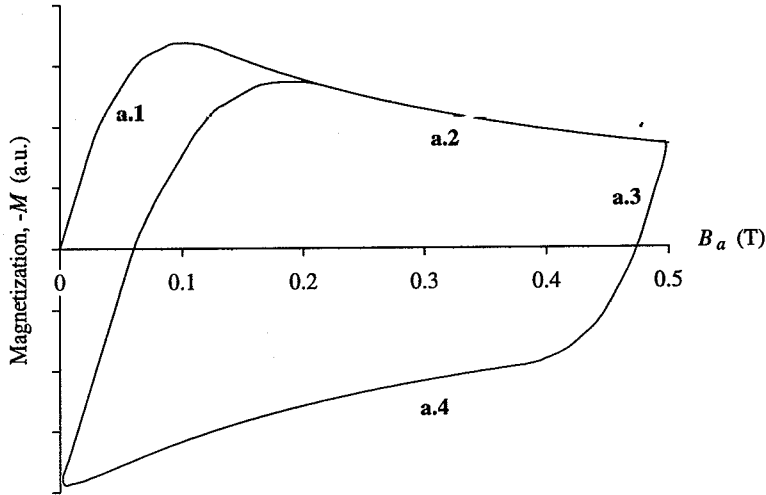


**Figure 3.2.** Magnetisation loop of a filament without transport current subject to a field cycle 0-0.5 T-0-0.5 T. The labels correspond to the magnetisation pattern as shown in Fig. 3.1a.

In high-field magnets, the central field is cycled between the fields  $B_1$  and  $B_2$  where  $\Delta B = (B_2 - B_1)$  is far larger than  $B_p$  (which is of the order of 10-100 mT for multifilamentary NbTi conductors). Therefore, most of the filaments in the strands remain fully penetrated during the field sweep and the magnetisation as given by eq. 3.2 varies according to the variation of the critical current with the field. A large magnetisation at the start of the ramp leads to large relative field distortions. Because the particles have to be injected at a small field  $B_{inj}$ , the filament size has to be small in order to reduce these field errors. The field  $B_{inj}$  has to be approached coming from a smaller field so that the magnetisation of the filaments does not reverse sign at the start of the ramp. Reduction of additional field distortions, caused by coupling currents and a non-uniform current distribution among the strands (see chapter 7), impose a more complicated field cycle before and during injection.

The hysteresis loss per cycle and per unit volume is given by the area enclosed within the hysteresis loop in the  $MB$  plane for zero frequency:

$$Q_{hys} = -\oint M(B_a) dB_a \quad [\text{Jm}^{-3}/\text{cycle}] \quad (3.3)$$

For a field cycle between  $B_1$  and  $B_2$  (with  $0 < B_1 < B_2 < 3$  T), the critical current density is represented by means of the Kim relation  $J_C(B) = J_0 B_0 / (|B| + B_0)$  (see section 2.4) so that:

$$Q_{hys} = -2 \frac{2d_f}{3\pi} \int_{B_1}^{B_2} \frac{J_0 B_0}{|B_a| + B_0} dB_a = \frac{4d_f J_0 B_0}{3\pi} \ln \left( \frac{|B_2| + B_0}{|B_1| + B_0} \right) \quad [\text{Jm}^3/\text{cycle}]. \quad (3.4)$$

The filament magnetisation for an applied field parallel to the filament is [Niessen, '93]:

$$M_1 = -\frac{1}{6} J_{C1} d_f \text{sgn}(\dot{B}_{a1}) \quad [\text{Am}^2], \quad (3.5)$$

but will be disregarded in this chapter since, in most applications, the angle between the applied field and the filament axis is close to  $90^\circ$ .

An additional transport current causes a decrease of the penetration field (see Fig. 3.1b) by a factor  $(1 - (J_r/J_C)^2) = (1 - (J_r/J_C)^2)$  [Rem, '86], with  $J_r$  the average current density in the filament. The magnetisation and the hysteresis loss are consequently reduced by the same factor for large field variations compared to the penetration field.

However, in the presence of a varying applied field, the transport current also causes an additional loss component which can be represented by a dynamic resistance [Druyvesteyn, '67], and results in an axial electric field over the filament [Hartmann, '89]:

$$E_{dyn} = \frac{4d_f}{3\pi} |\dot{B}_a| (J_r/J_C) \quad [\text{Vm}^{-1}] \quad \text{for } J_r < J_C. \quad (3.6)$$

The additional loss component  $J_r E_{dyn}$  is supplied by the current source and not by the external field, and can be expressed by:

$$J_r E_{dyn} = \frac{4d_f}{3\pi} J_C |\dot{B}_a| (J_r/J_C)^2 \quad [\text{Wm}^{-3}]. \quad (3.7)$$

The total energy loss  $Q_{hys}$  (i.e. the work done by the external field and the current supply) for a filament carrying a transport current and for field oscillations well above the penetration field is therefore (combining eqs. 3.2, 3.3 and 3.7):

$$\begin{aligned} Q_{hys} &= \frac{2d_f}{3\pi} \oint J_C \left( 1 - (J_r/J_C)^2 + 2(J_r/J_C)^2 \right) dB_a \\ &= \frac{2d_f}{3\pi} \oint J_C \left( 1 + (J_r/J_C)^2 \right) dB_a \quad [\text{Jm}^3/\text{cycle}], \end{aligned} \quad (3.8)$$

i.e. a factor  $(1 + (J_r/J_C)^2)$  larger than the loss as given by eq. 3.3 for a filament without transport current.

In the case of a filament carrying an AC transport current and subjected to a varying external field an additional loss component is present due to the varying self-field. In a magnet where the total field is achieved through the use of small diameter wire or multistrand conductor, the self-field variation is small compared to the external-field variation arising from the rest of the turns. Hence, the self-field loss does not make a substantial contribution to the total loss and is disregarded here.

An accurate value of the hysteresis loss for field variations  $\Delta B$  of the same order or smaller than  $B_p$  is calculated with a numerical model in which the cross-section of the filament is divided into discrete subregions, carrying either zero current or the critical current density. The variation in the external field and the transport current are represented by discrete steps. For each step the current in the subregions is calculated iteratively, since not only the external field but also the field generated by the other subregions determines the critical current of a subregion. A detailed description of this procedure is given elsewhere [Hartmann, '89].

The screening currents are often referred to as persistent currents as they can only be removed by driving the filament from the superconducting into the normal state. The persistent currents result in a residual field which increases with increasing filament diameter and increasing  $J_C$  (i.e. decreasing field or temperature). In accelerator magnets it is mainly this residual field that determines the acceptable filament diameter since the relative field errors can become large, especially at weak excitation. Since a high critical current density is required to have an efficient design, a decrease in the filament diameter is necessary for reducing the persistent currents.

A decrease in the filament diameter is often coupled with a decrease in the spacing  $b$  between the filaments. In the case of NbTi embedded in a copper matrix a spacing below about  $1\text{ }\mu\text{m}$  results in the so called 'proximity coupling' between neighbouring filaments. This proximity coupling is basically a tunneling of the Cooper pairs through the copper matrix and results in an enhanced effective diameter of the filament at low magnetic fields. Hence, a certain optimum in the filament diameter occurs for which the persistent currents are minimum. Measurements on SSC dipole magnets have shown that for a filament diameter of about  $4\text{ }\mu\text{m}$  the residual field is smallest, at a central field of  $0.33\text{ T}$  and a ratio  $b/d_f = 0.2$  [Green, '87].

### 3.3 The $J_C$ - $B$ relation

Eq. 3.2 shows that the magnetisation of a fully penetrated filament is proportional to the critical current density. The  $J_C$ - $B$  relation of a superconductor can therefore be determined by measuring the magnetisation in an external varying magnetic field. The cold part of the test set-up by which these magnetisation measurements are performed is shown in Fig. 3.3.

It consists of a concentric set of four pick-up coils that can be inserted in a superconducting solenoid providing an AC field of  $0.6\text{ T}$  maximum. The magnetisation is measured on a ring-shaped sample (with a circumference of  $130\text{ mm}$  maximum) inserted between the two upper pick-up coils. This ensures that both the inductive voltage and the empty coil effect are minimum. The pick-up coils are wound from a superconducting wire and are connected to a small superconducting sensing coil. The current in the circuit is proportional to the time integral of the pick-up voltage. The circuit can be regarded as a flux transformer, where the flux change in the pick-up set, due to the magnetisation of the sample, is transferred to the sensing coil. The flux in the sensing coil is measured using a Hall probe which is placed inside a superconducting PbBi shield, in order to exclude the stray field of the solenoid and other magnetic disturbances.

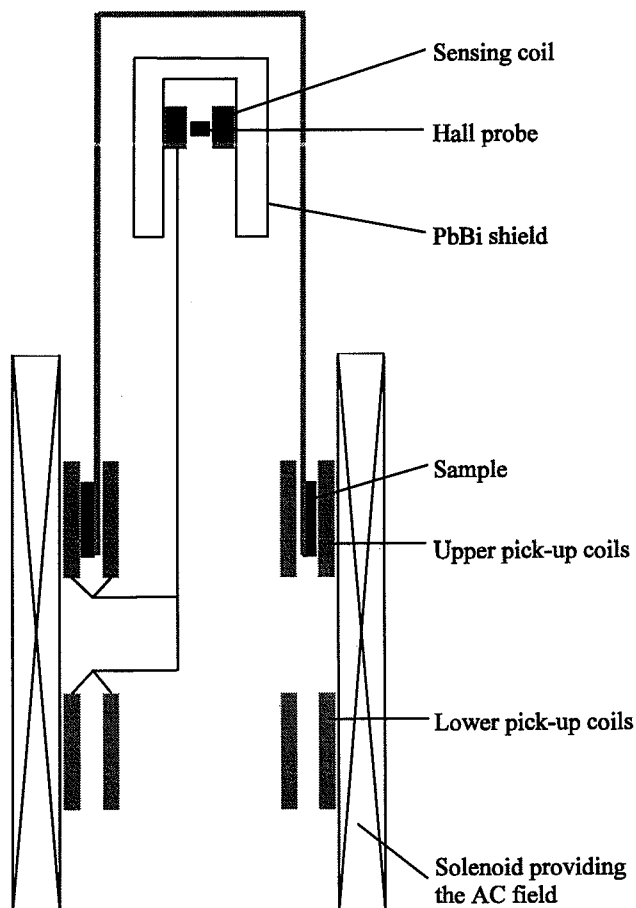


**Figure 3.3.** The cold part of the measuring system where the voltage of the Hall probe is a measure of the magnetisation of the sample.

Two heaters are present to enable a reset of the magnetic shield and the flux transformer in case flux has penetrated through the shield or is trapped in the flux-transformer circuit.

Characteristic measured magnetisation loops of two cables are shown in Fig. 3.4, including calculated magnetisation loops assuming the Kim relation for  $J_C(B)$  (see eq. 2.16) with  $J_0$  and  $B_0$  as fit parameters.

Especially the cables with a small filament diameter, namely I-2 and I-4 (see Table 2.4), show a relatively large increase of the magnetisation for small fields compared to the calculated magnetisation. The enhancement is attributed to the proximity effect which can be regarded as an increase of the effective filament diameter as explained before. This results in a discrepancy between the experimental results and the calculated magnetisation since the proximity effect is not incorporated in the numerical model.

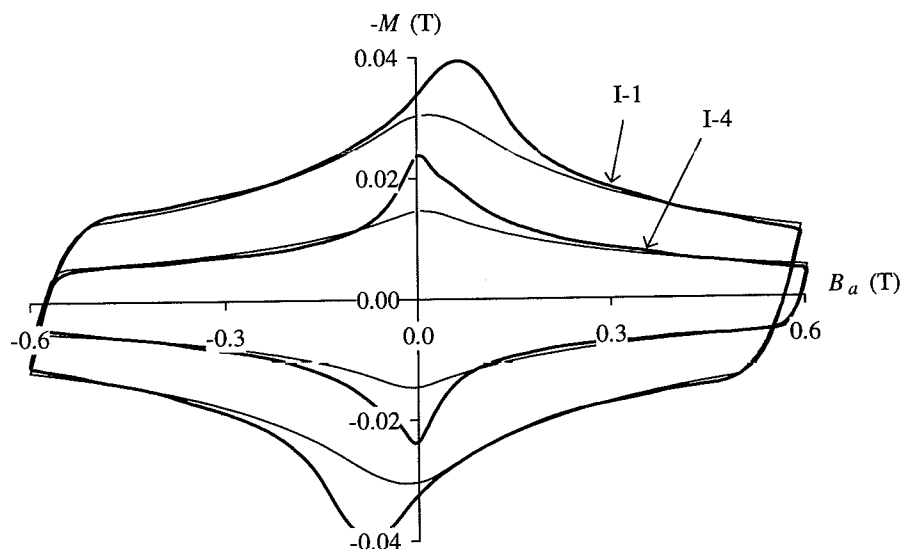


**Figure 3.4.** Magnetisation loops (bold lines) of cables I-1 and I-4 (see Table 2.4) subject to a sinusoidally oscillating field with an amplitude of 0.6 T and a frequency of 0.02 Hz. The thin lines are best fits, numerically calculated using the Kim relation for  $J_C(B)$ .

The peak in the magnetisation curve is always slightly displaced from the origin as the internal field is not zero, due to the screening currents. The displacement increases for increasing filament diameter and critical current density.

The  $J_C$ - $B$  relation of the filament (without the matrix) is determined by fitting the numerically calculated magnetisation (using the Kim relation for  $J_C(B)$  as given in eq. 2.16) to the experimentally determined magnetisation between 0.3 and 0.6 T. The results in terms of the fit parameters  $J_0$  and  $B_0$  are given in Table 3.1. The fit is at least valid in the field range from 0.3 to 0.6 T.

**Table 3.1.** Survey of the constants  $J_0$  and  $B_0$  of the Kim relation for several samples obtained by fitting the magnetisation loops with an amplitude of 0.6 T. The indicated critical current density at 0.6 T is the average current density over the cross-section of the strand.

	I-1	I-2	I-3	I-4	O-2
$J_0$ ( $10^{10}$ Am <sup>-2</sup> )	3.0	3.1	2.3	3.7	4.5
$B_0$ (T)	0.31	0.32	0.30	0.30	0.35
$J_C$ at 0.6 T, 4.2 K ( $10^9$ Am <sup>-2</sup> )	3.8	4.1	2.6	4.7	5.9

### 3.4 Interfilament coupling currents

The presence of a matrix results in the flow of coupling currents between the filaments of a strand when it is exposed to a changing magnetic field. Contrary to a normal conductor, specific current paths occur which are mainly determined by the boundary condition of almost zero electric field along the centres of the non-saturated filaments. The current paths are closed across the normal conducting matrix in which the heat is generated.

The interfilament coupling loss (IFCL) can be calculated using an anisotropic continuum model [Carr, '74] based on solving Maxwell's equations. Here another approach, proposed by Morgan, is followed based on the calculation of the induced currents between two twisted filaments in a strand [Morgan, '70]. The strand is assumed to have a circular cross-section with diameter  $d_s$  in which the filaments are arranged in concentric layers. Two filaments of the outer concentric layer, with diameter  $d_s^*$ , are shown in Fig. 3.5.

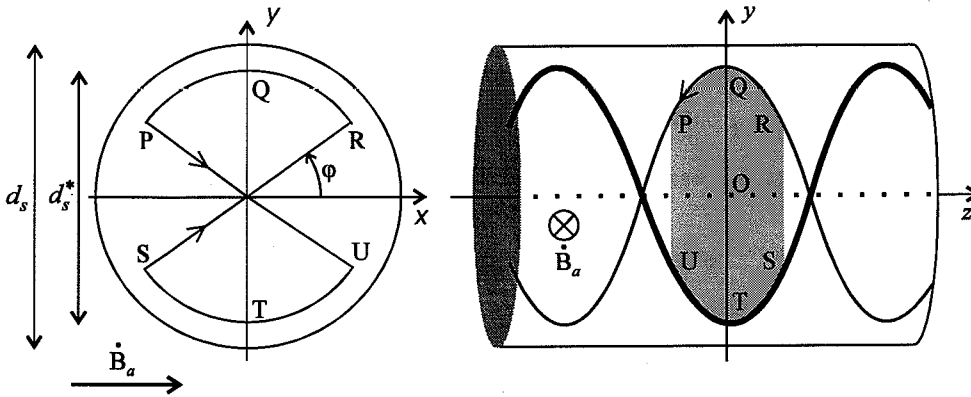


Figure 3.5. Cross-section of a strand and schematic view of a current path RQPUTS in which an electromotive force is generated due to an external applied-field variation.

If the strand is subjected to a varying magnetic field  $\dot{\mathbf{B}}_a$  in the  $x$ -direction, a field change  $\dot{\mathbf{B}}_i$  is induced by the interfilament coupling currents (IFCCs), so that the total field change  $\dot{\mathbf{B}}_s$  in the interior equals:

$$\dot{\mathbf{B}}_s = \dot{\mathbf{B}}_a + \dot{\mathbf{B}}_i \quad [\text{Ts}^{-1}]. \quad (3.9)$$

The homogeneous  $\dot{\mathbf{B}}_a$  over the whole cross-section will result in a homogeneous  $\dot{\mathbf{B}}_i$ , parallel to  $\dot{\mathbf{B}}_a$ , and thus in a homogeneous  $\dot{\mathbf{B}}_s$ . The induced voltage  $U_{ind}(z)$  is obtained from the surface RQPUTS:

$$U_{ind}(z) = -\int \dot{\mathbf{B}}_s dA = -4 \frac{1}{2} d_s^* \dot{\mathbf{B}}_s \int_0^z \cos(2\pi z / L_{p,f}) dz = -2 d_s^* \left( \frac{L_{p,f}}{2\pi} \right) \dot{\mathbf{B}}_s \cos(\varphi) \quad [\text{V}], \quad (3.10)$$

with  $L_{p,f}$  the twist pitch of the filaments and  $\varphi = (\pi/2 - 2\pi z / L_{p,f})$ .



Since there is no voltage drop along the superconducting filament, the voltage of any filament with position  $\varphi$  in a cross-section relative to the  $z$ -axis is:

$$U(\varphi) = -\frac{1}{4}U_{ind}(z) = \left(\frac{L_{p,f}}{2\pi}\right) \frac{d_s^* \dot{B}_s}{2} \cos(\varphi) \quad [\text{V}]. \quad (3.11)$$

Since  $x = d_s^* \cos(\varphi)/2$  the voltage will give rise to a homogeneous electric field parallel to  $\mathbf{B}_a$ :

$$\mathbf{E}_{\parallel} = -\frac{L_{p,f}}{2\pi} \dot{\mathbf{B}}_s \quad [\text{Vm}^{-1}]. \quad (3.12)$$

The  $z$ -component of the electric field, which is present due to the twist angle, is not taken into account. Since  $\mathbf{E}_{\parallel}$  is independent of  $d_s^*$  the solution holds for all filaments and therefore also for the complete strand. The electric field  $\mathbf{E}_{\parallel}$  creates a current density  $\mathbf{J}_{\parallel}$  flowing across the strand parallel to  $\mathbf{B}_s$ :

$$\mathbf{J}_{\parallel} = -\left(\frac{L_{p,f}}{2\pi}\right) \frac{\dot{\mathbf{B}}_s}{\rho_{eff}} \quad [\text{Am}^{-2}], \quad (3.13)$$

with  $\rho_{eff}$  the effective transverse resistivity which depends on the filling factor  $\eta$  as [Carr, '75]:

$$\rho_{eff}(\eta) = \rho_{mat} \left(\frac{1-\eta}{1+\eta}\right) \text{ or } \rho_{eff}(\eta) = \rho_{mat} \left(\frac{1+\eta}{1-\eta}\right) \quad [\Omega\text{m}], \quad (3.14)$$

whenever the filaments do or do not contribute to the transverse conduction respectively. The resistivity  $\rho_{mat}$  denotes the transverse resistivity of the matrix.

The current density  $\mathbf{J}_{\parallel}$  gives rise to a coupling power loss per unit volume:

$$P_{if} = \mathbf{J}_{\parallel} \mathbf{E}_{\parallel} = \left(\frac{L_{p,f}}{2\pi}\right)^2 \frac{\dot{B}_s^2}{\rho_{eff}} \quad [\text{Wm}^{-3}]. \quad (3.15)$$

The outer layer of filaments act as a return path for  $\mathbf{J}_{\parallel}$  so that the collected current  $I_f$  in the filaments (using the continuity of current) satisfies:

$$\frac{dI_f(\varphi)}{dz} = J_{\parallel} \cos(\varphi) \quad [\text{Am}^{-2}]. \quad (3.16)$$

Integration results in the induced axial surface current density  $I_f(\varphi)$  in the  $z$ -direction:

$$I_f(\varphi) = -\left(\frac{L_{p,f}}{2\pi}\right)^2 \frac{\dot{B}_s}{\rho_{eff}} \sin(\varphi) \quad [\text{Am}^{-1}]. \quad (3.17)$$

Assuming that the current flows through the outer layer of filaments at radius  $d_s^*/2$ , the total current  $I_{if}$  flowing at either side of the strand (positive at one side and negative at the other side) equals:

$$I_{if} = \pm 2 \int_0^{\pi/2} I_f(\varphi) \left( \frac{d_s^*}{2} \right) d\varphi = \pm \left( \frac{L_{p,f}}{2\pi} \right)^2 \frac{d_s^* \dot{B}_s}{\rho_{eff}} \quad [\text{A}]. \quad (3.18)$$

Since  $I_f(\varphi)$  varies with  $\sin(\varphi)$ , a uniform dipole-field change  $\dot{\mathbf{B}}_i$  in the interior of the strand is generated parallel and opposite to  $\dot{\mathbf{B}}_a$ :

$$\dot{\mathbf{B}}_i = \frac{\mu_0}{2d_s^*} I_{if} = - \left( \frac{L_{p,f}}{2\pi} \right)^2 \frac{\mu_0 \dot{\mathbf{B}}_s}{2\rho_{eff}} = -\tau_{if} \dot{\mathbf{B}}_s \quad [\text{T}]. \quad (3.19)$$

The constant of proportionality  $\tau_{if}$  is called the time constant of the IFCCs, and defined by:

$$\tau_{if} = \frac{\mu_0}{2\rho_{eff}} \left( \frac{L_{p,f}}{2\pi} \right)^2 \quad [\text{s}]. \quad (3.20)$$

The time constant increases by a factor of about 1.27 for square strands [Campbell, '82] and by a factor  $[1 + (\pi d_s/L_{p,f})^2]$  if the z-component of the electrical field is also taken into account (which is about 1.02 for a characteristic ratio  $d_s/L_{p,f}=0.05$ ).

Combining eqs. 3.9 and 3.19 gives the relation between the applied field and the internal field by means of the differential equation:

$$\dot{\mathbf{B}}_i + \frac{\mathbf{B}_i}{\tau_{if}} = -\dot{\mathbf{B}}_a \quad [\text{Ts}^{-1}]. \quad (3.21)$$

The energy loss  $Q_{if}$  per cycle and per unit volume is determined by integration of eq. 3.15. For a sinusoidally oscillating applied field:

$$B_a = B_a^m \cos(\omega t) \quad [\text{T}], \quad (3.22)$$

with amplitude  $B_a^m$  and angular frequency  $\omega=2\pi f$ , the energy loss equals:

$$Q_{if} = \oint P_{if} dt = \frac{2\tau_{if} \pi \omega (B_a^m)^2}{\mu_0 (1 + (\omega \tau_{if})^2)} \quad [\text{Jm}^{-3}/\text{cycle}]. \quad (3.23)$$

Using the anisotropic continuum model, a basically identical relation is obtained [Carr, '74].

More generally, the factor 2 in eq. 3.23 should be replaced by the shape factor  $n$ , which is equal to 2 for round and square wires. In the case of rectangular strands with a cross-section  $a \cdot b$  where  $a \gg b$ ,  $n = 1$  for  $\dot{\mathbf{B}}_a$  applied perpendicular to  $b$  and  $n = a/b$  for  $\dot{\mathbf{B}}_a$  applied perpendicular to  $a$  [Campbell, '82].

At low field amplitudes the magnetic moment of the filaments is large and the filaments can even become perfectly diamagnetic. In this case the strand should be treated as a material with an effective permeability [Campbell, '82]:

$$\mu_{eff} = \frac{n(1-\lambda)}{2\lambda+n(1-\lambda)} = (1-\lambda) \text{ for } n=2 \quad [\text{Hm}^{-1}], \quad (3.24)$$

with  $\lambda$  the copper-to-superconductor ratio. This results in a decrease of the time constant to  $\tau_{if,eff} = \mu_{eff} \tau_{if}$  (where  $\tau_{if}$  is the time constant when the filaments are completely penetrated), and in a decrease of the coupling power loss by a factor  $\mu_{eff}$ . So the energy loss equals:

$$Q_{if} = \frac{n\tau_{if}\pi\mu_{eff}^2\omega(B_a^m)^2}{\mu_0(1+(\mu_{eff}\omega\tau_{if})^2)} \quad [\text{Jm}^{-3} \text{ per cycle}], \quad (3.25)$$

and is significantly smaller compared to eq. 3.23 at low frequencies ( $\omega\tau_{if} \ll 1$ ).

The above-mentioned relations are valid as long as the currents in the filaments in the outer layer do not exceed the critical current. Beyond this limit the filaments become saturated and the excess currents have to return via the filaments in the more inner layers, which causes a decrease in the induced magnetic field  $B_i$ . The losses in a multifilamentary strand can therefore be classified in three frequency ranges:

- Low frequency,  $\omega\tau_{if} \ll 1$ . The inside of the strand is subjected to the external field since the screening by the IFCCs is very small. The hysteresis loss can be treated independently of the IFCL.
- Intermediate frequency,  $\omega\tau_{if} \geq 1$ . The inside of the strand is partially shielded by the IFCCs but the fields are still uniform. Due to the screening, the hysteresis loss is smaller than in the low-frequency range.
- High frequency,  $\omega\tau_{if} \gg 1$ . The inside of the strand is almost completely shielded since the applied field penetrates only a thin skin of the strand. The hysteresis loss approaches zero because only the outer layers of filaments are subjected to a field change.

As  $\tau_{if}$  is typically of the order of 10-100 ms, especially the first frequency range will be of interest in the case of the slowly varying fields which are present in accelerator magnets. Therefore, the decrease of the hysteresis due to the screening of the IFCCs is not discussed here, but an extensive treatment can be found in the literature [Pang, '80].

The characteristic distribution of the IFCCs over the cross-section of the strand is depicted in Fig. 3.6. Three different regions (besides the normal conducting core and outer shell) can be distinguished:

- region I: the filaments are completely saturated,
- region II: the filaments are partially saturated,
- region III: the filaments do not carry any IFCCs.

As a result, the transport current can only flow in region III, since a transport current flowing in region II would also pass through region I (due to the twist), thereby generating an additional loss.

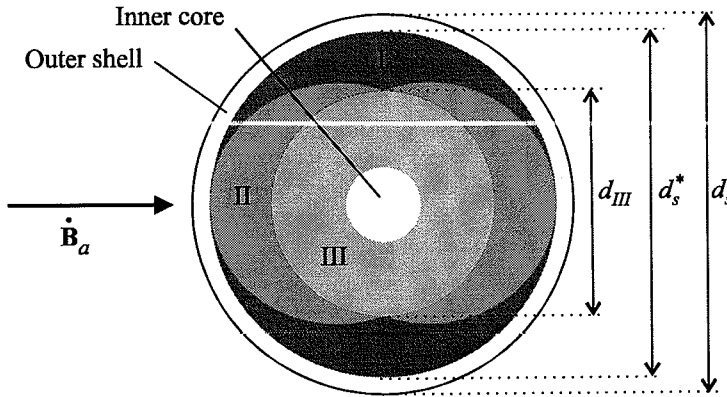


**Figure 3.6:** Current distribution in a wire without transport current, subject to a varying magnetic field, indicating three different regions: **I.** the filaments are completely saturated by the IFCCs, **II.** the filaments are partially saturated by the IFCCs, **III.** the filaments carry no IFCCs. The current profile is calculated by disregarding the influence of the central core.

The calculated diameter  $d_{III}$  of region III, where the filaments do not carry IFCCs and after disregarding the inner core [Klundert, van de, '90], equals:

$$d_{III} = d_s^* \left( 1 - \frac{L_{p,f} \dot{B}_a}{2\pi\eta J_C \rho_{eff}} \right) = d_s^* \left( 1 - \frac{4\pi\tau_{if} \dot{B}_a}{\eta J_C \mu_0 L_{p,f}} \right) \quad [\text{m}] \quad \text{for } \dot{B}_a L_{p,f} < 2\pi\eta J_C \rho_{eff}. \quad (3.26)$$

Hence, the maximum transport current  $I_{tr, str, max}$  in a strand is not only a function of the temperature and the applied magnetic field but also of the rate of change of the magnetic field. As the boundaries of the three regions are not influenced by a transport current [Hartmann, '89],  $I_{tr, str, max}$  can be expressed by:

$$I_{tr, str, max}(B_a, \dot{B}_a, T) = I_{C, str}(B_a, T) (d_{III} / d_s^*)^2 \quad [\text{A}], \quad (3.27)$$

which corresponds to within 5% with a more complicated relation given by Hartmann. Experimental results are in agreement with the above-mentioned expression [Rem, '85], [Roovers, '86]. Eq. 3.27 can be rewritten in terms of  $\tau_{if}$  using eqs. 3.20 and 3.26:

$$I_{tr, str, max}(B_a, \dot{B}_a, T) = I_{C, str}(B_a, T) \left( 1 - \frac{(\pi d_s^*)^2 \tau_{if} \dot{B}_a}{I_{C, str}(B_a, T) \mu_0 L_{p,f}} \right)^2 \quad [\text{A}]. \quad (3.28)$$

In sections 3.5 and 8.2.1 the relation is applied to estimate the decrease of the maximum transport current due to the IFCCs.

Practical conductors are often subdivided into several regions. A very common lay-out consists of the following three concentric layers with volume fractions  $v_1$ ,  $v_2$  and  $v_3$  respectively (see Figs. 2.9a and 3.6):

- a central core of normal-conducting material with resistivity  $\rho_1$ ,
- a ring filled with many filaments in a matrix with resistivity  $\rho_2 = \rho_{eff}$ ,
- an outer shell of normal-conducting material with resistivity  $\rho_3$ .

Characteristic values for  $\nu_1$ ,  $\nu_2$  and  $\nu_3$  for NbTi strands for accelerator magnets are 0.15, 0.75 and 0.10 respectively. The loss contributions of each layer for  $\omega\tau_{if} < 1$  can be summarised by [Kate, ten, '94]:

$$P_{if,1} = \nu_1 \left( \frac{L_{p,f}}{2\pi} \right)^2 \frac{\dot{B}_s^2}{\rho_1} \quad [\text{Wm}^{-3}], \quad (3.29)$$

$$P_{if,2} = \nu_2 \left( \frac{L_{p,f}}{2\pi} \right)^2 \frac{\dot{B}_s^2}{\rho_{eff}} \quad [\text{Wm}^{-3}], \quad (3.30)$$

$$P_{if,3} = \nu_3 \frac{\nu_1 + \nu_2}{\nu_1 + \nu_2 + 1} \left( \frac{L_{p,f}}{2\pi} \right)^2 \frac{\dot{B}_s^2}{\rho_3} \quad [\text{Wm}^{-3}]. \quad (3.31)$$

For  $\rho_1 = \rho_2 = \rho_{eff}$ , the subdivision in regions decreases the IFCL of the LHC strands by a factor of about 0.9 compared to eq. 3.15. If the filaments contribute to the transverse resistivity (see eq. 3.14), the decrease is a factor of about 0.8 for  $\eta = 0.35$ .

### 3.5 Interfilament time constants

The measurement set-up as described in section 3.3 is used to evaluate the IFCL of a cable, determined by the increase of the area of the  $M$ - $B$  curve for higher frequencies. The field is applied parallel to the cable width ( $\theta = \varphi = 90^\circ$ , see Fig. 4.1). This implies that the magnetisation is mainly determined by the hysteresis of the filaments and the interfilament coupling while the interstrand coupling is negligible, even for relatively low interstrand contact resistances (see section 4.4.1). Magnetisation loops of cable I-2 are shown in Fig. 3.7 for several frequencies.

At higher frequencies  $f = \omega/2\pi$  the curves become more and more elliptical with a phase shift between the internal field and the external field (according to eq. 3.21), equal to  $\arctan(\omega\tau_{if})$ .

A more accurate method to determine the time constant  $\tau_{if}$  is by calculating the total energy loss per cycle:

$$Q_{tot} = Q_{hys} + Q_{if} \quad [\text{J/cycle}], \quad (3.32)$$

by the surface of the  $M$ - $B$  curve, as a function of the frequency (see Fig. 3.8). The time constant can be deduced from the maximum of the  $Q_{tot}$ - $f$  relation. Note that the hysteresis loss decreases at higher frequencies due to the screening of the IFCCs which results in a shift of the maximum of the curve to slightly lower frequencies. The apparent increase of  $\tau_{if}$  could be significant when the IFCL is small compared to the hysteresis loss.

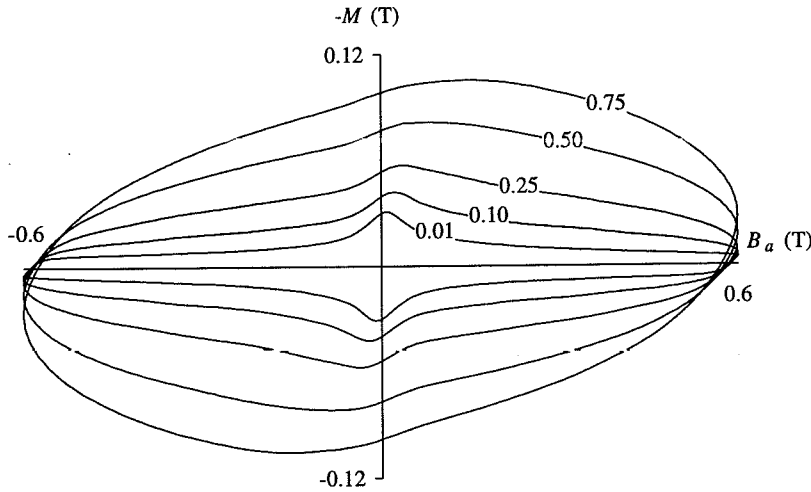


Figure 3.7. Magnetisation loops of cable I-2 exposed to an oscillating applied field with amplitude  $B_a^m = 0.6$  T at frequencies of 0.01, 0.1, 0.25, 0.5 and 0.75 Hz (without transport current).

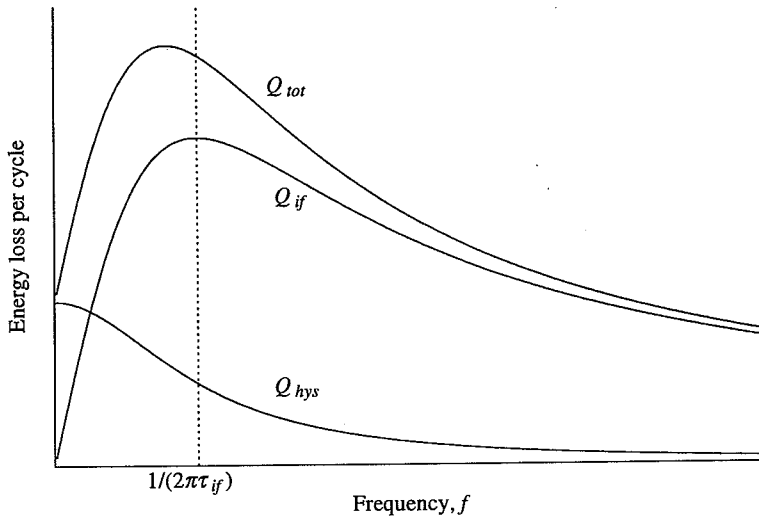
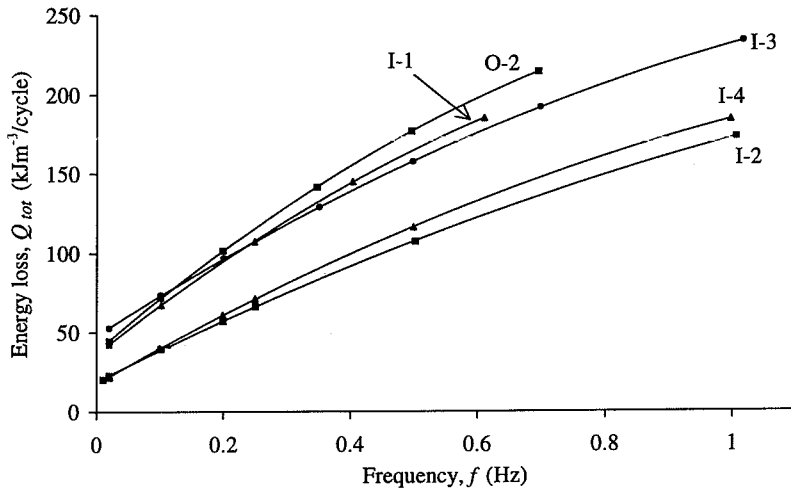


Figure 3.8. Characteristic  $Q_{tot}$ - $f$  relation for conductors which exhibit hysteresis loss and IFCL. A frequency-dependent hysteresis loss is assumed [Pang, '80]. Note that the apparent time constant calculated from the maximum of the  $Q_{tot}$ - $f$  curve, increases due to the screening of the interior of the strand by the IFCCs.

Here  $n\tau_{if}$  is determined from the slope of the  $Q_{tot}$ - $f$  relation for  $f \rightarrow 0$  according to eq. 3.25 assuming  $\mu_{eff} = 1$ . The  $Q_{tot}$ - $f$  relation of various samples exposed to a field sweep from -0.6 to 0.6 T is shown in Fig. 3.9. Table 3.2 shows a survey of the  $\tau_{if}$ -values of the samples assuming  $n=2$ .



**Figure 3.9.** The total energy loss of various cables as specified in Table 2.4 exposed to a field sweep between -0.6 and 0.6 T at frequencies between 0.02 and 1 Hz.

The ratio  $d_{III}/d_s^*$  as calculated using eq. 3.26 for  $n=2$ ,  $\dot{B}_a=0.1 \text{ Ts}^{-1}$  and  $I_C=500 \text{ A}$  is also given. The corresponding decrease of the maximum transport current (according to eq. 3.27) is smaller than 1% at  $\dot{B}_a=0.1 \text{ Ts}^{-1}$  and smaller than 0.05% at  $\dot{B}_a=0.0066 \text{ Ts}^{-1}$ , the average field-sweep rate during excitation as foreseen for the LHC dipole magnets, and will therefore not affect the maximum operation field in the magnets. In practice the decrease is even smaller since  $I_{C, str}$  increases if the transport current decreases (see also section 8.2) and because the time constant decreases at higher fields due to the magnetoresistance of the matrix.

**Table 3.2.** Survey of the  $\tau_{if}$ -values of several cables as deduced from the slope of  $Q_{tot}$ - $f$  relation with  $B_a^m=0.60 \text{ T}$  and assuming  $n=2$ . The calculated relative decrease  $i$  of the maximum transport current is included for a field-sweep rate of  $0.1 \text{ Ts}^{-1}$  (with  $I_{C, str}=500 \text{ A}$ ).

	I-1	I-2	I-3	I-4	O-2
$\tau_{if} \text{ (ms)}$	29	23	26	24	32
$d_{III}/d_s^*$ at $0.1 \text{ Ts}^{-1} \text{ (mm)}$	0.997	0.998	0.997	0.998	0.999
$i$ at $0.1 \text{ Ts}^{-1}$	0.994	0.995	0.995	0.995	0.997

In order to investigate the influence of adjacent strands on the hysteresis loss and IFCL, individual strands are removed from cable I-4 and kept in the original shape they have in the cable. The sample is referred to as I-4o.

Fig. 3.10 shows the ratio of the energy loss per cycle per volume between I-4 and I-4o as a function of the frequency. In the case of a large  $B_a^m$  (compared to the penetration field) and low frequencies, the field produced by the neighbouring strands is small compared to the applied field and the ratio approaches 1.

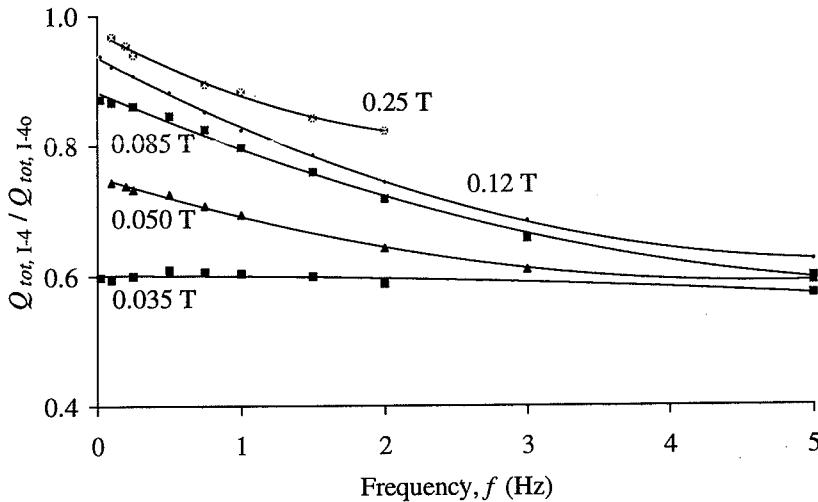


**Figure 3.10.** The energy loss (per unit volume) of the cable I-4 divided by the energy loss (per unit volume) of a strand in the 'cable shape' I-4o as a function of the frequency for several amplitudes of the applied field.

For small  $B_a^m$  the field produced by the persistent currents of the neighbouring strands is not negligible compared to the applied field and the demagnetisation of the cable becomes relevant, resulting in a ratio smaller than 1. Considering larger frequencies, the additional field produced by the IFCCs (being opposite to the applied field), reduces the total field, especially in the centre of the cable. This implies an even stronger decrease of the loss in the cable compared to the loss in individual strands.

The field variations in accelerator magnets are large and quasi DC; for example, the characteristic ramp for the LHC dipole magnets corresponds to a field sweep of about 8 T in 20 minutes. Even the fast de-excitation with a time constant of 100 s can be classified in the  $\omega\tau_{if} < 1$  regime. Hence, the hysteresis loss and IFCL in accelerator magnets can be directly determined by the losses in a single strand, and are not affected by the field produced by the persistent currents and IFCCs in the neighbouring turns.

### 3.6 Conclusions

Filament hysteresis and interfilament coupling are the main sources of loss inside a strand which is exposed to a varying magnetic field. The two loss components can be well separated by determining the magnetisation vs. frequency in the range  $\omega\tau_{if} < 1$ . In the case of larger frequencies the interior of the strand becomes partially or almost completely shielded by the screening currents and the hysteresis is no longer independent of the frequency. An additional transport current increases the hysteresis loss by a factor  $(1 + (J_r/J_C)^2)$ .



The strand losses (per unit volume) in an LHC-type NbTi cable are identical to the losses in a single strand (per unit volume), under the same conditions, if the applied field amplitude is large (compared to the penetration field) and the frequency is small ( $< 1/(2\pi\tau_{if})$ ). In the case of small field amplitudes and/or high frequencies the demagnetisation of the cable will cause a considerable decrease of the losses. The strand losses in dipole magnets, subject to a central-field sweep, which is large compared to the penetration field, can therefore be successfully estimated by a loss measurement on a single strand.

The mean time constants  $\tau_{if}$  of the interfilament coupling currents for various cables used in the LHC dipole model magnets are between 23 and 33 ms. The corresponding decrease in the maximum transport current due to the IFCCs during the field sweep from injection to operating field in LHC magnets will be smaller than 0.05% (not taking into account the possible temperature increase of the cable due to the loss).

## Chapter 4

# Interstrand coupling currents

*Interstrand coupling currents (ISCCs) are generated in a cable with non-insulated strands, exposed to a varying magnetic field. The corresponding coupling loss adds to the hysteresis loss and interfilament coupling loss which are discussed in chapter 3.*

*In order to calculate the ISCCs in a Rutherford-type cable, the cable is simulated by means of a network model. The typical distribution of the ISCCs across the cable width is illustrated and the dependence of the ISCCs on the cable geometry and contact resistances  $R_a$  and  $R_c$  between adjacent and crossing strands is investigated.*

*Typical distributions of the contact resistance and the field change across the cable width, which are present in accelerator magnets, are discussed. Variations along the length of the cable provoke additional coupling currents which are discussed in chapter 5.*

*Introduction of self- and mutual inductances between the strands as a new feature in the network model enables the calculation of time constants. Expressions are given of the time constants of single cables and stacked cables. The relations are essential to fully understand the source of the various time-dependent effects in magnets.*

*The parameters that affect  $R_c$  are briefly enumerated. The influence of the transverse pressure upon the cable on  $R_c$  is investigated by means of calorimetric and electrical methods. The results of both methods on several stacks of cable pieces are evaluated for varying pressure up to 100 MPa.*

## 4.1 Introduction

The *interfilament* coupling loss (IFCL) is often calculated by considering the multifilamentary superconductor as a continuum. To determine the *interstrand* coupling loss (ISCL) in cabled superconductors a discrete approach is more appropriate since the cable has a limited number of strands linked to each other through contact resistances with a spatial distribution.

The first analytical calculations of the interstrand coupling currents (ISCCs) in a Rutherford-type cable were performed by Wilson in the case of unsaturated strands for fields parallel as well as perpendicular to the large face of the cable [Wilson, '72]. In this approach the cable was considered as a solid strip, in which wires spiral uniformly, an approach also followed by other authors [Walters, '75], [Krempasky, '78].

In 1973 Morgan suggested calculating the ISCCs by modelling a Rutherford-type cable as a network of nodes interconnected by strands and cross-contact resistances  $R_c$  [Morgan, '73]. The network model could be applied to cables with unsaturated strands and with constant  $R_c$  and field-sweep rate  $\dot{B}$  in the longitudinal direction of the cable. The same type of network model is applied in 1980 to calculate the ISCCs for the ISABELLE cable [Courant, 80]. Since 1988 other network models have been developed [Sytnikov, '89a, '92, '94], [Niessen, '90a/b, '93] that can also handle saturated strands in finite cable pieces as well as infinitely long cables. Here a novel model is presented with several new features as surveyed in Table 4.1.

**Table 4.1.** Survey of the main features of several network models for simulating coupling currents in Rutherford-type cables (+: present, -: not present).

	[Morgan, '73]	[Sytnikov, '89a]	[Niessen, '93]	This thesis
Contact resistances (see Fig. 4.1)	$R_c$	$R_a, R_c$	$R_a, R_c$	$R_a, R_c$
Strand resistivity $\rho_s$	-	+	+	+
Keystone angle	-	-	-	+
Infinite length	+	+	+	+
Finite length	-	+	+	+
Transport current	-	+	+	+
Saturation	-	+	+	+
Inductances $L, M$	-	-	-	+
Self field	-	-	-	+
Field components <sup>a</sup>	$B_y$	$B_x, B_y$	$B_x, B_y$	$B_x, B_y, B_z$
$R_a$ - and $R_c$ -variations across the cable width	+	+	+	+
$R_a$ - and $R_c$ -variations over the cable length	-	+	+	+
ISCCs				
Time constant of a single cable	-	see text	-	+
Time constant of stacked cables and coils	-	-	-	+
Field $B_{is}$ produced by the ISCCs	-	-	-	+
BICCs (see chapter 5)				
Time constant of a single cable	-	-	-	+
Characteristic length	-	-	-	+
Field $B_{bi}$ produced by the BICCs	-	-	-	+

<sup>a</sup> See Fig. 4.1 for the definition of the coordinate system.

The main improvements are the possibilities to calculate the time-dependent behaviour of the coupling currents and to include various types of non-uniformities which are likely to be present in the cable of the coils. Time constants of the ISCCs are also given by Krempasky and Sytnikov, based on the general formulas derived for the *interfilament* coupling currents in a strand [Krempasky, '78], [Sytnikov, '94]. This approach is however not valid since the ISCCs in neighbouring turns are mutually coupled. In none of the models are temperature, cooling and quench propagation included.

The chapter starts with the description of the three-dimensional network model for a fully transposed Rutherford-type cable. The method for calculating the magnitude of the coupling currents and their time constants is explained. In section 4.3 several parameters are reviewed that affect the contact resistance  $R_a$  and  $R_c$ , such as the deformation and surface treatment of the strands, the curing temperature and the pressure.

Two regimes are distinguished throughout the chapter:

- *Weak excitation*, indicating that the total strand current  $I_{str}$  in each strand section in the cable is smaller than the critical current  $I_{c, str}$  of the strand.
- *Strong excitation*, indicating that in at least one strand section the critical current is reached.

In section 4.4 general formulas are given for the distribution of the ISCCs, their time constants and the generated loss for weak excitation. In the next section the case for strong excitation is illustrated.

In sections 4.6 and 4.7 attention is paid to non-uniformities in  $R_c$  and  $\dot{B}$  across the cable width, which are both present in accelerator magnets. The effect of distributions over the cable length will be discussed in chapter 5. In dipole magnets, for example, these effects can be large in and close to the coil ends and in the connections between different cable pieces.

The effect of the cable length on the ISCL is discussed in section 4.8 and is important for the evaluation of the ISCL of small cable pieces (typically smaller than one cable pitch).

In section 4.9 the increase of the time constant due to the stacking of cables into blocks is discussed. Using this approach it is possible to estimate time constants in coils if the time constant of a single cable is known. The correlation between the time constant and the ISCL is determined for stack geometries with non-uniform  $R_c$ -distributions.

The influence of the transverse pressure on  $R_c$  is analysed in the next section. This dependence is of special interest as the prestress and the Lorentz force vary over the length and the cross-section of a coil. Hence, a pressure-dependent  $R_c$  will directly cause  $R_c$ -variations over the cross-section of the coils. During a field sweep, the variations of  $R_c$  then result in local increases of the power loss, in boundary-induced coupling currents (see chapter 5), and in unexpected field errors. The  $R_c$ -value is experimentally investigated with a calorimetric and electrical method on several stacks of cable pieces subject to a transverse pressure between 0 and 100 MPa. The results of cables with SnAg-coated strands as well as soldered strands are evaluated.

## 4.2 Network model of a Rutherford-type cable

A Rutherford-type cable has a width  $w$  and a height  $h_1$  on edge 1 and  $h_2$  on edge 2, and consists of  $N_s$  strands, having a twist pitch  $L_{p,s}$ . In addition, Rutherford-type cables for accelerator magnets often have a small keystone angle  $\alpha_k$  (see eq. 2.14). The average height of the cable (or mid height) is given by  $h = (h_1 + h_2)/2$ .

The cable is modelled by a three-dimensional network of nodes interconnected by sections of strands and resistances (see Figs. 4.1 and 4.2). The strands are represented by lines with an infinitely small diameter. This implies that the distance between the line currents at both edges is equal to  $w(1-2/N_s)$  and the average distance between the line currents in both layers is  $h/2$ . The resistances  $R_a$  and  $R_c$  represent the resistances between adjacent and crossing strands.

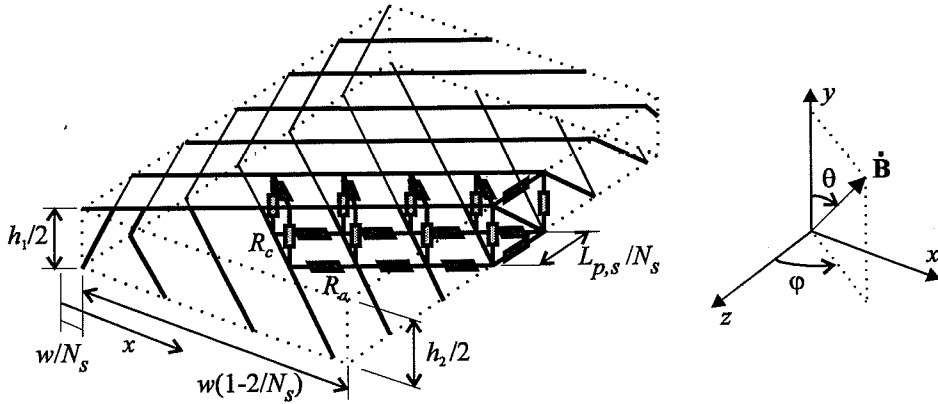


**Figure 4.1.** Network model of a Rutherford-type cable and definition of the angles  $\theta$  and  $\phi$ . The resistances tinged with dark and light grey indicate the resistances  $R_a$  and  $R_c$ . Since the strands are represented by line elements, the average distances between the line currents at both edges and at both layers are  $w(1-2/N_s)$  and  $h/2$  respectively. The length  $x$  denotes the position across the cable width and is 0 at the physical edge of the cable.

If the cable is exposed to a field change  $\dot{B}$ , coupling currents are generated in and between the strands of the cable. The currents  $I_a$  and  $I_c$  are the coupling currents between the strands of the cable through the contact resistances  $R_a$  and  $R_c$ . The currents  $I_s$  are the coupling currents in the strands.

The current  $I_{str}$  denotes the total current in a strand, i.e. the sum of the strand transport current  $I_{tr,str}$ , the interstrand coupling current  $I_s$  and additionally the boundary-induced coupling current  $I_{bi}$  (which is dealt with in chapter 5 and is 0 in this chapter). The sum of the strand transport currents equals the cable transport current  $I_{tr,cab}$ . At both edges of the cable the strands follow a skew path from one layer to the other. A strand element is a part of a strand in-between two nodes with length  $l_s$  and infinitely small diameter.

The aspect ratio  $\alpha_{cab}$  of the cable is defined as the cable width divided by the average cable height ( $\alpha_{cab} = w/h$ ), and is equal to  $\alpha_0 = N_s/4$  in the case of strands with a round cross-section. In practical cables  $\alpha_{cab}$  is slightly larger than  $\alpha_0$  caused by the cabling process.



The cable is subdivided into  $N_B$  calculation bands each, with a length  $L_{p,s}/N_s$ . Hence, the length of the cable is given by  $l_{cab}=N_B L_{p,s}/N_s$ . Each band consists of  $(N_s-1)$  calculation cells (see Fig. 4.2) and has  $(5N_s-3)$  unknown currents, namely:

- $(2N_s-2)$  strand currents  $I_{str}$ ,
- $2N_s$  currents between adjacent strands  $I_a$ ,
- $(N_s-1)$  currents between crossing strands  $I_c$ .

Note that the small sides of a band consists of four resistances  $R_a$  (numbers 1, 2,  $2N_s-1$  and  $2N_s$ ) but only two strand elements (numbers 2 and  $2N_s-1$ ), which are about twice as long as the other strand elements.

The field components parallel to the cable width  $B_{||}$ , perpendicular to the cable width  $B_{\perp}$  and normal to the cross-section of the cable  $B_z$  are given by (see Fig. 4.1):

$$B_x = B_{||} = B \sin \theta \sin \varphi \quad [T], \quad (4.1a)$$

$$B_y = B_{\perp} = B \cos \theta \quad [T], \quad (4.1b)$$

$$B_z = B \sin \theta \cos \varphi \quad [T]. \quad (4.1c)$$

Using Kirchhoff's laws the  $(5N_s-3)$  equations, needed to solve the current distribution in one band, can be set up. The following symbolic notations demonstrate the implementation in the computer program. The  $(5N_s-3)$  equations consist of:

- $(2N_s-2)$  equations in the nodes:

$$\sum I_a + \sum I_c + \sum I_{str} = 0 \quad [A]. \quad (4.2)$$

- $(3N_s-2)$  equations for a circuit:

$$\sum (I_a R_a) + \sum (I_c R_c) + \sum U_{str} = \dot{B}_{\perp A} A \quad [V], \quad (4.3a)$$

with  $\dot{B}_{\perp A}$  the component of  $\dot{B}$  normal to the enclosed surface  $A$  of the circuit, and  $U_{str}$  the voltage over a strand element. The enclosed surfaces are:

$$A_x = \frac{L_{p,s}}{2N_s} \frac{h}{2} = \frac{L_{p,s}h}{4N_s} \quad [m^2] \quad \text{for } \dot{\mathbf{B}} = \dot{B}_x \quad (\theta=90^\circ, \varphi=90^\circ), \quad (4.3b)$$

$$A_y = \frac{1}{2} \frac{L_{p,s}}{N_s} \frac{w(1-2/N_s)}{N_s/2-1} = \frac{L_{p,s}w}{N_s^2} \quad [m^2] \quad \text{for } \dot{\mathbf{B}} = \dot{B}_y \quad (\theta=0^\circ), \quad (4.3c)$$

$$A_z = \frac{w(1-2/N_s)}{(N_s-2)} \frac{h}{2} = \frac{wh}{2N_s} \quad [m^2] \quad \text{for } \dot{\mathbf{B}} = \dot{B}_z \quad (\theta=90^\circ, \varphi=0^\circ). \quad (4.3d)$$

- One constraint:

$$\sum I_a + \sum I_{str} = \sum I_a + \sum I_s + \left( \sum I_{bi} \right) + \sum I_{tr, str} = I_{tr, cab} \quad [A], \quad (4.4)$$

stating that all the currents flowing through the cross-section of the cable add up to the cable transport current  $I_{tr, cab}$ . Since the sum of the transport currents in the strands is

equal to the cable transport current, eq. 4.4 implies that the sum of the coupling currents through the cross-section of the cable is equal to 0. The currents  $I_{bi}$  are discussed in chapter 5 and are equal to 0 in this chapter.

Two calculation cells of Fig. 4.2 are enlarged (see Fig. 4.3) in order to illustrate how eqs. 4.2 and 4.3 can be rewritten and implemented in the network model.

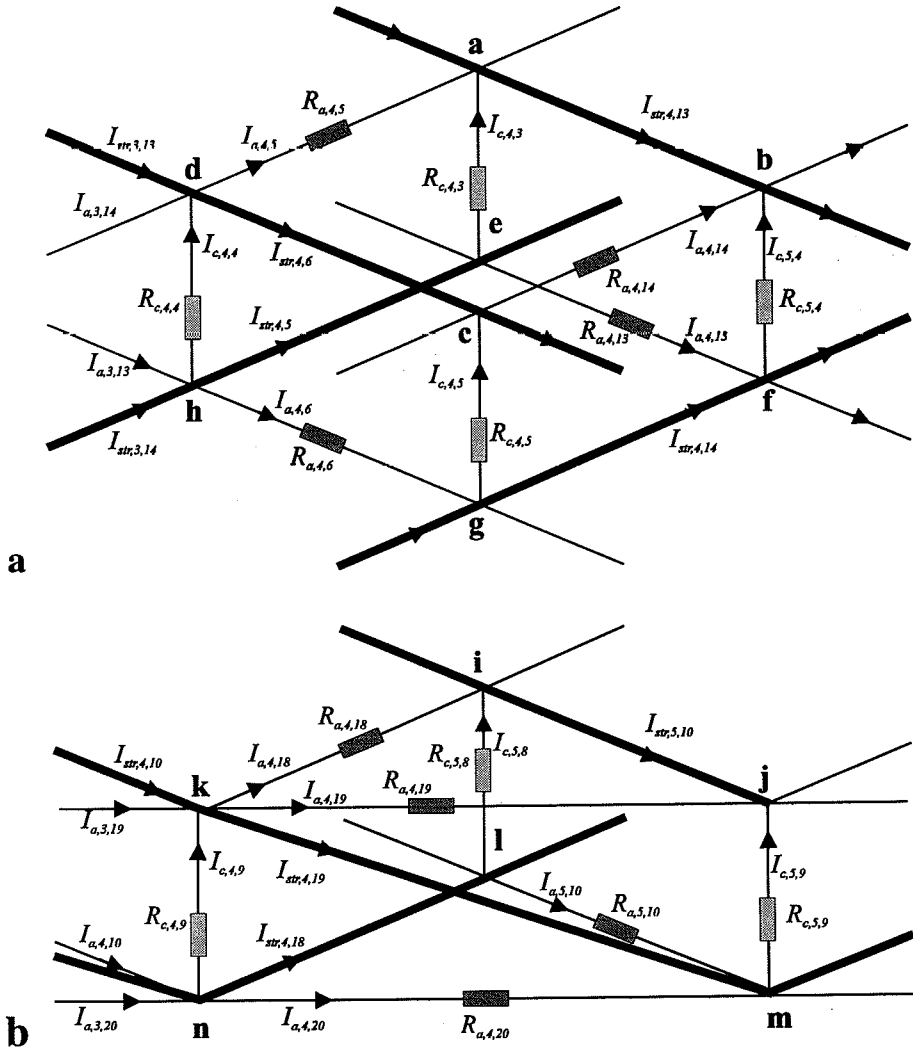


**Figure 4.3.** Enlargement of two calculation cells at  $N_b=4$  (see Fig. 4.2) of the network model with:  
 a. nodes **a, b, c, d** in the upper layer and nodes **e, f, g, h** in the lower layer,  
 b. nodes **i, j, k** in the upper layer and nodes **l, m, n** in the lower layer.  
 The last two indices of the currents and resistances refer to the band and the number of the section across the cable width.



The last two indices of the currents and resistances refer to the band and the number of the section across the cable width. This results in:

$$(I_{a,3,14} - I_{a,4,5}) + I_{c,4,4} + (I_{str,3,13} - I_{str,4,6}) = 0 \quad [\text{A}], \quad (4.5a)$$

$$(I_{a,3,19} - I_{a,4,18} - I_{a,4,19}) + I_{c,4,9} + (I_{str,4,10} - I_{str,4,19}) = 0 \quad [\text{A}], \quad (4.5b)$$

for the sum of the currents in nodes d and k respectively, and:

$$(I_{a,4,5} R_{a,4,5} - I_{a,4,14} R_{a,4,14}) + (U_{str,4,13} - U_{str,4,6}) = \dot{B}_y A_y \quad [\text{V}], \quad (4.6a)$$

$$(I_{a,4,18} R_{a,4,18} - I_{a,4,19} R_{a,4,19}) + U_{str,5,10} = \frac{1}{2} \dot{B}_y A_y \quad [\text{V}], \quad (4.6b)$$

for the circuits a-b-c-d and i-j-k respectively, and:

$$-I_{a,4,6} R_{a,4,6} + (I_{c,4,4} R_{c,4,4} - I_{c,4,5} R_{c,4,5}) + U_{str,4,6} = -\dot{B}_x A_x - \dot{B}_z A_z \quad [\text{V}], \quad (4.7a)$$

$$I_{a,4,19} R_{a,4,19} - I_{c,5,9} R_{c,5,9} - U_{str,4,19} = -\dot{B}_x A_x \quad [\text{V}], \quad (4.7b)$$

for the circuits d-c-g-h and k-j-m respectively.

The voltage  $U_{str}$  (see eq. 4.3a) over a strand element consists of a resistive part  $U_R$  and an inductive part  $U_{ind}$ . The inductive part will be discussed later. The resistive part can be described by the following three models.

- The power law:

$$U_R = U_{R,0} (I_{str} / I_{C,str})^n \quad [\text{V}], \quad (4.8)$$

with  $U_{R,0}$  the voltage at the critical current  $I_{str} = I_{C,str}$ . Small and large  $n$ -values indicate a gradual and sharp transition respectively. Using the power law implies that the set of equations 4.2-4.4 has to be solved iteratively, which considerably increases the computing time, especially for large  $n$ -values.

- A linear increase in the voltage for strand currents larger than  $I_{C,str}$  assuming that the surplus current  $(I_{str} - I_{C,str})$  flows through the resistive matrix, so that:

$$U_R = 0 \quad [\text{V}] \quad \text{for } I_{str} < I_{C,str}, \quad (4.9a)$$

$$U_R = R_{mat} (I_{str} - I_{C,str}) \quad [\text{V}] \quad \text{for } I_{str} > I_{C,str}, \quad (4.9b)$$

with  $R_{mat}$  the resistance of the magnetoresistive matrix:

$$R_{mat}(B) = \rho_{mat}(B) \frac{l_s}{(1-\eta)\pi d_s^2 / 4} \quad [\Omega], \quad (4.9c)$$

with  $l_s$  the length of the strand element,  $d_s$  the (effective) strand diameter,  $\rho_{mat}$  the resistivity of the matrix and  $\eta$  the volume fraction of superconductor in the strand. This approach limits the computing time since iteration is only required if one or more strand elements become saturated.

- A model similar to eqs. 4.9a-4.9c but taking into account the dynamic resistance as defined in section 3.2, and the decrease of the maximum strand current due to the IFCCs. The critical current  $I_{C, str}$  of the strand is therefore replaced by the maximum strand current  $I_{tr, str, max}$  (see eq. 3.28), so:

$$U_R = \frac{4d_f l_s}{3\pi} \frac{I_{str}}{I_{C, str}} |\dot{B}_{\perp s}| \quad [\text{V}] \quad \text{for } I_{str} < I_{tr, str, max}, \quad (4.10a)$$

$$U_R = \frac{4d_f l_s}{3\pi} \frac{I_{tr, str, max}}{I_{C, str}} |\dot{B}_{\perp s}| + R_{mat} (I_{str} - I_{tr, str, max}) \quad [\text{V}] \quad \text{for } I_{str} > I_{tr, str, max}, \quad (4.10b)$$

with  $\dot{B}_{\perp s}$  the field change perpendicular to the strand axis.

The  $UI$  relations of these three models are depicted in Fig. 4.4. The type of  $UI$  relation does not influence the ISCCs under weak excitation but it quantitatively affects the ISCCs under strong excitation.

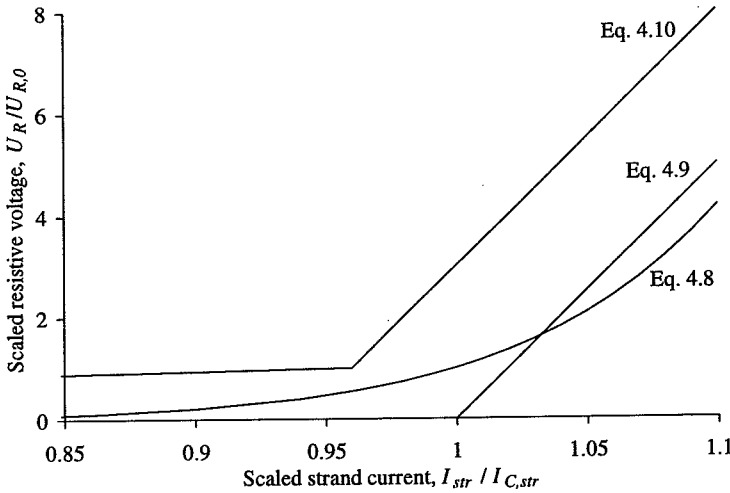


Figure 4.4. Voltage-current relations of eqs. 4.8 (with  $n=15$ ), 4.9 and 4.10 (using  $I_{tr, str, max} = 0.96 I_{C, str}$ ).

In chapter 5 the results of several simulations are presented assuming a constant strand resistivity  $\rho_s$  which is independent of the current and field. Within the network model a strand resistivity is correlated to a strand resistance between two nodes:

$$R_s = \rho_s \frac{l_s}{\pi d_s^2 / 4} \equiv \rho_s \frac{2L_{p,s}}{N_s \pi d_s^2} \quad [\Omega], \quad (4.11)$$

where the small twist angle is disregarded. For the strand elements at the thin edges of the cable (numbers 2 and  $2N_s-1$ , see Fig. 4.2) the strand resistance  $R_s$  is about twice as large.

The equations of band  $N_b$  contain not only currents of band  $N_b$  itself but also currents of bands  $(N_b-1)$  and  $(N_b+1)$  and, if mutual interactions are included, even more currents. This implies that for the first and the last band appropriate boundary conditions are required. Two different cases can be distinguished:

- The current distribution in all the bands is the same. In this case only one band has to be calculated, since:  $I_{a,Nb,i} = I_{a,Nb+1,i}$ ,  $I_{c,Nb,i} = I_{c,Nb+1,i}$  and  $I_{str,Nb,i} = I_{str,Nb+1,i}$ .
- The currents  $I_{str}$  in the first and last bands ( $N_b=1$  and  $N_b=N_B$ ) are given by the transport current in the strand  $I_{tr,str}$ . Obviously, this affects the equations of the type as given in eq. 4.2 for the two bands, so (see Fig. 4.2):

$$I_{str,1,i} = I_{tr,str} \text{ for } i=2 \text{ to } (N_s+1),$$

$$I_{str,NB,i} = I_{tr,str} \text{ for } i=2, (N_s+1) \text{ to } (2N_s-1).$$

A cable of finite length without transport current is simulated by the boundary conditions  $I_{tr,str}=0$ .

Non-steady-state situations are investigated by incorporating the self- and mutual inductances of the strand elements in the network model. The inductive part  $U_{ind}$  of the voltage of strand element  $i$  is given by:

$$U_{ind}^i = \sum_{j=1}^N M^{i,j} \dot{I}_{str}^j \quad [\text{V}], \quad (4.12)$$

with  $M^{ij}$  the mutual inductance between two strand elements. Groover has given an expression of the mutual induction between two wires of finite length placed in arbitrary positions [Groover, '46]. The summation has to be made over all the strand elements of all the bands, so  $N=(2N_s-2)N_B$ . However, in the network model only the mutual inductances are included if the strand elements are located within a length of about  $10l_s$  of each other. The computing time is then significantly reduced while the introduced error in the inductive voltage remains within 2%. The variable  $N_{MUT}$  is defined as the number of bands on each side of the calculation cell for which the mutual inductance is included.

In the numerical model the time derivative of the strand current is represented by the difference in current between two discrete time steps:

$$\dot{I}_{str}^j = \frac{I_{str,m}^j - I_{str,m-1}^j}{t_m - t_{m-1}} = \frac{I_{str,m}^j - I_{str,m-1}^j}{\Delta t_m} \quad [\text{As}^{-1}]. \quad (4.13)$$

Eq. 4.3a can then be rewritten so that the right-hand side is known:

$$\begin{aligned} \sum (I_{a,m} R_a) + \sum (I_{c,m} R_c) + \sum U_{R,m} + \frac{1}{\Delta t_m} \sum_{j=1}^N (M^{i,j} I_{str,m}^j) = \\ \dot{B}_{\perp A,m} A + \frac{1}{\Delta t_m} \sum_{j=1}^N (M^{i,j} I_{str,m-1}^j) \quad [\text{V}]. \end{aligned} \quad (4.14)$$

The results of two types of calculations are presented in the chapters 4 and 5:

- **Steady-state calculations.** The field change  $\dot{B}$  and the transport current are constant for a time much larger than all time constants involved. This implies that the coupling currents are constant so that the terms with the mutual inductances can be disregarded.
- **Step-response calculations.** The field change  $\dot{B}$  has a constant value (larger than 0) for  $t \leq 0$  s and equals 0 for  $t > 0$  s. The currents are calculated for about 40 time steps where each time step is defined so that the average of all the coupling currents decreases by about 2% of the initial value at  $t = 0$  s. If the solving routine in the computer program is too time-consuming, the number of time steps is reduced to 10-20. The decrease in time of each current  $I_a$ ,  $I_c$  and  $I_s$  is exponential and expressed by a time constant  $\tau_{is}$ . The time constant is determined by fitting the current values (at the discrete points in time) to the relation:

$$I = I_{t=0} e^{-t/\tau} \quad [\text{A}]. \quad (4.15)$$

Each current in the cable has its own time constant. An average time constant is defined as the time constant of the exponential decay of the average of all the currents  $I_s$  in the cable, the stack or the coil. The time constants of the ISCCs are referred to as:

- $\tau_{is,i}$ : the time constant of  $I_c$  or  $I_s$  at position  $i$  in a single cable piece (see section 4.4.2),
- $\tau_{is,cab}$ : the average time constant of a single cable piece (see section 4.4.2),
- $\tau_{is,st,i}$ : the average time constant of cable piece  $i$  within a stack of cable pieces (see section 4.9),
- $\tau_{is,st}$ : the average time constant of a stack of cable pieces (see section 4.9),
- $\tau_{is,M}$ : the average time constant of a magnet (see chapter 6).

In chapter 5 the step-response of the BICCs is discussed. The decay in time of the BICCs is not exponential. A characteristic time  $\tau_{bi}$  is defined as the time at which a BICC decays to 1/e of its initial value.

Within the network model the resistances  $R_a$  can be disregarded if the currents  $I_a$  are small compared to the currents  $I_c$ . In section 4.4.1 it will be shown that this assumption is valid if  $R_a \gg 4R_c/N_s$  (for a field change  $\dot{B}_\perp$ ) in the case of ISCCs. The smaller computing time makes this simplification especially suitable for step-response calculations. For the calculation of the BICCs the resistances  $R_a$  can be disregarded if  $R_a \gg R_c$ .

A matrix with dimensions  $N_B(5N_s-3)$  by  $N_B(5N_s-3)+1$  can be set up (see Fig. 4.5), containing all the equations of type 4.2-4.4 with  $I_a$ ,  $I_c$  and  $I_{str}$  as the unknown currents. The currents can be solved by rewriting the matrix so that the lower left triangle becomes zero. A faster solving routine can be used knowing that the matrix already contains large areas of zeros (since not all the mutual inductances are incorporated), which remain zeros if the matrix is rewritten. The matrix is therefore reduced by removing the lower-left and upper-right regions filled with zeros (see Fig. 4.5) which requires a different solving algorithm. The final size of matrix B is then (this is merely included to illustrate the large reduction in matrix size that is obtained):

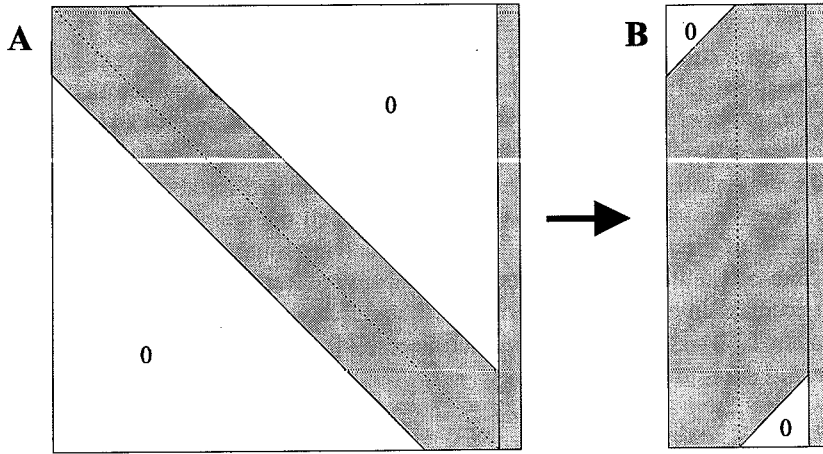


**Figure 4.5.** Reducing the size of the matrix used to solve the currents in a cable of finite length. The boundary conditions for the bands  $N_b=1$  and  $N_b=N_B$  result in the small areas filled with zeros in matrix B.

- $N_B(5N_s-3)$  by  $(5N_s-3)+1$  if the current distribution is independent of the longitudinal position in the cable,
- $N_B(5N_s-3)$  by  $3(5N_s-3)+1$  for steady-state calculations,
- $N_B(5N_s-3)$  by  $(2N_{MUT}+1)(5N_s-3)+1$  for step-response calculations.

The current distributions in larger cable pieces can be calculated using matrix B, since the internal memories of large computers are often limited to about 100-1000 Mb.

Calculations are performed varying all the parameters that are involved in the network model, i.e.  $w$ ,  $h_1$ ,  $h_2$ ,  $L_{p,s}$ ,  $N_s$ ,  $\dot{B}$ ,  $\theta$ ,  $\varphi$ ,  $R_a$ ,  $R_c$  and  $I_{tr,cab}$ . The results of the numerical simulations are then combined into relations that analytically describe the dependence of the currents, the loss and the time constants on the above mentioned parameters. Hence, each relation contains a factor of proportionality that quantitatively fits the analytical expression to the numerical results. The errors in the relations are:

- smaller than 2% for steady-state calculations,
- smaller than about 10% for the time constants  $\tau_{is}$  of the ISCCs,
- smaller than about 20% for the characteristic times  $\tau_{bi}$  of the BICCs.

The results of simulations performed in this way can be found in sections 4.4.1, 4.4.2, 4.9, 5.4.2-5.4.4, 5.6 and 5.7.

### 4.3 Contact resistances $R_a$ and $R_c$

The contact resistances  $R_a$  and  $R_c$  which are incorporated in the network model depend on several factors and circumstances. In this section attention is focused on  $R_c$  since it is shown in section 4.4.1 and chapter 5 that the magnitude of the coupling currents and the ISCL is dominated by  $R_c$  (if  $R_a$  and  $R_c$  are of the same order of magnitude and the field change is not directed in the  $x$ -direction). The following factors influence the  $R_c$  of a cable:

- **The level of oxidation of bare strands.** AC loss measurements on SSC dipole magnets illustrate that those magnets wound from strands which have undergone an ultraclean surface treatment exhibit a large ISCL [Ozelis, '93]. The  $R_c$  of bare strands is very difficult to control because the oxide layer that is formed on the strands is very sensitive to the heat treatment, cleaning and exposure time in air.
- **The surface treatment of the strand.** Applying coatings to the strands can increase or decrease  $R_c$  depending on the resistivity, thickness and hardness of the coating [Sumption, '94].
- **The pressure applied transversely on the cable.** Measurements on the UNK-type cable (zebra-type cable with half of the strands in a state of natural oxidation and the remainder having a 95%Sn5%Ag coating) show a decrease of a factor of 5 in  $R_c$  between 10 and 50 MPa [Andreyev, '85]. Unsoldered cables have shown a decrease in  $R_c$  of a factor 10 between 0 and 30 MPa, whereas the  $R_c$  of soldered cables changed less than 15% in the same range of pressure [Sytnikov, '89b]. Shear stress can also affect  $R_c$  but no experimental data are available.
- **The curing temperature.** Curing the cable insulation system will decrease  $R_c$ , especially at high curing temperatures in combination with large transverse pressures. AC loss measurements on 12 mm wide Rutherford-type cables show a large decrease in  $R_c$  if the cable is cured under pressure while curing without pressure hardly affects the ISCL [Lei, '93], [Kimura, '95]. After curing  $R_c$  increases by a factor of about 5 if the pressure is released after curing and reapplied after one or more days [Oberli, '95]. Curing can also change the transverse resistivity of the matrix [Mallick, '93] and hence the IFCL.
- **The matrix material.** The  $R_c$ -value is determined by both the matrix resistance and the contact resistance, of which the latter is usually dominant, at least for strands with a copper matrix. The resistance of the matrix can dominate in the case of a matrix with a high resistivity and give rise to a large  $R_c$  which is observed, for example, for strands with a Cu/Cu0.5%Mn matrix, even after curing at 180 °C at 50 MPa [Shintomi, '94].
- **The size of the contact surface.** Applying pressure on two strands with an originally round cross-section results in a hysteretic behaviour of  $R_c$  once the pressure is reduced [Avest, ter, '90]. This indicates that plastic deformation (i.e. an increase in the contact surface) causes a decrease of  $R_c$ . The effect is also demonstrated by AC loss measurements on cables with different packing factors or void fractions. A decrease in void fraction, which implies a larger contact surface, results in significantly larger coupling losses [Mower, '86], [Nijhuis, '95].
- **The soldering of the cable.** The solder in a cable fills the voids between the strands thereby giving it more stiffness and thermal stability. However, the solder also causes a decrease of  $R_c$  since the contact area between the strands increases.  $R_c$ -values of the order of  $10^{-7}$ - $10^{-6}$   $\Omega$ m have been measured in cables soldered with PbSn [Sytnikov, 89b]. Using alloys with a small percentage of indium or bismuth can significantly increase the resistivity of the solder and therefore reduce the coupling losses [Kwasnitza, '86].
- **The presence of a resistive barrier.** Insertion of a resistive strip in-between the two layers of the cable strongly enhances  $R_c$  [Sumption, '95].

In a coil, the above-mentioned factors affect the global  $R_c$  as well as local *distributions* of  $R_c$ . Variations in  $R_c$  are present:

- across the cable width (see section 4.6), mainly caused by:
  - the keystone of the cable, which results in a variation of the contact area between crossing strands,
  - a variation in pressure across the cable width (see Table 2.2),
- along the cable length (see chapter 5), mainly caused by:
  - the coil ends, where the strands of the cable diverge and reduce the contact area,
  - the soldered connections between two cables,
  - the varying pressure levels over the cross-section of the coil.

Furthermore,  $R_c$  can vary among the coils of a magnet or among the magnets in an accelerator ring due to, for example, different stress and oxidation levels.

## 4.4 Weak excitation

### 4.4.1 Steady-state calculations

In this section expressions for the total power loss and the current distribution in a cable are given under steady-state conditions for:

- weak excitation levels (i.e. the total current in each strand section is smaller than the critical current  $I_{C, str}$  of the strand),
- constant contact resistances (across the width and along the length of the cable),
- constant  $\dot{B}$ .

The set of eqs. 4.2-4.4 can now be solved taking  $U_R=0$  and  $U_{ind}=0$ .

The total generated power loss per metre of cable in the contact resistances  $R_a$  and  $R_c$  is determined following the method described at the end of section 4.2 and given by:

$$P_a = P_{a,\perp} + P_{a,\parallel} = 0.170 \frac{L_{p,s} w^2 (1 - 1/N_s)}{R_a} \dot{B}_\perp^2 + 0.125 \frac{L_{p,s} h^2}{R_a} \dot{B}_\parallel^2 \quad [\text{Wm}^{-1}], \quad (4.16)$$

$$P_c = 8.49 \cdot 10^{-3} \frac{L_{p,s} w^2 (N_s^2 - N_s)}{R_c} \dot{B}_\perp^2 \quad [\text{Wm}^{-1}], \quad (4.17)$$

with  $B_\perp$  and  $B_\parallel$  defined by eq. 4.1. In order to obtain the power loss per unit volume the above given relations have to be divided by the cross-section of the cable ( $w \cdot h$ ).

Eqs. 4.16 and 4.17 are, in first approximation, equal to the expressions derived by Morgan (for  $P_c$ ) and Sytnikov (for  $P_{a,\perp}$ ,  $P_{a,\parallel}$  and  $P_c$ ). A small difference concerns the factors  $(1-1/N_s)$  in eq. 4.16 and  $(N_s^2 - N_s)$  in eq. 4.17 which are calculated by these authors as 1 and  $N_s^2$  respectively [Morgan, '73], [Sytnikov, '89a]. The difference is caused by the simplified modelling of the edges in the network models of Morgan and Sytnikov. The power losses

also correspond to the expressions derived analytically by Wilson and Krempasky, if the average resistivity in the cable, which is used in their formulas, is written in terms of the contact resistances  $R_a$  and  $R_c$  (see for example eq. 4.33 where  $R_c$  is written in terms of  $\rho_c$ ) [Wilson, '72], [Krempasky, '78].

Eqs 4.16 and 4.17 show that the power loss in  $R_c$  is given by the field change  $\dot{B}_\perp$  while the power in  $P_a$  is also present for field changes  $\dot{B}_\parallel$ . The power loss  $P_{a\parallel}$  is, however, about a factor  $h^2/w^2 = (1/\alpha_{cab})^2$  smaller than  $P_{a\perp}$  (for  $\dot{B}_\perp = \dot{B}_\parallel$ ) and can therefore be neglected for almost all cables, since  $(\alpha_{cab})^2$  is usually larger than 10. The power loss generated by a longitudinal field change  $\dot{B}_z$  is not included in the equations as it is still another two orders of magnitude smaller than  $P_{a\parallel}$ .

The distributions of the currents  $I_a$ ,  $I_c$  and  $I_s$  as a function of the position  $x$  (and  $x'$ ) across the cable width are given by:

$$I_a(x) = \frac{L_{p,s}(x-0.5w)}{R_a(N_s+2)} \dot{B}_\perp \pm 0.25 \frac{L_{p,s}h}{R_a N_s} \dot{B}_\parallel \quad [\text{A}], \quad (4.18)$$

$$I_c(x') = 0.125 \frac{L_{p,s}w}{R_c} \dot{B}_\perp (1 - (2x'/w - 1)^2) \quad [\text{A}], \quad (4.19)$$

$$I_s(x) = 0.0415 \frac{L_{p,s}wN_s}{R_c} \dot{B}_\perp \cos(\pi x/w) \pm 0.25 \frac{L_{p,s}h}{R_a N_s} \dot{B}_\parallel \quad [\text{A}], \quad (4.20)$$

where the lengths  $x$  and  $x'$  have the discrete values:

$$x = w/N_s \text{ and } x = w - w/N_s \quad [\text{m}], \text{ at the edges of the cable,} \quad (4.21a)$$

$$x = (k - 1/2)w/N_s \quad [\text{m}] \text{ everywhere else, with } k=2, 3, 4, \dots, (N_s-1), \quad (4.21b)$$

for the currents  $I_a$  and  $I_s$ , and:

$$x' = kw/N_s \quad [\text{m}] \text{ with } k=1, 2, 3, \dots, (N_s-1), \quad (4.21c)$$

for the currents  $I_c$ . In the case of a field change  $\dot{B}_\parallel$ , the currents  $I_a$  and  $I_s$  have a constant value of which the sign depends on the layer of the cable being negative for the upper layer (see Fig. 4.1) and positive for the lower layer.

The current distributions for a field change  $\dot{B}_\perp$  are depicted in Fig. 4.6. A net current in the  $y$ -direction flows from one layer to the other through  $R_c$  and returns by the two strands that bend around the two thin edges of the cable. Note that  $I_c$  corresponds to the slope of the  $I_s$ - $x$  curve, if the small currents  $I_a$  are disregarded.

The coupling currents  $I_s$  increase linearly with the field-sweep rate until the sum of the transport current and the coupling current reaches the critical current  $I_{C, \text{str}}$  of the strand. The critical field-changes, at which the first strand element saturates, are given by (according to eq. 4.20):



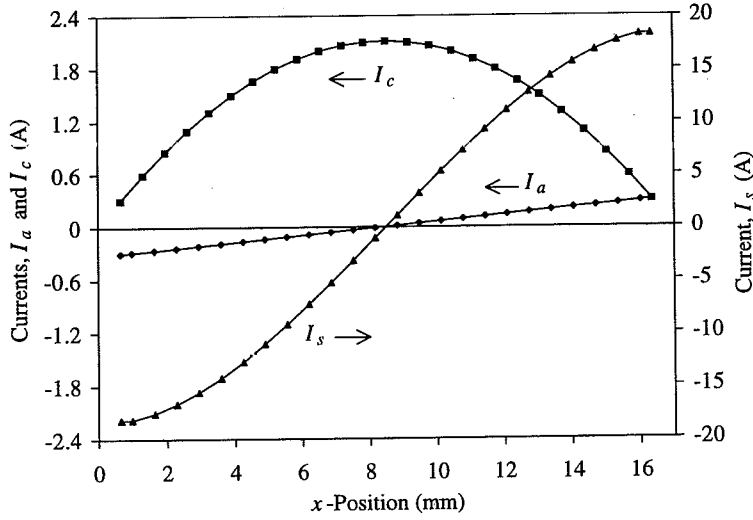


**Figure 4.6.** The current distributions of  $I_a$ ,  $I_c$  and  $I_s$  across the cable width ( $L_{p,s}=0.1$  m,  $R_a=R_c=1 \mu\Omega$ ,  $w=17$  mm,  $N_s=26$ ,  $\dot{B}_\perp=0.01$  T s $^{-1}$ ).

$$\dot{B}_{\perp,cr} = \frac{R_c(I_{C,str} - I_{tr,str})}{0.0415 L_{p,s} w N_s \cos(\pi / N_s)} \quad [\text{T s}^{-1}] \quad \text{for a field change } \dot{B}_\perp, \quad (4.22)$$

and:

$$\dot{B}_{\parallel,cr} = \frac{4 R_a N_s (I_{C,str} - I_{tr,str})}{L_{p,s} h} \quad [\text{T s}^{-1}] \quad \text{for a field change } \dot{B}_\parallel. \quad (4.23)$$

In section 4.5 the case  $\dot{B}_\perp > \dot{B}_{\perp,cr}$  is dealt with in more detail.

In a similar way the maximum transport current in a cable  $I_{tr,cab,max} = N_s I_{tr,str,max}$  can be determined by the transport current at which the first strand becomes saturated, so that:

$$I_{tr,str,max}(B_\perp, \dot{B}_\perp, T) = I_{C,str} - 0.0415 \frac{L_{p,s} w N_s}{R_c} \cos(\pi / N_s) |\dot{B}_\perp| \quad [\text{A}]. \quad (4.24)$$

A similar equation for a parallel field can be set up using eq. 4.20.

In the case of  $\dot{B}_\perp$ , the currents  $I_a$  can be disregarded compared to  $I_c$  if:

$$R_a \gg \frac{4 R_c}{N_s} = \frac{R_c}{\alpha_0} \quad [\Omega]. \quad (4.25)$$

In section 4.3 it is shown that in practice the resistances  $R_a$  and  $R_c$  in a cable decrease when the contact areas between adjacent, respectively crossing, strands increase. Since the contact areas depend on the cable geometry, (i.e. on  $N_s$ ,  $w$  and  $L_{p,s}$ ) it is hard to estimate the increase or decrease of the ISCCs and the ISCL if one of these parameters is changed. Multiplying

$R_a$  and  $R_c$  by the maximum contact areas (for strands with a square cross-section) gives effective resistances  $R_a^*$  and  $R_c^*$  which are likely to depend less on the cable geometry:

$$R_a^* \equiv l_s \frac{h}{2} R_a \equiv \frac{L_{p,s}}{2N_s} \frac{h}{2} R_a = \frac{wL_{p,s}}{N_s^2} R_a \quad [\Omega m^2], \quad (4.26)$$

$$R_c^* \equiv \frac{1}{2} \frac{L_{p,s}}{N_s} \frac{w}{(N_s - 1)/2} = \frac{L_{p,s}w}{(N_s^2 - N_s)} R_c \quad [\Omega m^2]. \quad (4.27)$$

Substituting these relations into eqs. 4.16, 4.17 and 4.20 (only considering  $\dot{B}_\perp$ ) results in the power losses  $P_{a,\perp}$ ,  $P_c$  and the current distribution  $I_s$ :

$$P_{a,\perp} = 0.170 \frac{L_{p,s}^2 w^3 (N_s - 1)}{R_a^* N_s^3} \dot{B}_\perp^2 \quad [W m^{-1}], \quad (4.28)$$

$$P_c = 8.49 \cdot 10^{-3} \frac{L_{p,s}^2 w^3}{R_c^*} \dot{B}_\perp^2 \quad [W m^{-1}], \quad (4.29)$$

$$I_s(x) = 0.0415 \frac{L_{p,s}^2 w^2}{R_c^* (N_s - 1)} \dot{B}_\perp \cos(\pi x / w) \quad [A]. \quad (4.30)$$

Similar equations for the  $I_a$  and  $I_c$  distributions can be derived. The equations clearly show that the coupling currents and power losses are very sensitive to the width of the cable and the cable pitch. In high-field accelerator magnets, the quench protection and the required field fix the range over which the width of the cable can be varied. For good mechanical stability the cable pitch is then limited to about  $6w < L_{p,s} < 10w$ . This implies that  $R_c$  is the only parameter which can essentially change the magnitude of the ISCCs and the ISCL.

#### 4.4.2 Step-response calculations

The coupling current in each resistance and in each strand section of a cable has its own time constant  $\tau_{is,i}$ , which can differ considerably from the average (global) time constant  $\tau_{is,cab}$ , especially for non-uniform  $R_a$ - and  $R_c$ -distributions. Fig. 4.7 shows the time-constant spectrum of the currents  $I_c$  and  $I_s$  in a 1 m long cable piece. The time constants are determined from the response of the ISCCs to a step decrease of  $\dot{B}_\perp$  from 1 to 0  $Ts^{-1}$  as explained in section 4.2. The time constants for  $R_a \ll R_c$  as well as for a field change  $\dot{B}_\parallel$  are not considered here.

The time constants increase towards the centre of the cable. In section 4.9 it is shown in a similar way that the time constant of a cable in a stack of cable pieces increases towards the centre of the stack. The average time constant of the ISCCs in a cable is defined as the time constant of the average of the currents  $I_c$  and  $I_s$  (and not as the average of the time constants of the currents  $I_c$  and  $I_s$ ). The average time constants of the currents  $I_c$  and  $I_s$  are equal within the accuracy of the calculations and are denoted by  $\tau_{is,cab}$ .

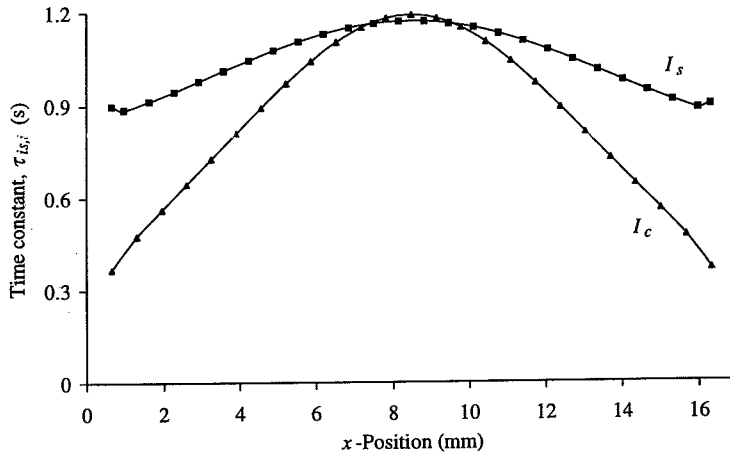


**Figure 4.7.** The distribution of the time constant  $\tau_{is,i}$  of the currents  $I_c$  and  $I_s$  across the cable width ( $L_{p,s}=0.1$  m,  $R_a=R_c=1 \mu\Omega$ ,  $w=17$  mm,  $h_1=h_2=2.6$  mm,  $N_s=26$ ).

The  $\tau_{is,cab}$ -value of a straight cable with strands having a round cross-section is numerically calculated as a function of  $N_s$ ,  $\alpha_{cab}$ ,  $L_{p,s}$  and  $R_c$ . The results can be expressed by the analytical relation:

$$\tau_{is,cab} = C \frac{L_{p,s}(N_s^2 - 4N_s)}{R_c} \quad [\text{s}], \quad (4.31)$$

for  $8 \leq N_s \leq 40$ . The fitting constant  $C$  varies between  $1.6 \cdot 10^{-8}$  and  $1.7 \cdot 10^{-8} \Omega \text{m}^{-1} \text{s}$  for twist angles between  $10^\circ$  and  $25^\circ$  and increases slightly for cables with a small keystone angle and for heavily compacted cables (about 10% for  $\alpha_{cab}=1.2\alpha_0$ ). The time constant is almost independent of the length if  $l_{cab} > L_{p,s}$ . The time constants of stacked cables (or coils) are treated in section 4.9.

It is interesting to compare the time constant  $\tau_{is,cab}$  of the ISCCs in a cable with the time constant  $\tau_{if}$  of the IFCCs in a single conductor. The time constant  $\tau_{if}$  of a conductor with a rectangular cross-section, subject to a field change normal to the wide side of the conductor is given by [Campbell, '82]:

$$\tau_{if} = \frac{7 \mu_0 \alpha_{cond} L_{p,f}^2}{480 \rho_{eff}} = 1.8 \cdot 10^{-8} \frac{\alpha_{cond} L_{p,f}^2}{\rho_{eff}} \quad [\text{s}], \quad (4.32)$$

with  $\alpha_{cond}$  the aspect ratio of the conductor. In order to compare  $\tau_{if}$  with  $\tau_{is,cab}$ , the contact resistance  $R_c$  has to be written in terms of an effective resistivity  $\rho_c$  in the y-direction:

$$R_c = \rho_c \frac{h/2}{A_c} = \rho_c \frac{(N_s^2 - N_s)h}{2L_{p,s}w} = \rho_c \frac{(N_s^2 - N_s)}{2L_{p,s}\alpha_{cab}} \quad [\Omega], \quad (4.33)$$

where  $h/2$  corresponds to the average distance between the centres of the strands of the upper and the lower layer and  $A_c$  denotes the maximum contact area between crossing strands (see also eq. 4.27). Combining eqs. 4.31 and 4.33 results in:

$$\tau_{is,cab} = C \frac{2L_{p,s}^2 \alpha_{cab} (N_s - 4)}{\rho_c (N_s - 1)} \cong 2C \frac{L_{p,s}^2 \alpha_{cab}}{\rho_c} \quad [\text{s}] \quad \text{for large } N_s, \quad (4.34)$$

with  $C$  the fitting constant from eq. 4.31. The relation shows that  $\tau_{is,cab}$  depends in the same way on  $L_{p,s}$ ,  $\alpha_{cab}$  and  $\rho_c$  as  $\tau_{if}$  depends on  $L_{p,f}$ ,  $\alpha_{cond}$  and  $\rho_{eff}$ . The factor  $2C$  in eq. 4.34 is about twice as large as the factor  $1.8 \cdot 10^{-8} \Omega \text{sm}^{-1}$  in eq. 4.32, which is probably caused by the different current distribution. In a conductor with a rectangular cross-section the coupling currents flow through the filaments located near the surface of the strands (thus at a distance equal to the thickness of the conductor), while in the network model the currents  $I_s$  flow in the centres of the strands (at a distance equal to half the thickness of the cable).

The time constant  $\tau_{is,cab}$  is a factor  $1.2\alpha_{cab}$  smaller than the time constants given by [Krempasky, '78] and [Sytnikov, '94]. The main reason for this difference will be explained in section 4.9.

The power loss can be expressed as a function of  $\tau_{is,cab}$  by combining eqs. 4.17 and 4.31:

$$P_c = 5.3 \cdot 10^5 \tau_{is,cab} \omega^2 \dot{B}_\perp^2 = \frac{2}{3\mu_0} \tau_{is,cab} \omega^2 \dot{B}_\perp^2 \quad [\text{Wm}^{-1}], \quad (4.35)$$

so that the power loss per unit volume equals:

$$P_c = \frac{2\alpha_{cab} \tau_{is,cab}}{3\mu_0} \dot{B}_\perp^2 \quad [\text{Wm}^{-3}]. \quad (4.36)$$

This equation is similar to the more general expression for the IFCL of a conductor with a rectangular cross-section, subject to a field change normal to the wide side of the conductor [Campbell, '82]:

$$P_{if} = \frac{\alpha_{cond} \tau_{if}}{\mu_0} \dot{B}_\perp^2 \quad [\text{Wm}^{-3}]. \quad (4.37)$$

Again, the difference of a factor  $2/3$  is probably caused by the different current distribution (as explained above) in the cable compared to that in a conductor with uniformly placed filaments over the cross-section.

Due to the good correlation between the eqs. 4.36 and 4.37 it is possible to estimate the time constant  $\tau_{is,cab,\parallel}$  for a field change  $\dot{B}_\parallel$ . For a solid conductor Campbell gives the relation  $P_{if} = \tau_{if} \dot{B}_\parallel^2 / \mu_0$ , so that (assuming the same difference of a factor of  $2/3$ ):

$$P_{a,\parallel} = \frac{2\tau_{is,cab,\parallel}}{3\mu_0} \dot{B}_\parallel^2 \quad [\text{Wm}^{-3}], \quad (4.38)$$

and thus (using eq. 4.16):

$$\tau_{is,cab,||} = \frac{3\mu_0}{2} 0.125 \frac{L_{p,s} h^2}{R_a w h} \cong 2.4 \cdot 10^{-7} \frac{L_{p,s}}{\alpha_{cab} R_a} \quad [\text{s}]. \quad (4.39)$$

This time constant is negligible compared to  $\tau_{is,cab}$  (for similar  $R_a$  and  $R_c$ ) and will be disregarded in the following.

## 4.5 Strong excitation

It has been shown in section 4.4 that for a transport current larger than the maximum transport current  $I_{tr,str,max}$  the strand currents at one edge of the cable (where the coupling currents  $I_s$  are maximum, see Fig. 4.6), reach their critical value  $I_{C,str}$ . The saturation will influence the 'normal' current distribution of  $I_a$ ,  $I_c$  and  $I_s$ , i.e. the distribution of the coupling currents under weak excitation.

The difference in the steady-state coupling-current distribution is illustrated for a cable with the following parameters:  $N_s=26$ ,  $w=17$  mm,  $h=2.25$  mm,  $L_{p,s}=120$  mm,  $R_c=1 \mu\Omega$ , and  $I_{C,str}=500$  A. A voltage-current relation is used as given in eq. 4.8 with  $n=20$  and an effective resistivity of the strand of  $10^{-14} \Omega\text{m}$  at the critical current  $I_{str}=I_{C,str}$ . The self-field of the cable is disregarded.

Figs. 4.8, 4.9 and 4.10 show the distribution of the currents across the cable width as a function of the transport current for  $\dot{B}_1=0.1 \text{ Ts}^{-1}$ .

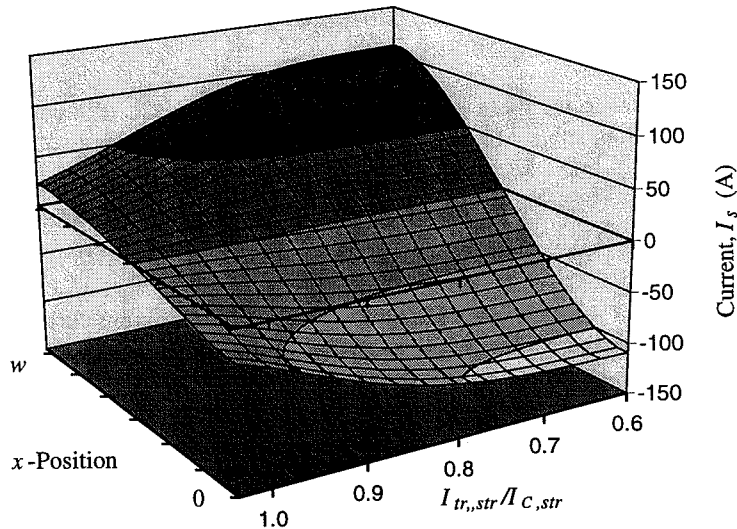


**Figure 4.8.** The distribution of the coupling currents  $I_s$  across the cable width as a function of the transport current (scaled to the critical current of the strand).

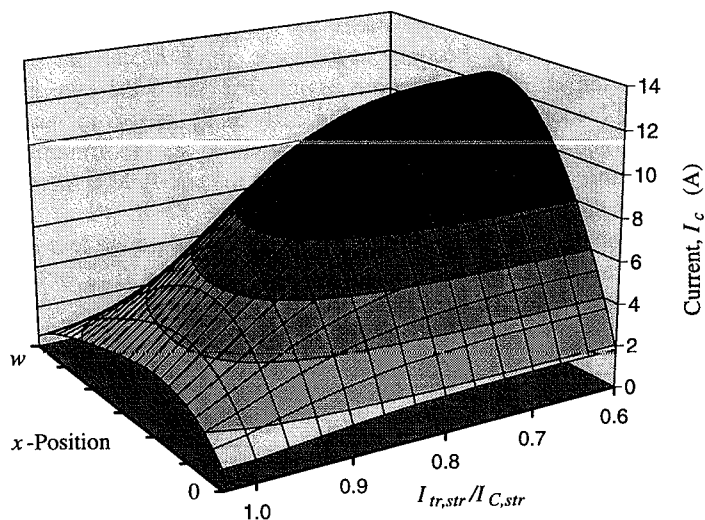


**Figure 4.9.** The distribution of the coupling currents  $I_c$  across the cable width as a function of the transport current (scaled to the critical current of the strand).

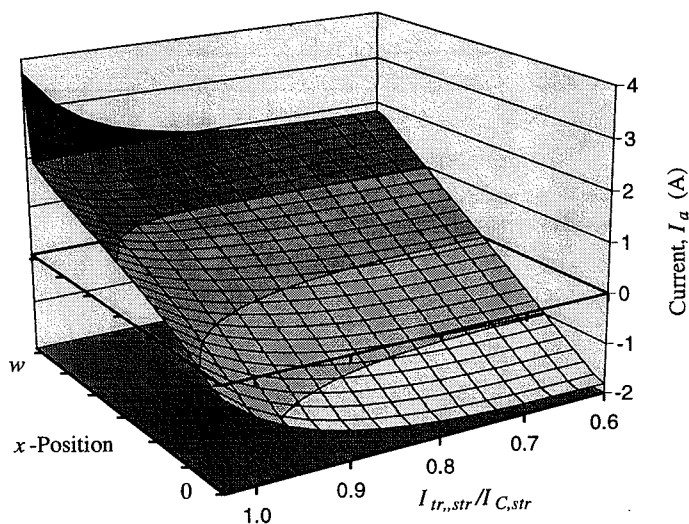


**Figure 4.10.** The distribution of the coupling currents  $I_a$  across the cable width as a function of the transport current (scaled to the critical current of the strand).

The transport current at which the first strand becomes saturated is  $I_{tr,str,max}=280$  A (according to eq. 4.24). Beyond this current level the voltage over the strands increases sharply with increasing current (see eq. 4.8) so that the voltage over the resistances  $R_a$  and  $R_c$  will decrease, since the electromotive force remains the same (see eq. 4.3a). The current distributions across the cable width become slightly asymmetric, i.e. the coupling current  $I_s$

decreases more on that side of the cable where the transport current and  $I_s$  have the same sign. Therefore, the currents  $I_c$  become asymmetric since  $I_c$  can be regarded as the derivative of  $I_s$  and the currents  $I_a$  become asymmetric since the sum of the coupling currents should be 0 (according to eq. 4.4). The currents  $I_a$  start to increase considerably when the effective strand resistance becomes comparable to  $R_a$ . Incorporating the self-field in the simulations further enhances the asymmetry since the self-field is larger at the edge of the cable where  $I_s$  has the same sign as  $I_{tr,str}$ .

Figs. 4.11, 4.12 and 4.13 show the total power loss  $P_{tot}$ , the power loss  $P_s$  in the strands and the relative decrease in the maximum strand current  $I_{s,max}$  as a function of the transport current for several field-sweep rates.

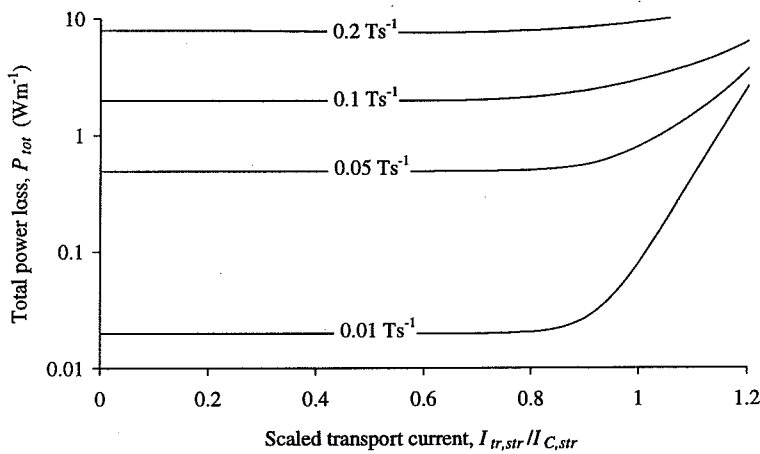


Figure 4.11. The increase in the total power loss  $P_{tot}$  as a function of the transport current (scaled to the critical current of the strand) at four different field-sweep rates.

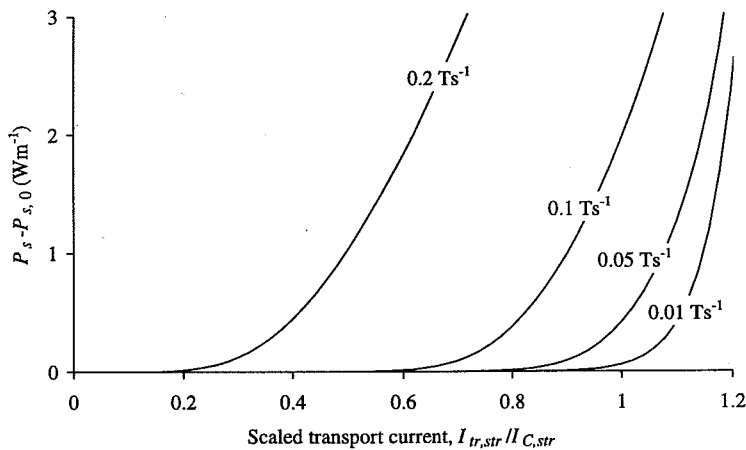
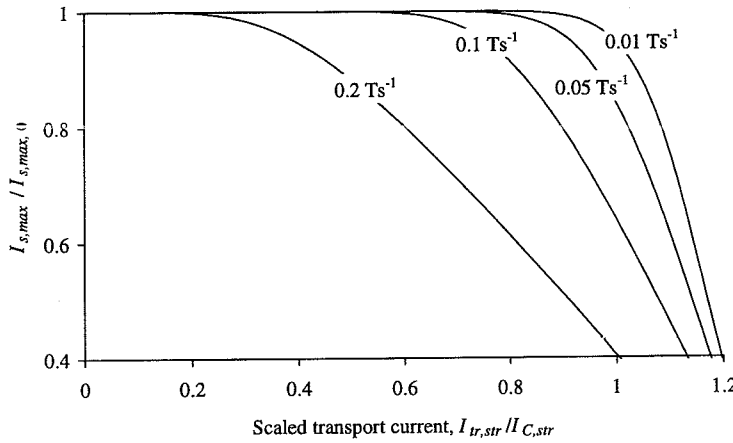


Figure 4.12. The increase in the power loss  $P_s$  in the strands as a function of the transport current (scaled to the critical current of the strand) at four different field-sweep rates.



**Figure 4.13.** The relative decrease in the maximum coupling current  $I_{s,max}$  as a function of the transport current (scaled to the critical current of the strand) at four different field-sweep rates.

The power loss  $P_{s,0}$  denotes the power loss in the strands for  $\dot{B}_\perp = 0$ . The current  $I_{s,max,0}$  denotes the steady-state value of  $I_{s,max}$  if the strands are not saturated (see eq. 4.20 with  $x = w/N_s$ ).

The currents  $I_s$  start to decrease as soon as the transport current  $I_{tr,str}$  approaches  $I_{tr,str,max}$  (see eq. 4.24). At this current the power loss  $P_s$ , generated in the strands (and given by the product of the voltage over the strand and the current through the strand), starts to increase. The total power loss, however, remains more or less constant until the transport current approaches the critical value. This is an important conclusion for the analysis of ramp-rate-induced quenches as discussed in chapter 8.

## 4.6 Cables with $R_c$ varying across the cable width

Cables are likely to have a certain distribution of  $R_c$  across the cable width due to their geometry as well as the pressure to which they are subjected in magnets. The following distributions are considered:

- S1: A constant  $R_c$  of  $1 \mu\Omega$  (as dealt with in section 4.4.1), which corresponds to the smallest  $R_c$  as observed in the LHC model magnets (see Table 6.3).
- R1: A linear increase of  $R_c$  from  $0.3 \mu\Omega$  at one edge to  $1.7 \mu\Omega$  at the other edge. This distribution can be the result of the keystone angle of the cable.
- R2: A linear increase of  $R_c$  from  $0.3 \mu\Omega$  in the centre of the cable to  $1.7 \mu\Omega$  at the edges.
- R3: A linear increase of  $R_c$  from  $0.3 \mu\Omega$  at the edges to  $1.7 \mu\Omega$  in the centre of the cable.
- I1: Simulation of a cable with a resistive barrier (or insulating strip) in-between the two layers of the cable. The  $R_c$ -value equals  $1 \mu\Omega$  on the two contacts close to both edges and equals  $1000 \mu\Omega$  in the centre (over  $5/6$  of the cable width).



Z1: Simulation of a 'zebra cable', i.e. a cable in which the even (or odd) strands have a soft metallic coating. Three different cross-contacts are assumed:

- $R_{c,1} = 1 \mu\Omega$  for the contacts (25%) between two strands with a coating.
- $R_{c,2} \gg 10 \mu\Omega$  for the contacts (25%) between two strands without a coating.
- $R_{c,3} \gg 10 \mu\Omega$  for the contacts (50%) between one strand with a coating and one strand without a coating.

Figs. 4.14 and 4.15 show  $I_s$  and  $P_c$  across the cable width for the distributions S1, R1, R2, R3 and I1 (with  $N_s=26$ ,  $R_d=1 \mu\Omega$ ,  $L_{p,s}=0.1$  m,  $w=17$  mm,  $h_1=h_2=2.6$  mm and  $\dot{B}_\perp=0.01$  Ts<sup>-1</sup>).

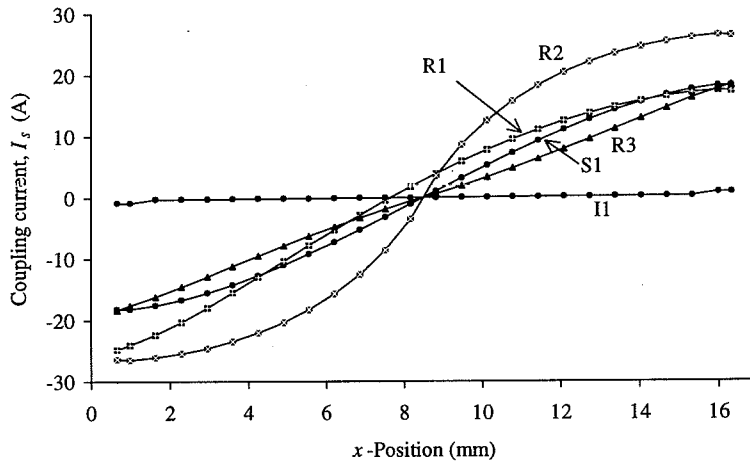


Figure 4.14. The coupling currents  $I_s$  across the cable width for several  $R_c$ -distributions.

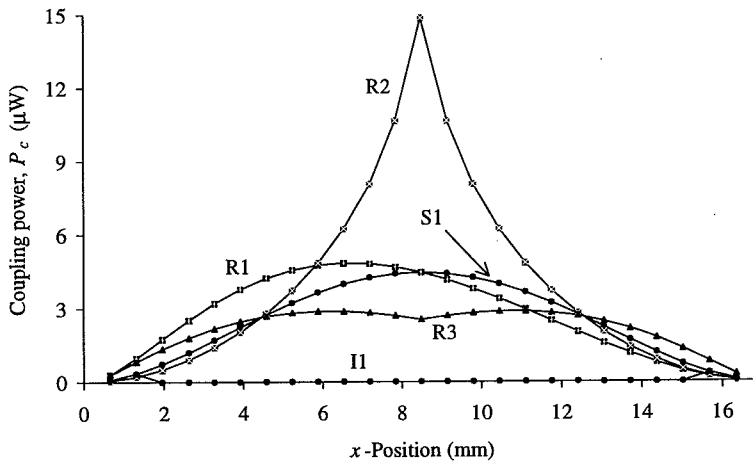


Figure 4.15. The coupling power loss  $P_c$  per contact (expressed in  $\mu$ W) across the cable width for several  $R_c$ -distributions.

The shape of the  $I_s$ -distributions is almost insensitive to the  $R_c$ -distribution for R1, R2 and R3. The coupling power (integrated along the width) is strongly enhanced if  $R_c$  in the centre of the cable is reduced. The ISCL is therefore reduced to almost zero if a resistive barrier is inserted in-between the two layers (distribution I1) even if  $R_c$  at both edges of the cable is small. The 'zebra cable' Z1 exhibits a loss that is a factor 4 smaller than the uniform distribution S1 since only 25% of the contacts have a small  $R_c$ .

In Table 4.2 the power losses  $P_{a,\perp}$  and  $P_c$ , the average time constant  $\tau_{is,cab}$  and the maximum coupling current  $I_{s,max}$  in the cable are surveyed. Note that  $P_{a,\perp}$  does not depend on the  $R_c$ -distribution in agreement with eq. 4.16.

The ratio between  $\tau_{is,cab}$  and  $P_c$  remains more or less constant (for given  $\dot{B}_\perp$ ) for each  $R_c$ -distribution across the cable width. The power loss can therefore be deduced if  $\tau_{is,cab}$  is known and conversely, independent of the  $R_c$ -distribution. The time constant for I1 is not relevant since in this case the power  $P_{a,\perp}$  is larger than  $P_c$ .

Variations in  $R_a$  across the cable width are not discussed since the loss  $P_{a,\perp}$  is much smaller than  $P_c$  (for  $R_a \cong R_c$ ). Variations in  $R_c$  along the length of the cable are extensively dealt with in chapter 5.

**Table 4.2.** Overview of  $P_{a,\perp}$ ,  $P_c$ ,  $I_{s,max}$  and  $\tau_{is,cab}$  for several distributions of  $R_c$  (cases R1-R3,I1,Z1) and of the field-sweep rate (cases B1-B4, see section 4.7) across the cable width.

Distribution	$P_{a,\perp}$ $10^{-3} \text{ Wm}^{-1}$	$P_c$ $10^{-3} \text{ Wm}^{-1}$	$I_{s,max}$ A	$\tau_{is,cab}$ s	$\tau_{is,cab}/P_c$ $\text{smW}^{-1}$
S1	0.47	16.0	18.2	1.17	73
R1	0.47	17.7	24.8	1.28	72
R2	0.47	25.5	26.4	1.92	75
R3	0.47	14.1	18.4	0.98	70
I1	0.47	0.24	0.91		
Z1	0.47	4.0	4.6	0.30	75
B1	0.52	17.1	17.9	1.15	67
B2	0.15	1.21	2.64	0.20	165
B3	0.36	11.6	15.6	1.14	99
B4	0.62	21.3	20.9	1.18	55

## 4.7 Cables with $\dot{B}_\perp$ varying across the cable width

During charging and discharging of magnets the field and hence the field change varies across the cable width. For example, at a central field of 10 T in a PBD magnet the field  $B_\perp$  near the midplane of the straight part changes from 10 T to 4.5 T in the inner coil, and from 4.5 T to -3 T in the outer coil (see Table 2.2). The following  $\dot{B}_\perp$ -distributions are simulated (with  $N_s=26$ ,  $R_a=R_c=1 \mu\Omega$ ,  $L_{p,s}=0.1 \text{ m}$ ,  $w=17 \text{ mm}$ ,  $h_1=h_2=2.6 \text{ mm}$ ):

- S1: A constant value of  $0.01 \text{ Ts}^{-1}$  (as dealt with in section 4.4.1).
- B1: A linear increase across the cable width from 0.003 to  $0.017 \text{ Ts}^{-1}$ .
- B2: A linear increase across the cable width from -0.02 to  $0.02 \text{ Ts}^{-1}$ .

B3: A linear increase from  $0.003 \text{ Ts}^{-1}$  in the centre of the cable to  $0.017 \text{ Ts}^{-1}$  at the edges.

B4: A linear decrease from  $0.017 \text{ Ts}^{-1}$  in the centre of the cable to  $0.003 \text{ Ts}^{-1}$  at the edges.

Note that the total flux through the cable is equal for distributions B1, B3 and B4 while it is 0 for B2. The steady-state distributions of  $I_s$  and  $P_c$  are depicted in Figs. 4.16. and 4.17. The mean time constant  $\tau_{is,cab}$  is almost independent of the  $\dot{B}_L$ -distribution (except in the case of B2) while the power loss varies considerably (see Table 4.2).

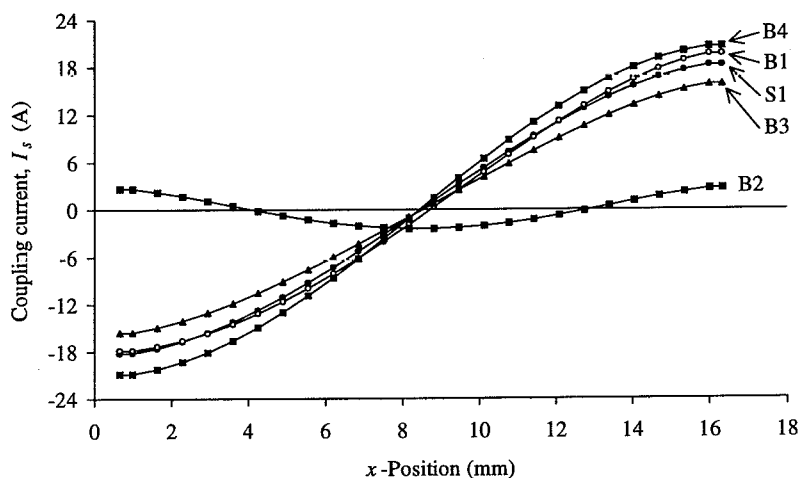


Figure 4.16. The coupling currents  $I_s$  across the cable width for several  $\dot{B}_L$ -distributions.

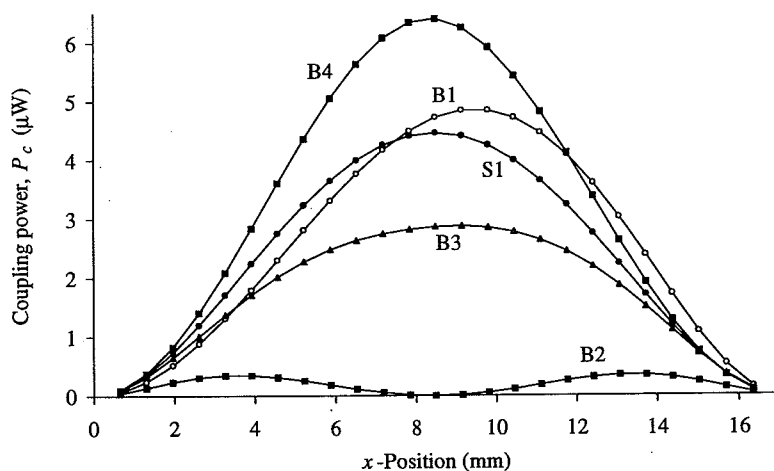


Figure 4.17. The coupling power loss  $P_c$  per contact (expressed in  $\mu\text{W}$ ) across the cable width for several  $\dot{B}_L$ -distributions.

Similar calculations (not included in Table 4.2) for cables for which  $R_c$  as well as  $\dot{B}_\perp$  vary across the cable width, show that the ratio  $\tau_{is,cab}/P_c$  is constant for given  $\dot{B}_\perp$ -distribution, independent of the  $R_c$ -distribution across the width. This implies that the exact  $\dot{B}_\perp$ -distribution has to be known in order to deduce the power loss from the time constant and conversely.

Variations in  $\dot{B}_\parallel$  are not discussed here since the power loss  $P_{a,\parallel}$  in a coil is negligible compared to  $P_{a,\perp}$  and  $P_c$ . The effect of longitudinal variations in  $\dot{B}_\perp$  on the current distribution and generated power is dealt with in detail in chapter 5.

## 4.8 Cables of finite length with constant $\dot{B}$

In section 4.4.1 the formulas for the steady-state power loss are given for a cable in which the coupling-current distribution is constant in the longitudinal ( $z$ -) direction. However, in a cable of finite length the coupling currents vary along the cable length. The effect of the length on the steady-state power losses  $P_a$  and  $P_c$  is investigated for a cable piece of length  $l_{cab}$  subject to a constant  $\dot{B}$ . The case of a finite cable with spatially non-uniform  $\dot{B}$  is evaluated in section 5.5.

Figs. 4.18 and 4.19 show  $P_a$  and  $P_c$  (expressed as the average loss for one metre of cable) as a function of the length  $l_{cab}$  (with  $R_a=R_c=1\ \mu\Omega$ ,  $N_s=26$ ,  $w=17\text{ mm}$ ,  $h=2.6\text{ mm}$ ,  $L_{p,s}=0.1\text{ m}$ ,  $\dot{B}=0.01\text{ Ts}^{-1}$ ). The shape of the curves is not influenced by the values of  $N_s$ ,  $w$ ,  $h$ ,  $L_{p,s}$  and  $\dot{B}$ , but is slightly affected by the ratio between  $R_a$  and  $R_c$ .

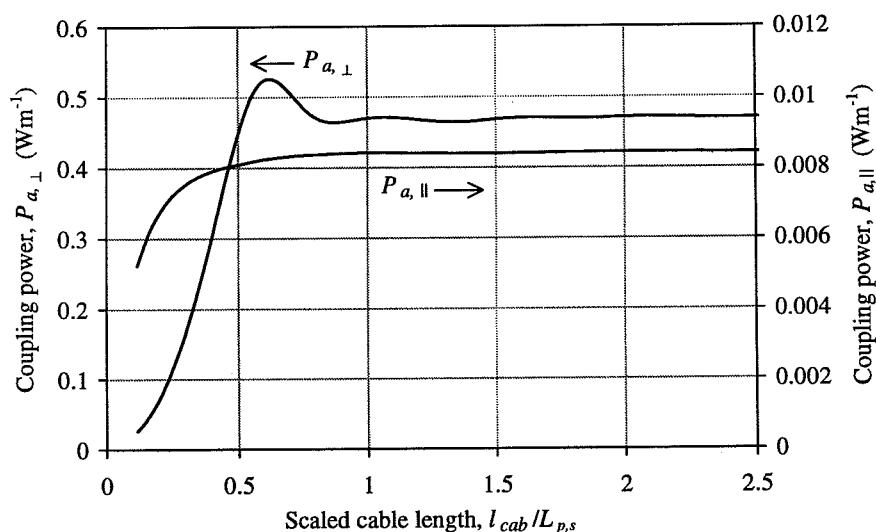


**Figure 4.18.** The coupling power losses  $P_{a,\perp}$  and  $P_{a,\parallel}$  (for the field changes  $\dot{B}_\perp$  and  $\dot{B}_\parallel$ ) of a cable of finite length as functions of the cable length expressed in units of the cable pitch.

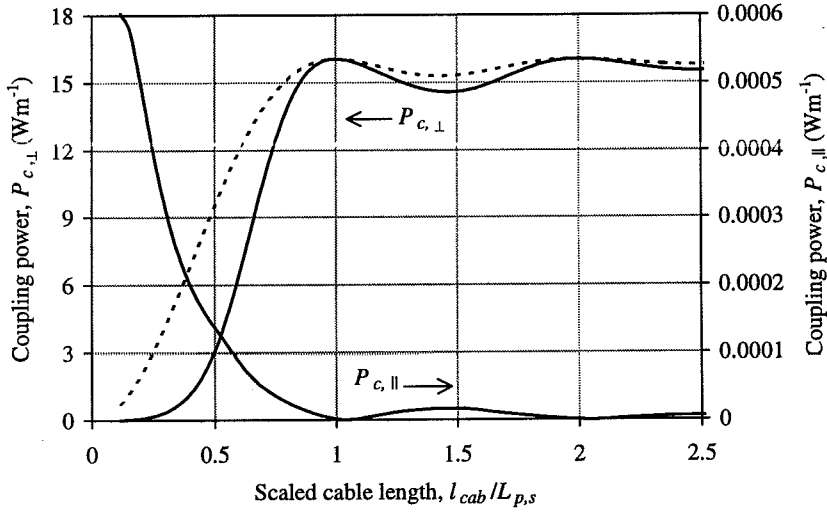


**Figure 4.19.** The coupling power losses  $P_{c,\perp}$  and  $P_{c,\parallel}$  (for the field changes  $\dot{B}_\perp$  and  $\dot{B}_\parallel$ ) of a cable of finite length as functions of the scaled cable length. The dotted curve shows the expression for  $P_{c,\perp}$  as obtained by Ries scaled to a power of  $16.4 \text{ Wm}^{-1}$  (see eq. 4.40).

The power loss is mainly generated in  $R_c$  for a field change  $\dot{B}_\perp$  (in agreement with eqs. 4.16 and 4.17) while it is generated in  $R_a$  for a field change  $\dot{B}_\parallel$ . Note the very small power loss  $P_{c,\parallel}$  which is not present for infinitely long cables (see eq. 4.17). The power loss in a cable piece with a length equal to an integer times the cable pitch corresponds to the power loss in a long cable (see eqs. 4.16 and 4.17), both for  $\dot{B}_\perp$  and  $\dot{B}_\parallel$ . The power losses decrease strongly for cable pieces shorter than the cable pitch. Hence, experimental results of the loss on a small cable piece have to be extrapolated (using the figures) to estimate the loss in a long cable.

Ries has presented the result of an analytical calculation of  $P_c$  of a hollow-twisted round cable [Ries, '81], showing that the power loss of a short section is related to the power loss for infinite length  $P_{c,inf}$  as:

$$\frac{P_c}{P_{c,inf}} = (1 - \sin(k\pi) / k\pi)^2, \quad (4.40)$$

with  $k = l_{cab}/L_{p,s}$ . This relation is depicted in Fig. 4.19 and shows clearly the same periodicity in the power loss with period  $L_{p,s}$  although the exact shape is different because the calculation is made for a hollow-twisted round cable. Numerical simulations are also performed on a 29-strand NET braided cable for  $\dot{B}_\perp$  and  $\dot{B}_\parallel$  [Niessen, '90b]. The power loss  $P_{c,\perp}$  of the round cable as well as the braided cable is periodic with period  $L_{p,s}$  and decreases strongly for  $l_{cab} < L_{p,s}$ . However, due to the cable geometry the shape of the  $P_c$ - $l_{cab}$  relations differ slightly.

## 4.9 Stacked cables

The steady-state power loss (per metre of cable) and coupling-current distribution for weak excitation is exactly the same for a stack of cables as for a single cable. Since the self-field of a stack differs from the self-field of a single cable, the steady-state power loss will only change if  $R_c$  is field-dependent or if strands become saturated. In coils the change in the steady-state power loss is negligible since the field produced by the transport current is much larger than the field caused by the ISCCs.

In section 4.4.2 it has been shown that the current in each strand section of a cable has its own time constant  $\tau_{is,i}$  while  $\tau_{is,cab}$  denotes the average time constant of a single straight cable. In a similar way the ISCCs in each cable of a stack of  $N_c$  cables have their own average time constants  $\tau_{is,st,i}$  (with  $1 \leq i \leq N_c$ ), which depend strongly on the configuration of the stack. The average time constant  $\tau_{is,st}$  of the ISCCs in a stack is determined from the step response of the average of all the ISCCs in the stack. As an example, both  $\tau_{is,st,i}$  and  $\tau_{is,st}$  are shown in Fig. 4.20 as a function of the number of cables  $N_c$  in the stack ( $\dot{B} = \dot{B}_L$ ,  $N_s = 26$ ,  $L_{p,s} = 0.1$  m,  $w = 0.017$  m,  $h = 2.6$  mm,  $R_c = 1 \mu\Omega$ ,  $R_a \gg R_c$ ).

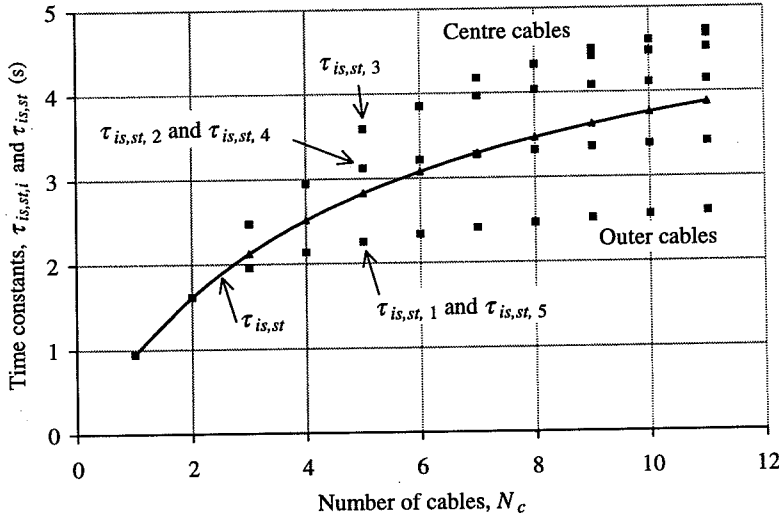


**Figure 4.20.** The average time constant  $\tau_{is,st,i}$  of the ISCCs in each cable of a stack of cables and the average time constant  $\tau_{is,st}$  of the ISCCs in the whole stack as a function of the number of cables  $N_c$  in the stack. As an example, the time constants of a stack of five cables are indicated where the numbers 1-5 refer to the location of the cable in the stack.

The time constant is minimum in the outer cables and increases towards the centre of the stack. The ratio  $\tau_{is,st}/\tau_{is,cab}$  is calculated using the network model, taking into account the mutual inductances between the strand elements of the  $N_c$  cable pieces, and satisfies:

$$\frac{\tau_{is,st}}{\tau_{is,cab}} = \frac{\alpha_{cab} N_c}{\alpha_{cab} + C(N_c - 1)}, \quad (4.41)$$

for  $8 \leq N_s \leq 40$ , with  $\alpha_{cab}$  the aspect ratio of the cable and  $C$  a constant which depends slightly on the number of strands in the cable, increasing from about 1.0 for  $N_s=8$  to 1.15 for  $N_s=40$ . The relation shows that the time constant of a stack increases with the number of cables and is limited to about  $\alpha_{cab}\tau_{is,cab}$ . The time constant of the ISCCs in LHC dipole magnets is dealt with in section 6.1. It was mentioned in section 4.4.2 that the time constants given by Krempasky and Sytnikov are about a factor  $1.2\alpha_{cab}$  larger than  $\tau_{is,cab}$ . In fact, they assumed that  $\tau_{is}$  is independent of the exact arrangement of the cables and their values should therefore correspond to  $\tau_{is,st}$  with  $N_c \rightarrow \infty$ . Hence, the analytically derived expressions of Krempasky and Sytnikov can be used as a rough estimate whereas eqs. 4.31 and 4.41 result in a precise value of the time constant (within 10-20%). Furthermore, eq. 4.41 should be applied when the time constants of single cables and stacked cables or coils are compared.

In section 4.6 it is shown that (for given  $\dot{B}$ ) the ratio  $\tau_{is,cab}/P_c$  is constant for arbitrary  $R_c$ -distributions. In the case of a given  $\dot{B}$ , the  $\tau_{is,st}$  and  $P_c$ -values for a stack of five cables are surveyed in Table 4.3 for several  $R_c$ -distributions, varying among the different cables as well as across the cable width. The ratio between  $\tau_{is,st}$  and the steady-state power loss  $P_c$  is more or less constant (just like the ratio  $\tau_{is,cab}/P_c$ ). The ISCL can therefore be deduced from the time constant of a stack of cables and conversely, even for a non-uniform  $R_c$ -distribution over the individual cables.

**Table 4.3.** The average time constant and the steady-state coupling power  $P_c$  (per metre of cable) of a stack of five cables with different  $R_c$  for each cable ( $L_{p,s}=0.1$  m,  $N_s=26$ ,  $w=17$  mm and  $h=2.6$  mm,  $\dot{B}_1=0.01$  T s<sup>-1</sup>).

$R_c$ ( $\mu\Omega$ ) for each cable					$\tau_{is,st}$	$\tau_{is,st}/P_c$	Relative
1	2	3	4	5	(s)	(sW <sup>-1</sup> m)	change
1	1	1	1	1	2.70	166	1.00
1	3	5	3	1	1.47	158	0.95
5	3	1	3	5	1.31	194	1.17
1	2	3	4	5	1.32	178	1.07
1 to 5 <sup>a</sup>	5 to 1 <sup>a</sup>	1 to 5 <sup>a</sup>	5 to 1 <sup>a</sup>	1 to 5 <sup>a</sup>	0.97	164	0.99

<sup>a</sup> A linear increase (or decrease) from 1 to 5 (or from 5 to 1)  $\mu\Omega$  across the cable width.

## 4.10 Influence of transverse pressure on $R_c$

### 4.10.1 Introduction

In section 4.3 the transverse pressure is shown to be one of the parameters by which  $R_c$  is affected. In high-field accelerator magnets the stress level varies significantly over the cross-section of the coils and can locally attain very large values of more than 100 MPa. It is therefore important to investigate to what extent  $R_c$  is affected by the transverse pressure  $P_\perp$  on the cable. Variations of  $R_c$  influence the field homogeneity of the magnet during field sweeps. Furthermore, a local decrease of  $R_c$  causes a local increase in the power loss and

can therefore strongly decrease the electromagnetic stability of the coil during a field sweep. Additionally, a non-uniform  $R_c$ -distribution generates boundary-induced coupling currents which further enhance the field distortions and reduce the stability (see chapters 5, 7 and 8). A new set-up is designed to determine  $R_c$  of Rutherford-type cables by means of calorimetric and electrical measurements on a stack of keystone cable pieces for an applied transverse pressure of up to 130 MPa.

The theoretical model for both methods is presented in the following two sections. The experimental set-up is discussed in section 4.10.4 and the evaluation of the results is given in section 4.10.5.

#### 4.10.2 Theoretical model for the calorimetric method

The total loss  $Q_{tot}$  in a cable (without transport current) exposed to a sinusoidally varying field:

$$B = B^m \sin(2\pi f t) \quad [T], \quad (4.42)$$

with amplitude  $B^m$  and frequency  $f$ , has three main contributions, i.e.:

- the filament hysteresis  $Q_{hys}$  (see section 3.2),
- the interfilament coupling loss  $Q_{if}$  (see section 3.4),
- the interstrand coupling loss  $Q_{is}$ , given by:

$$Q_{is} = Q_{is,\parallel} + Q_{is,\perp} = \oint P_{a,\parallel} dt + \left( \oint P_{a,\perp} dt + \oint P_c dt \right) \quad [J/cycle], \quad (4.43)$$

with  $P_{a,\parallel}$ ,  $P_{a,\perp}$  and  $P_c$  given by eqs. 4.16 and 4.17.

It can be calculated that in a ramped field  $P_{if} \gg P_{a,\parallel}$  by comparing eqs. 4.16 (with  $R_a > 1 \mu\Omega$ ) and 3.15 (with  $\dot{B}_s = \dot{B}_\parallel$  and using eq. 3.20 with  $\tau_{if} = 25$  ms). The total loss  $Q_{tot}$  is therefore equal to:

$$Q_{tot,\parallel} = Q_{hys} + Q_{if} \quad [J/cycle] \quad \text{for } \dot{B} = \dot{B}_\parallel \quad (\theta = 90^\circ, \text{ see Fig. 4.1}), \quad (4.44a)$$

$$Q_{tot,\perp} = Q_{hys} + Q_{if} + Q_{is,\perp} = Q_{tot,\parallel} + Q_{is,\perp} \quad [J/cycle] \quad \text{for } \dot{B} = \dot{B}_\perp \quad (\theta = 0^\circ). \quad (4.44b)$$

For  $0^\circ < \theta < 90^\circ$  the loss  $Q_{is,\perp}$  is proportional to  $\cos^2(\theta)$  (see eqs. 4.1b and 4.17). If  $P_{if}$  is of the same order or smaller than  $P_{a,\parallel}$ , the IFCL has to be determined from loss measurements on single strands.

The hysteresis loss and the IFCL can therefore be determined by measuring the total loss as a function of the frequency for an applied field change  $\dot{B}_\parallel$  as shown in Figs. 3.8 and 4.21. The hysteresis loss, which is independent of the frequency (for low frequencies), is given by the intercept of the  $Q_{tot,\parallel}$ - $f$  relation, whereas the slope of the  $Q_{tot,\parallel}$ - $f$  curve at  $f \rightarrow 0$  is related to the loss component  $Q_{if}$ . The loss  $Q_{is,\perp}$  can be determined from the slope of the  $Q_{tot,\perp}$ - $f$  curve once  $Q_{if}$  is known. In this analysis the assumptions are made that the IFCCs are not significantly affected by the screening of the ISCCs and do not depend on the angle between the applied field and the cable. The  $R_c$ -value is calculated from the ISCL using eq. 4.17.



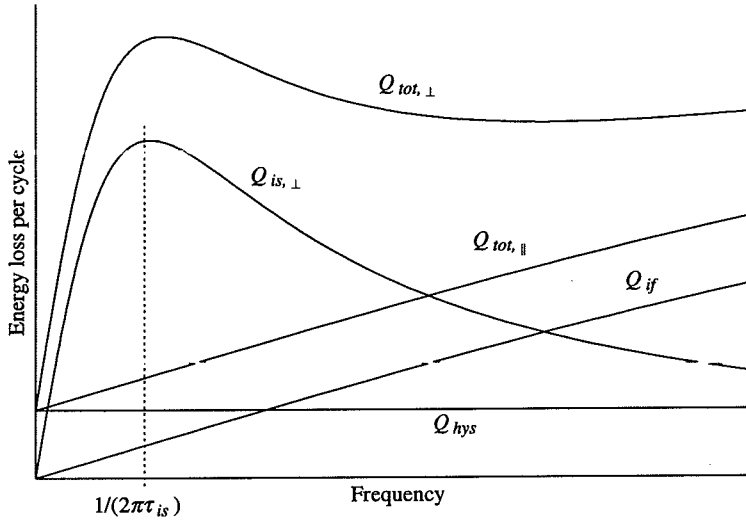


**Figure 4.21.** Characteristic frequency dependence of the loss components  $Q_{hys}$ ,  $Q_{if}$  and  $Q_{is,\perp}$  in a cable exposed to a sinusoidally varying magnetic field with frequency  $f$ . The loss component  $Q_{is,\parallel}$  is disregarded. The time constant  $\tau_{is}$  is assumed to be much larger than  $\tau_{if}$ .

The average time constant of the ISCCs in the stack is deduced from:

- the frequency  $f_m$  at which  $Q_{is,\perp}$  is maximum:  $\tau_{is,st,m} = 1/(2\pi f_m)$ , with the assumptions that the hysteresis loss is not influenced by the IFCCs and the ISCCs and that the IFCL is not influenced by the ISCCs,
- a combination of eqs. 4.31 and 4.41 or preferably, a direct calculation using the network model applied to the particular cable and stack. The calculated time constant  $\tau_{is,st,c}$  for the sample as described in section 4.10.5 is equal to:

$$\tau_{is,st,c} = 2.8 \cdot 10^{-5} \frac{L_{p,s}}{R_c} \quad [\text{s}]. \quad (4.45)$$

#### 4.10.3 Theoretical model for the electrical method

The  $R_c$ -value can also be determined by means of an electrical (or  $UI$ ) method. Two strands of a cable piece are connected to a current supply, while the voltage is measured over any combination of strands (see Fig. 4.22).

The current distribution is calculated using the network model as described in section 4.2 applied to a cable of finite length. The field change is taken as zero and the boundary conditions are formulated so that for the first band:  $I_{tr,p} = -I_{tr,q} = I$  where  $I$  is the current through the cable and  $p$  and  $q$  denote the strands that are connected to the current supply. In this section the current supply is connected to the opposite edges of the cable (strand positions  $p=1$  and  $q=N_s/2+1$ ), which leads to a more global  $R_c$ . In the case of a 26-strand cable, the voltages  $U_{1,j}$  between the strand at position 1 and the strands at positions  $j=2-26$  are depicted in Fig. 4.23 for a current of 1 A connected to strand positions 1 and 14.

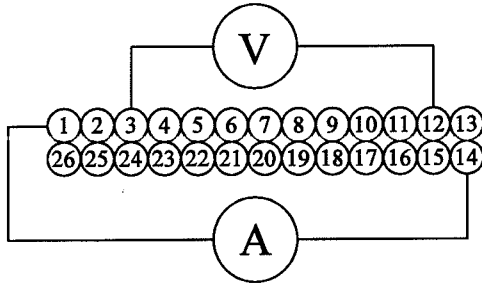


**Figure 4.22.** Illustration of the  $UI$  method. The strands at positions 1 and 14 (at one end of the cable piece) are connected to a current supply and the strands at positions 3 and 12 to a voltmeter.

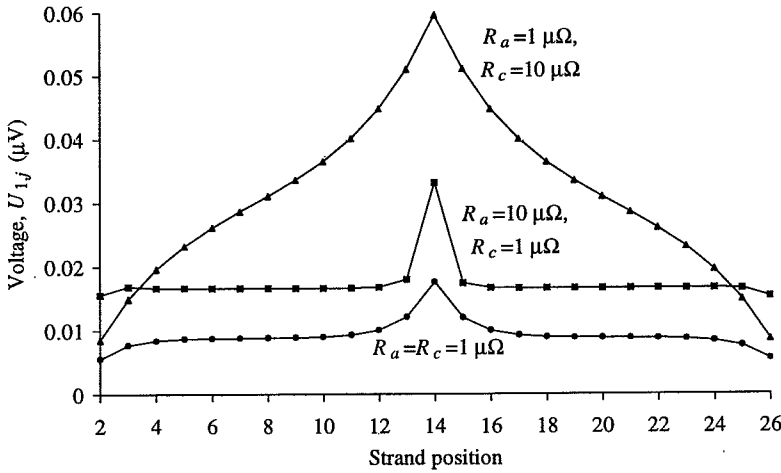


**Figure 4.23.** The voltage between strand 1 and the other strands ( $j=2-26$ ) of a 26-strand cable of length  $L_{p,s}$  for three combinations of  $R_a$  and  $R_c$  and a current of 1 A. The current supply is connected to the strands at positions 1 and 14.

The voltage is symmetric around  $j=N_s/2+1$  (i.e. 14 for  $N_s=26$ ) and depends strongly on the ratio between  $R_a$  and  $R_c$ . While  $U_{1,j}$  increases linearly (between  $j=2$  and  $j=N_s/2+1$ ) for  $R_a \ll R_c$ , only three voltage levels are present for  $R_a \gg R_c$ . The shape of the  $U_{1,j}$  curve is therefore a good indication of the ratio between  $R_a$  and  $R_c$ . Recent results of measurements on LHC-type cables agree very well with these calculations both for  $R_a \gg R_c$  and  $R_a \ll R_c$  (obtained by placing a resistive barrier between the two layers of the cable) [Richter, '95].

Fig. 4.24 shows the voltage  $U_{1,14} (=U_{ee})$  as a function of the cable length for three combinations of  $R_a$  and  $R_c$ . Numerical calculations of the voltage  $U_{ee}$  over the two edges of the cable as a function of  $R_a$ ,  $R_c$ ,  $(L_{p,s}/l_{cab})$  and  $N_s$  result in the analytical expressions:

$$U_{ee} = \left( \frac{R_a R_c}{R_a + R_c} \right) \frac{L_{p,s}}{l_{cab} N_s} I \quad [\text{V}] \quad \text{for } R_c \leq R_a \text{ and } \rho_s \rightarrow 0, \quad (4.46a)$$

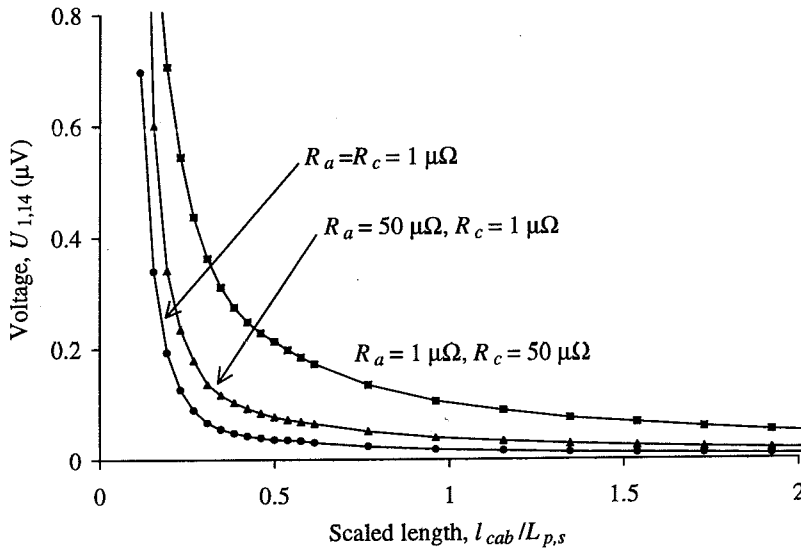


**Figure 4.24.** The voltage  $U_{1,14}$  as a function of the cable length for three combinations of  $R_a$  and  $R_c$  and a current of 1 A ( $N_s=26$ ). The current supply is connected to the strands at positions 1 and 14.

$$U_{ee} = \frac{L_{p,s}}{2R_a l_{cab} \sqrt{N_s}} I \quad [\text{V}] \quad \text{for } R_a \ll R_c \text{ and } \rho_s \rightarrow 0, \quad (4.46b)$$

where the current  $I$  is connected to the strand positions 1 and  $(N_s/2+1)$  at one end of the cable piece.

The  $UI$  method is very sensitive to local variations in  $R_a$  and  $R_c$ . The  $R_c$ -value can be accurately estimated if  $R_a \gg R_c$  and if the cable length is smaller than  $0.5L_{p,s}$ . For longer cable pieces the current distributes through many resistances. This implies that the voltage can decrease significantly (compared to eq. 4.46a) if only one resistance has a small value which would consequently lead to an apparently smaller  $R_c$ .

The  $UI$  method is therefore useful for *estimating*  $R_c$  of a cable since it is a fast and cheap method. Calorimetric loss measurements, however, are required to determine an accurate global  $R_c$  of the cable since the method is less sensitive to local variations in  $R_a$  and  $R_c$ . However, the  $UI$  method is the most accurate method for estimating  $R_c$  of a cable in which the ISCL is small compared to the IFCL. Calorimetric or magnetisation measurements do not give a precise  $R_c$  because the IFCL can depend slightly on the angle  $\theta$  due to the deformation of the strands.

#### 4.10.4 Experimental set-up

A new experimental set-up has been designed to investigate the relation between  $R_c$  of a Rutherford-type cable and the pressure  $P_\perp$  applied transversely on the cable. The sample is placed in-between two stainless steel bars (see Fig. 4.25) and pressure is applied by means of a series of bolts and can be increased up to 130 MPa.

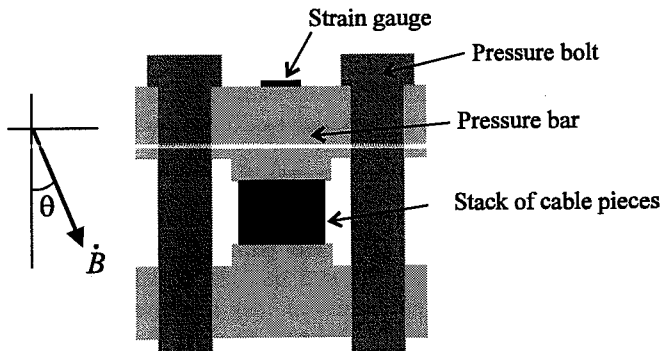


Figure 4.25. Schematic view of the cross-section of the stack of four cable pieces placed between two stainless steel pressure bars.

The sample consists of a stack of four cable pieces each with a length of three times the cable pitch (i.e. about 350-400 mm). The power loss of the sample (per metre of cable) is then equal to the power loss for an infinitely long cable (following section 4.8). The cable pieces are separated by electrically insulating foils to avoid coupling currents flowing between the different cable pieces.

Several strain gauges are glued onto the stainless steel bars to verify the change in pressure during cool-down from 300 K to 4.2 K. The accuracy of the pressure is within 10%. A superconducting dipole magnet provides an AC field with a maximum amplitude of 1 T, homogeneous over the whole sample volume. The stack can be rotated with respect to the AC dipole so that the loss can be measured as a function of the angle  $\theta$  between the applied field and the y-axis (with  $\varphi=90^\circ$ , see Fig. 4.1). The accuracy in the angle  $\theta$  is within a few degrees.

A bell jar, placed around the sample, collects the helium gas which boils off at the surface of the sample. The gas is directed through a tube and measured with a mass flowmeter at 300 K. The mass flowmeter is calibrated by means of an ohmic heater placed in the bell jar knowing that 1 W at 4.2 K will produce 17.4 liter of helium gas per minute at 300 K.

Additionally, voltage taps and current leads are connected to positions 1 and  $(N_s/2+1)$  (see Fig. 4.22) of one or more cable pieces in order to estimate  $R_c$  by means of the  $UI$  method.

#### 4.10.5 Results and discussion

The  $R_c$ -values of the following three cables, with SnAg-coated strands, are determined (see Table 2.4):

- Cable I-2. The stack of cable pieces is heat-treated for about 2 hours at a temperature of  $160^\circ\text{C}$  at 30 MPa. The  $R_c$ -value is deduced by means of the electrical and calorimetric methods at subsequently 30, 10, 30 and 80 MPa. The pressure is not released in-between the heat-treatment and the first measurement at 30 MPa, but is released for about 15 minutes in-between the first and second measurement (before applying 10 MPa).

- Cable I-4. The stack is not heat-treated. The  $R_c$ -value is deduced by means of the electrical and calorimetric methods at subsequently 10, 60, 100 and 30 MPa.
- Cable I-4 soldered with PbSn and denoted by cable I-4s. The stack is not heat-treated. The  $R_c$ -value is deduced by means of the calorimetric method at subsequently 10, 45 and 90 MPa.

All calorimetric measurements are performed using a triangular (samples I-4 and I-4s) or sinusoidal (sample I-2) applied field with an amplitude  $B^m$  between 25 and 400 mT. The measurements are corrected for the background boil-off and the very small eddy-current loss generated in the press itself. The results of loss measurements on sample I-4 as a function of the angle  $\theta$  are presented in Fig. 4.26 and show that  $Q_{is,\perp}$  scales with  $\cos^2(\theta)$ , which is in agreement with eqs. 4.1b and 4.17.

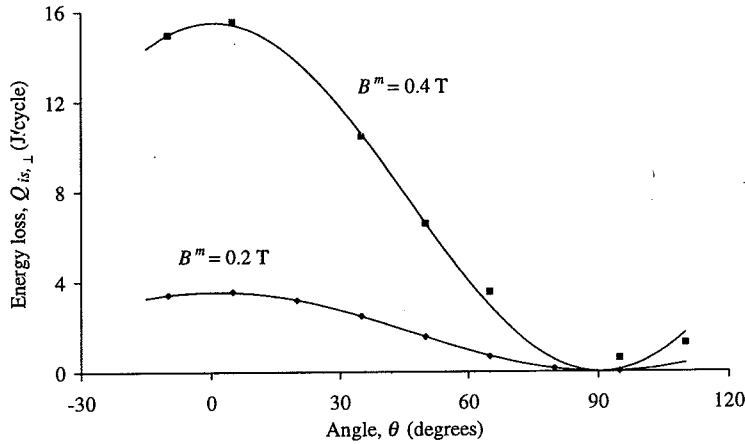


**Figure 4.26.** The ISCL per cycle of cable I-4 as a function of the angle  $\theta$  for  $B^m=0.2$  and  $0.4$  T,  $f=0.12$  Hz and  $P_{\perp}=30$  MPa. The solid curves are best fits assuming that  $Q_{is,\perp}$  is proportional to  $\cos^2(\theta)$ .

The losses of sample I-4 as a function of the frequency, for fields  $B_{\perp}$  and  $B_{\parallel}$  with an amplitude  $B^m$  equal to 400 mT and for pressures  $P_{\perp}$  of 10, 30, 60 and 100 MPa, are given in Figs. 4.27 and 4.28. These figures can now be compared with Fig. 4.21 and the different loss components can be determined according to the discussion in section 4.10.2. The hysteresis loss and IFCL are in good agreement with the AC magnetisation measurements. The variation in the IFCL for different pressures is probably caused by the error in the calorimetric measurements but does not significantly affect the deduction of  $R_c$ .

The  $Q_{is,\perp}$ - $f$  curve is obtained by subtracting the hysteresis loss and the IFCL (i.e.  $Q_{tot,\parallel}$ ) from the  $Q_{tot,\perp}$ - $f$  curve (see eq. 4.44b). The  $R_c$ -value is determined from the slope of the  $Q_{is,\perp}$ - $f$  curve for  $f \rightarrow 0$ . The time constant is then calculated using eq. 4.45 and denoted by  $\tau_{is,st,c}$ . The time constant is also deduced from the frequency  $f_m$  where  $Q_{is,\perp}$  is maximum, as described above, and referred to as  $\tau_{is,st,m}$ . The values of the contact resistances and time constants are given in Table 4.4.

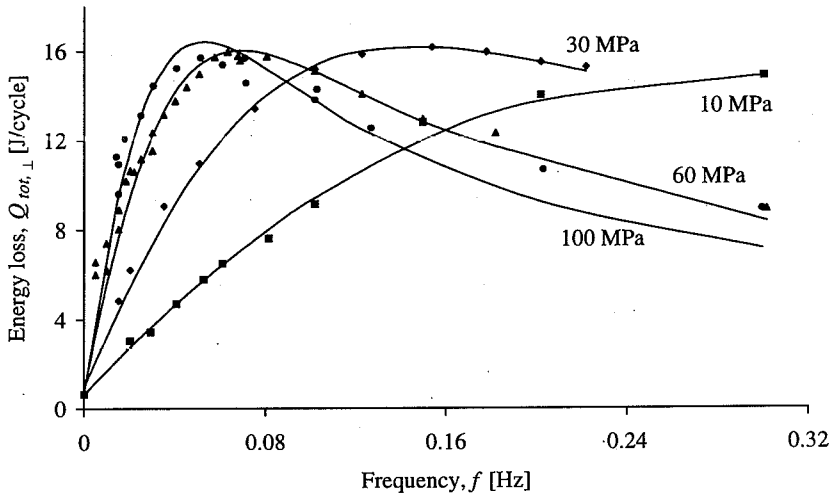


Figure 4.27. The energy loss per cycle  $Q_{tot,\perp}$  of sample I-4 as a function of the frequency for a field change  $\dot{B}_\perp$  with  $B^m=400$  mT and  $P_\perp=10, 30, 60$ , and 100 MPa.

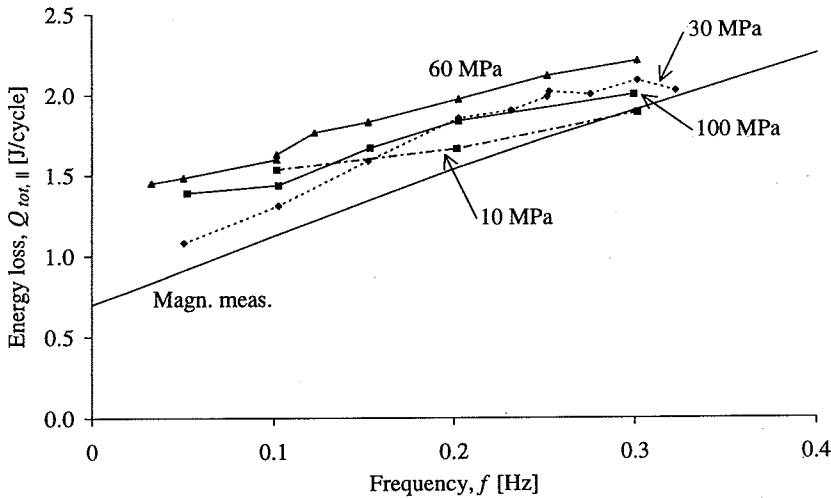


Figure 4.28. The energy loss per cycle  $Q_{tot,\parallel}$  of sample I-4 as a function of the frequency for a field change  $\dot{B}_\parallel$  with  $B^m=400$  mT for  $P_\perp=10, 30, 60$ , and 100 MPa. As a comparison, the loss deduced from the AC magnetisation on the same cable is included (see section 3.5)

The  $Q_{tot}$ - $f$  curves of samples I-2 and I-4s are determined in a similar way for a field change  $\dot{B}_\perp$  as well as  $\dot{B}_\parallel$ . Determination of the slope of the  $Q_{is,\perp}$ - $f$  curve at  $f=0$  in the case of sample I-4s is too inaccurate, due to its very small  $R_c$ . Therefore, only the time constants  $\tau_{is,st,m}$  are determined (see Table 4.4) and the  $R_c$ -values are deduced using eq. 4.45. The  $R_c$ -values of the three cables as a function of the transverse pressure are depicted in Fig. 4.29.

**Table 4.4.** Results of the calorimetric and electrical loss measurements on a stack of Rutherford-type cable pieces in terms of  $R_{c,UI}$ ,  $R_c$ ,  $\tau_{is,st,m}$  and  $\tau_{is,st,c}$  for several pressures.  $R_{c,UI}$  denotes the  $R_c$  as deduced by means of the *UI* method. The accuracy in the resistances and time constants is about 10-20%.

	$P_{\perp}$ (MPa)	$R_{c,UI}$ ( $\mu\Omega$ )	$R_c$ ( $\mu\Omega$ )	$\tau_{is,st,m}$ (s)	$\tau_{is,st,c}$ (s)
Cable I-2	30 $\pm$ 5	2.2	1.8	2.0	2.0
	10 $\pm$ 5	28	13	0.35	0.28
	30 $\pm$ 5	12	7.0	0.52	0.52
	80 $\pm$ 10	3.6	2.7	1.3	1.3
Cable I-4: Unsoldered	10 $\pm$ 5	11	7.3	0.49	0.45
	30 $\pm$ 5	5.0	3.2	1.1	1.0
	60 $\pm$ 10	2.9	1.6	2.3	2.1
	100 $\pm$ 10	-	1.3	2.7	2.5
Cable I-4: Soldered	10 $\pm$ 5		0.27 <sup>a</sup>	12	
	45 $\pm$ 10		0.30 <sup>a</sup>	11	
	90 $\pm$ 10		0.27 <sup>a</sup>	12	

<sup>a</sup> Estimated according to eq. 4.45 with the time constants  $\tau_{is,st,m}$

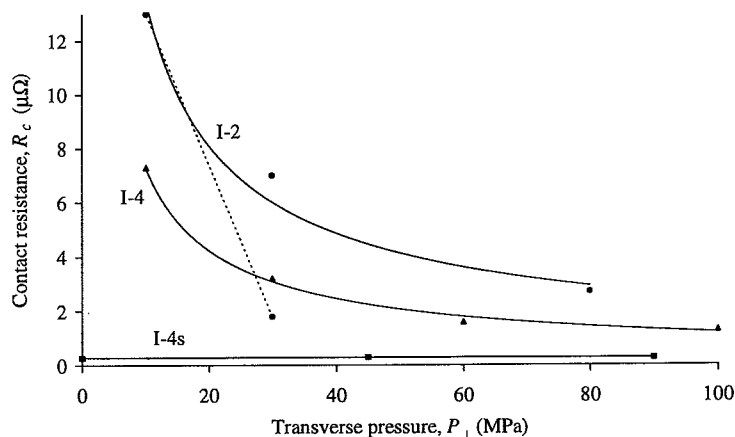


**Figure 4.29.** The average  $R_c$  as a function of the applied pressure  $P_{\perp}$  determined using the calorimetric method. The labels indicate the sample. The dotted line shows  $R_c$  of sample I-2 directly after the heat-treatment and before the pressure has been released to 0. The lines are fitted curves which are proportional to  $P_{\perp}^{-3/4}$ .

The  $R_c$ -value of cable I-4 decreases strongly for increasing transverse pressure and is proportional to  $P_{\perp}^{-3/4}$ . This implies that a representative  $R_c$  of a coil can only be obtained if  $R_c$  is determined at a pressure level that corresponds more or less to the average pressure level in the coil.

The  $R_c$ -value of cable I-2 has a similar pressure-dependence as cable I-4 once the pressure has been released completely (after the heat-treatment). Fig. 4.29 shows clearly

that  $R_c$  is reduced significantly due to the heat-treatment. The difference in  $R_c$  at 30 MPa (before and after the pressure has been released to 0), corresponds well to similar measurements (by means of the *UI* method) on cables with SnAg coated strands [Oberli, '95]. This implies that a representative  $R_c$  of a coil can only be obtained if the stack is exposed to exactly the same sequence of pressure and temperature as the coil.

The  $R_c$ -value of the soldered cable I-4s is about  $0.3 \mu\Omega$  (as deduced from the time constant of about 12 s) and almost pressure-independent. At large pressures of about 50-100 MPa,  $R_c$  is about 5 times smaller than those of the cables with SnAg coated strands. Note that an  $R_c$  of  $0.3 \mu\Omega$  corresponds well with the contact resistance within the splice (i.e. about  $N_s^2 \cdot 0.4 \text{ n}\Omega = 0.3 \mu\Omega$  for a splice of length  $L_{p,s}$ ).

The  $R_c$ -values of samples I-2 and I-4 are also determined by means of the *UI* method, using eq. 4.46a with the assumption  $R_a = 10R_c$ , and presented in Table 4.4. The  $R_c$ -values determined by means of the *UI* method are about a factor 1.5 to 2 larger than those deduced by means of the calorimetric method. The pressure-dependence is similar for both methods. This shows that the *UI* method should not be used for determining the exact  $R_c$  but is useful for obtaining a first order-of-magnitude estimate.

## 4.11 Conclusions

The interstrand coupling currents (ISCCs) and power loss (ISCL) in a Rutherford-type cable are calculated by modelling the cable by means of a discrete network of nodes connected by strands and contact resistances  $R_a$  and  $R_c$ . A new model is written and described which is up to now the most general and precise model available (section 4.2). It includes transport current, saturation (with several types of resistive transitions), self-field, self- and mutual inductances, keystone angle and spatial distributions of resistances and applied field (variations). Calculations can be performed on single cables (of finite and infinite length), stacked cables and coils (see chapter 6). For all these geometries the time constants of the ISCCs can be calculated. With the same model also the characteristics of the boundary-induced coupling currents (see chapter 5) are calculated by means of the amplitude, characteristic loop length and characteristic time. The fields caused by the coupling currents in cables and coils can be calculated.

The ISCCs and ISCL depend strongly on the width of the cable, especially because an increase in the width often implies an increase in the cable pitch.

In the case of cables where  $R_c$  varies across the cable width or cables subjected to field changes which vary across the cable width, no simple formulas can be given for the ISCCs. A first estimate of the ISCCs and ISCL can be obtained by using the  $R_c$ - and  $\hat{B}$ -values in the centre of the cable (sections 4.6 and 4.7). Therefore, a cable with a resistive barrier between the two layers of the cable exhibits no significant ISCL, unless  $R_a$  is very small.

The ratio between the average time constant  $\tau_{is}$  and the coupling power loss  $P_c$  is constant in the case of a single cable subjected to a given  $\hat{B}_\perp$  and is not significantly affected by a non-uniform  $R_c$ -distribution across the cable width. The ratio between  $\tau_{is}$  and  $P_c$  remains also



constant for a stack of cables and is not affected by spatial  $R_c$ -distributions over the cross-section of the stack (section 4.9). This implies that:

- the time constant of the ISCCs of any configuration of cables is directly related to the ISCL in the cables, and conversely,
- the ISCL and the time constant  $\tau_{is}$  can be calculated for any configuration of cables if the ISCL or the  $\tau_{is}$  of a single cable, a stack of cables or a coil is known.

The time constant of the ISCCs in a stack of cables increases with the number of cables in the stack with a maximum increase of about a factor  $\alpha_{cab}$  (section 4.9)

An increase in the transport current results in a gradual decrease of the coupling currents  $I_a$ ,  $I_c$  and  $I_s$  as soon as the sum of the strand transport current and the coupling current  $I_s$  reaches the critical current. The total coupling power loss remains more or less constant up to a transport current close to the critical current of the strand (section 4.5). The place where the power is generated shifts from the contacts to the filaments.

For a finite piece of cable, subject to a spatially uniform  $\dot{B}$ , the ISCL will vary as a function of the cable length with a period equal to the cable pitch. The loss in a long cable can be well deduced from the loss in a short cable if the latter has a length larger than the cable pitch  $L_{p,s}$  and preferably equal to an integer times  $L_{p,s}$  (section 4.8).

The  $R_c$ -value of a cable is deduced by calorimetric and electrical methods. The electrical (or  $UI$ ) method is sensitive to local variations in  $R_a$  and  $R_c$ , but is useful for a first estimate of  $R_c$  only. The calorimetric method gives an average  $R_c$  but is not accurate if the interfilament coupling loss is much larger than the ISCL (section 4.10).

Both methods are applied to a stack of keystoneed Rutherford-type cable pieces to investigate  $R_c$  as a function of the transverse pressure. Experimental results are obtained for two 17 mm wide cables with SnAg coated strands. If no solder is present between the strands, the average  $R_c$  decreases about one order of magnitude for an increase in pressure from 10 to 100 MPa. The  $R_c$ -values determined by means of the calorimetric method are about 2-4  $\mu\Omega$  at 60 MPa. The  $R_c$ -values determined by means of the  $UI$  method are about twice as large which shows that the  $UI$  method is useful in order to obtain a first estimate of  $R_c$ , but that the calorimetric method has to be used to obtain an accurate global  $R_c$ . The  $R_c$ -value decreases to about 0.3  $\mu\Omega$  and is pressure-independent, if the cable is filled with PbSn solder. A heat-treatment of the cable under pressure reduces  $R_c$  significantly but the reduction disappears if the pressure is released to 0 and increased again to the original value.

The  $R_c$ -value in coils made of Rutherford-type cables can be estimated by measuring  $R_c$  of a stack of cable pieces. It is however very important that the stack is exposed to the same pressure and temperature cycle as will the cable in the process of cable manufacturing, coil winding, curing of the cable insulation and operation.  $R_c$ -values obtained without pressure and without heat-treatment could give a far too optimistic indication of the expected ISCCs in magnets.

Experimentally obtained time constants of the ISCCs are in very good agreement with the calculated time constants using the network model, which validates the use of the network model for simulating the interstrand coupling in superconducting cables.

## Chapter 5

# Boundary-induced coupling currents

*In this chapter it is shown that spatial distributions in the field-sweep rate  $\dot{B}$  and in the contact resistances  $R_a$  and  $R_c$  along the length of a Rutherford-type cable provoke a non-uniform current distribution during and after a field sweep. The process is described by means of Boundary-Induced Coupling Currents (BICCs) flowing through the strands over lengths far larger than the cable pitch. The BICCs are represented by a characteristic length, time and propagation velocity.*

*Several longitudinal distributions of  $\dot{B}$  and  $R_c$  are considered which are present or likely to be present in accelerator magnets. Attention is especially focused on the cable-to-cable connections and the coil ends, where the cable bends around the beam pipe.*

*The dependence of the characteristics of the BICCs on the strand resistivity and the contact resistance between strands is calculated.*

*It is shown that BICCs are always present in coils made of cables with non-insulated strands and it is discussed whether  $R_c$ - or  $\dot{B}$ -variations are the dominant cause.*

*The BICCs are evaluated by means of a novel experiment in which a 1.3 m long Rutherford-type cable is exposed to a local field variation. The results clearly demonstrate the existence of BICCs and validate the use of the network model for calculating them.*

## 5.1 Introduction

In chapter 4 the ISCCs are dealt with in the case where the  $\dot{B}$ -variation along the length of the cable is uniform. However, in all magnets a certain spatial variation of the field is present along the length of the cable and hence a spatial variation of  $\dot{B}$  during a field sweep. In this chapter only variations in  $\dot{B}_\perp$  (i.e. the field change normal to the large face of the cable, see eq. 4.1) are considered since the magnitude of the interstrand and boundary-induced coupling currents is mainly affected by this component.

As an example, the field change  $\dot{B}_\perp$  (in the centre of the cable) along the length  $z$  of the cable in a 1 m long LHC dipole magnet is shown in Fig. 5.1 for a central-field-sweep rate of  $0.0066 \text{ Ts}^{-1}$ . Only the cable of the inner coil of one pole, having 13 turns, is shown with a total length of about 25 m (see also Figs. 2.2b and 2.3).

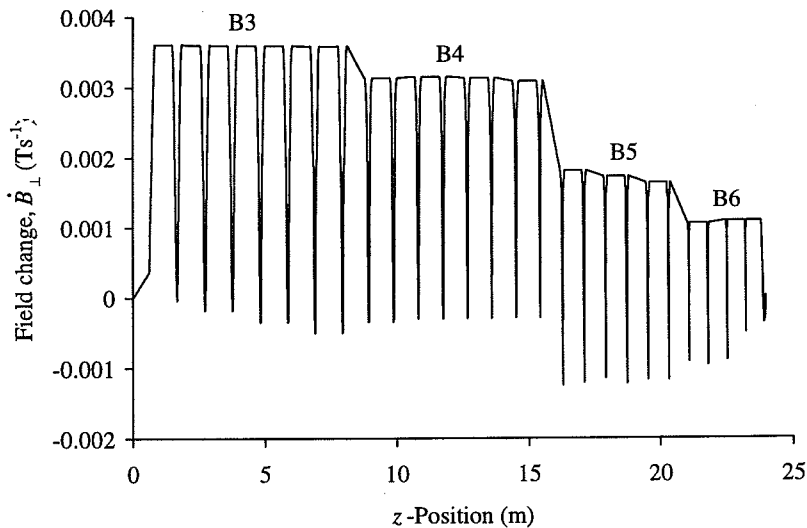


**Figure 5.1.** The field change  $\dot{B}_\perp$  along the length of the cable of the inner coil of one pole of a 1 m long LHC dipole magnet with a 50 mm aperture. The field change is the average field change in the centre of the cable. The central-field-sweep rate is  $0.0066 \text{ Ts}^{-1}$ . The labels indicate the block numbers (see Fig. 2.2b).

The sharp decreases in  $\dot{B}_\perp$  correspond to those parts in the coil where the cable bends around the beam pipe. The position  $z=0$  denotes the end of the current lead. Part of the curve ( $2.1 \text{ m} < z < 6.2 \text{ m}$ ) is enlarged in Fig. 5.2 in which  $\dot{B}_\perp$  at three different places across the cable width is depicted versus the scaled axial position of the cable. The spatial  $\dot{B}_\perp$ -distribution can be separated into two regimes:

- Strong variations for which  $|\Delta \dot{B}_\perp / \Delta z|$  is of the same order as  $|\dot{B}_{\perp, \max} / L_{p,s}|$ , with  $\Delta \dot{B}_\perp$  the change in  $\dot{B}_\perp$  over the longitudinal length  $\Delta z$  and  $\dot{B}_{\perp, \max}$  the maximum field change. An example is the average  $\dot{B}_\perp$ -variation between  $z=20L_{p,s}$  and  $z=21L_{p,s}$  (see Fig. 5.2) where  $|\Delta \dot{B}_\perp / \Delta z| = |\dot{B}_{\perp, \max} / L_{p,s}| = 0.0053 / 0.13 = 0.04 \text{ Ts}^{-1} \text{ m}^{-1}$ .

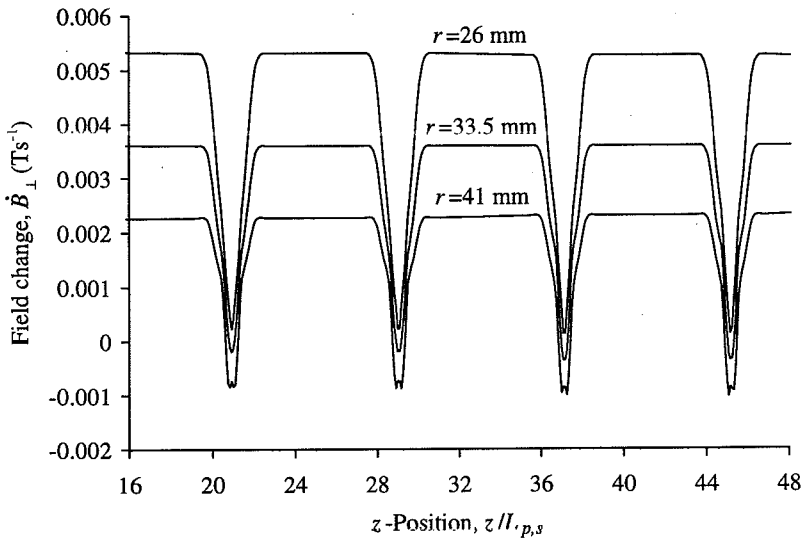


**Figure 5.2.** The field change  $\dot{B}_\perp$  along the scaled length of the cable of a 1 m long LHC dipole magnet with a 50 mm aperture. The field changes at three radii are shown (see Fig. 2.2a) for several turns of block 3 (B3). The central-field-sweep rate is  $0.0066 \text{ Ts}^{-1}$  and  $L_{p,s}$  is equal to 0.13 m.

- Weak variations for which  $|\Delta \dot{B}_\perp / \Delta z|$  is much smaller than  $|\dot{B}_{\perp, \max} / L_{p,s}|$ . An example is shown in Fig. 5.1 for the average variation of the field in the entire inner coil of the magnet, where  $|\Delta \dot{B}_\perp / \Delta z| = 0.0025/24 = 1 \cdot 10^{-4} \text{ Ts}^{-1} \text{ m}^{-1}$  while  $|\dot{B}_{\perp, \max} / L_{p,s}| = 0.0053/0.13 = 0.04 \text{ Ts}^{-1} \text{ m}^{-1}$ .

In accelerator dipole and quadrupole magnets both cases are present whereas, for example, in solenoid magnets mainly weak variations occur.

Besides spatial distributions of  $\dot{B}_\perp$  spatial distributions of  $R_c$  are also present in an accelerator magnet. In section 4.6 the case of a varying  $R_c$  across the cable width was discussed, which is due to the keystone angle and the gradient in the transverse pressure  $P_\perp$  across the cable width. However, variations in  $R_c$  along the cable length also occur and can be separated in:

- Variations over lengths far larger than  $L_{p,s}$  which are present in the entire cable since the transverse pressure varies considerably over the cross-section of the coil. Measurements of the contact resistances, performed on several sections of the inner coil of two SSC dipole model magnets, have shown that the contact resistances could vary by more than one order of magnitude over the turns of one coil [Kovachev, '93a/b, '94].
- Variations over lengths up to a few cable pitches which are present:
  - in the coil ends where the transverse pressure  $P_\perp$ , that strongly influences  $R_c$ , on the cable varies significantly; analysis of the cross-sections of coils has shown that in these parts of the magnet the average contact area between strands reduces to almost zero,
  - in the soldered connections between different cables in the magnet,
  - in local 'shorts' between strands.

Recently, the influence of spatial  $\dot{B}_\perp$ - and  $R_c$ -distributions on the coupling currents in Rutherford-type cables was also treated by Akhmetov et al., showing that the coupling currents  $I_s$  and  $I_c$  vary periodically with a period equal to the cable pitch [Akhmetov, '93a/'94/'95].

Egorov also concluded that the coupling currents and power can increase substantially due to the axial  $\dot{B}_\perp$ -variations although, under certain conditions, it can be imperceptible as well [Egorov, '94]. The coupling currents can increase up to magnitudes that, in combination with the transport current, saturate the strand and cause a quench or initiate a current redistribution.

Also Krempasky and Schmidt have recently shown that non-uniform  $\dot{B}$ -distributions provoke additional coupling currents exhibiting very long time constants [Krempasky, '95a/b]. Their approach was based on the solution of the diffusion equation which they applied to a two-wire configuration coupled through a transverse conductance.

An analytical solution of the decay of current loops as a function of time is given by Akhmetov et al. under weak and strong excitation levels [Akhmetov, '93b]. Computations are made in the case of an SSC dipole magnet, showing that the time constant under weak excitation can be as large as  $10^6$  s and decreases strongly if the transport current reaches 90% of its critical value.

The above-mentioned approaches demonstrate qualitatively that non-uniformities in the magnetic flux or cross-contact resistances always results in periodically varying coupling currents. In this chapter calculations are performed to investigate the current pattern caused by longitudinal  $\dot{B}_\perp$ - and  $R_c$ -variations more systematically. The calculations are made using the network model of a Rutherford-type cable as described in detail in section 4.2. Additional assumptions which are used in the simulations are given in section 5.3. The current patterns are evaluated by means of a new type of current, the so called '*Boundary-Induced Coupling Current* (BICC)', and illustrated in section 5.4.1. The term 'boundary' indicates that BICCs are generated by geometrical boundaries, boundaries in  $\dot{B}$  and internal boundaries such as changes in  $R_a$  and mainly  $R_c$ . The BICCs differ from the ISCCs with respect to:

- the length over which they flow in the strands, represented by a characteristic length  $\xi$ ,
- the characteristic time  $\tau_{bi}$  which they exhibit,
- the propagation velocity  $v_{bi}$ ,
- the magnitude  $I_{bi,0}$ .

In sections 5.4.1-5.4.4 the results are presented for a straight cable subject to a single ' $\dot{B}_\perp$ -step', which implies that one part of the cable is exposed to a field variation  $\dot{B}_\perp$  while the other part is not. Several formulas are presented by which the characteristic time and length of the BICCs can be estimated. In order to draw conclusions with respect to an entire coil, it is shown in section 5.4.5 how the results of a single  $\dot{B}_\perp$ -step can be applied to estimate the BICCs in a cable subject to an arbitrary longitudinal  $\dot{B}_\perp$ -variation.

In section 5.5 special attention is paid to the case of a cable which is partially exposed to a varying field. It is shown that the BICCs can cause a significant enhancement of the coupling power loss. The large characteristic lengths of the BICCs cause the loss to be also

dissipated in those parts of the cable which are not exposed to the local  $\vec{B}_\perp$ . In section 5.6 the case of a cable is investigated with  $R_c \gg R_a$  simulating, for example, a cable with a resistive barrier between the two layers. In section 5.7 the BICCs are calculated for a cable that is exposed to a uniform  $\vec{B}_\perp$  but has a local  $R_c$ -variation. The calculations are especially useful for understanding the influence of  $R_c$ -variations in the coil ends and cable-to-cable connections on the magnitude of the BICCs.

In section 5.8 a novel measurement set-up is described for investigating the BICCs in a straight Rutherford-type cable, subject to a local  $\vec{B}_\perp$ , by scanning the magnetic field along the cable length. The experimental results are compared to the calculations in order to understand the pattern of the BICCs and to validate the simulations.

In the next section the case of a cable with insulated strands is briefly discussed, since the current distribution has a certain resemblance to the current distribution as produced by the BICCs.

## 5.2 Cables with insulated strands

The current in each strand of a multistrand cable with insulated strands is constant through the total length of the cable. The current distribution in the cable subject to a homogeneous field can be easily derived since the current distributes itself among the strands in such a way that the voltages over all the strands of the cable are equal. The voltage over strand  $i$  consists of a resistive and an inductive part, and is given by:

$$U^i = U_R^i + U_{ind}^i = I_{str}^i (R_{ser}^i + \rho_s^i l_{str} / A_{str}) + \sum_{j=1}^{N_s} M^{ij} I_{str}^j \quad [\text{V}], \quad (5.1)$$

with  $I_{str}$  the strand current,  $R_{ser}$  the series (or joint) resistance of the transfer length near the current leads,  $\rho_s$  the strand resistivity,  $l_{str}$  the length of the strand,  $A_{str}$  the cross-section of the strand and  $M^{ij}$  the mutual inductance between strands  $i$  and  $j$ . This analytical approach can be used if the cable (with insulated strands) is subjected to a constant field (change) and is ramped without generating a large self-field compared to the field produced by the other turns. The transfer length consists of:

- the transfer across the copper of the current lead, the solder and the outer copper sheath of the strand (until the outermost layer of filaments),
- the transfer from the outermost layer of filaments to the more inner layers.

In general the first transfer trajectory is the major contribution to the resistance and the joint resistances can differ by a large amount. Eq. 5.1 shows that, once all the currents are stabilised (so that the inductive term can be disregarded), the current is distributed according to the relative values of the series and strand resistances. Hence, the distribution can strongly depend on:

- the current level because the strands can have a different voltage-current relation,
- the external field since the contact resistances can be magnetoresistive.

The strand currents under DC conditions always differ somewhat as it is impossible to achieve exactly the same soldering [Faivre, '81].

The contribution of the joint resistance  $R_{ser}$  and the strand resistance  $R_{str}$  to the total resistance  $R_{tot}$  is examined in the case of a dipole magnet. Therefore, both  $R_{ser}$  and  $R_{str}$  are calculated for the inner coil of a 1 m long PBD magnet (see Table 2.1).

- The joint resistance. The resistance of the soldered connection with length  $L_{p,s}$  between two Rutherford-type cables is typically 0.4 n $\Omega$ . For a 26-strand cable this implies about 10 n $\Omega$  on both ends of the strands, so in total 20 n $\Omega$  per strand.
- The strand resistance. Since the field (and hence the critical strand current) varies strongly over the cross-section of a magnet, the strand resistance has to be determined by integration along the total length  $l_{str}$  of the strand:

$$R_{str} = \frac{1}{A_{str}} \int_0^{l_{str}} \rho_s^i(I_{tr,str}) dz \quad [\Omega], \quad (5.2)$$

with  $A_{str}$  the cross-section of the strand. The power law of the voltage-current relation (see eq. 4.8) is used to describe the current dependence of  $\rho_s$ . Fig. 5.3 shows  $R_{str}$  as a function of the transport current for several  $n$ -values in eq. 4.8 (assuming  $\rho_s = 10^{-14} \Omega m$  at  $I_{tr,str} = I_{C,str}$ ). In the case of an operation current that is 90% of the critical current the resistance  $R_{str}$  is about  $10^{-6}$  to  $10^{-1}$  n $\Omega$  for  $n=30$  and  $n=10$  respectively.

At weak excitation levels the current distribution is dominated by the joint resistance whereas only for currents very close to the critical current does the strand resistance have to be taken into account, especially for long magnets made of a cable having a small  $n$ -value. Also in the case of cables with non-insulated strands the current distribution under DC conditions will be given by the differences in joint resistances among the strands.

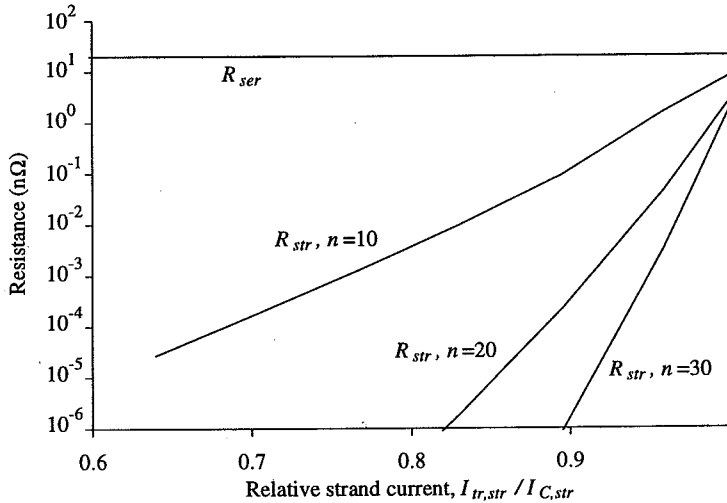


**Figure 5.3.** The resistance of the strands of an inner coil of a 1 m long LHC-type dipole magnet as a function of the scaled transport current for several  $n$ -values.  $R_{str}$  is almost proportional to the length of the magnet. The series resistance of 20 n $\Omega$ , corresponding to two cable-to-cable connections of 0.4 n $\Omega$ , is independent of the magnet length.

By changing the cable current, the strand currents will change according to their relative self- and mutual inductances. In the case of fully transposed cables, in which each strand has the same self- and mutual inductances with the other strands, the ramping of the total current will not affect the differences between the strand currents already created under DC conditions, if of course  $R_{ser}$  and  $\rho_s$  remain constant. In practice, however, a change of the current also causes a change of the field, and the strand resistivity can increase significantly due to the dynamic resistivity (see eq. 3.6):

$$\rho_{dyn} = \frac{A_{str}}{I_{tr,str}} E_{dyn} = \frac{d_f d_s^2}{3I_{C,str}(B,T)} \dot{B}_{\perp s} \quad [\Omega m], \quad (5.3)$$

with  $\dot{B}_{\perp s}$  the field change normal to the strand axis (disregarding the small twist angle of the filaments). The dynamic resistivity can easily be larger than the resistivity  $\rho_s$  under DC conditions. For example,  $\rho_{dyn} = 10^{-15} \Omega m$  at  $\dot{B}_{\perp s} = 0.1 \text{ Ts}^{-1}$  (for  $d_f = 10 \mu m$ ,  $d_s = 1.3 \text{ mm}$  and  $I_{C,str} = 1000 \text{ A}$ ), while  $\rho_s = 10^{-16} \Omega m$  at  $I_{tr,str} = 0.8 I_{C,str}$  (for  $n = 20$  and  $\rho_s = 10^{-14} \Omega m$  at  $I_{tr,str} = I_{C,str}$ ). In a coil each strand of the cable has an almost equal dynamic resistivity, so that a field-sweep will not cause differences between the strand currents due to different  $\rho_{dyn}$ .

Considering non-fully transposed cables (for example a 6 around 1 cable configuration), differences between the self- and the mutual inductances are present. During a current ramp, some strands will carry more current than others which can significantly decrease the quench current of such a cable if used in AC applications, see for example [Schermer, '79], [Faivre, '81], [Knoopers, '85]. These time constants of the (re)distribution process of the currents depend on the series and strand resistances and on the self- and mutual inductances. The time constants are therefore current-dependent since  $R_{ser}$  is magnetoresistive and  $R_{str}$  is strongly current-dependent.

The current distribution in non-fully transposed cables is not further discussed since all the strands of a Rutherford-type cable have almost the same length. Small differences in the lengths of less than 0.1% can be present due to, especially, the coil ends but they hardly affect the current distribution.

### 5.3 Simulating BICCs

The network model, as extensively described in section 4.2, is used to calculate the BICCs in a Rutherford-type cable. The longitudinal coordinate of the cable is denoted by  $z$ . The cable lengths from  $z=0$  to the ends of the cable are referred to as  $l_{cab,1}$ , for  $z < 0$ , and  $l_{cab,2}$ , for  $z > 0$  (see Fig. 5.4). The end of the cable is either the physical end (with or without a cable-to-cable connection) or a part where the strands are in the normal state (and hence have a relatively large strand resistivity).

Throughout the chapter the *strand sections* are denoted by the *strand position* (see Fig. 5.5) which is independent of the longitudinal position, while the (physical) *strands* are denoted by the *strand number*  $i$ . So, each strand will subsequently pass through all the strand positions.



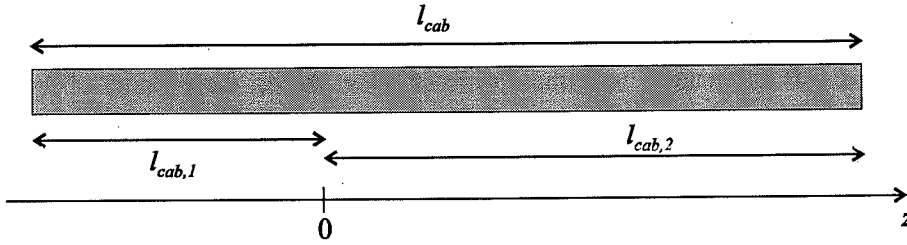


Figure 5.4. Definition of the lengths in a cable.

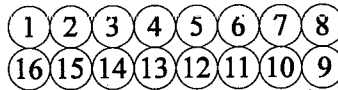


Figure 5.5. Numbering of the strand positions in the cross-section of a 16-strand Rutherford-type cable.

At  $z = k \cdot L_{p,s}$  (with  $k$  an integer), the strand numbers correspond to the strand position numbers. Hence, at  $z = 0$ , strand 1 bends around the edge of the cable while at  $z = L_{p,s}/4$  strand 1 is located near the centre of the cable.

The calculations are performed assuming that:

- The strands in the cable have the same length. This implies that all strands have the same self-inductance, whereas the values of the mutual inductance depend on the relative position of the strands in the cable.
- The strands have the same series resistances  $R_{ser}$ .
- The strand currents are smaller than the critical current ( $I_{str} < I_{C, str}$ , i.e. the strands are not saturated) and the strand resistivity  $\rho_s$  is the same for all the strands and is assumed to be independent of the current in the strand. In the network model the strand resistivity is included by means of a resistance  $R_s$  between two nodes as given by eq. 4.11.
- A non-uniform current distribution within the strand (due to persistent currents and interfilament coupling currents) is not taken into account.
- Only the field change  $\dot{B}_\perp$  is considered because the field changes  $\dot{B}_\parallel$  and  $\dot{B}_z$  (see Fig. 4.1) turn out to have a much smaller effect. At a first approximation, the ratio of the magnitudes of the BICCs for  $\dot{B}_\perp$  and  $\dot{B}_\parallel$  is equal to the ratio of the magnitudes of the ISCCs for  $\dot{B}_\perp$  and  $\dot{B}_\parallel$  (see eq. 4.20).
- The contact resistance  $R_a$  between adjacent strands is much larger than the contact resistance  $R_c$  between crossing strands ( $R_a \gg R_c$ ). Only section 5.6 deals with the specific case where  $R_a \ll R_c$ , simulating the presence of a resistive barrier between the two layers of the cable.
- In the ends of the cable the distribution of the ISCCs is given by the solution for a cable without longitudinal non-uniformities that is exposed to the local  $\dot{B}$ , which leads to the solutions obtained in section 4.4.1. Other boundary conditions, however, do not influence the results from a qualitative point of view.

The assumptions imply that the transport current is uniformly distributed among the strands. In the following the term 'steady-state' denotes the condition that the cable is exposed to a certain  $\dot{B}_\perp$ -distribution for a time much larger than all characteristic times involved.

Most of the simulations are performed by subsequently changing all the parameters in the network model, namely  $h$ ,  $w$ ,  $L_{p,s}$ ,  $N_s$ ,  $R_c$ ,  $R_a$ ,  $\dot{B}_\perp$  and  $\rho_s$ . The results are presented as analytical formulas that describe the dependence of the currents, time constants and decay lengths on the above-mentioned parameters. Therefore, each analytical relation contains one or more constants of proportionality that are needed to fit the numerical results to the analytical expressions.

Many simulations and, in particular, step-response calculations require a large-size matrix as shown in section 4.2. To reduce the computing time, the simulations are often performed on cables with only 8 or 10 strands. Also a large strand resistivity is used in order to decrease the length over which the BICCs decay (see section 5.4.2) and hence the matrix size. Extrapolation to cables with more strands and a small strand resistivity could therefore result in less accurate solutions. The estimated error in the constants of proportionality are given for each analytical expression.

## 5.4 Cables exposed to a $\dot{B}_\perp$ -step

The characteristic BICC distribution in a cable is illustrated in section 5.4.1 by means of a step increase in  $\dot{B}_\perp$  along the length of the cable. The magnitude of the BICCs as well as the characteristic length  $\xi$  are dealt with in section 5.4.2, the characteristic time  $\tau_{bi}$  in section 5.4.3 and the propagation velocity of the BICCs in section 5.4.4.

In section 5.4.5 it is shown how the solution of the BICCs for an arbitrary  $\dot{B}_\perp$ -distribution can be obtained by considering it as a superposition of  $\dot{B}_\perp$ -steps. Specific longitudinal variations, which are likely to occur in a magnet, such as:

- $\dot{B}_\perp$  which linearly increases from 0 to a certain value, simulating that part of a magnet where the cable enters the magnet,
- $\dot{B}_\perp$  which is small over a certain length of the cable, simulating the coil ends, where the cable bends around the beam pipe,

can be treated by this approach. Field variations across the cable width only slightly change the distribution of the ISCCs (see section 4.7) but do not generate BICCs, and are therefore not dealt with in this chapter.

### 5.4.1 Characteristic BICC pattern

A 16-strand cable is considered (with  $R_c=1\ \mu\Omega$ ,  $R_a=10\ \mu\Omega$ ,  $d_s=1.3\ \text{mm}$  and  $L_{p,s}=100\ \text{mm}$ ) which is exposed to a field change  $\dot{B}_\perp$  of 0 for  $z<0$  and  $0.01\ \text{T s}^{-1}$  for  $z\geq 0$ . The transport current  $I_{tr,str}$  in the strands is equal to 20 A.

The characteristic coupling-current pattern in the cable is illustrated by means of the current in a given strand as well as the current at a given strand position. Fig. 5.6 depicts the current in two *strands* (numbers 2 and 12).

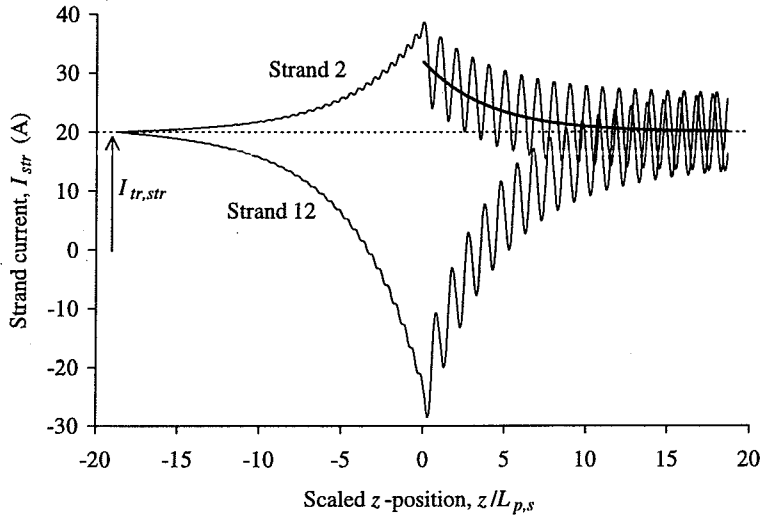


**Figure 5.6.** The characteristic pattern of the strand currents in two strands of a Rutherford-type cable subject to field changes of 0 for  $z < 0$  and  $0.01 \text{ Ts}^{-1}$  for  $z \geq 0$  (Regime A:  $\rho_s = 2 \cdot 10^{-14} \Omega \text{m}$ ). The transport current is shown by a dotted line. The bold line shows the transport current and the BICC in strand 2 for  $z \geq 0$ .

The strand current can be regarded as a superposition of three components:

- The transport current which is equal to 20 A all along the strand.
- The oscillating term, with an average equal to 0, related to the ISCCs which are mainly present for  $z \geq 0$ . The maximum ISCC is about 7 A and corresponds to the ISCC for a cable without longitudinal variations (see eq. 4.20). The amplitude of the ISCC pattern remains constant for  $z \geq 0$ .
- The BICC which is maximum close to the  $\dot{B}_\perp$ -step and decays quasi-exponentially for  $z < 0$  as well as  $z \geq 0$  with a characteristic length  $\xi$ , which is equal for all the strands. The magnitude of the BICCs can be different for  $z < 0$  and  $z \geq 0$ , as shown in Fig. 5.6 where the bold line represents the current in strand 2 corrected for the ISCC contribution. The difference depends on the strand number and its maximum is equal to the maximum value of the ISCCs.

Fig. 5.7 depicts the same strand currents but now when  $\rho_s$  is much smaller. The contribution of the ISCCs remains the same. The BICCs, however, decay quasi-linearly towards zero instead of quasi-exponentially and their magnitude is much larger than in the previous case.

Two regimes can be distinguished:

**Regime A.** The BICCs decay quasi-exponentially along the length and approach 0 clearly before the end of the cable. In this case a characteristic length  $\xi$  of the BICCs can be defined as the length over which the BICCs decay to  $1/e$  of their initial value. The length of the cable is at least several times  $\xi$  and the boundary conditions at the ends of the cable do not influence the magnitude and the decay length of the BICCs.

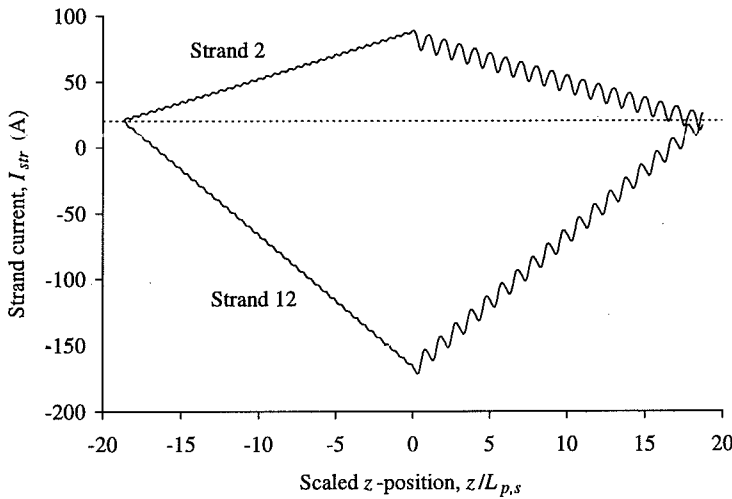


**Figure 5.7.** The characteristic pattern of the strand currents in two strands of a Rutherford-type cable subject to field changes of 0 for  $z < 0$  and  $0.01 \text{ Ts}^{-1}$  for  $z \geq 0$  (Regime B:  $\rho_s = 2 \cdot 10^{-17} \Omega \text{m}$ ). The transport current is shown by a dotted line.

**Regime B.** The BICCs decay quasi-linearly towards the boundary values at the end of the cable, which therefore influence the decay. In general the boundary conditions impose that the BICCs are 0 at the ends of the cable. Different boundary conditions, however, will give a qualitatively similar behaviour but quantitatively different results.

The intermediate regime, where the decay of the BICCs is somewhere in-between an exponential and a linear one, is not dealt with in this chapter. An estimate of the characteristics of the BICCs can be obtained by assuming a linear decay. In section 5.4.2 the parameters are discussed that define whether the BICCs decay quasi-exponentially or quasi-linearly.

In order to illustrate the current distribution in the cable more clearly, the strand current at a given *strand position* will now be analysed under the same conditions as applied in Figs. 5.6 and 5.7. The strand current at the edge of the cable (position 1, see Fig. 5.5) is depicted in Figs. 5.8 and 5.9 for regimes A and B. Fig. 5.10 shows an enlargement of Fig. 5.8 for  $-2L_{p,s} < z < 2L_{p,s}$  for two strand positions.

The average strand current at the edge is equal to  $I_{tr,str} = 20 \text{ A}$  for  $z < 0$  and is about 13 A for  $z \geq 0$  which corresponds to the sum of  $I_{tr,str}$  and the ISCC (of about -7 A) for a cable without longitudinal variations shown as a bold line in Fig. 5.8. Hence, the strand current at a given *strand position* can be regarded as a superposition of:

- the transport current,
- an oscillating part from the BICCs,
- the ISCCs of which the value depends on the strand position (see, for example, Fig. 4.6). This can be seen in Fig. 5.10 where the ISCC is about -7 A at position 1 while it is about 0 at position 5.

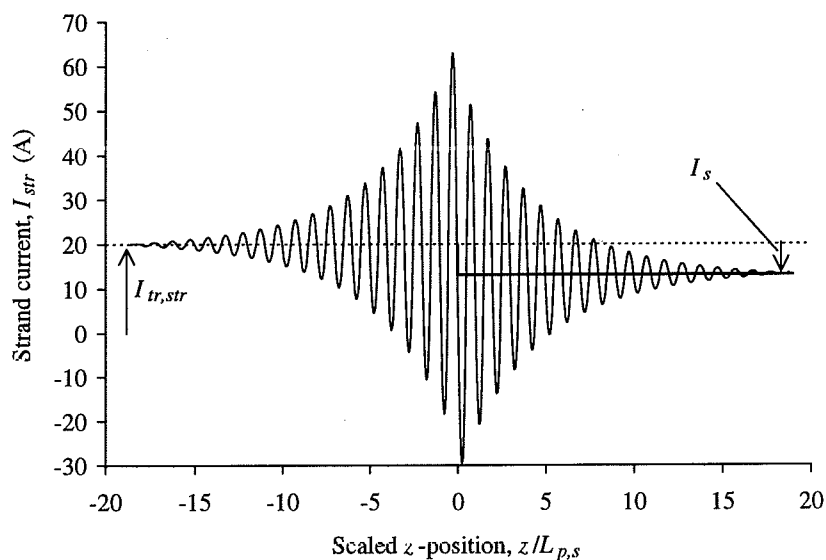


**Figure 5.8.** The characteristic pattern of the strand current at *position 1* of a Rutherford-type cable subject to field changes of 0 for  $z < 0$  and  $0.01 \text{ Ts}^{-1}$  for  $z \geq 0$  (Regime A:  $\rho_s = 2 \cdot 10^{-14} \Omega\text{m}$ ). The transport current is shown by a dotted line, and the ISCC by a bold line.

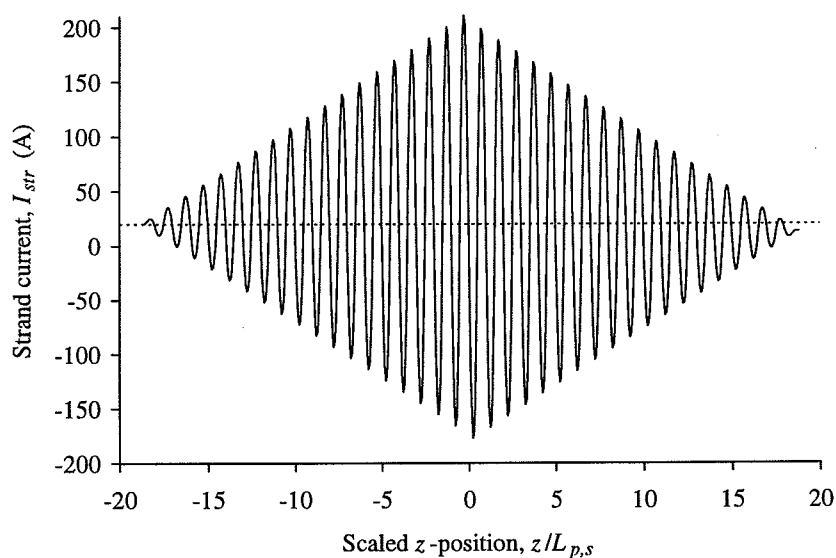


**Figure 5.9.** The characteristic pattern of the strand current at *position 1* of a Rutherford-type cable subject to field changes of 0 for  $z < 0$  and  $0.01 \text{ Ts}^{-1}$  for  $z \geq 0$  (Regime B:  $\rho_s = 2 \cdot 10^{-17} \Omega\text{m}$ ). The transport current is shown by a dotted line.

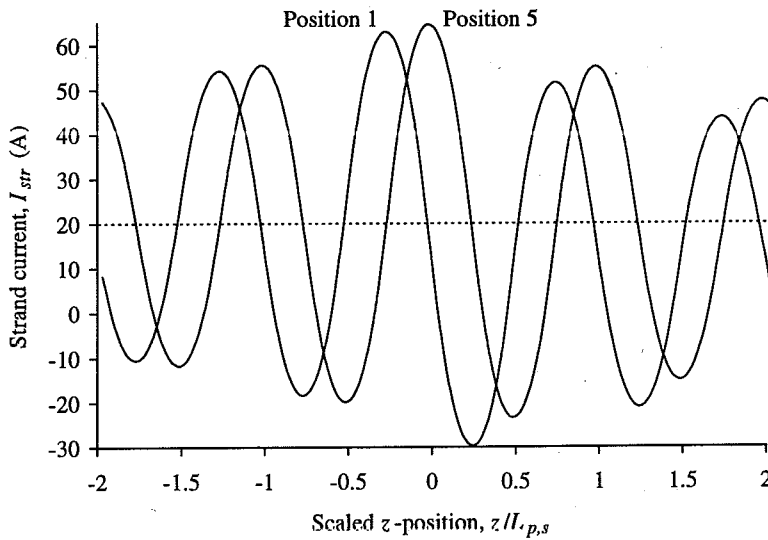


**Figure 5.10.** The characteristic pattern of the strand current at positions 1 and 5 of a 16-strand Rutherford-type cable subject to field changes of 0 for  $z < 0$  and  $0.01 \text{ Ts}^{-1}$  for  $z \geq 0$  (Regime A:  $\rho_s = 2 \cdot 10^{-14} \Omega \text{m}$ ). The transport current is shown by a dotted line.

If the transport currents in the strands are not equal, an additional variation of the current at a given strand position is present.

A regular pattern exists in the magnitudes of the BICCs. In each cross-section of the cable opposite strands (for example 3 and 11 or 7 and 15, see Fig. 5.5) carry BICCs with the same magnitude but with an opposite sign. Adjacent strands have only slightly different BICCs as shown in Fig. 5.11. For  $z=0$  the maximum BICCs occur in the centre of the cable i.e. at positions  $N_s/4$  and  $3N_s/4$ .

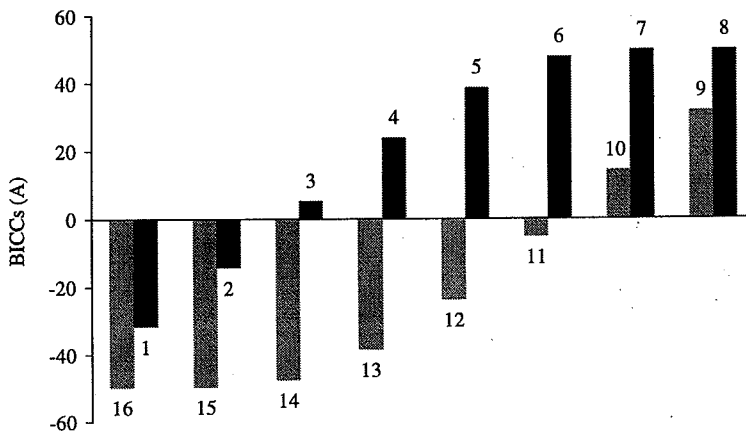


**Figure 5.11.** Illustration of the magnitude of the BICCs in a 16-strand cable at a certain  $z$ -position. The labels indicate the strand positions as given in Fig. 5.5.

The regular pattern is typical for BICCs and causes them to generate more pronounced field errors than in the case of a random current distribution among the strands, such as that caused by different joint resistances. The magnitudes of the BICCs change mainly due to cross-over currents  $I_c$  flowing between the upper (positions 1 to  $N_s/2$ ) and lower layers (positions  $N_s/2+1$  to  $N_s$ ) through the contact resistances  $R_c$ . The currents in  $R_a$  contribute only slightly to the magnitude of the BICCs (for  $R_a \geq R_c$ ). Hence, the currents  $I_c$  correspond to the change in the current  $I_{str}$  in the axial direction of the strand (see Figs. 5.6 and 5.7). This implies that the strands carrying large BICCs are more heated than the strands carrying small BICCs, which in turn results in a periodic behaviour of  $I_c$  and, therefore, the coupling power  $P_c$  along the cable length.

It is important that the decay of the BICCs along the length is only quasi-exponential or quasi-linear if the  $R_c$  is constant. In the case of a cable with a longitudinal  $R_c$ -variation, the change of the BICCs along the cable length will vary according to the local  $R_c$ . This implies that, for example, the slope  $dI_{bi}/dz$  of the linear decay shown in Fig. 5.7 will not be constant along the length but will locally increase (decrease) in sections with smaller (larger)  $R_c$ . This will be discussed in more detail in section 5.8.3.

In Fig. 5.12 the coupling power loss is shown in the entire cable for regimes A and B. At each  $z$ -position the power loss is calculated by the individual losses in each contact summed over all the  $(N_s-1)$  contacts in one band (see Fig. 4.2). The values are then divided by the length of one band ( $=L_{p,s}/N_s$ ) to obtain the local power loss per unit length of cable.

In the case of constant  $\dot{B}_1$  and  $R_c$  along the cable length the cross-over currents  $I_c$  are  $z$ -independent and result in a constant power loss  $P_c$  of 0 for  $z < 0$  and  $2.21 \cdot 10^{-3} \text{ Wm}^{-1}$  for  $z \geq 0$  (see eq. 4.17), shown as a dotted line in Fig. 5.12. The BICCs enhance the ISCL since the average power loss is larger than 0 for  $z < 0$  and larger than  $2.21 \cdot 10^{-3} \text{ Wm}^{-1}$  for  $z \geq 0$ .

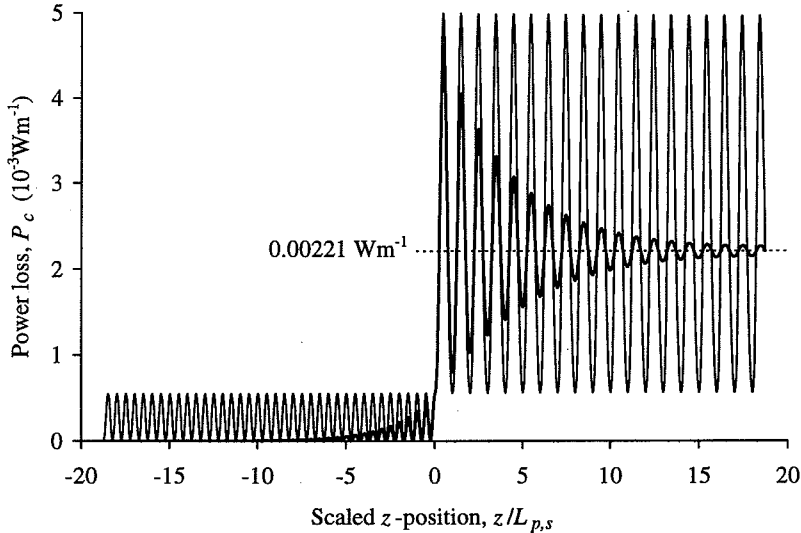


**Figure 5.12.** The characteristic pattern of the ISCL in a Rutherford-type cable subject to field changes of 0 for  $z < 0$  and  $0.01 \text{ Ts}^{-1}$  for  $z \geq 0$ . Bold line:  $\rho_s = 2 \cdot 10^{-14} \Omega\text{m}$ , regime A. Normal line:  $\rho_s = 2 \cdot 10^{-17} \Omega\text{m}$ , regime B.

The increase is more pronounced if the magnitude of the BICCs is larger, so that the enhancement of the power loss is larger for regime B than regime A. Note that for regime B the amplitude of the  $P_c$ -variations remains constant on both sides of the  $\dot{B}_\perp$ -step while the amplitude decreases for regime A. The reason for this is that the maximum  $dI_{str}/dz$  per twist pitch, which is related to the amplitude of the  $P_c$ -variations, remains constant for regime B while it decreases for regime A (see Figs. 5.6 and 5.7).

It is interesting to see that for regime B the maximum ISCL for  $z < 0$  corresponds to the minimum ISCL for  $z \geq 0$ . The same holds for regime A close to  $z = 0$ . This implies that for  $z \geq 0$  the mean currents through  $R_c$  (in one band) due to a constant  $\dot{B}_\perp$  are twice as large as those due to the  $\dot{B}_\perp$  step. The maximum local ISCL for  $z \geq 0$  is therefore  $(3/2)^2 = 2.25$  times larger than the ISCL without  $\dot{B}_\perp$ -step. For  $z < 0$  the maximum local ISCL is  $(1/2)^2 = 0.25$  times the ISCL (at  $z \geq 0$ ) without  $\dot{B}_\perp$ -step. The enhancement of the ISCL due to a  $\dot{B}_\perp$ -step is discussed in more detail in section 5.5.

In Fig. 5.13 the coupling power loss in each resistance  $R_c$  is shown for regime A for  $3L_{p,s} < z < 6L_{p,s}$ . A periodic pattern (with period  $L_{p,s}$ ) is present where parts having large and small local power losses alternate.

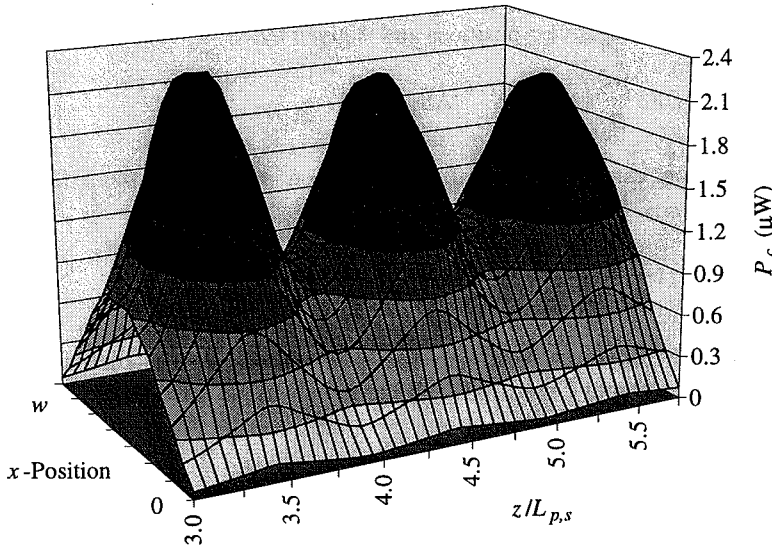


**Figure 5.13.** The characteristic pattern of the ISCL across the cable width (with  $w = 10.4$  mm) of a Rutherford-type cable subject to field changes of 0 for  $z < 0$  and  $0.01 \text{ Ts}^{-1}$  for  $z \geq 0$  (Regime A:  $\rho_s = 2 \cdot 10^{-14} \Omega \text{m}$ ).

Half of the strands are less heated than the average since they 'slalom' in between the hot spots. These strands correspond to those with small BICCs. The other half of the strands, which carry large BICCs, are heated more than the average. Hence, the spots with a large local power loss correspond to those areas where strands with large BICCs cross each other.



Although the power loss fluctuates strongly, this does not imply that the actual temperature of the strands fluctuates to the same extent. Due to the good thermal conductivity inside the cable the temperature will probably be quite uniform under normal operating conditions in an accelerator magnet.

### 5.4.2 Magnitude and characteristic length of BICCs under steady-state conditions

The following analytical relations for  $\xi$  and  $I_{bi,max}$  in regimes A and B are derived by a fit to the numerical calculations. The errors in the fitting constants are about 5-10%. The calculations are performed for  $8 \leq N_s \leq 40$ . For larger  $N_s$  the simulations become too time-consuming. However, the relations probably also hold for cables with  $N_s > 40$  although the indicated errors could increase by a factor 2.

#### Regime A.

The BICC in strand  $i$  (see for example Fig. 5.6) can be approximated by (neglecting the small periodic signal for  $z < 0$ ):

$$I_{bi,i}(z) = I_{bi,0} \sin(2\pi(i-0.5)/N_s) e^{-|z|/\xi} \quad [\text{A}], \quad (5.4)$$

where  $I_{bi,0}$  is defined as the average between the maximum magnitude of the BICCs at positive and negative  $z$ -positions and is given by:

$$I_{bi,0} = 0.88 \frac{w\xi}{R_c} (1 - e^{-N_s/9.6}) \Delta \dot{B}_\perp \quad [\text{A}]. \quad (5.5)$$

The relation can be expressed as a function of the maximum ISCC,  $I_{s,max}$ , by combining eqs. 5.5 and 4.20, assuming  $\cos(\pi x/w) = 1$  and  $\Delta \dot{B}_\perp = \dot{B}_\perp$ :

$$I_{bi,0} = 21 \frac{\xi}{L_{p,s} N_s} (1 - e^{-N_s/9.6}) I_{s,max} \quad [\text{A}]. \quad (5.6)$$

The impact of these relations for practical cables is discussed later. The characteristic length  $\xi$  is equal for all the strands in the cable and is given by:

$$\xi = 0.50 \frac{L_{p,s}}{N_s} \sqrt{R_c / R_s} \quad [\text{m}]. \quad (5.7)$$

For  $R_s = 0$  the BICCs have to be calculated using the formulas for regime B. The length  $\xi$  can be expressed in terms of  $\rho_s$  by combining eqs. 4.11 and 5.7:

$$\xi = 0.50 \sqrt{\frac{R_c L_{p,s} \pi d_s^2}{2 \rho_s N_s}} \quad [\text{m}]. \quad (5.8)$$

The relation is shown in Fig. 5.14 for several resistivities.  $\xi$  can be large for practical superconductors especially for small  $\rho_s$  and large  $R_c$ . It is important that  $\rho_s$  denotes

an effective strand resistivity that the BICCs 'see' which could be different from the strand resistivity that the transport current 'sees'. A brief discussion and an estimate of this effective resistivity is given in section 7.7.5. Note that in the case of normal conducting strands with a large resistivity,  $\xi$  is very small so that, in fact, no BICCs are present.

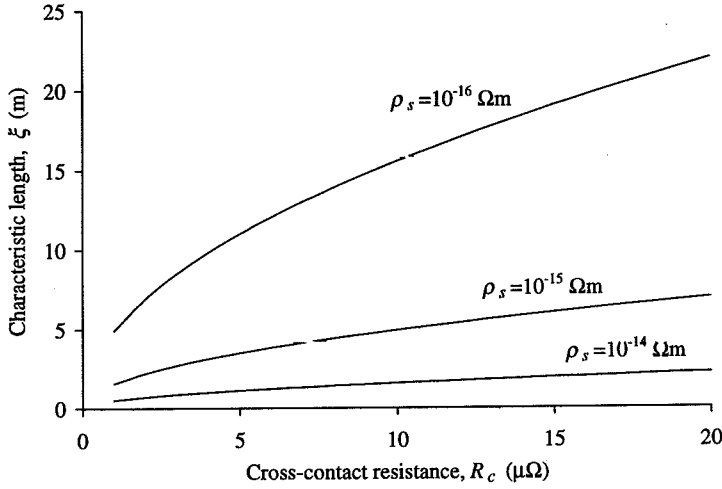


Figure 5.14. Calculated characteristic lengths  $\xi$  of a 26-strand Rutherford-type cable with  $d_s = 1.3$  mm and  $L_{p,s} = 0.1$  m.

If  $\xi$  is much larger than the lengths  $l_{cab,1}$  (for  $z < 0$ ) and  $l_{cab,2}$  (for  $z \geq 0$ ) then the BICCs have to be calculated using the formulas for regime B. If  $\xi$  is of the same order as  $l_{cab,1}$  (or  $l_{cab,2}$ ) then the exact BICC pattern cannot be described by simple analytical relations but the relations for regime A or B can be used as a first approximation.

### Regime B.

A similar expression for  $I_{bi,0}$  is obtained as eq. 5.4 with the difference being that the BICCs depend linearly on the cable length:

$$I_{bi,i}(z) = I_{bi,0} \sin(2\pi(i-0.5)/N_s) \left(1 - |z|/l_{cab,i}\right) \quad [\text{A}], \quad (5.9)$$

with  $l_{cab,i} = l_{cab,1}$  for  $z < 0$  and  $l_{cab,i} = l_{cab,2}$  for  $z \geq 0$ . The maximum magnitude of the BICCs in the cross-section of the cable equals:

$$I_{bi,0} = 1.0 \frac{w l_{cab,eff}}{R_c} (1 - e^{-N_s/19.6}) \Delta \dot{B}_\perp \quad [\text{A}], \quad (5.10)$$

with:

$$l_{cab,eff} = 2 \frac{l_{cab,1} l_{cab,2}}{l_{cab,1} + l_{cab,2}} \quad [\text{m}]. \quad (5.11)$$

Again, the current  $I_{bi,0}$  can be written as a function of  $I_{s,max}$ , by combining eqs. 5.10 and 4.20, assuming  $\cos(\pi x/w)=1$  and  $\Delta \dot{B}_\perp = \dot{B}_\perp$ :

$$I_{bi,0} = 25 \frac{l_{cab,eff}}{L_{p,s} N_s} \left(1 - e^{-N_s/9.6}\right) I_{s,max} \quad [A]. \quad (5.12)$$

The maximum magnitude  $I_{bi,0}$  of the BICCs for practical cables (i.e.  $N_s$  is about 20-40) is, in first approximation, about a factor  $\xi/L_{p,s}$  (regime A, see eq. 5.6) or  $l_{cab,eff}/L_{p,s}$  (regime B, see eq. 5.12) larger than the maximum ISCC. This factor explains the large difference in the magnitude of the BICCs shown in Figs. 5.8 (with  $I_{bi,0} \approx 50$  A) and 5.9 (with  $I_{bi,0} \approx 200$  A) since  $l_{cab,eff} \sim 4\xi$  for the given simulation parameters.

The impact of the BICCs becomes clear by considering a dipole coil, where  $\Delta \dot{B}_\perp \approx \dot{B}_\perp$  in the coil ends (see Fig. 5.1). For large  $\xi$  (regime A) or  $l_{cab,eff}$  (regime B) the BICCs can attain very large values, even at small field-sweep rates and large contact resistances. For example,  $I_{bi,0} = 92$  A for  $N_s = 26$ ,  $w = 0.017$  m,  $\xi = 10$  m,  $R_c = 10 \mu\Omega$  and  $\Delta \dot{B}_\perp = 0.0066$  Ts<sup>-1</sup> (regime A).

Note that the magnitude of the BICCs is proportional to  $\dot{B}_\perp$ , provided that  $\xi$  (for regime A) is independent of  $\dot{B}_\perp$ . This is an important conclusion that is used in chapter 7 in order to distinguish the field distortions caused by the BICCs and those caused by a non-uniform current distribution among the strands (due to different joint resistances).

Although the magnitude of the BICCs varies considerably between regimes A and B, the maximum in the local power loss is the same (see Fig. 5.12), because the slope  $dI_{str}/dz$  is the same for  $z \rightarrow 0$ , and therefore also the local currents  $I_c$  for  $z \rightarrow 0$ .

In this section a constant  $R_c$  along the cable is assumed. However, as discussed in the introduction of this chapter, spatial  $R_c$ -variations are always present in a coil. The BICCs caused by these variations are discussed in section 5.7 in the case of a constant  $\dot{B}_\perp$ . However, spatial  $R_c$ -distributions also change the magnitude of BICCs provoked by a  $\dot{B}_\perp$ -step. In general the local increase of the BICCs, i.e.  $dI_{bi}/dz$ , (see for example Figs. 5.6 and 5.7) is inversely proportional to the local  $R_c$ . This means that all the sections in a cable having a small  $R_c$  could enhance the magnitude of the BICCs, even if these sections are placed in a low-field region of the magnet. A typical example is the joint between the cables of two poles. An example of the influence of a local decrease in  $R_c$  on the magnitude of the BICCs is given in section 5.8.3. Expressions for all typical  $R_c$ - and  $\dot{B}_\perp$ -variations along the cable length cannot be given since the number of combinations is much too large.

The BICCs can only attain the steady-state values if:

- the total current (i.e. the sum of the transport current, the ISCC and the BICC) in each strand section remains smaller than the critical current,
- the characteristic time of the BICCs is smaller than the time during which the cable is exposed to a field change. In the next section the characteristic time of the BICCs is discussed by means of their step response.

### 5.4.3 Characteristic time of BICCs

The development of the BICCs in time is investigated by introducing self- and mutual inductances between the strands as discussed in section 4.2. As an example, the decay of the BICCs in an 8-strand cable (with  $d_s=1$  mm,  $\rho_s=1.2 \cdot 10^{-14}$   $\Omega$ m and  $L_{p,s}=0.1$  m) is calculated for:

$$\begin{aligned} t \leq 0: & \quad \dot{B}_\perp = 0 \quad \text{for } z < 0 \quad \text{and} \quad \dot{B}_\perp = 0.01 \text{ Ts}^{-1} \quad \text{for } z \geq 0, \\ t > 0: & \quad \dot{B}_\perp = 0 \quad \text{for } z < 0 \quad \text{and} \quad \dot{B}_\perp = 0 \quad \text{for } z \geq 0. \end{aligned}$$

At  $t=0$  the BICCs have attained their steady-state values and decay quasi-exponentially along the length (see eq. 5.4). For  $t>0$  the BICCs decay to 0, starting from the initial value at  $t=0$ , as illustrated in Fig. 5.15, where the decay of the BICCs at several  $z$ -positions is depicted as a function of the time. The moment at which the BICCs start to decay propagates through the cable. Near  $z=0$  the decay is instantaneous, whereas for larger  $z$  the decay starts after a certain time. This propagation is discussed in section 5.4.4.

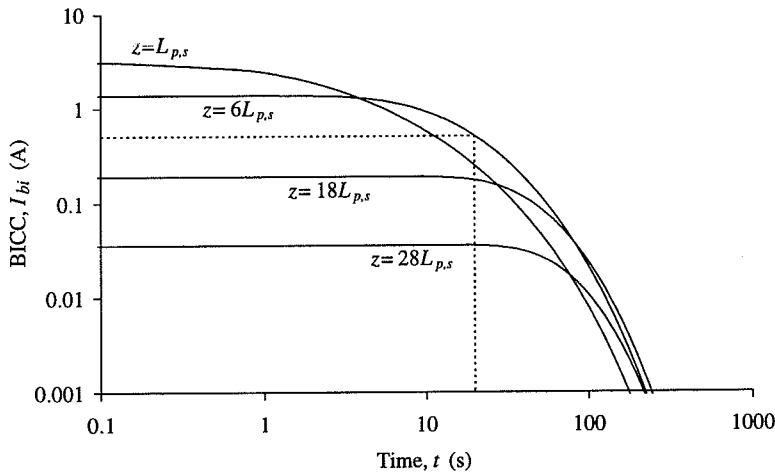


**Figure 5.15.** The decay of the BICC in a given strand as a function of the time at several  $z$ -positions. The dotted line shows the characteristic time at  $z=6L_{p,s}$  i.e. the period during which the BICC at  $z=6L_{p,s}$  has decayed to  $1/e$  of its initial value.

The relative decay is identical for all the strands. Since the decay as a function of the time is not exponential, the following *characteristic* times are defined:

- $\tau_{bi}(z)$ : The time during which the BICCs at position  $z$  decay to  $1/e$  of their initial values (see section 5.4.4).
- $\tau_{bi,av}$ : The time during which the average of the absolute value of all the BICCs in the whole cable decays to  $1/e$  of its initial value.

The characteristic times are calculated for both regimes with the same approach as used for the calculation of  $\tau_{is,cab}$  (see section 4.4.2), i.e. in the case of a straight cable having strands with a round cross-section. The characteristic times increase slightly for cables with a small

keystone angle or highly compressed cables. The results of the numerical calculations are expressed by analytical relations which are valid for  $8 \leq N_s \leq 40$  with an error in the constants of proportionality of about 20%.

### Regime A.

The characteristic time  $\tau_{bi,av}$  satisfies:

$$\tau_{bi,av} = 2.4 \cdot 10^{-8} \frac{L_{p,s}}{R_s} = 1.2 \cdot 10^{-8} \frac{N_s \pi d_s^2}{\rho_s} \quad [\text{s}], \quad (5.13)$$

where the constants have the dimensions  $\Omega \text{sm}^{-1}$ . If  $\rho_s = 0$  the BICCs should be calculated using the formulas for regime B so that eq. 5.13 is no longer relevant. The times  $\tau_{bi,av}$  are about 30% larger than the times  $\tau_{bi}(0)$ .

Eq. 5.13 shows that  $\tau_{bi,av}$  is independent of  $R_c$ , which can be understood by considering the cable as a simple  $LR$ -circuit, where  $L$  represents the effective inductance of the strands over a length  $\xi$  and  $R$  represents the effective resistance of the parallel connected resistances  $R_c$ . Hence,  $L$  is linear in  $\xi$  and  $R$  is linear in  $R_c/\xi$ . Since the time constant of an  $LR$ -circuit is given by  $\tau = L/R$ , the time constant  $\tau_{bi,av}$  is proportional to  $\xi/(R_c/\xi) = \xi^2/R_c$ . This implies that  $\tau_{bi,av}$  is independent of  $R_c$ , because  $\xi^2$  is linear in  $R_c$  (see eq. 5.7).

### Regime B.

Since the BICCs decay linearly towards the end of the cable, the time constant  $\tau_{bi,av}$  is now related to the lengths  $l_{cab,1}$  and  $l_{cab,2}$  and can be expressed by:

$$\tau_{bi,av} = 6.2 \cdot 10^{-8} \frac{l_{cab,1} l_{cab,2} N_s^2}{L_{p,s} R_c} \quad [\text{s}], \quad (5.14)$$

where the constants has the dimension  $\Omega \text{sm}^{-1}$ . The characteristic time  $\tau_{bi,av}$  can be expressed as a function of the interstrand time constant of a single cable by combining eqs. 5.14 and 4.31:

$$\tau_{bi,av} = 3.8 \frac{l_{cab,1} l_{cab,2}}{L_{p,s}^2} \tau_{is,cab} \quad [\text{s}] \quad \text{for large } N_s. \quad (5.15)$$

Note that for  $l_{cab,1} = l_{cab,2} = l_{cab}/2$  the characteristic time  $\tau_{bi}$  is about a factor  $(l_{cab}/L_{p,s})^2$  larger than  $\tau_{is,cab}$ .

The time constant is either limited by the effective strand resistivity (regime A) or by the lengths and the cross-contact resistance (regime B) as shown in Fig. 5.16 for a 26-strand straight cable with lengths of 22 m and 110 m (as an example). The horizontal lines show eq. 5.13 while the lines which are inversely proportional to  $R_c$  represent eq. 5.14. The bold curve shows the characteristic time  $\tau_{bi,av}$  as a function of  $R_c$  in the case of a cable with  $l_{cab,1} = 2$  m and  $l_{cab,2} = 20$  m. If  $R_c$  is small, the BICCs decay before the end of the cable

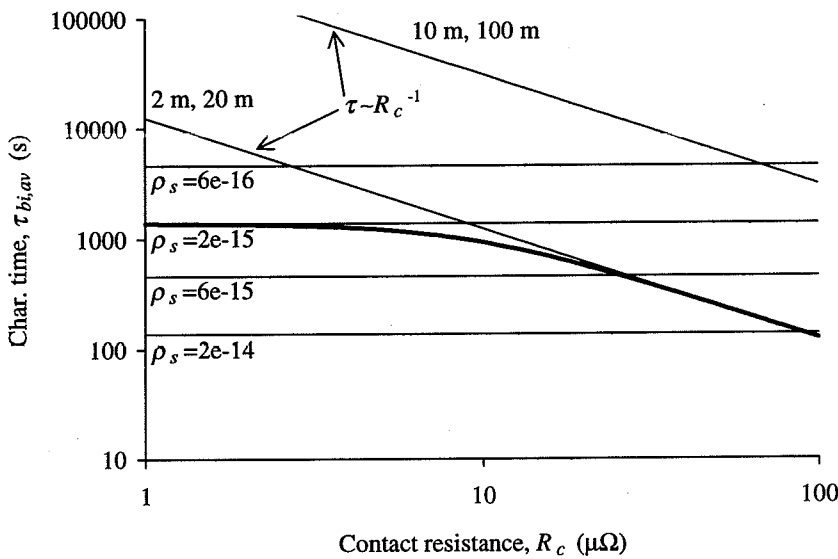


**Figure 5.16.** The characteristic time  $\tau_{bi,av}$  as a function of the contact resistance  $R_c$ . The horizontal curves refer to regime A while the linearly decreasing curves represent regime B (where the two labels indicate the lengths  $l_{cab,1}$  and  $l_{cab,2}$ ). The bold line shows the actual characteristic time  $\tau_{bi,av}$  in a cable with  $l_{cab,1}=2$  m and  $l_{cab,2}=20$  m ( $N_s=26$ ,  $d_s=1.3$  mm,  $L_{p,s}=0.13$  m).

(regime A) so that  $\tau_{bi,av}$  is independent of  $R_c$  (see eq. 5.13). If  $R_c$  is large, the characteristic time of the BICCs is limited by the lengths (regime B). The bold line deviates slightly for the region in-between regimes A and B. The above implies that similar coils with different  $R_c$  exhibit about the same  $\tau_{bi,av}$  if the BICCs decay over a length  $\xi$  (regime A), while they exhibit different  $\tau_{bi,av}$  if the BICCs decay over the whole cable (regime B).

The characteristic times of the BICCs in a coil can change (compared to a straight cable) due to the mutual inductances between the BICCs of the various turns. The interaction of the ISCCs between the turns of a stack of cable pieces causes an increase in the time constant of the ISCCs (see section 4.9) of about a factor 4-5 for LHC dipole magnets (see section 6.2.3) because the ISCC-distribution across the cable width is similar for each turn. However, the BICCs at a given strand position oscillate along the length with a phase that varies for each turn, since the length of each turn is different (see Fig. 2.3). Hence,  $\tau_{bi,av}$  in a coil depends on the exact geometry of the coil, and can be a few times smaller or larger than  $\tau_{bi,av}$  in a single straight cable. Of course, in an actual coil a spectrum of  $\tau_{bi,av}$  is present due to the numerous  $\hat{B}_1$ -variations located at different positions with respect to the cable ends and possibly in sections with different  $R_c$ .

In section 3.4 it is shown that the IFCL can be expressed by  $P_{if}=n\tau_{if}\hat{B}_{1s}^2/\mu_0$  with  $n$  a shape factor equal to 2 for strands with a round cross-section. A similar relation is shown to be present between  $P_c$  and  $\tau_{is,cab}$  (see eq. 4.36). However, it is important to note that such a relation is *not* present between  $\tau_{bi,av}$  and the enhancement of the ISCL due to the BICCs.

#### 5.4.4 Propagation velocity of BICCs

In section 5.4.3, the characteristic time  $\tau_{bi}(z)$  is defined as the time during which the BICCs at position  $z$  decay to  $1/e$  of their initial values. As an example,  $\tau_{bi}(z)$  is depicted in Fig. 5.17 for an 8-strand cable with  $d_s=1.3$  mm,  $L_{p,s}=0.1$  m,  $R_c=0.1 \mu\Omega$  and  $\rho_s=1.1 \cdot 10^{-14} \Omega\text{m}$  (regime A).

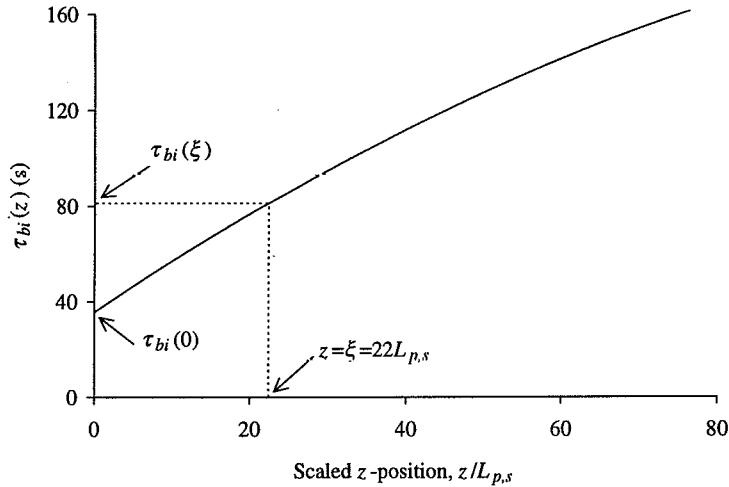


**Figure 5.17.** The time  $\tau_{bi}$  at which the BICCs decay to  $1/e$  of their initial values as a function of the  $z$ -position. The average propagation velocity  $v_{bi,av}$  corresponds to the inverse of the slope of the curve between  $z=0$  and  $z=\xi$ .

The characteristic time can be expressed by:

$$\tau_{bi}(z) = \tau_{bi}(0) + \frac{z}{v_{bi}(z)} \quad [\text{s}], \quad (5.16)$$

where  $v_{bi}(z)$  is defined here as the propagation velocity of the BICCs through the cable which increases slightly with increasing  $z$ . In other words, the propagation velocity expresses the time it takes before a strand current at a certain distance from the  $\hat{B}$  non-uniformity starts to change due to an additional BICC contribution (besides the transport current and the ISCC). The time dependent behaviour of the BICCs in a cable shows a certain similarity with electromagnetic waves that are characterised by a propagation velocity, and attenuation and dispersion along the length. In a coil the propagation velocity will probably be imperceptible since the BICCs caused by the numerous non-uniformities interfere and partially cancel. The increase in the characteristic time is, however, experimentally observed in a 1.3 m long cable (see section 5.8.3).

In the following an average velocity is defined over a length  $\xi$  (for regime A) and  $l_{cab,i}/2$  (for regime B) as:

$$v_{bi,av} = \frac{\xi}{\tau_{bi}(\xi) - \tau_{bi}(0)} \quad [\text{ms}^{-1}] \quad \text{for regime A,} \quad (5.17)$$

and:

$$v_{bi,av} = \frac{l_{cab,i}/2}{\tau_{bi}(l_{cab,i}/2) - \tau_{bi}(0)} \quad [\text{ms}^{-1}] \quad \text{for regime B,} \quad (5.18)$$

with  $l_{cab,i} = l_{cab,1}$  for  $z < 0$  and  $l_{cab,i} = l_{cab,2}$  for  $z \geq 0$ .

The average propagation velocity is numerically calculated for regimes A and B and can be analytically described by the following formulas which are valid for  $8 \leq N_s \leq 40$  with an error in the constants of proportionality of about 20%.

**Regime A.**

$$v_{bi,av} = 2.2 \cdot 10^7 \frac{\sqrt{R_c R_s}}{N_s} \quad [\text{ms}^{-1}], \quad (5.19)$$

which is equal to (using the expressions for  $\xi$  and  $\tau_{bi,av}$  given by eqs. 5.7 and 5.13):

$$v_{bi,av} = \frac{\xi}{\tau_{bi,av}} \quad [\text{ms}^{-1}]. \quad (5.20)$$

Combining eqs. 5.17 and 5.20 shows that  $\tau_{bi}(\xi) = \tau_{bi,av} + \tau_{bi}(0) = 2.3\tau_{bi}(0)$  since  $\tau_{bi,av} = 1.3\tau_{bi}(0)$  (see the remark after eq. 5.13), as can also be seen in Fig. 5.17.

**Regime B.**

$$v_{bi,av} = 1.7 \cdot 10^7 \frac{L_{p,s} R_c}{N_s^2 l_{cab,2}} \quad [\text{ms}^{-1}] \quad \text{for } z \geq 0, \quad (5.21)$$

which can be combined with eq. 5.14 to give:

$$v_{bi,av} = \frac{l_{cab,1}}{\tau_{bi,av}} \quad [\text{ms}^{-1}] \quad \text{for } z \geq 0. \quad (5.22)$$

In a similar way,  $v_{bi,av}$  for  $z < 0$  is equal to  $l_{cab,2}/\tau_{bi,av}$ .

### 5.4.5 Arbitrary $\dot{B}_\perp$ -distributions

Due to the discrete nature of the cable, any distribution of  $\dot{B}_\perp$  along the cable length can be modelled by a multi-step function, the value of which varies at each band (with a length of  $L_{p,s}/N_s$ ) of the cable. Hence, there is a total of  $N_B = l_{cab} N_s / L_{p,s}$  steps, where  $z=0$  corresponds to the end of the cable (i.e.  $l_{cab,1}=0$  and  $l_{cab,2}=l_{cab}$ ). The multi-step function can be replaced by  $N_B$  single-step functions as long as the set of equations is completely linear, that is as long as  $\rho_s$  is independent of the current through the strand. The steady-state distribution of the BICCs can then be calculated as a summation of the BICCs of the  $N_B$  single-step functions, each with a field variation  $\Delta \dot{B}_{\perp,m}$ . According to eq. 5.4, the BICC in strand number  $i$  for regime A can be written as:



$$I_{bi,i}(z) = \sum_{m=0}^{N_B-1} I_{bi,0,m} \sin(2\pi(i-0.5+m)/N_s) e^{-|z-mL_{p,s}/N_s|/\xi} \quad [\text{A}], \quad (5.23)$$

with (see eq. 5.5):

$$I_{bi,0,m} = 0.88 \frac{w\xi}{R_c} (1 - e^{-N_s/9.6}) \Delta \dot{B}_{\perp,m} \quad [\text{A}]. \quad (5.24)$$

A similar expression can be derived for regime B by combining eqs. 5.9-5.11. An illustration is given in Fig. 5.18 for an 8-strand cable subject to a linear increase in  $\dot{B}_{\perp}$  over a length  $l_t = 5L_{p,s}/8$ . Only the single-step functions for which  $\Delta \dot{B}_{\perp,m} \neq 0$  are shown.

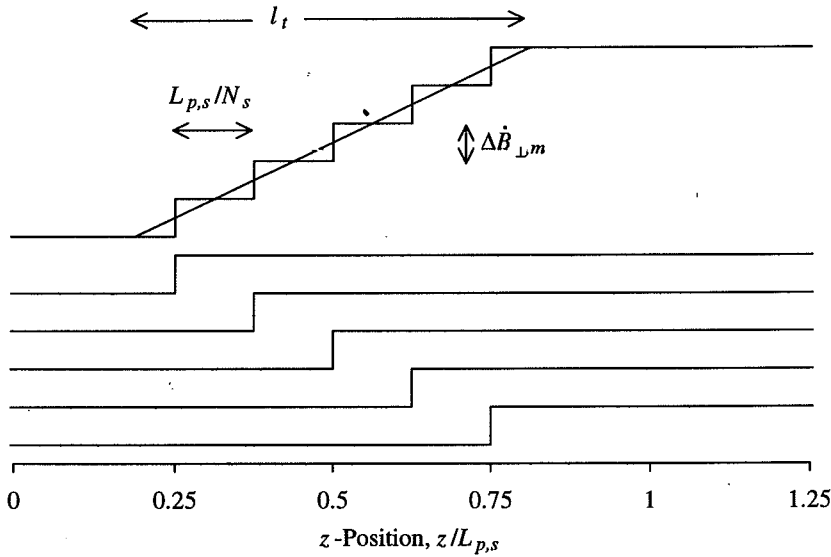


**Figure 5.18.** Representation of a linear increase in  $\dot{B}_{\perp}$  by a multi-step function and consecutively by five single-step functions, shifted in the  $z$ -direction by a distance of one band length ( $=L_{p,s}/N_s$ ).

Assuming  $l_t \ll l_{cab}$  and  $\xi \ll l_{cab}$  it can be easily seen that for regime A:

- The BICCs are maximum if the  $\dot{B}_{\perp}$ -transition happens in a single step, since the summation in eq. 5.23 can never be larger than  $I_{bi,0}$  as defined by eq. 5.5. The largest magnitude of the BICCs for an arbitrary  $\dot{B}_{\perp}$ -variation is therefore directly given by eq. 5.5.
- The magnitudes of the BICCs depend on the length  $l_t$ . Minima are present for  $l_t = k \cdot L_{p,s}$  with  $k=1, 2, 3, \dots$  and will be almost zero if  $\xi \gg l_t$ . Maxima are present for  $l_t = (k+0.5) \cdot L_{p,s}$  with  $k=0, 1, 2, \dots$  and decrease with increasing  $k$ .

Also the coupling power loss will have minima and maxima since the power is linear to the square of the coupling currents. The same conclusions hold for regime B, where the minima will be almost zero if  $l_{cab,eff} \gg l_t$ .

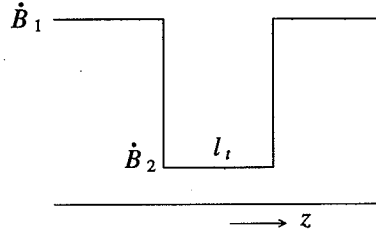
It has been shown in section 5.1 that two types of  $\dot{B}_\perp$ -variations can be distinguished in a magnet:

- strong variations where  $|\Delta \dot{B}_\perp / \Delta z|$  is of the same order as  $|\dot{B}_{\perp, \max} / L_{p,s}|$ ,
- weak variations where  $|\Delta \dot{B}_\perp / \Delta z|$  is much smaller than  $|\dot{B}_{\perp, \max} / L_{p,s}|$ .

According to eq. 5.24, an important conclusion is that the BICCs caused by strong variations are usually much larger than the BICCs caused by weak variations.

In a similar way it can be shown that a  $\dot{B}_\perp$ -dip over a width  $l_t$ , i.e.:

- $\dot{B}_\perp = \dot{B}_1$  for  $z < 0$ ,
- $\dot{B}_\perp = \dot{B}_2$  for  $z > 0$  and  $z < l_t$ ,
- $\dot{B}_\perp = \dot{B}_1$  for  $z > l_t$ ,



will also result in a minimum of the power loss for  $l_t = k \cdot L_{p,s}$  with  $k=1, 2, 3, \dots$  and a maximum for  $l_t = (k+0.5) \cdot L_{p,s}$  with  $k=0, 1, 2, \dots$

## 5.5 Cables that are partially exposed to $\dot{B}_\perp$

In the previous sections it is shown that BICCs are present in a cable which is exposed to a varying  $\dot{B}_\perp$  in the  $z$ -direction. The magnitude of the BICCs varies along the length due to currents through  $R_c$ , which results in an additional loss, also in those parts of the cable where  $\dot{B}_\perp$  is equal to 0. The enhancement of the ISCL due to BICCs is dealt with in this section for a cable with length  $l_{cab}$  which is locally subjected to  $\dot{B}_\perp$  over a length  $l_a$  (see Fig. 5.19) centred along the cable.

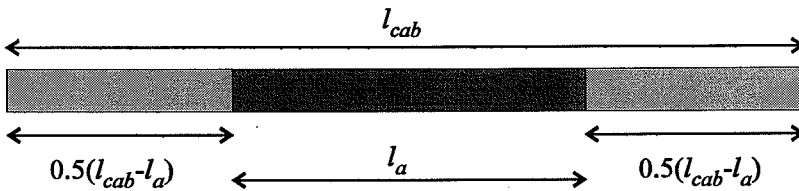


Figure 5.19. Illustration of a cable with length  $l_{cab}$  that is exposed to a varying magnetic field  $\dot{B}_\perp$  over a length  $l_a$  located in the axial centre of the cable.

The typical enhancement of the ISCL in the case of a very small strand resistivity (regime B) is investigated as a function of:

- the length  $l_a$  for a constant cable length  $l_{cab} = 2$  m (case I, see Fig. 5.20),
  - the cable length  $l_{cab}$  for a constant length  $l_a = 2.5 L_{p,s}$  (case II, see Fig. 5.21),
- with  $N_s = 16$ ,  $L_{p,s} = 0.1$  m,  $w = 8$  mm,  $R_a = 100 \mu\Omega$ ,  $R_c = 1 \mu\Omega$ ,  $\rho_s = 2.5 \cdot 10^{-18} \Omega m$ ,  $\dot{B}_\perp = 0.01$  Ts<sup>-1</sup>.

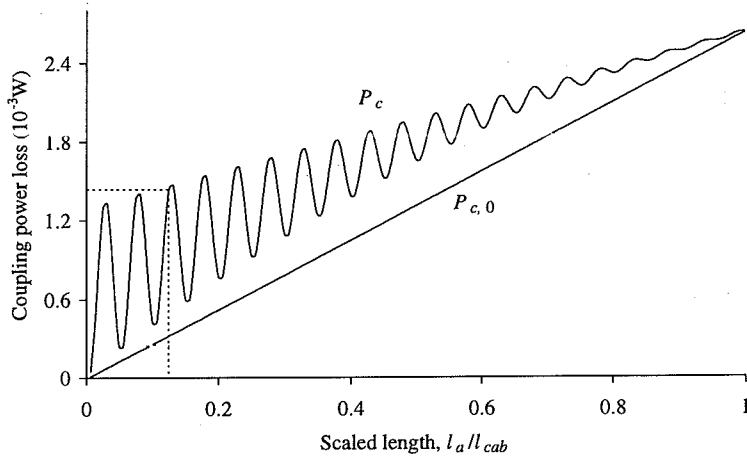


Figure 5.20. The coupling power loss in a cable with length  $l_{cab}=2$  m exposed to a locally applied  $\hat{B}_\perp$  of length  $0 < l_a < 2$  m. The dotted line shows the power loss for  $l_a=0.25$  m and corresponds to the value as given in Fig. 5.21.

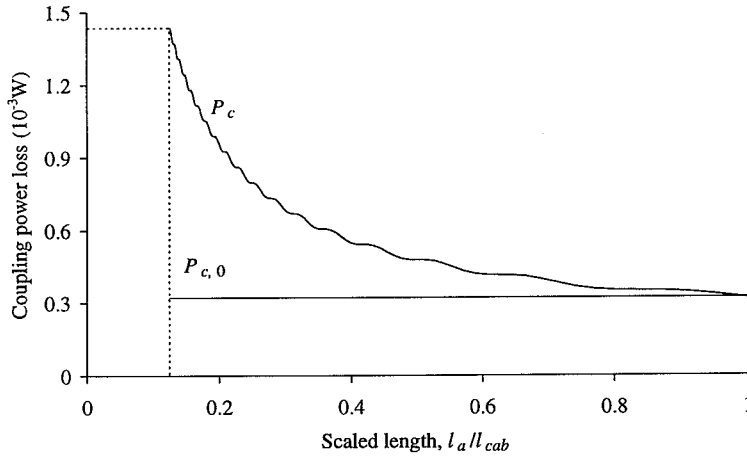


Figure 5.21. The coupling power loss in a cable with length  $l_{cab}$  exposed to a locally applied  $\hat{B}_\perp$  of length  $l_a=0.25$  m. The cable length is varied between 0.25 m and 2 m. The dotted line shows the value for  $l_{cab}=2$  m and corresponds to the value as given in Fig. 5.20.

The power loss  $P_{c,0}$  is equal to the power loss if no BICCs are present and is calculated using eq. 4.17, multiplied by  $l_a$ . The dotted lines in both figures correspond to the same case namely  $l_a=0.25$  m  $= 2.5L_{p,s}$  and  $l_{cab}=2$  m  $= 20L_{p,s}$ .

The maxima in the power loss of Fig. 5.20 correspond to  $l_a=(k+0.5)L_{p,s}$  (see also section 5.4.5). The ISCL at the minima ( $l_a=kL_{p,s}$ ) is larger than  $P_{c,0}$  since the BICCs of the two  $\hat{B}_\perp$ -steps do not completely cancel due to the longitudinal decrease of the BICCs. The total loss in the cable increases significantly, especially for small  $l_a$  compared to  $l_{cab}$ .

The maxima will be less pronounced if the characteristic length of the BICCs is much smaller than  $l_{cab}$  (regime A).

The relative increase of the ISCL,  $P_c/P_{c,0}$ , for case I varies between two limits as can be seen in Fig. 5.20. The upper limit is given by the maxima in  $P_c$ , i.e. at  $l_a = (k+0.5)L_{p,s}$  whereas the lower limit corresponds to  $l_a = k \cdot L_{p,s}$ . The relative increase of the ISCL for case II gradually decreases for increasing ratio  $l_a/l_{cab}$ . The scaled ISCL is depicted in both cases in Fig. 5.22.

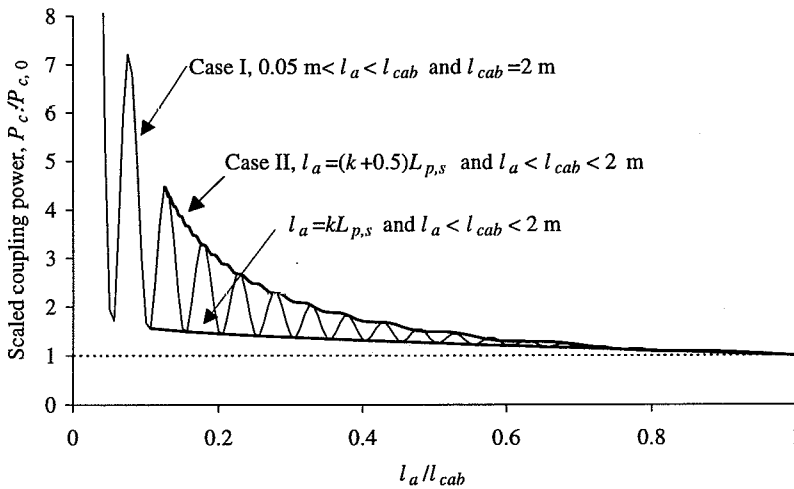


**Figure 5.22.** The relative enhancement of the ISCL in a cable that is locally exposed to  $\vec{B}_\perp$  over a length  $l_a$ . Case I:  $l_{cab} = 2$  m,  $0.05l_{cab} < l_a < l_{cab}$ . Case II:  $l_a = 2.5L_{p,s} = 0.25$  m,  $l_a < l_{cab} < 2$  m. The lower bold line shows also the case  $l_a = 2L_{p,s} = 0.2$  m,  $l_a < l_{cab} < 2$  m.

An important conclusion is that a loss measurement on a cable with  $l_a < l_{cab}$  will not result in a representative ISCL, and hence  $R_c$ . The enhancement of the ISCL depends on the ratio between  $l_a$  and  $l_{cab}$  and on the magnitude of the BICCs. The difference will be negligible if the strand resistivity is large so that  $\xi < l_a$ . To determine the representative loss of a long cable, the loss that is locally dissipated at the cable part of length  $l_a$  has to be measured by means of magnetisation or calorimetric measurements where the pick-up coils and the bell jar (which collects the evaporated helium) respectively cover only the length  $l_a$  of the cable.

In a dipole magnet the increase in the ISCL due to the BICCs cannot be calculated using the above figures since the  $\vec{B}_\perp$ -distribution is very complicated. However, a simple analysis shows that the increase is small since the local  $\vec{B}_\perp$ -dips are relatively small compared to the cable length (see Fig. 5.1). For example, in the case of a 1 m long LHC-type dipole the ratio  $l_a/l_{cab}$  is about 0.99 for each  $\vec{B}_\perp$ -dip. The total length of the  $\vec{B}_\perp$ -dips is about 20% of the cable length and thus  $l_a/l_{cab} = 0.8$ . According to Fig. 5.22 the enhancement of the ISCL will then be about 10% maximum, but will be smaller in practical coils since the BICCs generated by the various  $\vec{B}_\perp$ -dips will partially cancel. Calculations with the network model in which the whole  $\vec{B}_\perp$ -distribution is incorporated shows that the increase is smaller than 5% and 1% for dipole magnets with lengths of 1 m and 10 m respectively.

## 5.6 $\dot{B}_\perp$ -steps with $R_c \gg R_a$

It is shown in section 5.4 that the magnitude of the BICCs can be reduced by increasing  $R_c$  where it is assumed that  $R_a \gg R_c$ . However, for large  $R_c$  (for example by placing a resistive barrier between the two layers of the cable) some BICCs are still generated due to the presence of the adjacent resistances  $R_a$ . The following relations describe the characteristic length and magnitude for regimes A and B deduced from numerical simulations and are valid for  $8 \leq N_s \leq 40$ . The errors are about 10% for all the fitting constants.

### Regime A.

Eq. 5.4 describes the  $z$ -dependence of the BICCs with the following new expressions for  $I_{bi,0}$  and  $\xi$ :

$$I_{bi,0} = 0.45 \frac{wL_{p,s}}{N_s \sqrt{R_a R_s} N_s} \Delta \dot{B}_\perp \quad [\text{A}], \quad (5.25)$$

and:

$$\xi = 0.058 \sqrt{\frac{R_a}{R_s}} N_s^{0.13} \quad [\text{m}]. \quad (5.26)$$

Note that these relations are qualitatively quite different from eqs. 5.5 and 5.7 since  $R_a$  and  $R_c$  have, of course, a very different effect on the current distribution in the cable. Combining eqs. 5.5, 5.7 and 5.25 shows that the magnitude  $I_{bi,0}$  if  $R_c \ll R_a$  is a factor  $F$  larger than the magnitude if  $R_c \gg R_a$  with:

$$F = 1.0 \sqrt{\frac{R_a N_s}{R_c}} (1 - e^{-N_s/9.6}) \approx \sqrt{\frac{R_a N_s}{R_c}} \quad \text{for large } N_s. \quad (5.27)$$

### Regime B.

Eq. 5.9 describes the  $z$ -dependence of the linearly decaying BICCs with:

$$I_{bi,0} = 2.2 \frac{w l_{cab,eff}}{R_a N_s} \Delta \dot{B}_\perp \quad [\text{A}]. \quad (5.28)$$

The factor  $F$  as defined above is equal to (combining eqs. 5.10 and 5.28):

$$F = 0.46 \frac{R_a N_s (1 - e^{-N_s/9.6})}{R_c}. \quad (5.29)$$

The two values of  $F$  clearly show that a resistive barrier between the two layers of the cable strongly reduces the BICCs, especially for cables with a large number of strands. Assume, for example, a 30-strand cable with  $R_a = 10 \mu\Omega$ ,  $R_c = 1 \mu\Omega$ . Inserting a resistive barrier and soldering the cable could result in  $R_a = 1 \mu\Omega$  and  $R_c \gg R_a$ . The magnitude of the BICCs will then decrease by a factor  $F = 5.5$  (regime A) to 14 (regime B).

A local decrease in  $R_c$  (for example in a cable-to-cable connection) does not change the magnitude of the BICCs significantly (for a characteristic case of  $R_a=1\ \mu\Omega$  and  $R_c=100\ \mu\Omega$  and  $0.5\ \mu\Omega$  in the connection).

## 5.7 Non-uniform $R_c$ -distributions

In accelerator magnets  $R_c$  is likely to change across the cable width due to the keystone angle and the gradient in the transverse stress. This variation, however, does not generate BICCs as long as the variation is constant along the cable length. Longitudinal  $R_c$ -variations can be present along the whole cable of a pole, in the soldered connections, in local 'shorts' between strands and in the coil ends (see also section 5.1).

Each longitudinal variation in  $R_c$  generates BICCs with a characteristic length, a characteristic time, a propagation velocity and a magnitude in a similar way to that with a non-uniform  $\dot{B}_\perp$ .

The magnitude of the BICCs is investigated for a cable with a change in  $R_c$  along the cable length from  $R_{c,1}=R_{c,1}$  for  $z<0$  to  $R_{c,2}=R_{c,2}$  for  $z\geq 0$ . Fig. 5.23 shows the current in the strand at position 1 (see Fig. 5.5) along the length of the cable for  $R_{c,1}=1.5\ \mu\Omega$  and  $R_{c,2}=0.5\ \mu\Omega$  ( $N_s=16$ ,  $d_s=1.3\ \text{mm}$ ,  $I_{tr,str}=0\ \text{A}$ ,  $\rho_s=2\cdot 10^{-14}\ \Omega\text{m}$ ,  $\dot{B}_\perp=0.01\ \text{T s}^{-1}$ ).

Note the similarity of the current pattern compared to Fig. 5.8. The average strand currents at the edge are about  $-4.5\ \text{A}$  for  $z<0$  and  $-13.5\ \text{A}$  for  $z\geq 0$  and correspond to the ISCCs for a cable without longitudinal variations. Just as in the case of a step in  $\dot{B}_\perp$ , the BICCs can be regarded as currents that are maximum close to the  $R_c$  non-uniformity and decay quasi-exponentially (regime A) or quasi-linearly (regime B) towards 0.

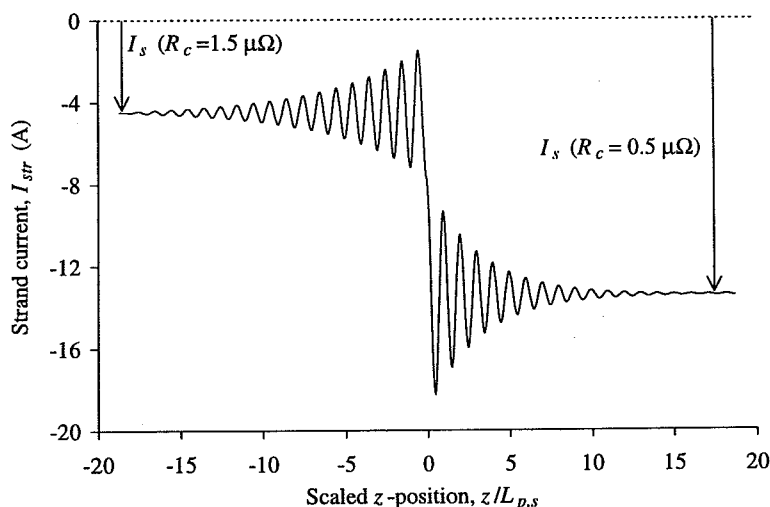


**Figure 5.23.** The characteristic pattern of the strand current at position 1 of a cable with a change in  $R_c$  from  $R_{c,1}=1.5\ \mu\Omega$  for  $z<0$  to  $R_{c,2}=0.5\ \mu\Omega$  for  $z\geq 0$ . The cable is subject to a field change of  $0.01\ \text{T s}^{-1}$  (Regime A:  $\rho_s=2\cdot 10^{-14}\ \Omega\text{m}$ ).

**Regime A.**

The characteristic length is different for  $z < 0$  and  $z \geq 0$ . The two characteristic lengths  $\xi_1$  and  $\xi_2$  are given by eq. 5.7 where  $R_c$  should be replaced by  $R_{c,1}$  and  $R_{c,2}$  respectively. For  $8 \leq N_s \leq 40$ , the decay of the BICCs along the length is given by eq. 5.4 with  $\xi = \xi_1$  for  $z < 0$  and  $\xi = \xi_2$  for  $z \geq 0$  and:

$$I_{bi,0} = 1.1 \frac{wN_s}{R_{c,eff}} \xi_{eff} \sqrt{\frac{R_s}{R_{c,i}}} (1 - e^{-N_s/9.6}) \dot{B}_\perp \quad [\text{A}], \quad (5.30)$$

with  $R_{c,i} = R_{c,1}$  for  $z < 0$  and  $R_{c,i} = R_{c,2}$  for  $z \geq 0$ ,

$$\frac{1}{R_{c,eff}} = \left| \frac{1}{R_{c,1}} - \frac{1}{R_{c,2}} \right| \quad [\Omega^{-1}], \quad (5.31)$$

and:

$$\xi_{eff} = \frac{\xi_1 \xi_2}{\xi_1 + \xi_2} \quad [\text{m}]. \quad (5.32)$$

The error in the fitting constant 1.1 is smaller than 10%.

**Regime B.**

The more complicated relations of  $I_{b,0}$  for regime B are disregarded here as well as the expressions for  $\tau_{bi,av}$  and  $v_{bi,av}$  for the two regimes.

BICCs due to a longitudinal  $R_c$ -variation are only generated if, at the place of the  $R_c$ -variation, the cable is exposed to a varying field  $\dot{B}_\perp$ . This implies that the  $R_c$ -variations in the splices and near the coil ends result in BICCs that are much larger than the BICCs caused by  $R_c$ -variations in the pole-to-pole connections and the connections between the cable and the current lead (which are located outside the high-field region of the coil).

In section 5.4.5 it is shown that an arbitrary  $\dot{B}_\perp$ -variation can be regarded as a finite summation of  $\dot{B}_\perp$ -steps. In a similar way the BICCs for an arbitrary  $R_c$ -distribution can be calculated by a summation of steps in  $\xi_{eff}/R_{c,eff}$ . Random distributions of  $R_c$  will not lead to considerable BICCs since the BICCs produced by all the small steps will mainly cancel. Cable sections where the average  $R_c$  is likely to differ, such as the coil ends and the splices, can be well simulated by two  $R_c$ -steps.

The magnitude of the BICCs provoked by an  $R_c$ -step and a  $\dot{B}_\perp$ -step is investigated by means of the characteristic case of the coil ends of a dipole magnet. This clarifies whether  $R_c$ - or  $\dot{B}_\perp$ -variations are the dominant source of BICCs. In the coil ends, the  $\dot{B}_\perp$ -variation is large since the cable bends around the beam pipe, and  $R_c$  is probably large since the strands are in weak contact. Here the  $\dot{B}_\perp$ - and the  $R_c$ -variations are assumed to be step-like.

The following parameters are taken for the characteristic case of a PBD magnet as specified in Table 2.1:  $N_s=26$ ,  $w=0.017$  m,  $L_{p,s}=0.1$  m,  $d_s=1.3$  mm,  $\Delta \dot{B}_\perp = \dot{B}_\perp$  (see Fig. 5.1). The resistance  $R_{c,end}$  in the ends is assumed to be much larger than the resistance  $R_c$  in the straight part so that  $R_{c,eff}=R_c$ . Combining eqs. 5.5 and 5.30, the ratio  $F$  between  $I_{bi,0}$  in the case of a  $\dot{B}_\perp$ -step and an  $R_c$ -step is approximately:

$$F = \frac{I_{bi,0}^{\dot{B}\text{-step}}}{I_{bi,0}^{R_c\text{-step}}} = \frac{8 \cdot 10^{-7}}{\sqrt{\rho_s}}, \quad (5.33)$$

which is much larger than 1 provided that  $\rho_s$  is smaller than  $10^{-14}$   $\Omega\text{m}$ .

In section 7.7.5 the effective strand resistivity is estimated to be smaller than a few times  $10^{-14}$   $\Omega\text{m}$ . An important conclusion is, therefore, that the BICCs in superconducting coils are mainly caused by  $\dot{B}_\perp$ -variations whereas  $R_c$ -variations only have a minor effect.

## 5.8 Experimental observation of BICCs in a 1.3 m long cable

### 5.8.1 Introduction

In sections 5.4.1-5.4.5 expressions are given for the characteristic lengths and magnitudes of BICCs in a straight cable. The formulas are derived for single  $\dot{B}_\perp$ - and  $R_c$ -steps and it is shown how more complex  $\dot{B}_\perp$ - and  $R_c$ -distributions can be dealt with. The major problem in estimating the BICCs in a coil is related to the partial cancelling of the BICCs produced by the numerous non-uniformities. Also the unknown effective strand resistivity prevents a good quantitative estimate of the BICCs. The characterisation of BICCs in magnets, by means of measurements of the magnetic field in the aperture of a magnet (see chapter 7), can therefore hardly be used to validate the formulas as derived in the previous sections.

In order to prove the existence of BICCs and to validate the formulas a new experimental set-up has been designed and constructed by which several parameters that affect the characteristics of the BICCs can be varied independently. It is based upon the measurement of the magnetic field, caused by the BICCs, along the length of a single straight cable. The cable can be locally subjected to a  $\dot{B}_\perp$ -variation and the  $R_c$  of the cable can be spatially changed. A description of the set-up and the features that can be implemented are given in section 5.8.2.

A discussion of the experimental results is presented in section 5.8.3. The field caused by the BICCs, the characteristic time, the propagation velocity and the decay pattern are analysed as a function of the field-sweep rate for several  $R_c$ -distributions. The results are compared to the numerically calculated formulas in order to validate the network model for modelling BICCs. The main purpose is to obtain a good qualitative agreement between the measurements and the calculations, whereas a good quantitative agreement is probably not possible since the exact spatial distribution of  $R_c$  is not well-known.



### 5.8.2 Experimental set-up

The test set-up has been designed in such a way that the characteristics of the BICCs, i.e.:

- the magnitude,
- the characteristic time,
- the propagation velocity,
- the decay along the length,

can be investigated for various spatial distributions of  $R_c$  and  $\dot{B}_\perp$ .

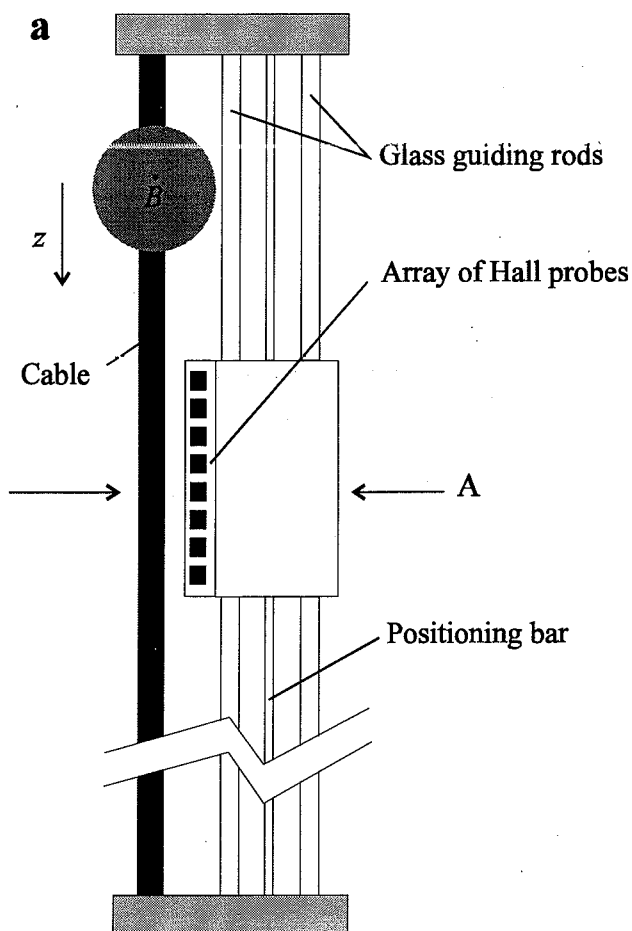
The schematic front view and cross-section are shown in Fig. 5.24. The set-up is installed vertically in a cryostat and immersed in liquid helium at 4.2 K. A keystoneed Rutherford-type cable (cable I-1, see Table 2.4) with a length of 1.3 m (which corresponds to  $10L_{p,s}$ ) is clamped over a length of 1.1 m ( $=8.5L_{p,s}$ ) between two pressure bars. A transverse pressure on the cable of 15 MPa maximum can be applied by means of 30 bolts. The  $R_c$ -value can therefore be easily varied along the cable length. The strands in the two end sections of the cable, with a length of 10 cm, are in loose contact but can be soldered together to simulate the influence of the joint resistances on the characteristics of the BICCs.

A stainless-steel heater is fixed on the large faces of the cable in order to drive the cable from the superconducting into the normal state. The heater is electrically insulated from the pressure bar and the cable.

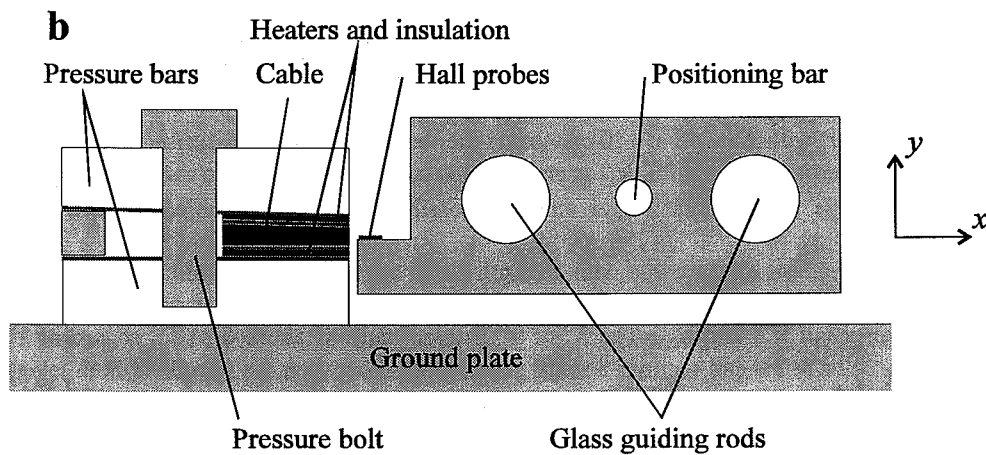
The field in the y-direction is determined by an array of eight Hall probes, each having an active area of about  $1 \text{ mm}^2$ . The centre of the probes is located at a distance of 2 mm from the narrow side of the cable. The probes are fixed on a small sledge which can move in the longitudinal direction over two glass guiding rods. The z-position of the sledge can be adjusted from outside the cryostat by means of a positioning bar with an accuracy better than 0.2 mm.

Two strands of the cable are connected to a current supply in order to calibrate the Hall probes. Furthermore, it can be investigated whether the BICCs are affected by an additional transport current in one of the strands.

A transverse field of 1.4 T maximum can be applied by means of a set of superconducting coils, located on both sides of the cable. The centre of the magnet is located at  $z=0$ . The cable lengths on either side of the magnet centre are 19 cm ( $=1.4L_{p,s}$ ) and 111 cm ( $=8.5L_{p,s}$ ). The  $\dot{B}_\perp$ -distribution along the cable caused by the set of coils when ramped from 0 to 1.4 T in 10 s is shown in Fig. 5.25. In the following the  $\dot{B}_\perp$ -value refers to the maximum field-sweep rate at  $z=0$ .



**Figure 5.24.**  
**a.** Front view of the set-up.  
**b.** Cross-section of the set-up at A (see a.).



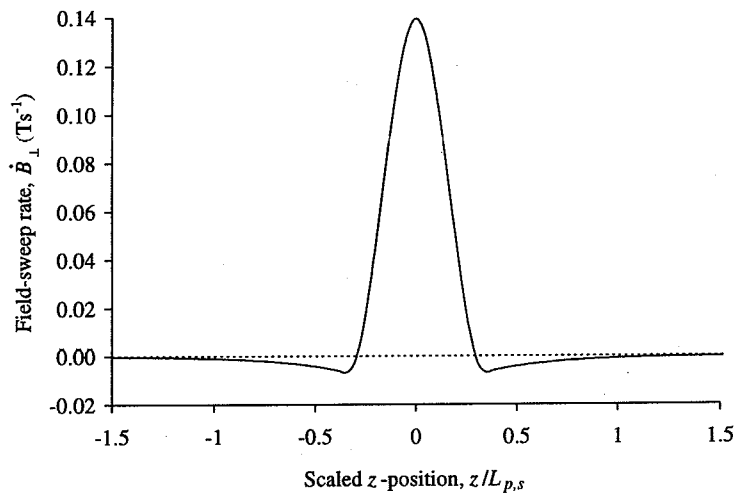


Figure 5.25. The applied field change  $\dot{B}_1$  at the centre of the cable ( $x=w/2$ , see Fig. 4.1) along the cable length, for a field sweep of the set of coils from 0 to 1.4 T in 10 s.

The distribution of the contact resistance over the cable length can be, in first approximation, represented by five regions with contact resistances  $R_{c,1}$  to  $R_{c,5}$  (see Fig. 5.26). The contact resistance  $R_a$  is assumed to be larger than  $R_c$  and will be disregarded.

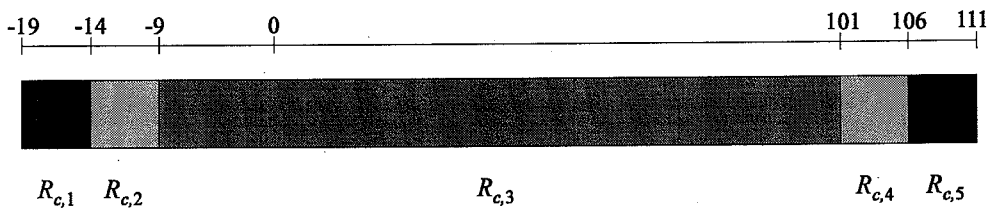


Figure 5.26. Approximation of the distribution of the cross-contact resistance along the cable length by means of five regions with different  $R_c$ . The z-position (in cm) is shown at the top.

The central part with a length of 110 cm covers the section which is pressurised at about 10-15 MPa. According to Fig. 4.29,  $R_{c,3}$  is about 10-20  $\mu\Omega$ . However, due to the steep slope of the  $R_c$ - $P_1$  curve a significant larger value is possible for sections subject to a smaller pressure.

The end sections of the cable with a length of 10 cm have almost infinite  $R_c$  since the strands are in very poor contact with each other. Half of the end sections can be soldered, resulting in small  $R_{c,1}$  and  $R_{c,5}$ . The  $R_c$  of a soldered cable is about 0.3  $\mu\Omega$ , according to Fig. 4.29. Since in the end sections a small gap is present between the strands of both layers of the cable,  $R_c$  is estimated to be a few times larger.

### 5.8.3 Results and discussion

The magnitude of the steady-state BICCs for the given  $\dot{B}_\perp$ - and  $R_c$ -distributions are calculated by means of the network model. The simulations are performed for a cable with the same geometry and number of strands as the measured cable. The field caused by the BICCs is calculated using the approach as discussed in section 7.2. Calculations of the characteristic time and the propagation velocity for this cable with its specific  $\dot{B}_\perp$ - and  $R_c$ -variations are not performed. First estimates of the characteristic time and propagation velocity are made using the formulas given in sections 5.4.3 and 5.4.4 and are compared to the measured values.

The field  $B_{bi}$ , produced by the BICCs, and the characteristic time are determined as a function of the  $z$ -position in the range  $0.5L_{p,s} < z < 7.5L_{p,s}$ . Measurements are performed for three different  $R_c$ -distributions along the cable length (see Fig. 5.26):

- I: a cable with unsoldered ends, i.e.  $R_{c,1}$ ,  $R_{c,2}$ ,  $R_{c,4}$  and  $R_{c,5}$  are much larger than  $R_{c,3}$ ,
- II: a cable with one soldered end, i.e.  $R_{c,1}$  is about  $1 \mu\Omega$ , whereas the other  $R_c$ -values remain unchanged,
- III: a cable with two soldered ends, i.e.  $R_{c,1}$  and  $R_{c,5}$  are about  $1 \mu\Omega$ , whereas the other  $R_c$ -values remain unchanged.

The field measured by the Hall probes consists of:

- the stray field of the magnet,
- the field  $B_{is}$  produced by the ISCCs,
- the field  $B_{if}$  produced by the IFCCs,
- the field  $B_{bi}$  produced by the BICCs, and
- the field  $B_m$  due to the filament magnetisation caused by the stray field of the magnet and by the field produced by all the coupling currents.

Field  $B_{bi}$  can be quite easily distinguished from the other field contributions, because:

- the magnitudes of fields  $B_{is}$  and  $B_{if}$  are negligible compared to the magnitude of the field  $B_{bi}$ ,
- the stray field and the magnetisation due to the stray field can be determined using a very small field-sweep rate,
- the magnetisation due to the coupling currents is relatively small compared to the amplitude of field  $B_{bi}$  itself.

The characteristic fields  $B_{bi}$  as measured with the Hall probes are shown in Fig. 5.27 at a field sweep from 0 to 1.4 T with  $0.019 \text{ Ts}^{-1}$  for case II (a cable with one soldered end). The figure shows clearly that the fields  $B_{bi}$  approach their steady-state values during the ramp and decay with a characteristic time of about 10 s as soon as the the field-sweep is finished.

Since the characteristic times during and after the field sweep are equal, it can be concluded that the BICCs are not significantly affected by the dynamic resistivity of the strand, which is proportional to  $\dot{B}_\perp$  (see eq. 5.3). Measurements at various field-sweep rates prove that the steady-state fields (and hence the BICCs) are proportional to  $\dot{B}_\perp$  whereas the characteristic time is independent of  $\dot{B}_\perp$ . Both results agree with the calculations (see eqs. 5.5, 5.10, 5.13 and 5.14).

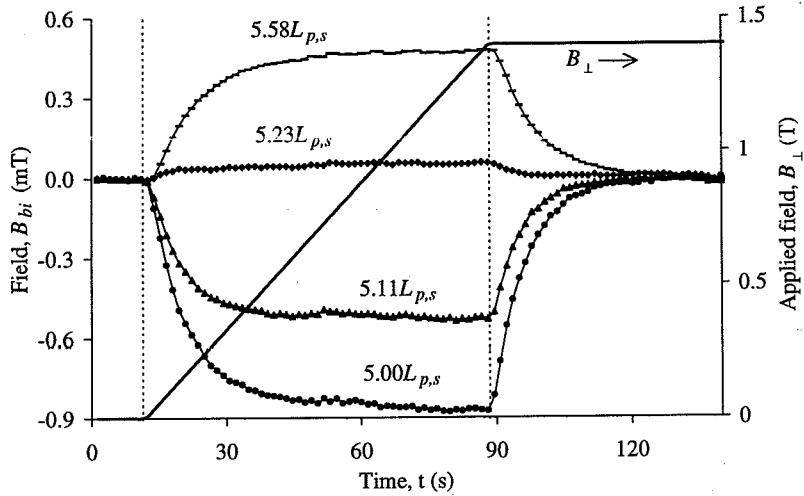


**Figure 5.27.** Field  $B_{bt}$  measured simultaneously by four Hall probes during and after a field sweep from 0 to 1.4 T (see the straight line) with  $\dot{B}_\perp = 0.019 \text{ Ts}^{-1}$ . The labels indicate the  $z$ -position of the Hall probe. The dotted lines show the start and the end of the field sweep.

The steady-state  $B_{bt}$ -values are measured along the cable for  $0.5L_{p,s} < z < 7.5L_{p,s}$  and depicted in Fig. 5.28 for case I with  $\dot{B}_\perp = 0.068 \text{ Ts}^{-1}$ . The continuous line corresponds to the calculated field using the network model with a finite and constant resistance  $R_{c,3}$ , infinite resistances  $R_{c,1}$ ,  $R_{c,2}$ ,  $R_{c,4}$ ,  $R_{c,5}$  and a very small strand resistivity, so that the BICCs can be classified in regime B (see section 5.4.1).

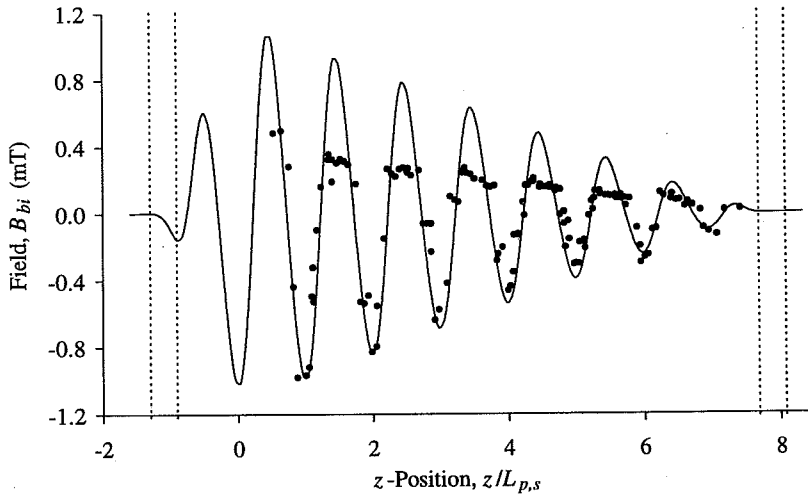


**Figure 5.28.** Field  $B_{bt}$  as a function of the  $z$ -position for case I with  $\dot{B}_\perp = 0.068 \text{ Ts}^{-1}$ . The dotted lines show the boundaries between the sections with different  $R_c$  (see Fig. 5.26). The continuous line corresponds to the calculated field using the network model.

The magnitude of the quasi-sinusoidally varying field, which depends in this case only on  $R_{c,3}$ , corresponds to the measured field assuming  $R_{c,3}=100\ \mu\Omega$ . This value is large compared to the expected value of  $10\text{--}20\ \mu\Omega$ , which could be caused by an overall decrease in the pressure on the cable (see Fig. 4.29), due to different shrinkage of the pressure bolts, the cable, the heaters and the insulation (see Fig. 5.24b) during cool-down. An increase in  $R_c$  near  $z=0$  also results in significantly smaller BICCs even if  $R_c$  in the rest of the cable is much smaller.

The shape of the curve (with period  $L_{p,s}$ ) does not depend on  $R_{c,3}$  and corresponds very well with the measured one. Both the calculated curve and the measured points decay linearly to 0 at the end of the cable which prove that also the BICCs decay linearly to 0 (see also Fig. 5.9 as a comparison). The flattening in the maxima of the measured field is caused by one or a few strands that carry slightly smaller BICCs than expected. This is probably due to local variations in  $R_c$ , especially at  $z<0$ . Another possibility is that the surfaces of one or a few strands are more oxidised than the others or that some strands have a large effective strand resistivity. The linear decay imposes a certain maximum limit to the effective strand resistivity  $\rho_s$ . According to eq. 5.8,  $\rho_s$  should be smaller than a few times  $10^{-13}\ \Omega\text{m}$ . If it is larger, the characteristic length is smaller than 1 m which would result in a quasi-exponential decay.

Fig. 5.29 shows the characteristic time  $\tau_{bi}(z)$  of the BICCs as a function of the  $z$ -position, determined from the decay of the field after a ramp from 1.4 T to 0 with  $\dot{B}_\perp=-0.068\ \text{Ts}^{-1}$ . The time  $\tau_{bi}$  at position  $z$  is taken as the period during which the field  $B_{bi}$  at position  $z$  has decayed to  $1/e$  of its steady-state value. The characteristic times are calculated for those positions which correspond to the maxima and minima in the field  $B_{bi}$  of Fig. 5.28.

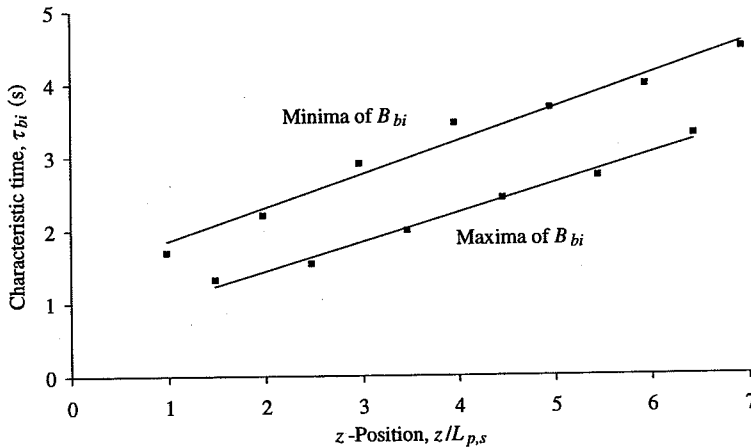


**Figure 5.29.** The characteristic time of the BICCs as a function of the  $z$ -position determined after a field sweep from 1.4 T to 0 with  $\dot{B}_\perp=-0.068\ \text{Ts}^{-1}$ . The  $\tau_{bi}$ -values are determined at those positions which correspond to the maxima and minima in  $B_{bi}$  of Fig. 5.28. The lines are linear fits.

Both curves are almost parallel, showing that the propagation velocity (see section 5.4.4) is more or less constant. The average time constant is slightly larger in the minima than in the maxima. This difference is directly related to the flattening in the curves of Fig. 5.28, since a flattening implies a larger series resistance in the BICC loop and hence a decrease of the characteristic time (see eq. 5.14).

It is interesting to investigate whether the formulas given in sections 5.4.3 and 5.4.4, which are valid in the case of a single  $\dot{B}_\perp$ -step, can also be applied to estimate the average characteristic time  $\tau_{bi,av}$  and propagation velocity  $v_{bi,av}$  for this cable exposed to the  $\dot{B}_\perp$ -distribution as shown in Fig. 5.25.

- The average time constant can be calculated using eq. 5.14 taking  $R_c=100\ \mu\Omega$ ,  $l_{cab,1}=0.09\text{ m}$ ,  $l_{cab,2}=1.01\text{ m}$ ,  $N_s=26$  and  $L_{p,s}=0.13\text{ m}$ , which results in  $\tau_{bi,av}=0.3\text{ s}$ . The estimated characteristic time is about a factor 7 smaller than the measured one (see Fig. 5.29 at about  $z=3L_{p,s}$ ).
- The average propagation velocity for  $z \geq 0$  is estimated using eq. 5.21, which results in  $v_{bi,av}=1.7 \cdot 10^7 L_{p,s} R_c / (N_s^2 l_{cab,2}) = 0.3\text{ ms}^{-1}$ . This value corresponds exactly to the experimentally obtained  $v_{bi,av}$  as deduced from the average slope of Fig. 5.29:  $v_{bi,av} = \Delta z / \Delta \tau_{bi} = 2.4 L_{p,s} \text{ s}^{-1} = 0.3\text{ ms}^{-1}$ .

It can be concluded that the observed phenomena, i.e.:

- the *linear* decrease of the BICCs towards the end of the cable,
  - the oscillation of  $B_{bi}$  with a *period* equal to  $L_{p,s}$ , and
  - the presence of a characteristic time which increases almost *linearly* along the cable,
- agree qualitatively very well with the calculations using the network model. Quantitative comparison of the average characteristic time and propagation velocity is difficult because the exact  $R_c$ -distribution over the length is not known and the formulas 5.14 and 5.21 are only valid for a  $\dot{B}_\perp$ -step.

In order to investigate the influence of sections with small  $R_c$  on the characteristics of BICCs, the  $R_c$ -distribution along the cable length is changed by soldering the ends of the cable with SnAg. Field  $B_{bi}$  is depicted in Figs. 5.30 and 5.31 for cases II (i.e. very small  $R_{c,1}$ ) and III (i.e. very small  $R_{c,1}$  and  $R_{c,5}$ ).

The magnitude of  $B_{bi}$  increases strongly due to the local solderings, whereas the phase remains constant, in good agreement with the result from the network model. The calculated field, using the network model, can be fitted to the measurements by assuming a very small effective strand resistivity and taking:

- $R_{c,1}=1.2\ \mu\Omega$  and  $R_{c,3}=100\ \mu\Omega$  (case II),
- $R_{c,1}=1.2\ \mu\Omega$ ,  $R_{c,3}=100\ \mu\Omega$  and  $R_{c,5}=4\ \mu\Omega$  (case III).

A simple way to estimate  $R_{c,5}$  is by considering the increase in the magnitude of the BICCs near  $z=0$  of case III compared to case II. Fig. 5.31 shows clearly that the increase is about a factor 2 (near  $z=0$ ) which implies that for  $z>0$  about half of the BICCs return through the resistances  $R_{c,3}$  and the other half through  $R_{c,5}$ . Assuming a very small  $\rho_s$ , this implies that the equivalent resistance of the parallel  $R_{c,3}$ 's is about equal to that of the parallel  $R_{c,5}$ 's. Hence,  $R_{c,3}/101 \approx R_{c,5}/5$  (see Fig. 5.26) or  $R_{c,5} \approx 5\ \mu\Omega$  which agrees well with  $R_{c,5}$  as obtained by the direct simulation using the network model.

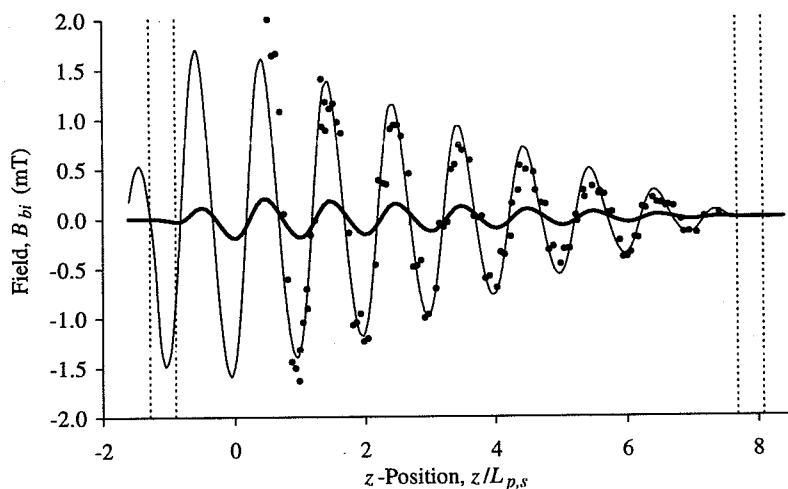


**Figure 5.30.** Field  $B_{bi}$  as a function of the  $z$ -position for case II with  $\dot{B}_\perp = 0.016 \text{ Ts}^{-1}$ . The dotted lines show the boundaries between the sections with different  $R_c$ . The continuous lines correspond to the calculated field using the network model. The bold line shows the fitted curve of case I (see Fig. 5.28) scaled to  $\dot{B}_\perp = 0.016 \text{ Ts}^{-1}$ .

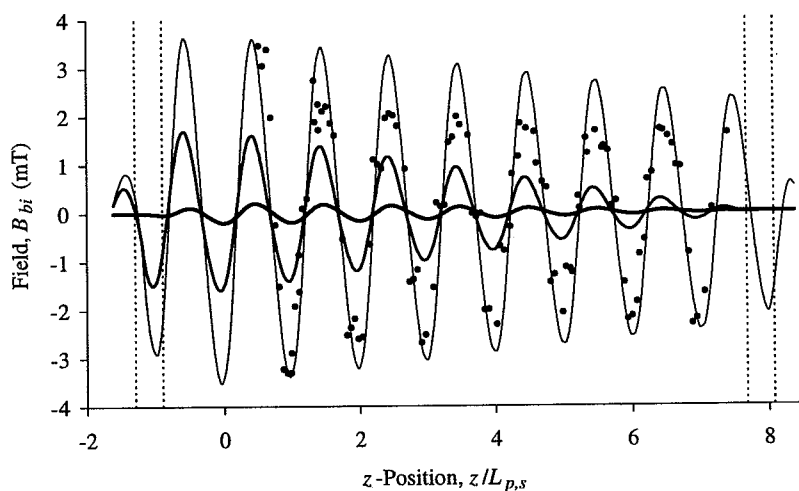


**Figure 5.31.** Field  $B_{bi}$  as a function of the  $z$ -position for case III with  $\dot{B}_\perp = 0.016 \text{ Ts}^{-1}$ . The dotted lines show the boundaries between the sections with different  $R_c$ . The continuous line corresponds to the calculated field using the network model. The bold lines correspond to cases I and II (see Figs. 5.28 and 5.30) scaled to  $\dot{B}_\perp = 0.016 \text{ Ts}^{-1}$ .

It can therefore be concluded that a local 'dip' in  $R_c$  influences the magnitude of the BICCs especially if the 'dip' is close to the  $\dot{B}_\perp$  non-uniformity and if  $R_c$  is locally much smaller than the mean  $R_c$  of the cable. Consider, for example, the cable of a dipole coil with a mean



$R_c$  equal to  $R_{c,cab}$  and a joint with length  $l_{joint}$  and  $R_c = R_{c,joint}$  located at a distance  $l_{diff}$  from the  $\dot{B}_\perp$ -variation. The joint will only significantly affect the magnitude of the BICCs (if classified in regime B) caused by the  $\dot{B}_\perp$ -variation if the distance  $l_{diff}$  is smaller than a few times  $(R_{c,cab}/R_{c,joint})l_{joint}$ .

If the BICCs are classified in regime A, the joint only affects the BICCs if the distance between the joint and the  $\dot{B}_\perp$ -variation is smaller than the characteristic length of the BICCs.

Note that the above discussion is valid for a joint located in a region with  $\dot{B}_\perp = 0$ . If, however, the joint is placed in a varying field, then additional BICCs will be induced (as discussed in section 5.7) caused by the  $R_c$ -step which is present at the boundary between the joint and the rest of the cable.

The characteristic times of cases II and III increase, compared to case I, by about a factor 4 and 10 respectively. Although no calculations are performed, the increase can be well understood by considering that the average loop length of the BICCs becomes larger while the series resistance in the loops (i.e., in first approximation, the equivalent resistance of the parallel  $R_c$ 's) becomes smaller. The propagation velocity of the BICCs remains constant for  $0.5L_{p,s} < z < 7.5L_{p,s}$ . Simulations on small cables show a similar result, where the propagation velocity at position  $z$  is mainly determined by the local  $R_c$  at position  $z$ .

The large characteristic times of up to 30 s (for case III) show that very large  $\tau_{bi,av}$ -values of the order of  $10^5$  s may occur in magnets, with  $R_c \approx 1\text{--}10 \mu\Omega$  and a cable length much larger than 1 m, if the BICCs are classified in regime B (see also Fig. 5.16). This implies that the characteristic times of about 100 s which are measured in the aperture of the LHC dipole model magnets (see sections 7.7.1-7.7.5) have to be attributed to BICCs of regime A, decaying over much smaller lengths than the actual length of the cable in the magnet.

## 5.9 Conclusions

So-called Boundary-Induced Coupling Currents (BICCs) are generated in (Rutherford-type) cables, which are exposed to a varying field, if the field sweep rate or the contact resistances vary along the cable length.

BICCs differ from the 'normal' interstrand coupling currents because they stay in the strands over long distances of  $10\text{--}10^3$  times the cable pitch (or the length of the cable). BICCs propagate through the cable and exhibit large characteristic times of  $10\text{--}10^5$  s (for practical cables) which are several orders of magnitude larger than the time constant of the interstrand coupling currents.

The decay of the BICCs along the length of the cable is either quasi-exponential (regime A) or quasi-linear (regime B) (section 5.4.1). The type of decay is determined by the ratio between  $R_c$  and the effective strand resistivity. For large ratios the decay is quasi-linear towards 0 at the ends of the cable whereas for smaller ratios the BICCs decay exponentially towards 0 with a characteristic length. The slope of the decay varies according to the local  $R_c$  in the cable.

The BICCs are mainly caused by variations in the field change  $\dot{B}_\perp$  transverse to the cable width, and their magnitude increases strongly if the lengths of the  $\dot{B}_\perp$ -variations are of the same order or smaller than the cable pitch (see section 5.4.5). In the case of a dipole magnet this implies that the field variations in the coil ends cause large BICCs whereas the gradual variation of  $\dot{B}_\perp$  to which the total cable is exposed only causes relatively small BICCs.

In practical coils, the magnitude of the BICCs caused by  $\dot{B}_\perp$ -variations is much larger than the magnitude caused by  $R_c$ -variations (see section 5.7). This implies that the soldered cable-to-cable connections cause smaller BICCs than the  $\dot{B}_\perp$ -variations in the coil ends. However, local decreases in  $R_c$  (and hence also cable-to-cable connections) could significantly increase the magnitude and the characteristic time of the BICCs caused by a  $\dot{B}_\perp$ -step. This implies that also in cables having a large  $R_c$ , BICCs will be present if the cable is locally soldered (even if the soldered parts are located in a low-field region).

The presence of BICCs causes an additional power loss, also in those parts of the cable which are not subject to the varying field. The relative increase of the power loss is large compared to the 'normal' interstrand coupling loss if only a small part of the cable is exposed to a field variation (see section 5.5). In accelerator dipole and quadrupole magnets the enhancement of the power loss is smaller than 10% of the interstrand coupling loss.

The magnitude of the BICCs can be reduced by increasing the contact resistances  $R_a$  and especially  $R_c$ . Insertion of a resistive barrier in-between the two layers of a Rutherford-type cable (with originally  $R_a=R_c$ ) can reduce the magnitude of the BICCs by about one order of magnitude (see section 5.6).

The existence of BICCs is experimentally demonstrated in a 1.3 m long Rutherford-type cable exposed to a small local field change. The characteristics of BICCs, such as the decay along the length, the decay as a function of the time and the propagation velocity are qualitatively in very good agreement with the results based on the network model. The influence of local soldering of the cable, simulating the cable-to-cable connections in a coil, on the characteristics of the BICCs corresponds to the network results as well. Quantitative differences of up to a factor of about 5 are probably caused by the unknown variations in  $R_c$  along the cable. The fact that the magnitude of BICCs in a single cable is already hard to assess shows that the BICCs in an entire coil will be even more complicated to calculate, especially if the spatial  $R_c$ -distribution is not well-known.

Large characteristic times of  $10^4$ - $10^5$  s of the BICCs in accelerator dipole magnets (with  $R_c$  of the order of 1-10  $\mu\Omega$ ) imply that the BICCs are classified in regime B and can attain large magnitudes if the ends of the cables are soldered, even if the strands in the rest of the cable are in poor electrical contact. BICCs exhibiting characteristic times of the order of  $10^2$ - $10^3$  s have to be classified in regime A, and their magnitude is much less sensitive to  $R_c$  in the soldered ends of the cable. In a coil, a combination of these two regimes is present.

In dipole and quadrupole accelerator magnets the BICCs cause sinusoidally varying field distortions along the magnet axis with a large characteristic time, an amplitude proportional to the central-field-sweep rate and a period equal to the cable pitch. These field distortions will be discussed in detail in chapter 7. The effect of the BICCs on the stability of a coil is discussed in chapter 8.



## Chapter 6

# Coupling-current losses in accelerator dipole magnets

*This chapter deals with the losses during ramping in superconducting magnets and in particular in the LHC-type dipole magnets. The filament magnetisation, the coupling loss in the wedges and the resistive loss are briefly discussed.*

*The interfilament coupling loss (IFCL) is analysed as a function of the central-field-sweep rate, the time constant of the interfilament coupling currents and a geometry factor that expresses the field variation over the cross-section of the coil.*

*In a similar way, the interstrand coupling loss (ISCL) is investigated as a function of the field-sweep rate, the cross-contact resistance and a geometry factor that denotes the ratio between the local field normal to the cable width and the central field. The increase of the average time constant of the ISCCs in a coil as compared to a single cable is dealt with as well. The ratio between the time constant and the coupling power loss is investigated for several variations of the cross-contact resistance over the cross-section of the coils.*

*Characteristic values for the loss of LHC dipole magnets are given in the case of a nominal field cycle and the distribution of the various loss components over the cross-section of the coils is illustrated.*

*Experimental results are presented of the losses during ramping in 11 LHC dipole model magnets, with lengths of 1 and 10 m. The losses are determined as the difference between the stored energy and the extracted energy during field sweeps between 0.02 and 0.2 Ts<sup>-1</sup>. Differences in the coupling loss among the various model magnets are explained by means of different contact resistances.*

## 6.1 Introduction

During charging and discharging of superconducting magnets energy is dissipated through several mechanisms. The main contributions are due to the magnetisation of the superconducting filaments, the interstrand coupling currents (ISCCs), the interfilament coupling currents (IFCCs) and the resistive loss in the cable-to-cable connections. Smaller contributions originate from the magnetisation of the iron yoke and the eddy currents in the copper wedges and collars.

The induced coupling currents not only cause energy loss but they also cause field distortions and reduce the temperature margin of the coil during (de-)excitation. A good understanding of the loss components is therefore important as they have a major impact on the installed cryogenic power, the allowable excitation ramp-rate, the electromagnetic stability and the quench-protection scheme.

In section 6.2 the various loss components are discussed.

The filament magnetisation and the IFCL are qualitatively treated by means of the theory presented in chapter 3. Representative values of the losses during ramping in LHC dipole magnets are made, using the experimental results on short pieces of LHC-type cables (see sections 3.3 and 3.5). The field shape over the cross-section of the coils is expressed by a field geometry factor  $\beta_{str}$  which is defined as the local field at the strand divided by the central field of the magnet.

The ISCL in a coil is calculated by modelling the turns of the coil by means of a network of nodes interconnected by strand sections and contact resistances  $R_c$  as discussed in detail in chapter 4. The turns of the coil are subject to the local field variation and the mutual interaction between the ISCCs of all the turns is taken into account. The ISCL depends mainly on the field change  $\dot{B}_\perp$  normal to the cable width and is expressed as a function of the average contact resistance  $R_c$  of the cable. The ratio between the perpendicular field component and the central field is expressed by the factor  $\beta_p$ . The enhancement of the coupling loss, due to the boundary-induced coupling currents (see chapter 5), is disregarded since the exact increase is hard to calculate but is at least one order of magnitude smaller than the total coupling loss.

The ratio between the ISCL of a magnet and the average time constant  $\tau_{is,M}$  of the ISCCs is investigated for various  $R_c$ -distributions over the blocks of the inner coil. A good understanding of the time constants is essential to evaluate time-dependent effects in magnets.

In section 6.3 the method is described by which the losses during ramping of the LHC dipole model magnets are measured. The method is based on the electrical measurement of the stored energy during excitation of the coil and the extracted energy during de-excitation. The advantages of the electrical method as compared to other measurement techniques are discussed.

In section 6.4 the experimental results of the losses during ramping of 11 LHC dipole model magnets are presented. The hysteresis loss is compared to the calculated values. The coupling-current loss is presented by means of average  $R_c$ -values. The results are used to evaluate:

- The expected energy loss during 'normal' excitation of the LHC dipole magnets, and during a fast de-excitation (in the case a quench occurred in a series connected magnet).

- The difference between the  $R_c$ -values of the two apertures and four poles of a twin-aperture magnet. Large differences imply that the  $R_c$ -distribution over the cross-section of the coil could vary strongly, which in turn enhances the field distortions caused by the coupling currents (see chapter 7).
- The  $R_c$ -values of similar cables that are used in different magnets.

Furthermore, quantitative knowledge of the average  $R_c$  of the various magnets is necessary to correlate:

- the ramp-rate induced field errors with the ISCCs, as discussed in chapter 7,
- the ramp-rate limitation of the quench current with the ISCCs and the ISCL, as discussed in chapter 8.

## 6.2 Loss components in magnets

In chapters 3 and 4 the losses at strand and cable levels are dealt with in detail. In this section the losses at magnet level are discussed. The calculations are based upon the formulas obtained in the above-mentioned chapters, taking into account the geometry of the magnet and the interaction between the turns. The characteristic power-loss distribution over the cross-section of the coils is illustrated, using the experimentally determined values for the  $J_c$ - $B$  relation (see section 3.3), the interfilament time constant  $\tau_{if}$  (see section 3.5) and the cross-contact resistance  $R_c$  (see section 4.10).

The losses in the mechanical structure are not dealt with in detail but are calculated to be small compared to the other loss components.

The eddy-current loss in the collar pieces of the LHC dipole magnets is small since they consist of separate aluminium or stainless steel plates of 5 mm thickness. The energy loss is about 0.4 J during excitation and 3 J during a fast de-excitation in a 1 m long twin-aperture magnet, assuming a resistivity of the collars of  $10^{-9} \Omega\text{m}$ . This is smaller than 1% of the total losses during (dis)charging (see Table 6.2).

The magnetisation loss in the iron yoke is estimated to be about 40 mJ per kg iron for a field cycle between 0 and 1.7 T [Andreyev, '85]. In the case of a 1 m long twin-aperture magnet, this implies a loss of about 20 J for a nominal field sweep between 0.5 and 8.4 T. This is about 10% of the expected hysteresis loss in the filaments (assuming a filament diameter of 5  $\mu\text{m}$ ) of about 200 J per metre (see Table 6.2).

The mechanical work of the coils due to their deformation during a field sweep is disregarded.

In sections 6.2.1-6.2.4 the field variation in the coil ends is disregarded and the turns are considered to be infinitely long. The enhancement of the loss due to the BICCs is not taken into account.

### 6.2.1 Hysteresis loss

The hysteresis loss  $Q_{hys}$  in the superconducting filaments has already been dealt with in section 3.2. Here full penetration of the filaments is assumed, which is usually the case in high-field accelerator magnets because the field is much larger than the penetration field.

The hysteresis loss (per unit volume) of the filaments for a field cycle with a small field-sweep rate  $\dot{B}$  is given by eq. 3.8 (at constant temperature):

$$Q_{hys} = \frac{2d_f}{3\pi} \oint J_C(B) \left( 1 + (I_{tr}/I_C(B))^2 \right) |\dot{B}_{\perp f}| dt \quad [\text{Jm}^3/\text{cycle}], \quad (6.1)$$

where  $B_{\perp f}$  denotes the local field perpendicular to the filament axis. The relation between the critical current and the field is given by eqs. 2.16 and 2.17 (or 2.18). A possible interaction between the filaments of the strand is included in the  $I_C$ - $B$  relation since experimental results are usually obtained on a strand and not on single filaments. The hysteresis loss depends on the initial and final field values of the cycle and, for low  $\dot{B}$ , not on the field-sweep rate. The hysteresis loss in the coil ends is not treated here but can be calculated in exactly the same way by taking into account the field distribution in the ends.

In section 3.5 it is concluded that for small  $\dot{B}$  and high fields (compared to the penetration field) the hysteresis loss of a single strand is not affected by the other strands of the cable. This also implies that the hysteresis loss in each turn of a coil is not significantly affected by the other turns. The hysteresis loss  $Q_{hys,i}$  of turn  $i$  is therefore equal to the sum of the hysteresis losses of all the strands in the cable subject to the local field. Likewise, the hysteresis loss of the magnet is determined by the sum of the hysteresis loss of all the turns. The average field  $B_{\perp f}$  of all the filaments in a strand is expressed by the field  $B_{str}$ . Since the local field  $B_{str}$  of each strand varies, it is convenient to write the loss as a function of the central field  $B_{ce}$ . The field geometry factors  $\beta_{str,i,j}$  relate the field  $B_{str,i,j}$  at turn  $i$  and strand position  $j$  to the central field:

$$B_{str,i,j} = \beta_{str,i,j} B_{ce} \quad [\text{T}]. \quad (6.2)$$

The total hysteresis loss of a coil during a field sweep  $B_{ce,1}$ - $B_{ce,2}$ - $B_{ce,1}$  (at constant temperature) can then be written as:

$$E_{hys,coil} = f(d_f, I_C(B), I_{tr}, \beta_{str,i,j}, B_{ce,1}, B_{ce,2}) \quad [\text{J}]. \quad (6.3)$$

The coils of multishell magnets are usually made of different cables (in order to obtain a good grading of the current density) with a different  $I_C$ - $B$  relation and possibly a different filament diameter. The hysteresis loss of each coil is therefore expressed by a relation of the form of eq. 6.3. Quantitative results of the hysteresis loss of LHC dipole magnets for a nominal operation cycle are given in section 6.2.5.

### 6.2.2 Interfilament coupling loss

The power loss density  $P_{if}$  in strands with a round or square cross-section in a ramped field is given by (combining eqs. 3.15 and 3.20):

$$P_{if} = \frac{2\tau_{if}}{\mu_0} \dot{B}_{\perp s}^2 \quad [\text{Wm}^{-3}], \quad (6.4)$$

with  $B_{\perp s}$  the field perpendicular to the strand axis. Eq. 6.4 is valid as long as the field is large compared to the penetration field and the filaments are not saturated.

In section 3.5 it is concluded that for small frequencies and large fields (compared to the penetration field) the IFCL of a single strand is not influenced by the other strands of the cable. This also implies that the IFCL of a single turn of a coil is not affected by the neighbouring turns so that the coupling power loss  $P_{if,i}$  of turn  $i$  in a coil is equal to the sum of the power losses of all the individual strands  $j$  in the turn (subject to the local field change  $\dot{B}_{str,i,j}$ ). The IFCL of turn  $i$  for one aperture of length  $l_M$  (disregarding the ends) can then be expressed as a function of the central-field-sweep rate  $\dot{B}_{ce}$ :

$$P_{if,i} = \frac{2\tau_{if,i}}{\mu_0} V_i \beta_{str,i}^2 \dot{B}_{ce}^2 \quad [\text{W}], \quad (6.5)$$

with:

$$V_i = 4whp_{cab}l_M \quad [\text{m}^3], \quad (6.6)$$

the volume of turn  $i$ ,  $p_{cab}$  the packing factor of the cable (about 0.9) and:

$$\beta_{str,i}^2 = \frac{1}{N_s} \sum_{j=1}^{N_s} \beta_{str,i,j}^2. \quad (6.7)$$

The factor 4 in eq. 6.6 refers to the four quadrants of an aperture. Note that  $w$ ,  $h$  and  $p_{cab}$  can be different for the various coils of a multishell magnet.

The  $(\beta_{str,i})^2$ -values are shown in Fig. 6.1 for two dipole-magnet geometries. The IFCL is mainly generated in the inner coil and near the pole of the outer coil. The IFCL in a block and in the coil are equal to the sum of the losses of the individual turns in the block and coil respectively. The IFCL during a nominal field sweep is given in section 6.2.5.

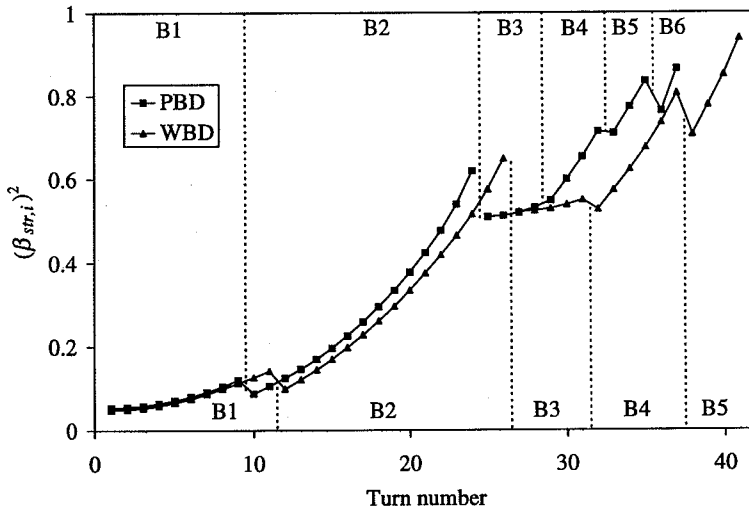


Figure 6.1. The field geometry factor  $(\beta_{str,i})^2$  for each turn of the PBD and WBD magnets (see Table 2.1). The labels B1-B6 at the top and B1-B5 at the bottom refer to the blocks of the PBD and WBD designs respectively (see Fig. 2.2b).



### 6.2.3 Interstrand coupling loss

The steady-state ISCL of a cable, subject to a transverse field change, is dealt with in detail in section 4.4.1. Here the increase of the ISCL due to the spatial distribution of  $\dot{B}_\perp$  along the cable length as well as the coupling loss in the resistances  $R_a$  are disregarded. According to eq. 4.17, the coupling power loss  $P_{c,i}$  per turn can then be written as:

$$P_{c,i} = 8.49 \cdot 10^{-3} \frac{L_{p,s} w^2 (N_s^2 - N_s)}{R_{c,i}} 4l_M \beta_{P,i}^2 \dot{B}_{ce}^2 \quad [\text{W}], \quad (6.8)$$

with  $R_{c,i}$  the average  $R_c$  of turn  $i$ . The factor  $4l_M$  is introduced since the ISCL in eq. 4.17 is given per unit length of cable while the ISCL in eq. 6.8 is given for one aperture of length  $l_M$  which consists of four quadrants.

The factors  $\beta_{P,i}$  are the field geometry factors that express the ratio between the local effective transverse field of turn  $i$  and the central field. Variations of  $\dot{B}_\perp$  across the cable width that affect the coupling power loss (see section 4.7), are incorporated in the factors  $\beta_{P,i}$ . The factors  $(\beta_{P,i})^2$  for each turn of the PBD and WBD magnets are shown in Fig. 6.2.

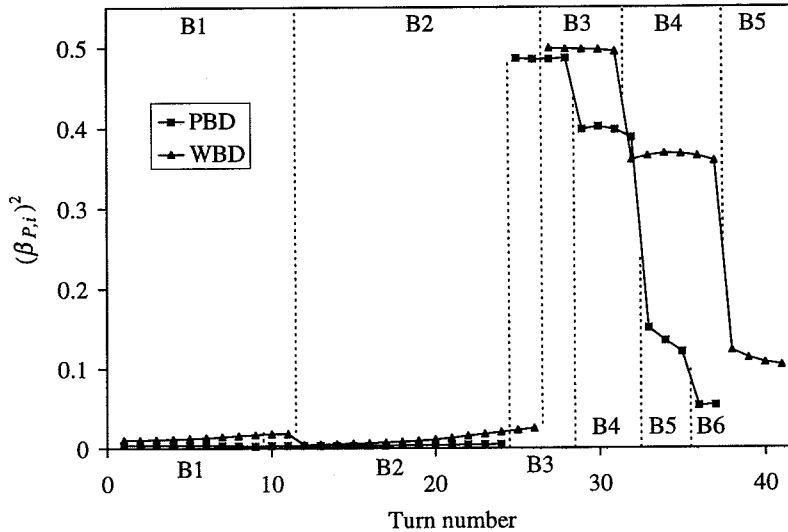


**Figure 6.2.** The field geometry factor  $(\beta_{P,i})^2$  for each turn of the PBD and WBD magnets (see Table 2.1). The labels B1-B6 at the bottom and B1-B5 at the top refer to the blocks of the PBD and WBD designs (see Fig. 2.2b) respectively.

The ISCL is mainly generated in the inner coil (B3-B6 for the PBD magnet and B3-B5 for the WBD magnet) and especially in the turns close to the midplane due to the large field component perpendicular to the cable width (assuming similar cable pitches and contact resistances of the inner and outer coils). Note that  $\beta_P$  is very small near the midplane of the outer coil (B1) because  $\dot{B}_\perp$  changes sign which results in a very small ISCL (see Fig. 4.17).

The steady-state ISCL of the coil is obtained by summation of the ISCL over all the turns. A first estimate of the ISCL for an arbitrary coil wound from Rutherford-type cables can be easily obtained using eq. 6.8 where the factors  $\beta_{P,i}$  are calculated by taking the field component normal to the cable width of turn  $i$  in the centre of the cable. In the case of a cable with  $R_a \ll R_c$  eq. 6.8 has to be extended with the power loss  $P_a$  in the resistances  $R_a$  given by eq. 4.16. Note that different field geometry factors have to be used for  $P_a$  that express the ratio between the local effective parallel field and the central field.

Due to the mutual interaction between the ISCCs of the various turns, the average time constant  $\tau_{is,M}$  of the ISCCs in a magnet will be considerably larger than the average time constant  $\tau_{is,cab}$  of the ISCCs in a single cable (see also section 4.9). The time constant  $\tau_{is,M}$  is numerically calculated using the network model where the mutual inductances between all the strands of the various turns are incorporated. The influence of the ISCCs of the outer coil is disregarded in order to limit the computing time. This results in an error in the calculated  $\tau_{is,M}$  of less than 5% if the  $R_c$ -values and cable pitches of the inner and outer coils are equal.

The mean time constant of the ISCCs in a magnet is then proportional to the time constant  $\tau_{is,cab}$  of the ISCCs in the cable of the inner coil (see eq. 4.31):

$$\tau_{is,M} = K \tau_{is,cab} \quad [\text{s}] . \quad (6.9)$$

The constant of proportionality  $K$  depends on the magnet geometry and is equal to 4.5 for the PBD magnet and 4.3 for the WBD magnet (both values with an error of about 10%). Also for other coil configurations, such as the HERA- and the SSC-dipole geometries the factor  $K$  will be about 4-5. The factor  $K$  can be roughly approximated by calculating the ratio  $\tau_{is,M}/\tau_{is,cab}$  using eq. 4.41 taking  $\alpha_{cab}=7.5$  and  $N_c=16$  and assuming  $\tau_{is,M}=\tau_{is,st}$ . The number  $N_c=16$  is used since the ISCL in a dipole coil is mainly generated in B3 and B4 which form a stack of 16 cables (for the PBD magnet) for quadrants 1 and 4 or 2 and 3 (see Fig. 2.2b). The factor  $K$  is somewhat smaller than the calculated ratio  $\tau_{is,M}/\tau_{is,cab}=5$  due to the presence of a wedge between blocks 3 and 4.

It is shown in section 4.9 that, for a given field-sweep rate, the ratio  $\tau_{is,st}/P_c$  is almost independent of the  $R_c$ -distribution among the cable pieces (up to differences of a factor 5). Here the ratio between the average time constant of the magnet  $\tau_{is,M}$  and the coupling power loss  $P_{c,M}$  is investigated by systematically varying  $R_c$  over the four blocks of the inner coil of the PBD magnet (see Table 6.1).

Note that these values cannot be easily correlated to the results given in Table 4.3 since the field change is not constant over the cross-section of the coils. The given time constants are average values for the blocks or the magnet, since in an actual coil, the current  $I_s$  in each strand section of each turn has its own time constant. The factor  $\tau_{is,M}/P_{c,M}$  is almost independent of the  $R_c$ -distribution even though  $R_c$  is varied by a factor of 5. This is caused by the presence of the wedges which decrease the mutual inductances between the blocks which can therefore be regarded as independent parts. This can be easily seen in Table 6.1 where a decrease of  $R_c$  in one block does not affect the time constants of the other blocks.

**Table 6.1.** Average time constants of the ISCCs in the four blocks B3, B4, B5 and B6 and in the whole PBD magnet M, and total coupling power loss (for one aperture with a length of 1 m) for various  $R_c$ -distributions over the four blocks ( $\dot{B}_{ce}=0.066 \text{ Ts}^{-1}$ ,  $L_{p,s}=0.1 \text{ m}$ ,  $N_s=26$ ).

$R_c (\mu\Omega)$				$\tau_{is,av} (s)$				$\tau_{is,M}$	$P_{c,M}$	$\tau_{is,M}/P_{c,M}$
B3	B4	B5	B6	B3	B4	B5	B6	(s)	(W)	(sW <sup>-1</sup> )
10	10	10	10	0.46	0.39	0.47	0.30	0.42	1.14	0.37
2	10	10	10	2.02	0.42	0.48	0.31	1.32	3.50	0.38
10	2	10	10	0.46	1.74	0.55	0.31	1.06	2.86	0.37
10	10	2	10	0.45	0.40	2.00	0.33	0.58	1.53	0.38
10	10	10	2	0.46	0.39	0.48	1.27	0.46	1.23	0.37

Variations of  $R_c$  within a block lead to variations of the ratio  $\tau_{is}/P_c$  within the block (as already discussed in section 4.9), and so to variations of  $\tau_{is,M}/P_{c,M}$ . For large  $R_c$ -variations of a factor of 10 within one block, the ratio  $\tau_{is,M}/P_{c,M}$  can change by an average of 10%.

Hence, it can be concluded that, if the power loss is known, the time constant can be deduced (and conversely) for an arbitrary  $R_c$ -distribution over the blocks and within the blocks, with an accuracy of about 10% for  $R_c$ -variations up to a factor of 10. This implies that the decay of the voltage over a magnet after a field sweep gives the ISCL and therefore the average  $R_c$  (if the regulation of the current supply is perfect). However, no information is obtained about the other loss components of the magnet such as the resistive loss and the hysteresis loss.

## 6.2.4 Losses in the connections and the wedges

In the resistive cable-to-cable connections between the poles and the coils an ohmic loss power:

$$P_R = I^2 R_{tot} \quad [\text{W}], \quad (6.10)$$

is generated, where  $R_{tot}$  denotes the sum of the resistances of all cable-to-cable connections in the magnet (see section 2.2). Note that the resistances, and therefore the power  $P_R$ , depend on the field due to the magnetoresistance and possibly slightly on the current and the field-sweep rate. A good approximation of the resistive loss for a given field cycle is obtained by integration of eq. 6.10 using a value of the resistance at the mean field level (see section 6.2.5).

The eddy-current power loss in the copper wedges  $P_{wed}$  of one aperture is inversely proportional to the resistivity  $\rho_{cu}$  of copper and proportional to  $\dot{B}_{ce}^2$  and satisfies:

$$P_{wed} = \frac{C_{wed} l_M}{\rho_{cu}(B)} \dot{B}_{ce}^2 \quad [\text{W}], \quad (6.11)$$

where  $C_{wed}$  depends on the number and geometry of the wedges and the field distribution over the cross-section of the wedges. Taking one aperture of the PBD magnet,  $C_{wed}$  is about  $3 \cdot 10^{-8} \text{ m}^4$ , so that  $P_{wed}$  is about 7 mW for  $\rho_{cu}=4 \cdot 10^{-10} \Omega\text{m}$  and  $\dot{B}_{ce}=0.01 \text{ Ts}^{-1}$ .

The energy losses in the connections and the wedges during a nominal field sweep are given in the next section.

### 6.2.5 Total loss

The energy loss of one aperture of a magnet of length  $l_M$  during a triangular field cycle  $B_{ce,1}$ - $B_{ce,2}$ - $B_{ce,1}$  (with  $B_{ce,2} > B_{ce,1}$ ) with constant field-sweep rate  $\dot{B}_{ce}$  is determined by integration of eqs. 6.5, 6.8, 6.10 and 6.11:

$$Q_{tot} = Q_{hys} + \sum_{i=1}^{N_T} \left( \oint P_{if,i} dt + \oint P_{is,i} dt \right) + \oint P_R dt + \oint P_{wed} dt \quad [\text{J/cycle}], \quad (6.12)$$

with:

$$\oint P_{if,i} dt = \frac{2\tau_{if}}{\mu_0} (4whp_{cab} l_M) 2\beta_{str,i}^2 \left[ (B_{ce,2} - B_{ce,1}) \dot{B}_{ce} - \tau_{if} \dot{B}_{ce}^2 \right] \quad [\text{J/cycle}], \quad (6.13)$$

$$\oint P_{is,i} dt = 8.49 \cdot 10^{-3} \frac{L_{p,s} w^2 (N_s^2 - N_s)}{R_{c,i}} 4l_M \beta_{P,i}^2 * 2 \left[ (B_{ce,2} - B_{ce,1}) \dot{B}_{ce} - \tau_{is,M} \dot{B}_{ce}^2 \right] \quad [\text{J/cycle}], \quad (6.14)$$

and:

$$\oint P_R dt = \oint \frac{B_{ce}^2 R_{tot}}{T_M^2} dt = \oint \frac{B_{ce}^2 R_{tot}}{T_M^2} \frac{1}{\dot{B}_{ce}} dB_{ce} = \frac{2R_{tot}}{3T_M^2 \dot{B}_{ce}} (B_{ce,2}^3 - B_{ce,1}^3) \quad [\text{J/cycle}], \quad (6.15)$$

with  $N_T$  the number of turns in the coils and  $T_M [\text{TA}^{-1}]$  the field factor of the magnet. The loss contributions in the iron yoke and the collars are disregarded here.

Measurements of losses during ramping are usually performed with ramp times (from  $B_{ce,1}$  to  $B_{ce,2}$  and reversely) of the order of  $10^1$ - $10^3$  s. The term  $\tau_{if} \dot{B}_{ce}^2$  in eq. 6.13 can therefore be neglected since the time constant  $\tau_{if}$  (which is of the order of 10-100 ms, see section 3.5) is much smaller than the ramp time. The term  $\tau_{is,M} \dot{B}_{ce}^2$  in eq. 6.14 should be taken into account for small ramp times since  $\tau_{is,M}$  is of the order of 1-10 s for LHC-type cables (see section 6.4).

The energy loss in the wedges depends on the relation between the resistivity of the copper and the magnetic field. A simple expression can be used to estimate the loss by assuming a field-independent resistivity which is equal to the resistivity of the copper at a field  $(B_{ce,2} + B_{ce,1})/2$ , so that:

$$\oint P_{wed} dt = 2 \frac{C_{wed} l_M}{\rho_{cu}} (B_{ce,2} - B_{ce,1}) \dot{B}_{ce} \quad [\text{J/cycle}]. \quad (6.16)$$

The ISCL, the IFCL and the hysteresis loss of one aperture of a PBD magnet are depicted in Fig. 6.3. The resistive loss in the connections is not shown since the loss is locally dissipated. The losses are calculated for a field cycle between 0 and 2 T and are depicted for each turn individually. This cycle is chosen as it is often applied in the loss measurements during ramping (see section 6.4).

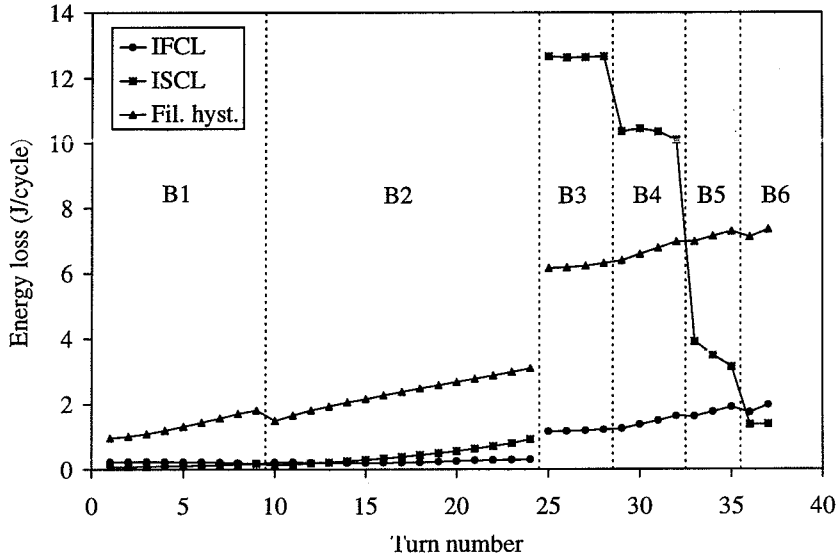


**Figure 6.3.** The hysteresis loss, IFCL and ISCL for each turn of the straight part of one aperture of a 1 m long PBD magnet (see Fig. 2.b2 for the numbering of the turns and the blocks). The loss is calculated for a field cycle between 0 and 2 T with  $\dot{B}_{ce}=0.1 \text{ Ts}^{-1}$ ,  $R_c=10 \mu\Omega$ ,  $L_{p,s}=0.10 \text{ m}$ ,  $B_0=0.31 \text{ T}$ ,  $J_0=3.2 \cdot 10^{10} \text{ Am}^{-2}$ ,  $d_f=10 \mu\text{m}$  and  $\tau_{if}=25 \text{ ms}$ .

The losses in the strand are based on the experimental results of an LHC-type cable with  $B_0=0.31 \text{ T}$ ,  $J_0=3.2 \cdot 10^{10} \text{ Am}^{-2}$ ,  $d_f=10 \mu\text{m}$  and  $\tau_{if}=25 \text{ ms}$  (see chapter 3). The contact resistance  $R_c$  is taken as  $10 \mu\Omega$ . Note that:

- the hysteresis loss increases near the pole of the magnet where the field is maximum,
- the hysteresis loss in the outer coil is relatively large compared to the coupling losses since the hysteresis loss is mainly generated at small fields where the critical current density is large,

the IFCL in the LHC dipole magnets is about 5 times smaller than the ISCL for  $R_c=10 \mu\Omega$  and  $\tau_{if}=25 \text{ ms}$ . A survey of the various loss components during a nominal field sweep of the PBD and WBD magnets is given in Table 6.2. The IFCL and the ISCL are calculated using eqs. 6.13 and 6.14 with:

$$\sum_{i=1}^{N_T} \beta_{str,i}^2 = 5.1 + 8.5 = 13.6, \quad (6.17)$$

and:

$$\sum_{i=1}^{N_T} \beta_{p,i}^2 = 0.09 + 4.04 = 4.13, \quad (6.18)$$

where the two numbers indicate the summations over the turns of the outer and the inner coil respectively.

**Table 6.2.** The energy loss of the various components for a nominal field sweep between 0.6 and 8.4 T with  $\dot{B}_{ce}=0.0066 \text{ Ts}^{-1}$  and a fast exponential de-excitation with a time constant  $\tau_d=100 \text{ s}$  for the PBD and WBD magnets at 1.9 K. The losses are given per metre for a twin-aperture magnet.  $R_c=2 \mu\Omega$ ,  $\tau_{fr}=25 \text{ ms}$ ,  $L_{p,s}=0.12 \text{ m}$ . The ISCL is inversely proportional to  $R_c$ . The filament diameter is  $5 \mu\text{m}$  for both magnets.

	Excitation: $0.0066 \text{ Ts}^{-1}$		Fast de-excitation: $\tau_d=100 \text{ s}$	
	PBD	WBD	PBD	WBD
Hysteresis loss (J)	210	200	210	200
IFCL (J)	7	6	46	42
ISCL (J)	170	210	1150	1390
Resistive loss (J)	38	26	4.1	2.8
Loss in the wedges <sup>a</sup> (J)	1.2	1.1	8	7
Loss in the collars <sup>b</sup> (J)	0.4	0.4	3	3
Loss in the iron yoke <sup>c</sup> (J)	20	20	20	20
Total (J)	450	460	1440	1660
Average heat load (W)	0.38	0.39	14.4	16.6

<sup>a</sup> assuming a resistivity that linearly increases from  $2 \cdot 10^{-10} \Omega\text{m}$  at 0.6 T to  $10 \cdot 10^{-10} \Omega\text{m}$  at 8.4 T.

<sup>b</sup> an estimate assuming a resistivity of the collars of  $10^{-9} \Omega\text{m}$ .

<sup>c</sup> an estimate assuming a loss of 20 mJ per kg iron for a mean field sweep in the yoke from 0 to 1.7 T.

The hysteresis loss is calculated using the  $I_C$ - $B$  relations described by eqs. 2.16 and 2.18 with  $B_0=0.31 \text{ T}$ ,  $J_0=3.2 \cdot 10^{10} \text{ Am}^{-2}$ ,  $C_1=112 \cdot 10^3 \text{ A}$ ,  $C_2=7.8 \cdot 10^3 \text{ AT}^{-1}$  and  $T=1.9 \text{ K}$ .

The resistive loss is the loss for one twin-aperture magnet and is calculated for four splices (each with a resistance that linearly increases from 0.3 n $\Omega$  at 0.6 T to 1.5 n $\Omega$  at 8.4 T) and three pole-to-pole connections (with a constant resistance of 0.2 n $\Omega$ ). Note that the resistive loss is independent of the magnet length since the number of cable-to-cable connections is fixed.

The losses are expressed for a twin-aperture magnet per metre of length. The resistive loss is divided by the magnetic length of the magnets, i.e. 9 m for the PBD magnet and 13.15 m for the WBD magnet (see Table 2.1), in order to obtain a representative value of the loss in a long magnet. During a nominal field sweep the loss is dominated by the hysteresis loss, the resistive loss and, for small  $R_c$ , the ISCL. The average heat load, for a total ramp time of about 1160 s, defined as the energy loss divided by the ramp time, is about 0.37 W, which can be reduced to about 0.25 W for  $R_c > 10 \mu\Omega$ . In the case of a fast de-excitation, the main contributions are caused by the hysteresis loss and the ISCL and an initial heat load, calculated by the energy loss divided by the de-excitation time constant, of about 15 W is present, which can be reduced to 5 W for  $R_c > 10 \mu\Omega$ .

At nominal field a stationary heat-load at 1.9 K is present due to heat inleaks, resistive heating and beam-induced heating, and is estimated to be about 0.35 W per metre of cryostat [LHC, '93]. Therefore, the heat-load during the ramp to nominal field increases by a factor of about 2 compared to the stationary situation. During fast de-excitation the increase is a factor of about 40 for  $R_c=1 \mu\Omega$  and reduces to a factor of about 8 for very large  $R_c$  (so that the ISCL is almost 0).

### 6.3 Measuring losses of a magnet during ramping

The energy loss of a magnet can be measured by means of the following four methods:

- **'Boil-off method'**. At an operating temperature around 4.2 K, the energy loss is deduced from the amount of evaporated helium during continuous field sweeps. The method is inaccurate when the helium evaporation at constant excitation is large compared to the dissipation caused by the field sweep. Another draw-back is the time needed to reach an equilibrium between the power loss and the helium evaporation. This method is applied, for example, to measure the AC loss of a 500kVA AC coil [Akita, '92].
- **'Temperature method'**. At an operating temperature around 1.9 K, the energy dissipation during one or more field sweeps is determined from the temperature increase of the helium bath. When the amount of helium in the cryostat is large, the increase in temperature is often too small to deduce the loss accurately. The method is used to determine the loss of an LHC quadrupole magnet [Genevey, '95]. Also the loss of a toroidal pancake model is deduced by the temperature increase of the helium under forced-flow cooling [Hosono, '93].
- **'Electrical method'**. The energy loss during a field cycle is given by the difference between the stored energy during excitation and the extracted energy during de-excitation. The method is recommended for determining the loss in superconducting magnets pulsed at low ramp rates [Gömöry, '85] and is applied for measuring the losses during ramping of SSC magnets [Ozelis, '93] and LHC magnets (see section 6.4).
- **'Pick-up-coil method'**. The magnetisation of the coils can be determined by using pick-up coils located within the aperture, around the coils or around the collars. However, assumptions with respect to the mutual inductance between the pick-up coils and the magnetisation currents in the cable are required. A large error is likely to be present if  $R_c$  is small and varies strongly over the cross-section of the coils.

Additionally the following three methods can be used to estimate the mean time constant of the ISCCs and hence  $R_c$ :

- **'Step-response method'**. The decay of the voltage signal over the magnet after a linear field sweep gives the time constant  $\tau_{is,M}$ . The ISCL can then be deduced since the ratio between  $P_{is,M}$  and  $\tau_{is,M}$  is constant for a given  $\dot{B}_{ce}$  and a given coil geometry (see section 6.2.3). The time constant is difficult to determine from the voltage signal when the inductive voltage is large or when the power supply is poorly regulated. The method is used to deduce the coupling loss of one LHC dipole model magnet [Tixador, '90].
- **'Field-distortion method'**. In section 7.4 it is shown that the ratio between the dipole field  $B_{is}$ , induced by the ISCCs in the aperture of a magnet, and the average  $R_c$  is constant for a given  $\dot{B}_{ce}$ . This implies that the ISCL can be deduced from a measurement of the field distortion  $B_{is}$  during a field sweep. In chapter 7 this method is further worked out and is experimentally evaluated for several LHC dipole magnets.
- **'Phase-shift method'**. The time constant  $\tau_{is,M}$  can be deduced from the phase shift between the current through the cable and the voltage over the cable for a sinusoidally

varying current. The results of AC loss measurements on a 500kVA AC coil using this method [Akita, '92] correspond well with the measurements using the 'boil-off method' as described above.

Here the energy loss is determined by means of the electrical method because:

- The loss of both individual magnets in the twin-aperture structure can be deduced and, therefore, also variations in the ISCL, and thus  $R_c$ , between both apertures. Also an estimate of the difference between the mean  $R_c$  in both poles of the same aperture is possible. With the 'boil-off method' and the 'temperature method' only the total energy loss of the whole magnet can be determined because both apertures are contained in the same cryostat.
- All loss components are determined, which is not possible with the 'step-response method', the 'field-distortion method' and the 'phase-shift method'.
- No assumptions have to be made about the distribution of the coupling currents over the cross-section of the magnet. The electrical method can be regarded as a measurement of the loss of a 'black box'. Independent of the location of the loss within the 'box', the loss is equal to the difference between the energy that is needed to charge the magnet and the energy that is delivered during discharging.

The hysteresis loss, the resistive loss and the total coupling loss ( $Q_{if} + Q_{is}$ ) can be separated by measuring the energy loss per cycle as a function of the central-field-sweep rate  $\dot{B}_{ce}$ . The method is similar to the one described in section 4.10.2 except that in the case of a magnet the losses  $Q_{if}$  and  $Q_{is}$  cannot be separated since the field direction in a magnet cannot be changed. Hence, the loss  $Q_{is}$  is deduced by subtracting the loss  $Q_{if}$  (calculated using  $\tau_{if}$  as determined from the magnetisation measurement) from the total coupling loss.

A measurement consists of one triangular cycle in which the central field is ramped up with a given ramp rate  $\dot{B}_{ce}$  from  $B_{ce,1}$  to  $B_{ce,2}$  and ramped down from  $B_{ce,2}$  to  $B_{ce,1}$  with  $-\dot{B}_{ce}$ . After the ramp-up and the ramp-down the transport current is kept constant for at least 50 s in order to let the ISCCs decay to zero. The energy loss of each magnet is determined during 6 to 20 triangular field sweeps with sweep rates between  $0.02 \text{ Ts}^{-1}$  and  $0.2 \text{ Ts}^{-1}$ . In order to investigate the field-dependence of the loss components, the energy loss is determined for two or more cycles with different field levels  $B_{ce,1}$  and  $B_{ce,2}$ .

The transport current  $I_{tr,cab}$  is measured by means of a current transformer (with  $U_{DCCT} = C_{DCCT} I_{tr,cab}$  with  $C_{DCCT} = 10^{-4} \text{ VA}^{-1}$ ) with a reproducibility better than  $20 \mu\text{V}$  or 0.2 A. During a field cycle the voltage  $U_{DCCT}$  and the voltage  $U_M$  over the magnet are integrated and the average current and voltage are determined during time intervals  $\Delta t$  of about 0.3 s:

$$I_{tr,cab,n} = \frac{1}{\Delta t} \int_{t_1}^{t_1+\Delta t} \frac{U_{DCCT}}{C_{DCCT}} dt \quad [\text{A}], \quad (6.19)$$



$$U_{M,n} = \frac{1}{\Delta t} \int_{t_1}^{t_1+\Delta t} U_M dt \quad [\text{V}], \quad (6.20)$$

and stored in a PC as shown in Fig. 6.4.

The loss is calculated by summation of the  $N$  incremental energies, so that:

$$Q_{tot} = \sum_{n=1}^N U_{M,n} I_{tr,cab,n} \Delta t \quad [\text{J/cycle}], \quad (6.21)$$

which can be regarded as the difference between the stored energy during excitation and the extracted energy during de-excitation.

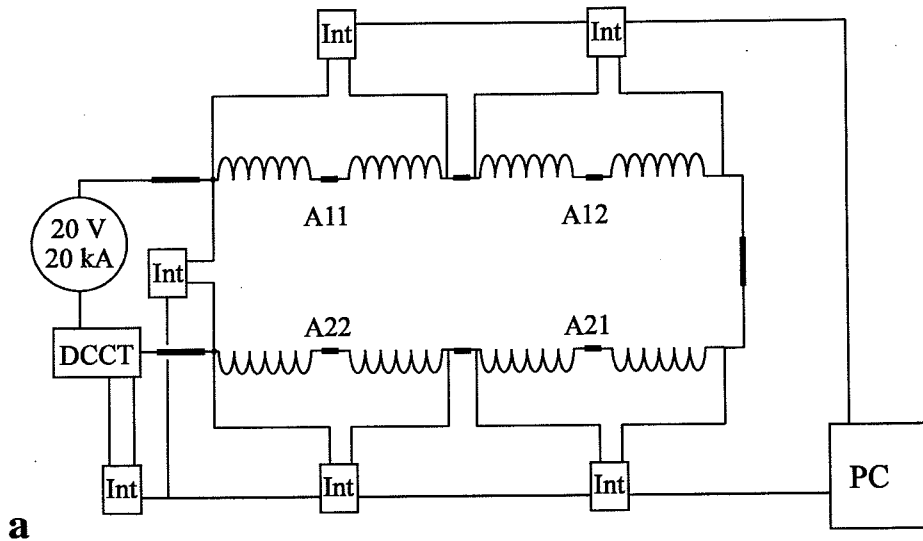
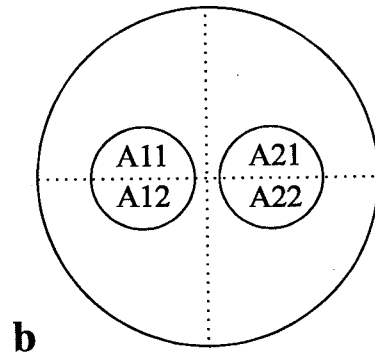


**Figure 6.4. a.** The 'electrical method' for measuring losses of a superconducting magnets during field cycle between  $B_{ce,1}$  and  $B_{ce,2}$ . Simultaneously the voltages over all the four poles and the whole dipole magnet are measured.

**b.** Schematic view of the cross-section of a dipole magnet, indicating the nomenclature of the poles. The poles A11 and A12 form aperture 1 (or A1) and the poles A21 and A22 form aperture 2 (or A2).



The voltages over the poles are measured simultaneously, besides the total voltage over the magnet, in order to investigate the differences in the losses between the poles. It is important that the filament magnetisation and the coupling losses, that are dissipated in the various parts of the magnet, are supplied by the magnetic field. This implies that a local energy dissipation is measured as an additional voltage in both poles and not only in the pole in which the energy is dissipated. The ratio of the voltages in both poles is related to the contribution of both poles to the local field. Energy loss near a pole results, therefore, mainly in an increase of the voltage in that pole while energy loss near the midplane results in an almost equal voltage in both poles. Only the resistive loss and the transport-current loss (i.e. the second term in eq. 6.1) are measured as a voltage over the same pole where the losses are dissipated. Hence, a difference in the measured loss between two poles cannot be carried back to a difference in  $R_c$  between the two poles since the distribution of  $R_c$  over the cross-section of the magnet is unknown. In general, the measured difference is smaller than the actual difference, since the mutual interaction between the poles causes a levelling of the loss voltages.

This effect is even more pronounced for the measured loss in the various coils of a multishell magnet. Although the loss is mainly generated in the inner coil(s), the required energy is supplied by the magnetic field which is mainly generated by the outer coil(s). So, even if voltage taps are present on the splice(s) between the various coils, the 'electrical method' will not reveal the actual loss in the separate coils. Of course, the same reasoning holds for the measured loss of a single block or turn.

The actual filament-magnetisation and the IFCL in the separate coils can be well estimated from short sample measurements. In the case of the ISCL,  $R_c$  is assumed to be constant all over the cross-section of the coils. The ISCL for each turn can then be determined since  $\beta_p$  (see Fig. 6.2) is known for each turn.

The accuracy of the electrical method depends on:

- The ratio between the stored energy and the energy loss during a cycle. A smaller ratio results in a more accurate loss measurement. Therefore, the energy loss can be determined more precisely by using large field-sweep rates, which increases  $Q_{tot}$ , and small fields  $B_{ce,2}$ , in order to decrease the stored energy.
- The noise and the reproducibility of the power supply.
- The time interval  $\Delta t$ . A small  $\Delta t$  results in a more accurate summation in eq. 6.21. It is possible as well to use non-integrating voltmeters with a high sampling rate. A carefully adjusted bucking coil, which compensates for the inductive component of the voltage, is preferable in order to avoid erratic results if the noise of the power supply is large.
- The drift of the voltmeters or integrators in time. Especially at small sweep rates a small drift could lead to inaccurate results. Correction for a linear drift in time is possible by performing offset measurements before and after the field cycle.

The above implies that the error of the loss measurements increases significantly for smaller field-sweep rates. This results in a relatively large error in the determination of the hysteresis loss, which is deduced from the intercept of the  $Q_{tot}-\dot{B}_{ce}$  curve at  $\dot{B}_{ce}=0$  (if the resistive loss is negligible), especially for field cycles with a large ISCL and a small hysteresis loss. Of course, performing more field cycles decreases the error in the deduction of the various loss components.

## 6.4 Experimentally determined $R_c$ -values of LHC magnets

The total energy loss of the 1 m long LHC dipole model magnets for cycles between 0 and 2 T is depicted in Fig. 6.5. This cycle is chosen in order to decrease the ratio between the stored energy and the energy loss and, therefore, to increase the accuracy. The field-sweep rate  $\dot{B}_{ce}$  varies between 0.02 and 0.2 Ts<sup>-1</sup>. A smaller  $\dot{B}_{ce}$  leads to a considerable increase in the relative error.

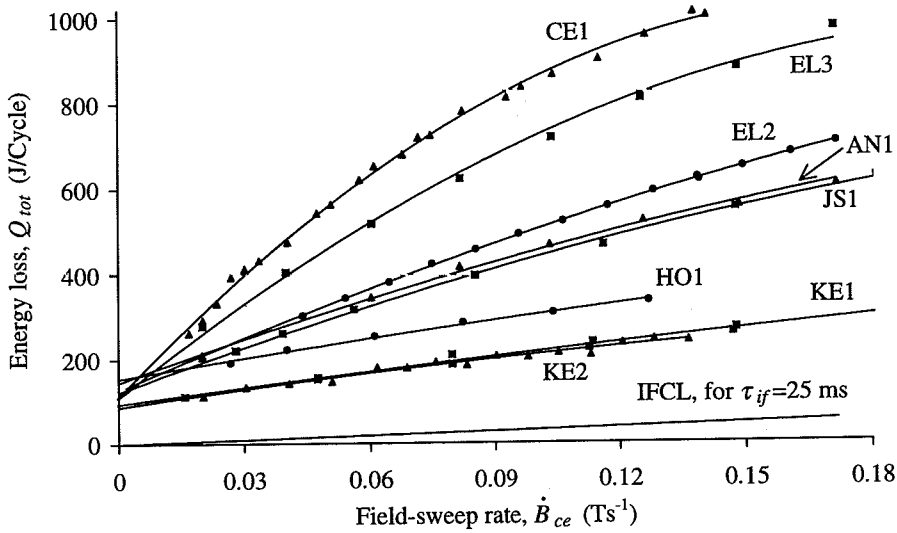


**Figure 6.5.** The energy loss per cycle and per aperture as a function of the field-sweep rate for the 1 m long dipole magnets CE1, EL3, EL2, AN1, JS1, HO1, KE1 and KE2 (from top to bottom) for a field cycle between 0 and 2 T. The solid lines represent fitting curves using eq. 6.12. The calculated IFCL is included assuming  $\tau_{if}=25$  ms.

The various loss components are evaluated by fitting the measured  $Q_{tot}-\dot{B}_{ce}$  values with eq. 6.12, neglecting the very small loss contribution from the wedges.

- The resistive loss of the connections is too small to be deduced, because the currents are small and the field-sweep rates large. Using eq. 6.15 with  $R_{tot}=2$  n $\Omega$  gives a resistive loss of about 1 J for the given field cycle at the minimum field-sweep rate of 0.02 Ts<sup>-1</sup>. Voltage measurements across the connections at constant transport current give an average resistance per connection of typically 0.5 to 1 n $\Omega$  (at about 5 T).
- The hysteresis loss is given by the intercept at  $\dot{B}_{ce}=0$  because the resistive loss is negligible. The error in  $Q_{hys}$  is about 10-50 J (per aperture per metre length) and is mainly due to the noise of the power supply which makes it very hard to perform accurate measurements at small field-sweep rates. As already discussed in the previous section, the error increases for magnets with a large coupling loss compared to the hysteresis loss.

- The IFCL is calculated using the  $\tau_{if}$ -values deduced from the short sample measurements (see section 3.5) in combination with eqs. 6.13 and 6.17. If  $\tau_{if}$  of a cable is not known, it is assumed to be equal to 25 ms. The IFCL corresponding to this value is also shown in Fig. 6.5, demonstrating that the IFCL makes up only a minor contribution to the total coupling losses.
- The ISCL results in an average  $R_c$  in the coil. No distinction can be made between the  $R_c$ -values of the inner and outer coils. In the case of similar  $R_c$  in both coils, the ISCL is mainly generated in the inner coil and the deduced  $R_c$  corresponds within 5% to  $R_c$  in the inner coil. No accurate  $R_c$  can be determined if the cable that is used in the outer cable has a much smaller  $R_c$  than the one used in the inner coil.

The second-order behaviour of the curves (see eq. 6.14) can be clearly seen for the magnets with a large ISCL (i.e. with a large time constant  $\tau_{is,M}$ ).

Loss measurements on the poles show that the hysteresis loss does not vary significantly among the poles, as expected since the  $J_C$ - $B$  relation of the strands of the poles are the same. An example is given in Fig. 6.6 where the loss of the four poles of the 10 m long AN2 model magnet is depicted. The relative difference between the intercepts (that is the hysteresis loss) of the four curves is less than 5%. The difference in the coupling loss between the four poles is discussed later.

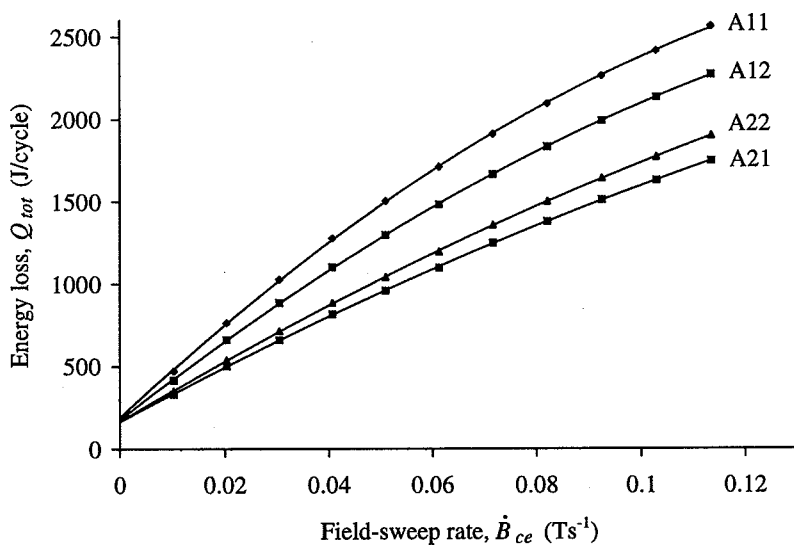


**Figure 6.6.** The energy loss in the four poles of the AN2 model magnet as a function of the field-sweep rate for a field cycle 0-2.0 T. The fitted curves (using eq. 6.12) show clearly that the four poles exhibit the same hysteresis loss whereas the ISCL varies by a factor of at least 1.5.

The results in terms of  $Q_{hys}$  and  $R_c$  for all field cycles are listed in Table 6.3. The bath temperature  $T_b$  is 1.8-2.0 K unless otherwise indicated. Only the average  $R_c$  of the whole magnet is included in the table.

**Table 6.3.** Results of the loss measurements on LHC model magnets in terms of the experimentally determined hysteresis loss  $Q_{hys,exp}$ , the calculated hysteresis loss  $Q_{hys,calc}$ , the cross-contact resistance  $R_c$  and the time constant  $\tau_{is,M}$  (calculated and deduced from a fit).

Magnet (see Table 2.3)	Cool- down	$B_{cr,1}$ T	$B_{ce,2}$ T	$Q_{hys,exp}$ J/cycle	$Q_{hys,calc}$ J/cycle	$R_c$ $\mu\Omega$	$\tau_{is,M,calc}$ s	$\tau_{is,M,fit}$ s
<b>1 m models</b>								
AN1	2	2.0	7.5	178	178	2.7	2.0	
	4	0	2.0	145	145	3.7	1.4	
	4	2.0	5.8	158	124	3.6	1.5	
CE1	2	0	2.0	144	63	1.4 (1.2 <sup>a</sup> )	3.8	4.8
	2	2.0	4.1	51	32	1.3 (1.2 <sup>a</sup> )	4.1	5.3
	2	0	3.0	139	78	1.2 (1.1 <sup>a</sup> )	4.4	
	3	2.0	6.1	135	49	1.3 (1.2 <sup>a</sup> )	4.1	
	4	0	2.0	149	64	1.7 (1.3 <sup>a</sup> )	3.1	4.1
	4	2.0	4.1	74	32	1.6 (1.4 <sup>a</sup> )	3.3	4.2
EL1	2	2.0	7.1	90	195	1.7 (1.9 <sup>a</sup> )	3.1	
	3	0	2.0	132	184	1.8	3.0	2.4
	3	2.0	6.2	184	184	1.9	2.8	
EL2	2	0	2.0	157	151	3.2	1.7	
	2 <sup>b</sup>	0	2.0	116	110	2.8	1.9	
	2	2.0	5.0	71	107	2.9	1.8	
	2 <sup>b</sup>	2.0	4.8	58	67	3.0	1.8	
	3	0	2.0	128	151	3.0	1.8	1.9
	3	2.0	5.5	113	124	3.1	1.7	1.6
	4	0	2.0	140	151	3.0	1.8	1.7
HO1	3	0	2.0	145	180	6.7	0.8	
JS1	2	2.0	7.5	65	145	3.7 (4.0 <sup>a</sup> )	1.4	
	3	2.7	7.5	113	129	3.7	1.4	
	3	2.0	8.2	145	163	3.7	1.4	
	4	0	2.0	125	130	3.6	1.5	
	5	0	2.0	109	130	3.0	1.8	1.6
KE1 <sup>c</sup>	2	0	2.0	95		6.1		
KE2 <sup>c</sup>	1	0	2.0	97		7.6		
<b>10 m models</b>								
AN2	2	0	2.0	$6.2 \cdot 10^2$	$6.5 \cdot 10^2$	1.6	3.3	3.5
	2	2.0	4.1	$3.1 \cdot 10^2$	$3.0 \cdot 10^2$	1.7	3.1	3.4
	2	0	4.1	$11 \cdot 10^2$	$9.5 \cdot 10^2$	1.6	3.3	3.5
AN3	1	0	2.0	$7.9 \cdot 10^2$	$6.5 \cdot 10^2$	6.2	0.8	
	1	2.0	4.1	$5.1 \cdot 10^2$	$3.0 \cdot 10^2$	6.8	0.7	
NO1	1	0	2.0	$6.8 \cdot 10^2$	$6.5 \cdot 10^2$	4.0	1.3	
	1	2.0	4.1	$6.8 \cdot 10^2$	$3.0 \cdot 10^2$	4.3	1.2	

<sup>a</sup>  $R_c$  determined by using the calculated hysteresis loss as a fixed point in the fit.

<sup>b</sup> Measurements performed at  $T_b = 4.3$  K.

<sup>c</sup> See [Yamamoto, '93] for more details of the different geometry. The hysteresis loss is not calculated.

The hysteresis loss is calculated numerically using the Kim relation (see eq. 2.16 with  $B_0$  and  $I_0 = J_0 \pi d_f^2 \eta / 4$  as specified in Table 3.1). The parameters  $B_0$  and  $I_0$  are assumed to be 0.31 T and  $3.0 \cdot 10^{10} \text{ Am}^{-2}$  for those cables which are not mentioned in Table 3.1. A linear relationship is taken between the critical current and the field for fields larger than 2-3 T (see eq. 2.18 with  $C_1 = 112 \cdot 10^3 \text{ A}$  and  $C_2 = 7.8 \cdot 10^3 \text{ AT}^{-1}$ ). The calculated  $Q_{hys,cal}$ -values (see Table 6.3) are in fair agreement with the experimentally determined hysteresis loss  $Q_{hys,exp}$  taking into account the error in  $Q_{hys,exp}$  and the errors in the constants as used in the  $I_C$ - $B$  relation.

The calculated hysteresis loss of the CE1 magnet is a factor 2 smaller than the measured loss. The difference is probably caused by the large coupling loss (and hence the steep slope of the  $Q_{loss}$ - $\dot{B}_{ce}$  curve), which increases the inaccuracy in the extrapolated value for  $Q_{hys,exp}$ . The calculated hysteresis losses of one series of field cycles of the EL1 and the JS1 magnets are a factor 2 larger than the measured losses, probably caused by the large stored energy of these cycles in combination with the small number of field sweeps. For all these cycles  $R_c$  is also determined by taking the calculated hysteresis loss as a fixed point in the fit. This results in a decrease of  $R_c$  for the CE1 magnet and in an increase of  $R_c$  for the EL1 and the JS1 magnets.

The following conclusions hold with respect to the average  $R_c$  in the magnets:

- $R_c$  does not depend on the electromagnetic force on the cable and is not significantly magnetoresistive. This can be clearly seen by comparing the  $R_c$ -values deduced from field cycles at low (ca. 0-2 T) and high (up to 8 T) excitation, performed during the same cool-down.
- $R_c$  does not depend on the temperature (between 1.9 K and 4.3 K) since the ISCLs at 4.3 K and 1.9 K are equal. This is expected since no parameter that influences  $R_c$  (see section 4.3) varies significantly between 1.9 and 4.3 K.
- The average  $R_c$  of the poles differ for most of the magnets by at least 10-30%. As an example, the total losses of the four poles of the 10 m long AN2 model magnet are shown in Fig. 6.6 for a field sweep between 0 and 2 T. The average  $R_c$ -values for each aperture are about  $1.3 \mu\Omega$  for A1 and  $2.0 \mu\Omega$  for A2. Average  $R_c$ -values per pole can be calculated assuming that the loss, as measured on a pole, is generated in the same pole. This results in  $R_c$ -values of  $1.2 \mu\Omega$  (A11),  $1.4 \mu\Omega$  (A12),  $2.1 \mu\Omega$  (A21) and  $1.9 \mu\Omega$  (A22). However, the actual differences between  $R_c$  of the two poles of the same aperture are probably even larger as explained in section 6.3. This will cause larger skew harmonics during excitation of the magnets than expected from the estimated average  $R_c$  per pole (see chapter 7).

Within the accuracy of the measurement method it cannot be concluded that  $R_c$  depends on the number of cool-downs. Magnets that have been remeasured several times over a period of 2-3 years do not show any clear change in  $R_c$ .

For several series of measurements the ISCL is sufficiently large to deduce the time constant  $\tau_{is,M}$  by fitting the measurements with eq. 6.12. The time constants  $\tau_{is,M,fit}$  obtained by fitting are in good agreement with the time constants  $\tau_{is,M,calc}$  (see Table 6.3) calculated using the constant ratio between  $P_{is,M}$  and  $\tau_{is,M}$  (for a given field-sweep rate). This validates

the network model for modelling the ISCCs and the corresponding time constants in superconducting magnets.

Table 6.4 shows a brief survey of the  $R_c$ -values of all magnets arranged with respect to the cable as used in the inner coil. Although the number of magnets is too small to perform and obtain reliable statistics it can be seen that the  $R_c$ -values of different magnets made with the same cable correspond rather well for cables I-1, I-2 and I-5. Only in the case of cable I-3 is there a variation of a factor 3-4 between the magnets EL1, EL2 and HO1. This difference could originate from any of the circumstances as discussed in section 4.3. A different stress level during the curing process and different oxidation levels of the strand surface (possibly caused by the period between manufacturing the cable and winding the coil) are the most plausible causes.

**Table 6.4.** Average values of the cross-contact resistance of the inner coil for 11 LHC dipole model magnets, assuming that the  $R_c$ -values of the outer coils are of the same order or larger than those of the inner coils. TA=twin-aperture magnet, SA=single-aperture magnet.

Magnet	Type	Cable for the inner layer	Coating/soldering	$R_c$ $\mu\Omega$
AN1	1 m TA	I-1	zebra <sup>a</sup>	2.7-3.7
JS1	1 m TA	I-1	zebra <sup>a</sup>	3.0-3.7
AN2	10 m TA	I-2	SnAg	1.6-1.7
CE1	1 m TA	I-2	SnAg	1.1-1.4
EL1	1 m TA	I-3	SnAg	1.8-1.9
EL2	1 m SA	I-3	SnAg	2.8-3.2
HO1	1 m TA	I-3	SnAg	6.7
KE1	1 m SA	I-5	bare	6.1
KE2	1 m TA	I-5	bare	7.6
AN3	10 m TA	I-6	SnAg	6.2-6.8
NO1	10 m TA	I-7	SnAg	4.0-4.3

<sup>a</sup> see section 4.6

## 6.5 Conclusions

In the coils of superconducting accelerator magnets the main loss contributions are related to filament magnetisation, interfilament coupling, interstrand coupling and resistive loss. Additionally, smaller loss contributions are present in the mechanical structure, in particular the hysteresis loss in the iron yoke and the eddy-current loss in the collar pieces.

The hysteresis loss in the filaments can be directly estimated from the AC magnetisation of a single strand. The error between the measured and the calculated hysteresis loss is generally 20% and is mainly caused by the noise of the power supply which makes accurate loss measurements at small field-sweep rates very difficult. The hysteresis loss is about a factor 1.5 larger at 1.9 K compared to 4.3 K for the same field cycle. The enhancement is due to the increase of the critical current density of NbTi. The filament hysteresis is the dominant loss contribution for small central-field-sweep rates of the order of  $10^{-2}$  Ts<sup>-1</sup> and weak-field excitation.

For larger field-sweep rates or strong field excitations the coupling losses dominate. The IFCL and the ISCL of a magnet can be separated once the IFCL of a strand or cable is known. In the LHC dipole model magnets the ISCL is at least a factor 10 larger than the IFCL and is mainly generated in the inner coil near the midplane. While the IFCCs are characterised by a time constant of about 25 ms, the ISCCs exhibit time constants of about 1 to 5 s, attributed to a small contact resistance  $R_c$  between crossing strands of about 1 to  $8 \mu\Omega$ . The effect of such small  $R_c$  on the field homogeneity and temperature margin during ramping is discussed in chapters 7 and 8.

The experimentally deduced time constants of the ISCCs correspond well with calculated values using the network model in combination with the determined  $R_c$ -values. This validates the use of the network model to calculate the ISCCs and their time constants in superconducting magnets.

The eddy-current losses in the copper wedges and collar pieces are small compared to the coupling losses in the cable and the magnetisation loss in the iron yoke is small compared to the magnetisation loss in the filaments.

Experimental results on LHC dipole model magnets show that the  $R_c$ -values of cables with SnAg-coated strands:

- are temperature-independent (between 1.9 K and 4.3 K),
- vary by a factor of up to 1.5 between the two poles of the same aperture,
- do not depend on the field level and therefore do not significantly depend on the Lorentz force on the cable and on the matrix resistivity.

Three magnets in which the same cable is used have been shown to exhibit an ISCL which differs by a factor 3-4. The difference in  $R_c$  is probably due to different stress levels (during curing) and surface conditions of the strands between the models. Three other cables are all used in two magnets. No large differences in  $R_c$  between the two magnets are observed for these cables.

The energy dissipation during a nominal field sweep from 0.6 to 8.4 T is dominated by the hysteresis loss, the resistive loss and, for small  $R_c$ , the ISCL and is about 450 J (for  $R_c = 2 \mu\Omega$ ) per metre for a twin-aperture magnet (see Table 6.2). The average heat-load is about 0.38 W for excitation in about 20 minutes. A fast de-excitation, with a de-excitation time constant of 100 s, leads to an energy dissipation of about 1500 J (for  $R_c = 2 \mu\Omega$ ), mainly caused by the hysteresis loss and the ISCL, and consequently an average heat load of 15 W. If  $R_c > 10 \mu\Omega$ , the average heat load can be reduced to 0.25 W for a nominal field sweep and 5 W for a fast de-excitation.

The losses in superconducting accelerator magnets during ramping can be well determined by means of the 'electrical method', based on the measurement of the difference between the stored energy and the extracted energy during a field cycle. The method is relatively fast and accurate, especially for field cycles at low excitation levels where the stored energy is small. The hysteresis loss and coupling losses can be well distinguished with an accuracy that is mainly limited by the noise and the regulation of the power supply.





## Chapter 7

# Coupling-current induced field distortions

*This chapter deals in particular with the additional magnetic fields caused by the interstrand coupling currents (ISCCs) and the boundary-induced coupling currents (BICCs) during a field sweep of coils made of multistrand conductors. Field distortions caused by the interfilament coupling currents and a non-uniform current distribution are briefly discussed.*

Field  $\mathbf{B}_{is}$  caused by the ISCCs is calculated starting from the ISCC-distribution as determined in chapter 6. The spatial distribution of the cross-contact resistance  $R_c$  in the coils determines which harmonic components are influenced. A minimum  $R_c$ -value can be defined in order to ensure that the field induced by the ISCCs remains below the acceptance limit determined by the magnet specifications.

The field  $\mathbf{B}_{bi}$  caused by the BICCs is shown to vary sinusoidally along the magnet axis. The magnitude of the distortions is strongly influenced by small variations in the magnet length, transposition pitch,  $R_c$ -distribution and effective strand resistivity and is therefore very difficult to calculate.

Methods are discussed by which the fields  $\mathbf{B}_{is}$  and  $\mathbf{B}_{bi}$  can be distinguished from the fields caused by the filament magnetisation, the fabrication tolerances and a non-uniform current distribution.

Experimental results are presented of  $\mathbf{B}_{is}$  and  $\mathbf{B}_{bi}$  in 1 m and 10 m long LHC dipole model magnets. The magnitudes of the harmonic components of  $\mathbf{B}_{is}$  are evaluated and compared with calculated values based on the average  $R_c$  in the coils. The magnitude and the characteristic time of  $\mathbf{B}_{bi}$  will be dealt with, and an estimate is made of the characteristic length of the BICCs and the effective strand resistivity.

## 7.1 Introduction

Especially in accelerator magnets, field distortions are of a major concern since the particle motion becomes unstable above certain values of the higher harmonics, resulting in considerable beam losses and a smaller luminosity. Correction magnets are present in accelerators and are especially suitable for correcting the field distortions that are the same for all magnets.

A good understanding of the field distortions requires a classification of the various fields that contribute to the total field in the aperture of a magnet and the origins from which these fields are created. In superconducting coils made of monolithic conductors the field distortions are dominated by the following three components:

- The field  $\mathbf{B}_{geo}$  related to fabrication tolerances of the various components. This field changes during excitation of the magnet, since the electromagnetic forces change and cause a deformation of the coils.
- The field  $\mathbf{B}_m$  caused by the persistent currents in the filaments is, in first approximation, proportional to the filament diameter and the critical current density  $J_c(B, T)$ . The field quality of superconducting magnets at low excitation is therefore strongly influenced by the persistent currents since the critical current density is large. This phenomenon is well understood and experimental results and calculations are usually in good agreement (see for example [Caspi, '87], [Wanderer, '93], [Zhao, '93]) provided that the  $J_c(B, T)$  relation is sufficiently known. If the properties of the superconductor are uniform, field  $\mathbf{B}_m$  follows the symmetry of the main field so that only the normal odd harmonics  $B_1, B_3, \dots$  are present. The time dependence of the persistent currents, which is related to flux creep in the superconductor [Anderson, '62], [Kim, '62], is, however, less defined. Experimental results on the time dependence of the persistent currents in the Tevatron [Finley, '87] and in HERA [Brück, '90] have shown a logarithmic decay in time with a characteristic change of a few percent per decade. Measurements on short cable pieces show a similar decay although the time dependence is less pronounced, see e.g. [Gilbert, '89], [Marken, '92].
- The field  $\mathbf{B}_f$ , produced by the IFCCs, is linear with the central-field-sweep rate and inversely proportional to the effective transverse resistivity of the strand and decreases at higher levels of excitation due to the magnetoresistance of the matrix.

While the preceding field distortions are well understood, the use of multistrand cables in accelerator magnets has caused additional field errors that exhibit an anomalous time dependence during and after field sweeps. Sinusoidal variations in the axial direction of the magnet have been observed in HERA magnets, where the amplitude and phase depend strongly on the actual and preceding excitation cycles of the magnet [Brück, '91a/'91b]. Results on a RHIC prototype dipole magnet show that the axial variations are caused by unbalanced currents and not by magnetisation of the filaments [Sampson, '95]. Measurements on SSC dipole magnets at BNL have shown that the amplitude of the axial variations depends on the central-field-sweep rate  $\dot{B}_{ce}$  if the contact resistance  $R_c$  is small, while the amplitude is almost independent of  $\dot{B}_{ce}$  if  $R_c$  is large [Ghosh, '93/'94]. Measurements on the SSC magnets have also shown that the amplitude of the periodic

pattern during the ramp increases with time [Devred, '94]. Since the first observation at HERA, the sinusoidally varying field errors are thought to be related to a *Non-Uniform Current Distribution (NUCD)* among the strands due to different joint resistances, locally very small  $R_c$  and differences between the inductances of the strands. However, the observed effects could not be explained by the existing models. With the new description of the BICCs as presented in chapter 5, it is possible to describe the additional field distortions in cabled superconductors by three types of fields:

- The field  $\mathbf{B}_{is}$  caused by the ISCCs, which is proportional to the central-field-sweep rate  $\dot{B}_{ce}$  and, in first approximation, inversely proportional to the average contact resistance  $R_c$  between the strands. This linear dependence of  $\mathbf{B}_{is}$  on  $\dot{B}_{ce}$  and  $1/R_c$  has been observed in SSC dipole magnets [Ogitsu, '92a/'92b/'93/'94]. In section 7.4 it will be shown that especially the higher harmonics depend strongly on the spatial  $R_c$ -distribution in the coils. The measured multipole components of  $\mathbf{B}_{is}$  of several SSC dipole magnets are used to estimate the  $R_c$ -distribution over the cross-section of the coils in these magnets [Devred, '94].
- The field  $\mathbf{B}_{nucd}$  caused by a non-uniform distribution of the transport current among the strands, mainly due to differences between the joint resistances of the strands (see section 5.2). Field  $\mathbf{B}_{nucd}$  is invariant to  $\dot{B}_{ce}$  and can depend on the excitation level due to the magnetoresistance of the connections. Field  $\mathbf{B}_{nucd}$  has a periodic pattern along the magnet length with a period equal to the cable pitch.
- The field  $\mathbf{B}_{bi}$ , caused by the BICCs, is proportional to  $\dot{B}_{ce}$ . Also  $\mathbf{B}_{bi}$  varies sinusoidally along the magnet axis with a period equal to the cable pitch. Field  $\mathbf{B}_{bi}$  can be large if large gradients in the field-sweep rate are present along the cable in the coil.

The total field in the aperture of a magnet can be regarded as a superposition of the various field components:

$$\mathbf{B} = \mathbf{B}_{tr} + \mathbf{B}_{geo} + \mathbf{B}_m + \mathbf{B}_{if} + \mathbf{B}_{nucd} + \mathbf{B}_{is} + \mathbf{B}_{bi} \quad [\text{T}], \quad (7.1)$$

with  $\mathbf{B}_{tr}$  the field produced by the transport current, flowing uniformly in the cable. The coupling-current induced field error  $\mathbf{B}_{cc}$  is given by those components that are proportional to  $\dot{B}_{ce}$ :

$$\mathbf{B}_{cc} = \mathbf{B}_{if} + \mathbf{B}_{is} + \mathbf{B}_{bi} \quad [\text{T}]. \quad (7.2)$$

This chapter mainly deals with these three field distortions quantified in the straight part of the magnet.

In section 7.2 the methods are presented by which the fields  $\mathbf{B}_{if}$ ,  $\mathbf{B}_{is}$  and  $\mathbf{B}_{bi}$  are calculated. In sections 7.3-7.5 the magnitudes of  $\mathbf{B}_{if}$ ,  $\mathbf{B}_{is}$  and  $\mathbf{B}_{bi}$  are presented for the particular case of LHC dipole magnets. It is shown that when  $R_c$  of the cable is specified, predictable and limited, the lower field harmonics of  $\mathbf{B}_{is}$  can meet the requirements concerning the field quality of a magnet. The effect of a non-uniform  $R_c$  between the two poles of an aperture on field  $\mathbf{B}_{is}$  is dealt with. Large variations in  $R_c$  between the two poles of an aperture are deduced from the loss measurements as presented in chapter 6. It is shown that the magnitude of  $\mathbf{B}_{bi}$  is hard to assess since the BICCs are caused by numerous  $\dot{B}$ - and  $R_c$ -variations in the various turns of the coils.

In section 7.6 several methods are discussed by which the coupling-current induced fields can be determined and distinguished from each other. Experimental results are presented of the field errors  $\mathbf{B}_{cc}$  observed in four LHC dipole magnets. An estimate is given of the individual components  $\mathbf{B}_{is}$  and  $\mathbf{B}_{bi}$  by analysis of the time dependence and variations in the axial direction of field  $\mathbf{B}_{cc}$ .

## 7.2 Calculating coupling-current induced field distortions

### Field $\mathbf{B}_{if}$

According to eqs. 3.18 and 3.20, the IFCCs in a strand with a round cross-section, subject to a ramped field  $B_{\perp s}$  normal to the strand axis (i.e. in the  $y$ -direction), can be represented by two net coupling currents:

$$I_{if} = \pm \frac{2\tau_{if} d_s^*}{\mu_0} B_{\perp s} \quad [\text{A}], \quad (7.3)$$

flowing at either side of the strand. In order to calculate the field caused by these currents, they are located at their centre of gravity, i.e. at distances  $x = \pm \pi d_s^*/8$  from the centre of the strand [Avest, ter, '91]. The currents  $I_{if}$  in the strands of a coil turn will gradually increase and decrease since the field varies across the cable width. It is therefore more convenient to calculate the field  $\mathbf{B}_{if}$  taking the currents in each *strand position* (see Fig. 5.5) instead of the currents in each *strand*. The small field contribution in the  $z$ -direction is disregarded here because the fields in the  $z$ -direction caused by all the strand currents in the cable cancel almost completely (at least in the straight part of the magnet).

According to the law of Biot and Savart, the field at a position  $\mathbf{z} = x + iy$  caused by a current  $I_{if}$  at position  $\mathbf{r} = x_1 + iy_1$  is:

$$\mathbf{B}_{if} = \frac{\mu_0 I_{if}}{2\pi(\mathbf{z} - \mathbf{r})} \quad [\text{T}]. \quad (7.4)$$

The iron yoke which surrounds the collars enhances the field. When the yoke is not saturated, its permeability is uniform, and the inner boundary is a perfect cylinder. The increase in the field can then be calculated using the image-current method [Hague, '62], which implies that for a line current  $I$  located at position  $\mathbf{r}$  inside a yoke of radius  $R_{ir}$  and relative permeability  $\mu$ , an image current  $I^*$  with magnitude:

$$I^* = \frac{\mu - 1}{\mu + 1} I \cong I \quad [\text{A}] \quad \text{for } \mu \gg 1, \quad (7.5)$$

is located at position:

$$\mathbf{r}^* = \frac{R_{ir}^2}{r} \mathbf{r} \quad [\text{m}]. \quad (7.6)$$

The field  $\mathbf{B}_{if}$  caused by the current  $I_{if}$  is thus the sum of the fields created by the current itself and the image current:

$$\mathbf{B}_{if} = \frac{\mu_0}{2\pi} \left( \frac{I_{if}}{(z-r)} + \frac{I_{if}^*}{(z-r^*)} \right) [\text{T}]. \quad (7.7)$$

In the aperture of a magnet, where  $|z| < |r|$ , eq. 7.7 can be expanded into a Taylor series:

$$\mathbf{B}_{if} = -\frac{\mu_0 I_{if}}{2\pi} \left( \frac{1}{r} \sum_{n=1}^{\infty} (z/r)^{n-1} + \frac{1}{r^*} \sum_{n=1}^{\infty} (z/r^*)^{n-1} \right) [\text{T}]. \quad (7.8)$$

Eq. 7.8 can be rewritten as:

$$\begin{aligned} \mathbf{B}_{if} &= -\frac{\mu_0 I_{if}}{2\pi r} \sum_{n=1}^{\infty} (1 + (r/R_{ir})^{2n}) (z/r)^{n-1} \\ &= -\frac{\mu_0 I_{if}}{2\pi r_0} \sum_{n=1}^{\infty} (1 + (r/R_{ir})^{2n}) (r_0/r)^n (z/r_0)^{n-1} [\text{T}], \end{aligned} \quad (7.9)$$

showing that all multipoles are present in the field produced by a single line current. The total field  $\mathbf{B}_{if}$  in a magnet is calculated by summation of the individual fields (i.e. eq. 7.9) over all the strand positions in each turn of the cross-section of the coils.

#### Field $\mathbf{B}_{is}$

In chapter 4 it is shown that the ISCCs can be regarded as currents flowing along a zigzag path parallel to the cable axis. Away from the cable, the field produced by the zigzag currents can be well approximated by an infinitely long straight current-line  $I_s$  located at the centre of the zigzag path and normal to the  $x$ - $y$  plane. Again, the small contribution of the field in the  $z$ -direction is disregarded.

The field  $\mathbf{B}_{is}$  caused by the zigzag current  $I_s$  is then calculated in exactly the same way as the field  $\mathbf{B}_{if}$  in the case of a current  $I_{if}$ . The total field is calculated by summation of all the fields caused by all the ISCCs in each turn of the coil.

#### Field $\mathbf{B}_{bi}$

The field errors caused by the BICCs are difficult to calculate. First of all, the BICCs in the whole magnet have to be calculated taking into account the  $R_c$ - and  $\tilde{B}_1$ -distributions along the cable length and across the cable width. Each strand is then subdivided into four segments per cable pitch corresponding to the four faces of the cable (see Fig. 7.1).

In a strand segment the BICC is assumed to be constant which is valid if  $\xi \gg L_{p,s}/2$  (regime A, see eq. 5.4) or  $l_{cab} \gg L_{p,s}/2$  (regime B, see eq. 5.9). The field at the origin caused by a current  $I_{bi}$  in a segment situated between the positions  $\mathbf{r}_1 = (x_1, y_1, z_1)$  and  $\mathbf{r}_2 = (x_2, y_2, z_2)$  satisfies [Durand, '68]:

$$\mathbf{B}_{bi} = \frac{\mu_0 I_{bi}}{4\pi} \frac{(\mathbf{r}_1 + \mathbf{r}_2) \mathbf{r}_1 \times \mathbf{r}_2}{r_1 r_2 (r_1 r_2 + \mathbf{r}_1 \cdot \mathbf{r}_2)} [\text{T}]. \quad (7.10)$$

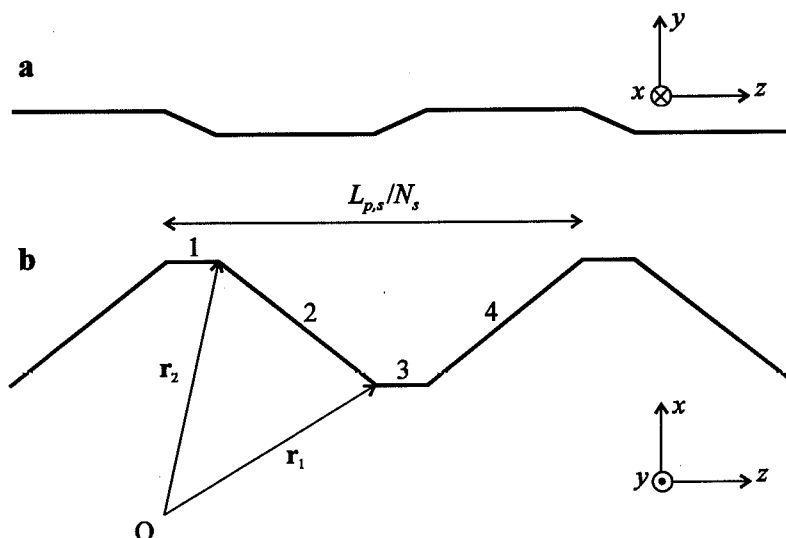


**Figure 7.1.** Calculation of the field in point O caused by a current in a strand of a Rutherford-type cable by considering the four faces of the cable separately. a. front view of the side face. b. front view of the top face.

The total field in the aperture of the magnet is calculated by summation of the fields produced by the BICCs of each strand segment of each turn. The  $z$ -component of  $\mathbf{B}_{bi}$  is disregarded since the fields in the  $z$ -direction caused by the four strand segments cancel almost completely.

A multipole expansion of  $\mathbf{B}_{bi}$  of the order  $n$  is obtained by a Fourier analysis of the fields calculated on at least  $2n$  places at a given radius relative to the magnet axis. All multipole components of  $\mathbf{B}_{bi}$  exhibit a characteristic time which is related to the characteristic time  $\tau_{bi,av}$  of the BICCs. An upper limit of the time constant can be estimated using Fig. 5.16 or eq. 5.14, assuming that the BICCs flow through the entire cable. For example the maximum  $\tau_{bi}$  for the inner coil of a 1 m long LHC dipole model with  $N_s=26$ ,  $L_{p,s}=0.13$  m,  $R_c=4 \mu\Omega$ ,  $l_{cab,1}=l_{cab,2}=12$  m is of the order of  $10^4$  s. The characteristic time can be considerably smaller if the BICCs decay quasi-exponentially and can be estimated using eq. 5.13. The characteristic time can also be reduced due to the mutual interaction between the BICCs of neighbouring turns as discussed in section 5.4.3.

### Field $\mathbf{B}_{nucd}$

The field caused by a NUCD among the strands is calculated in exactly the same way as the field  $\mathbf{B}_{bi}$ . The magnitudes of all the multipole components are unpredictable, since the joint resistances are unknown and the fields caused by the BICCs in the various turns partially cancel. Field  $\mathbf{B}_{nucd}$  is proportional to the transport current if the ratio between the joint resistances of the strands is independent of the excitation level, up to currents near the critical current, where the strand resistivity itself starts to affect the total strand resistance (see section 5.2).

### 7.3 Field $\mathbf{B}_{if}$ in dipole magnets

The field  $\mathbf{B}_{if}$  of two LHC dipole magnet designs is calculated for a central-field-sweep rate  $\dot{B}_{ce}=0.01 \text{ Ts}^{-1}$ . The matrix resistivity is assumed to be constant over the cross-section of the coil so that  $\tau_{if}$  is also constant. This implies that, during a field sweep, besides a current  $I_{if}$  at position  $(r, \phi)$ , a current  $I_{if}$  is also present at  $(r, -\phi)$  and currents of magnitude  $-I_{if}$  at  $(r, \pi-\phi)$  and at  $(r, \pi+\phi)$ . Therefore, the  $I_{if}$ -distribution follows the symmetry of the main field so that only the normal odd harmonics  $B_1, B_3, B_5, \dots$  are generated.

The multipole components of  $\mathbf{B}_{if}$  are presented in Table 7.1 at the reference position  $x_0=0.01 \text{ m}$ ,  $y_0=0$  in the aperture of the magnet and for a characteristic  $\tau_{if}$  of 0.025 s (see Table 3.2).

Similar to the IFCCs, field  $\mathbf{B}_{if}$  is proportional to  $\dot{B}_{ce}$  and  $\tau_{if}$ . As a comparison, the total field  $\mathbf{B}_m$  due to the persistent currents in the filaments of the strands is also given at a central field of 0.58 T and a temperature of 1.9 K (calculations of the separate contributions for each block are given in [Wolf, '92]).

The results clearly show that for the PBD and WBD magnets, all the multipole components of  $\mathbf{B}_{if}$  are more than one order of magnitude smaller than those of  $\mathbf{B}_m$ . During operation of LHC, the relative harmonic components of  $\mathbf{B}_{if}$  at the start of the ramp (with  $B_{inj}=0.58 \text{ T}$ ,  $\dot{B}_{ce}=0.0066 \text{ Ts}^{-1}$ ) are smaller than  $10^{-5}$  while at higher excitation levels they further decrease by more than one order of magnitude. Therefore, the influence of the IFCCs on the field homogeneity of high-field accelerator magnets is negligible.

**Table 7.1.** Absolute field errors  $\mathbf{B}_{if}$  and  $\mathbf{B}_{is}$  for two LHC dipole designs at  $x_0=0.01 \text{ m}$ ,  $y_0=0$  for  $\tau_{if}=0.025 \text{ s}$ ,  $R_c=1 \mu\Omega$ ,  $L_{p,s}=0.1 \text{ m}$  and  $\dot{B}_{ce}=0.01 \text{ Ts}^{-1}$ . As a comparison, the field  $\mathbf{B}_m$  (at 1.9 K) due to the persistent currents is included for  $B_{ce}=0.58 \text{ T}$ , calculated for the given filament diameters [Verweij, '92/'94]. Note that the units vary from  $10^{-4} \text{ T}$  to  $10^{-6} \text{ T}$ .

Pink Book Dipole magnet.		Inner coil: $d_f=5 \mu\text{m}$ .			Outer coil: $d_f=5 \mu\text{m}$ .			$\mathbf{B}_m$ Total
$n$	Units	$\mathbf{B}_{if}$ Inner coil	Outer coil	Total	$\mathbf{B}_{is}$ (see section 7.4) Inner coil	Outer coil	Total	
$B_1$	$10^{-4} \text{ T}$	+0.10	+0.041	+0.14	+58	+7.3	+65	-4.2
$B_3$	$10^{-4} \text{ T}$	-0.044	-0.013	-0.057	+2.0	+0.1	+2.1	-2.3
$B_5$	$10^{-5} \text{ T}$	+0.065	-0.0068	+0.058	-1.8	-0.31	-2.1	+1.5
$B_7$	$10^{-6} \text{ T}$	-0.031	+0.0031	-0.028	-0.018	+0.0036	-0.015	-0.92
$B_9$	$10^{-6} \text{ T}$	+0.015	+0.00017	+0.015	+0.43	+0.007	+0.44	+0.41
White Book Dipole magnet.		Inner coil: $d_f=7 \mu\text{m}$ .			Outer coil: $d_f=6 \mu\text{m}$ .			$\mathbf{B}_m$ Total
$n$	Units	$\mathbf{B}_{if}$ Inner coil	Outer coil	Total	$\mathbf{B}_{is}$ (see section 7.4) Inner coil	Outer coil	Total	
$B_1$	$10^{-4} \text{ T}$	+0.052	-0.011	+0.041	+51	+9.1	+60	-6.3
$B_3$	$10^{-4} \text{ T}$	-0.024	-0.013	-0.037	+1.6	+0.016	+1.6	-2.1
$B_5$	$10^{-5} \text{ T}$	+0.033	-0.0019	+0.031	-0.34	-0.24	-0.57	+1.0
$B_7$	$10^{-6} \text{ T}$	-0.046	+0.0035	-0.043	-0.82	+0.15	-0.67	-1.8
$B_9$	$10^{-6} \text{ T}$	+0.012	-0.000015	+0.012	+0.24	+0.0026	+0.25	+0.43



## 7.4 Field $B_{is}$ in dipole magnets

It is shown in section 4.4.1 that the ISCCs in a Rutherford-type cable are mainly caused by a field change  $\dot{B}_\perp$  normal to the cable width. The steady-state distribution of the ISCCs across the cable width for a uniform  $\dot{B}_\perp$  is given by eq. 4.20:

$$I_s(x) = 0.0415 \frac{L_{p,s} w N_s}{R_c} \dot{B}_\perp \cos(\pi x / w) \quad [\text{A}], \quad (7.11)$$

where  $x$  varies between  $w/N_s$  and  $(w-w/N_s)$ . The sinusoidal pattern of the ISCCs is slightly influenced if  $\dot{B}_\perp$  varies across the cable width and is strongly influenced if  $\dot{B}_\perp$  changes sign across the width (see section 4.7). The steady-state ISCCs can be calculated for each turn taking into account the local  $\dot{B}_\perp$ -distribution across the cable width. The field change  $\dot{B}_{\perp,i}$  for turn  $i$  can then be written as a function of the central-field-sweep rate  $\dot{B}_{ce}$ :

$$\dot{B}_{\perp,i} = \beta_{I,i} \dot{B}_{ce} \quad [\text{Ts}^{-1}], \quad (7.12)$$

with  $\beta_{I,i}$  the field geometry factor that depends on the shape of the field variation  $\dot{B}_\perp$  across the cable width of turn  $i$ . The  $\beta_{I,i}$ -values are shown in Fig. 7.2.

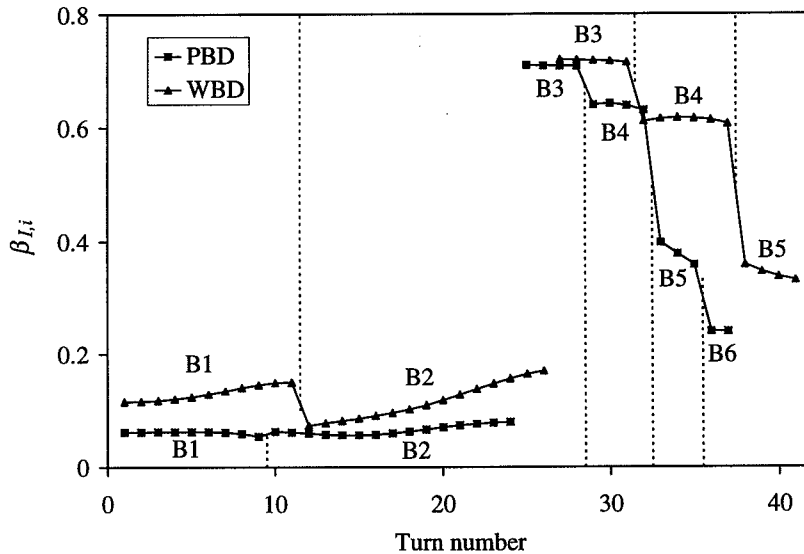


Figure 7.2. The field geometry factor  $\beta_I$  for each turn of the PBD and WBD magnets. The labels indicate the block number.

The maximum  $\beta_I$  of about 0.7 occurs near the midplane and is a representative value of accelerator dipole magnets with a 'two-shell' geometry (see section 2.2). The  $\beta_I$ -values of blocks 1 and 2 can be used to calculate the maximum ISCC in each turn but the pattern is no longer sinusoidal because  $\dot{B}_\perp$  changes sign across the cable width. The distribution of the ISCCs over the cross-section of one quadrant of the 5-block LHC dipole design (WBD

magnet) is illustrated in Fig. 7.3. In the case of excitation of the magnet, the ISCCs near the aperture for the inner coil, and almost everywhere in the outer coil have the same sign as the transport current. During de-excitation the ISCCs reverse sign while the transport current, of course, does not.

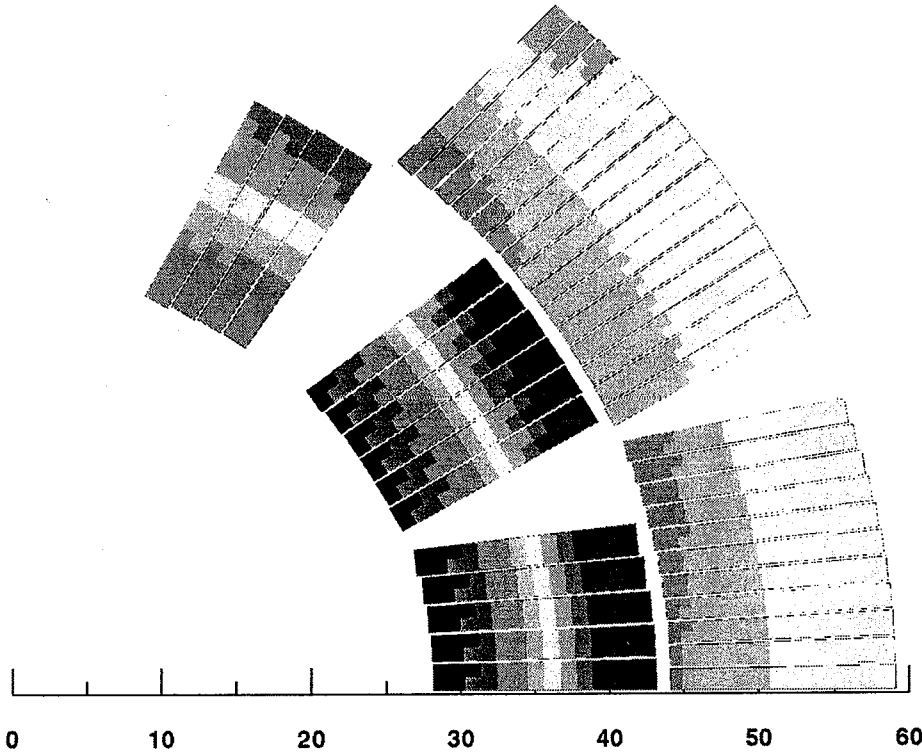


Figure 7.3. The distribution of the ISCCs over the cross-section of a WBD magnet with constant  $R_c$  in the coils. The dark colours indicate large positive or negative currents.

The  $I_s$ -distribution in a dipole coil with a symmetric  $R_c$ -distribution around the midplane also follows the symmetry of the main field, similar to the IFCCs, so that only the normal odd harmonics  $B_1, B_3, B_5, \dots$  are generated. These multipoles are calculated for the PBD and WBD magnets with  $R_c = 1 \mu\Omega$  and  $L_{p,s} = 0.1$  m and presented in Table 7.1. Similar to the ISCCs, the field errors are proportional to  $L_{p,s}$  and  $\dot{B}_{ce}$  and inversely proportional to  $R_c$ . The difference between the fields  $\mathbf{B}_{is}$  of the two designs is small. Field  $\mathbf{B}_{is}$  is much larger than field  $\mathbf{B}_{if}$  (for  $R_c < 10 \mu\Omega$ ), especially for the lower harmonics. Hence, field  $\mathbf{B}_{if}$  can be neglected in eq. 7.2 compared to field  $\mathbf{B}_{is}$  for all the dipole model magnets given in Table 2.3.

The relative dipole component at small excitation levels is large which causes a difference between the dynamic and static main-field component at the start of the ramp. This causes a tune shift since the fundamentals of the quadrupole and dipole magnets may change considerably at the start of the ramp. In the case of the LHC dipole magnets  $R_c$

should be at least 50-100  $\mu\Omega$  to achieve an acceptable tune shift at the start of the ramp, assuming a constant field-sweep rate  $\dot{B}_{ce}=0.0066 \text{ Ts}^{-1}$  [Verweij, '94]. Also the relative sextupole component of  $\mathbf{B}_{is}$  is a few times  $10^{-4}$  at the start of the ramp and is of the same order but opposite to that of field  $\mathbf{B}_m$ . An  $R_c$ -value larger than 10  $\mu\Omega$  is preferable in order to keep all the higher multipole components of  $\mathbf{B}_{is}$  about one order of magnitude smaller than those of  $\mathbf{B}_m$ . The results, as surveyed in Table 7.1, show that the main contribution to field  $\mathbf{B}_{is}$  is related to the ISCCs in the inner coil. Hence, especially the  $R_c$  of the inner coil has to be sufficiently large in order to meet the field specifications of a 'two-shell' magnet.

A decrease of the field-sweep rate (especially near injection, where the relative field errors are large) also reduces  $\mathbf{B}_{is}$  since the ISCCs are proportional to  $\dot{B}_{ce}$ . This, however, decreases the effective running time of the accelerator and very small field-sweep rates should therefore be avoided.

Not only should the mean  $R_c$  in a coil be limited but differences in  $R_c$  between the magnets in the accelerator also have to be restricted in order to limit the variation in the main field between magnets (especially at the start of the ramp). A good reproducibility of  $R_c$  in all the cables of the magnets is necessary to meet this requirement.

The calculated dipole and sextupole components of  $\mathbf{B}_{is}$  of other accelerator dipole magnets (with a 'two-shell' geometry) are presented in Table 7.2.

**Table 7.2.** The absolute multipole components  $B_1$  and  $B_3$  caused by the ISCCs calculated for several accelerator dipole magnets at  $x_0=0.01 \text{ m}$ ,  $y_0=0$ . The central field increases at a rate of  $0.01 \text{ Ts}^{-1}$ . The fields are calculated for a uniform  $R_c$  of 1  $\mu\Omega$  as well as a uniform  $R_c^*$  of  $2.6 \mu\Omega\text{mm}^2$  (see eq. 4.27).

	LHC (PBD)	LHC (WBD)	SSC <sup>a</sup>	HERA	Tevatron <sup>a</sup>	RHIC <sup>a</sup>
Central field (T)	10	8.4	6.6	4.7	4.4	3.5
Cable width (mm)	17	15	12	10	7.8	9.7
Nr. of strands	26	28	30	24	23	30
$L_{p,s}$ (mm)	100	100	86	95	66	73
$R_c=1 \mu\Omega$						
$B_1 (10^{-4} \text{ T})$	65	60	62	17 (16 <sup>a</sup> )	6	7
$B_3 (10^{-4} \text{ T})$	2.1	1.6	4	0.8 (0.7 <sup>a</sup> )	0.3	0.4
$R_c^*=2.6 \mu\Omega\text{mm}^2$						
$B_1 (10^{-4} \text{ T})$	65	45	28	11	2	2
$B_3 (10^{-4} \text{ T})$	2.1	1.2	1.8	0.5	0.1	0.1

<sup>a</sup> [Devred, '94]

The field errors of the various magnets cannot be simply scaled to the cable geometry since field  $\mathbf{B}_{is}$  is a complicated function of both the cable geometry and the magnet geometry such as the number of turns and the diameter of the aperture. Note that  $R_c$  of the magnets will probably be rather different, even for identical surface conditions of the strand, since the average contact area of  $R_c$  varies significantly (see eq. 4.33). The fields are therefore also calculated for constant  $R_c^*$ , following  $R_c=R_c^*(N_s^2-N_s)/(L_{p,s}w)$  (see eq. 4.27). The latter values give a better picture of the variations in the field errors between the magnets for strands

with the same surface conditions. It is clear that the dipole and sextupole components increase strongly for an increase in the cable width. In practical accelerator dipole magnets (with a 'two-shell' geometry) the cable width is, in first approximation, proportional to the central field (see Fig. 1.1). An important conclusion is therefore that the contact resistance of a cable has to be larger to meet the field specifications in accelerator dipole magnets with a larger field. For 'three- or four-shell' geometries  $R_c$  can be relatively smaller.

Additional field distortions caused by the ISCCs are present if  $R_c$  varies over the cross-section of the coils. In the case that both poles of an aperture have different contact resistances  $R_{c,P1}$  and  $R_{c,P2}$ , skew-even multipoles are induced (as illustrated in section 2.2), which are given in Table 7.3 for the PBD and WBD magnets.

**Table 7.3.** Absolute field errors  $B_{is}$  for LHC dipole magnets at  $x_0=0.01$  m,  $y_0=0$  for  $\dot{B}_{ce}=0.01$  Ts<sup>-1</sup>,  $R_{c,P1}=2/3$   $\mu\Omega$ ,  $R_{c,P2}=2$   $\mu\Omega$  and  $L_{p,s}=0.1$  m. The normal-odd multipoles are exactly the same as those given in Table 7.1. Note that the units vary from  $10^{-4}$  T to  $10^{-6}$  T.

	Units	PBD			WBD		
		Inner coil	Outer coil	Total	Inner coil	Outer coil	Total
$A_2$	$10^{-4}$ T	-17	-1.6	-18	-15	-2.4	-17
$A_4$	$10^{-4}$ T	-1.9	-0.094	-2.0	-1.4	-0.11	-1.5
$A_6$	$10^{-5}$ T	-1.4	+0.0075	-1.4	-1.1	+0.00026	-1.1
$A_8$	$10^{-6}$ T	-1.3	+0.0046	-1.3	-0.56	-0.023	-0.59

While the normal-odd harmonics are proportional to  $(1/R_{c,P1} + 1/R_{c,P2})$ , the skew-even harmonics are proportional to  $(1/R_{c,P1} - 1/R_{c,P2})$ . This implies that the sign of the normal-odd harmonics is likely to be equal for all the magnets in an accelerator while the sign of the skew-even multipoles of  $B_{is}$  will vary from magnet to magnet if differences in  $R_c$  of the two poles have a non-systematic cause. Table 7.3 shows that especially the  $A_2$  and  $A_4$  components of  $B_{is}$  are large compared to values of a few times  $10^{-4}$  which are usually regarded as just acceptable. Hence, the difference between the average  $R_c$  of the two poles of an aperture has to be limited in order to meet the field specifications of the magnets. These harmonics can be reduced by one order of magnitude by using either cables with  $R_c > 10$   $\mu\Omega$  or cables for which  $R_c$  is almost constant and uniform so that  $|1/R_{c,P1} - 1/R_{c,P2}| < 10^5$   $\Omega^{-1}$ .

In practical coils each turn of each quadrant of an aperture is likely to have a different average  $R_c$ , which implies that a field sweep will also result in normal-even and skew-odd multipoles. In theory, the  $R_c$ -distribution over the cross-section of the magnet can then be calculated if the multipole components of  $B_{is}$  are known. In practice, even for small  $R_c$ ,  $B_{is}$  can only be determined up to about ten multipoles which implies that there are much more unknown local  $R_c$ -values than known multipole components. Only with additional assumptions (such as minimisation of the difference in  $R_c$  between adjacent turns) can a rough estimate of the  $R_c$ -distribution be obtained. The measured multipole components of  $B_{is}$  in several SSC dipole magnets have been used to estimate the  $R_c$ -distribution over the cross-section of the coils in the magnet [Ogitsu, '92a], [Devred, '94]. This approach is not

used in this chapter since the results would be too speculative, especially if field  $\mathbf{B}_{bi}$  is large compared to  $\mathbf{B}_is$ .

## 7.5 Field $\mathbf{B}_{bi}$ in dipole magnets

It can be calculated (using the method as described in section 7.2) that the field  $\mathbf{B}_{bi}$  caused by the BICCs in a single straight cable varies with a sinusoidal shape along the cable. Field  $\mathbf{B}_{bi}$  in a magnet is caused by many BICCs flowing in each turn, and will also have a sinusoidal shape since a superposition of sine functions is also a sine function.

The magnitude of the BICCs (and therefore the amplitude of  $\mathbf{B}_{bi}$ ) is, however, difficult to calculate since it depends strongly on the  $R_c$ - and  $\rho_s$ -distributions over the cross-section of the coils, which are both more or less unknown. Furthermore, according to section 5.5, the magnitude of the BICCs depends strongly on the ratio between the length of the field variations with respect to the cable pitch. Consider, for example, the BICCs caused by the two coil ends in one turn of a 10 m long dipole magnet, with a straight part of  $100L_{p,s}$ . The magnitude of the BICCs could change completely if the number of twist pitches in the straight part of the magnet between the two coil ends changes by 0.5. An increase (decrease) of only 0.5% in  $L_{p,s}$ , which implies that the straight part would correspond to  $99.5L_{p,s}$  ( $100.5L_{p,s}$ ), results in a considerable change in the magnitude of the BICCs, and hence  $\mathbf{B}_{bi}$  (unless, of course, the BICCs decay with a characteristic length smaller than about half the magnet length, i.e.  $\xi < 50L_{p,s}$  in this case). Since the fabrication tolerances of the cable pitch are often larger than 0.5%, the field  $\mathbf{B}_{bi}$  in similar magnets can be rather different.

The following remarks can be made:

- The amplitude of the multipole components of  $\mathbf{B}_{bi}$  in high-field accelerator dipole magnets can easily attain values of  $10^{-4}$  to  $10^{-3}$  T for  $\dot{B}_{ce}=0.01 \text{ Ts}^{-1}$ . Simulations show that large BICCs usually result in large values of *all* multipoles of  $\mathbf{B}_{bi}$ . It is, however, possible that only some harmonics are affected while others are not.
- The phase of the sinusoidally varying field  $\mathbf{B}_{bi}$  is usually different for each harmonic component.
- An amplitude modulation in  $\mathbf{B}_{bi}$  will occur if the transposition twists of the cables in the inner and outer coils are different since, in that case, the period of the BICC pattern in both coils is different.
- Large skew-even multipoles of  $\mathbf{B}_{bi}$  are likely to occur due to the  $180^\circ$  symmetry in the aperture (i.e. the two splices are located at  $180^\circ$  from each other, so either in quadrants Q1 and Q3 or in quadrants Q2 and Q4, see Fig. 2.2a). This implies that, if a BICC is present at position  $(r, \phi)$  it is likely that a BICC is also present at position  $(r, \pi + \phi)$ , which corresponds to the characteristic current pattern of skew-even multipoles.

Note that, although the amplitude of field  $\mathbf{B}_{bi}$  can be large, the integral value of  $\mathbf{B}_{bi}$  over the entire length of the magnet is almost zero. The effect of sinusoidally varying fields on the particle motion is not well-known and it is beyond the scope of this thesis to investigate this. In section 7.7.5 the field  $\mathbf{B}_{bi}$ , as estimated from the field distortion  $\mathbf{B}_{cc}$ , in four LHC dipole model magnets is presented in order to have a first quantitative estimate of the magnitude of the field.

## 7.6 Experimental methods to determine $B_{cc}$

In the aperture of a magnet, only the sum of the magnetic fields caused by all the currents in the coil can be measured as given by eq. 7.1. Common methods to measure this field are:

- Rotating pick-up coils (RPCs). The voltage over a coil, rotating in the aperture, is integrated over given angular intervals. The main field harmonics can be determined using a fast Fourier transformation of the integrated voltages. Detailed descriptions of the method are given in the literature (for example [Walckiers, '92]).
- Fixed pick-up coils (FPCs). Integration of the voltage over a non-rotating coil gives the flux perpendicular to the coil surface. A field of order  $n$  can be determined by a combination of  $n$  FPCs located at intermediate angles of  $360^\circ/n$  in accordance with Fig. 2.1.
- Hall probes. A specific multipole component can be determined with  $n$  Hall probes in a similar configuration to that for the FPCs.

The various contributions to the total field (see eq. 7.1) can be separated by considering the characteristics of the currents that cause them. In Table 7.4 these characteristics with respect to the excitation level, the field-sweep rate and the  $z$ -position are presented. The characteristic time denotes the period during which the fields decay once the field sweep is finished.

**Table 7.4.** Survey of the characteristics of the various field distortions in superconducting magnets. The characteristic times are typical values calculated in the case of an LHC dipole magnet.

Field	Origin	Dependence on the field	Dependence on $\dot{B}_{ce}$	Dependence on the $z$ -position	Char. time
$B_{geo}$	Fabr. tolerances	Yes	No	Possible, but not sinusoidal	$\rightarrow 0$
$B_m$	Pers. currents	Yes	No	No	$\rightarrow \infty^a$
$B_{if}$	IFCCs	Yes	Linear	No	$< 0.2$ s
$B_{nucd}$	NUCD	Yes	No	Sinusoidal with period $L_{p,s}$	$>> 10$ s
$B_{is}$	ISCCs	No	Linear	Possible, but not sinusoidal	$< 10$ s
$B_{bi}$	BICCs	Yes	Linear	Sinusoidal with period $L_{p,s}$	$>> 10$ s

<sup>a</sup> The estimated effect of the flux creep is about 2% per decade in time

According to Table 7.4, the fields  $B_{geo}$ ,  $B_m$ ,  $B_{if}$  and  $B_{is}$ , that do not vary sinusoidally in the axial direction can be determined with a RPC or FPC with a coil length equal to  $k \cdot L_{p,s}$  ( $k=1, 2, 3, \dots$ ). A combination of two Hall probes spaced  $(k+0.5)L_{p,s}$  apart in the axial direction is also insensitive to the magnitudes of  $B_{nucd}$  and  $B_{bi}$  (if the amplitudes of  $B_{nucd}$  and  $B_{bi}$  are  $z$ -independent). For small field-sweep rates, the measured field errors are dominated by  $B_{geo}$  and  $B_m$  which can be separated since:

- $B_m$  is relatively large at weak excitation levels while  $B_{geo}$  is relatively large at strong excitation levels.
- The persistent currents at 1.8 K are significantly larger than those at 4.3 K (at the same field) since the critical current at 1.9 K is about 50% larger than at 4.3 K. Field  $B_{geo}$  remains unchanged between 4.3 K and 1.9 K.

The ramp-rate-dependent fields  $B_{if}$  and  $B_{is}$  can be determined by measuring the field as a function of the field-sweep rate, as illustrated in Fig. 7.4. Fields  $B_{if}$  and  $B_{is}$  cannot be separated experimentally. The  $R_c$ -values of the magnets of which the field errors are presented in section 7.7 are smaller than  $10 \mu\Omega$  so that  $B_{if}$  is negligible compared to  $B_{is}$  (see Table 7.1).

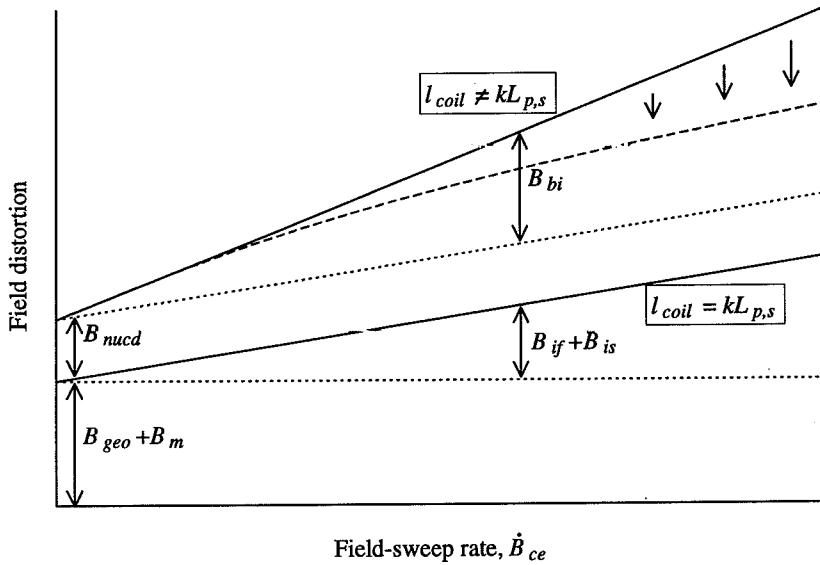


**Figure 7.4.** The various field distortions as functions of the field-sweep rate for different lengths of the pick-up coil. The arrows  $\downarrow$  indicate that field  $B_{bi}$  becomes smaller than the steady-state value if the time of the field sweep is small compared to the characteristic time of the BICCs.

Fields  $B_{nucd}$  and  $B_{bi}$  can be deduced from a field measurement with a coil length unequal to  $kL_{p,s}$ . Both fields can be separated by performing field measurements as a function of the field-sweep rate as illustrated in Fig. 7.4. The most accurate method to deduce  $B_{nucd}$  and  $B_{bi}$  is by means of RPCs which can move along the magnet axis. The length of the coil should be small compared to the cable pitch.

Specific field harmonics can also be determined with longitudinally moving Hall probes or FPCs. The amplitude of the sinusoidally varying field errors is related to  $B_{nucd}$  and  $B_{bi}$ . A configuration of three Hall probes, which could move along the magnet axis, was successfully used to determine small variations of the normal- and skew-sextupole components in the HERA dipole magnets (Brück, '91).

Note that the actual  $B$ - $\dot{B}_{ce}$  curve will deviate from a straight line (see Fig. 7.4) at larger  $\dot{B}_{ce}$  i.e. at smaller ramp times because the BICCs, having large characteristic times, cannot attain their steady-state magnitudes during the ramp.

It is possible as well, to distinguish the different field components by analysis of the decay of the field variations in time, as will be shown in section 7.7.1.

## 7.7 Experimental results of field $B_{cc}$ in LHC dipole magnets

In the following sections it will be shown that the ISCCs and the BICCs cause considerable field distortions in dipole magnets. In sections 7.7.1-7.7.4 experimental results are presented of fields  $B_{is}$  and  $B_{bi}$  in four LHC dipole model magnets. Field  $B_{if}$  is disregarded since the  $R_c$ -values of the magnets are between 1 and  $6 \mu\Omega$  so that  $B_{if} \ll B_{is}$  (see Table 7.1). The results are obtained on only a few magnets and are used to obtain a first quantitative estimate of the ramp-rate-induced field errors.

The presentation is difficult to survey because the field in the aperture of the magnets is measured by different methods and often under different conditions (see Table 7.5). Furthermore, the measurements are performed using sets of existing non-ideal pick-up coils, with lengths varying between 30 mm and 2000 mm.

**Table 7.5.** Survey of the type of field measurements which were performed to estimate the field errors  $B_{is}$  and  $B_{bi}$  in four LHC dipole model magnets.  
#Pos denotes the number of  $z$ -positions and #SR denotes the number of field-sweep rates.

Magnet	Length (m)	Hall Probe		FPC			RPC		
		#Pos	#SR	Length (mm)	#Pos	#SR	Length (mm)	#Pos	#SR
CE1	1	1	12	200, 240	5	5	200, 240	5	5
EL2	1	-	-	-	-	-	200	3	3
AN2	10	-	-	750	1	4	30	9 & 5 <sup>a</sup>	1 & 3 <sup>a</sup>
AN3	10	-	-	2000	4 <sup>b</sup>	5	750	4 <sup>b</sup>	4

<sup>a</sup> 9 positions at 1 field-sweep rate and 5 positions at 3 sweep rates

<sup>b</sup> 2 positions per aperture

Measurements on two 1 m long magnets are performed with pick-up coils at five fixed positions on the axis of the magnet. Two coils, with lengths of 240 mm, cover the ends of the magnet and are referred to as H12 (near the connection end, see Fig. 2.3) and H67 (near the non-connection end). Three coils, with lengths of 200 mm, cover the straight part and are denoted by H3, H4 and H5. The space between the coils is about 4 mm in the axial direction. The lengths of the coils in the straight part correspond to about  $1.5L_{p,s}$ , so that both  $B_{is}$  and  $B_{bi}$  are measured.

The measurement bench for the 10 m long magnets is provided with a RPC which can be moved in the axial direction. Measurements have been performed with a 750 mm long coil as well as a 30 mm long coil. The axial direction is denoted by  $z$  with  $z=9.252$  m the axial centre of the magnet. The coils can be moved between  $z=3.625$  m (connection end) and  $z=12.625$  m (non-connection end). Additionally, measurements are performed with four FPCs of 2000 mm length located in the aperture of the straight part of the 10 m long AN3 magnet.

In the following four sections the results of the field measurements on four magnets, specified in Table 7.5, are discussed. The presence of  $B_{is}$  and  $B_{bi}$  is demonstrated by analysis of the axial variations and the time dependence of  $B_{cc}$ . In section 7.7.5 a survey is given of the main experimental results.



### 7.7.1 1 m long CE1 magnet

The field component in the  $y$ -direction of the CE1 magnet during the second cool-down is determined using a Hall probe located at  $x=0$ ,  $y=23$  mm in aperture 1 of the magnet. During and after a field sweep from  $B_{ce,2}=3$  T to  $B_{ce,1}=0$  T the current as well as the Hall voltage are simultaneously measured for different field-sweep rates  $\dot{B}_{ce}$ . In order to express the field during the field sweep, eq. 7.1 is rewritten, assuming that the coupling currents are zero at the beginning of the field sweep:

$$B_y(t) = B_{tr,y} + B_{m,y} + B_{geo,y} + B_{nucd,y} + B_{is,0}(1 - e^{-t/\tau_{is}}) + B_{bi,0}(1 - e^{-t/\tau_{bi}}) \quad [\text{T}], \quad (7.13)$$

with  $\tau_{is}$  and  $\tau_{bi}$  the characteristic times of the ISCCs and the BICCs at position  $x=0$ ,  $y=23$  mm and  $t$  the time (with  $t=0$  at the start of the field sweep). The last two contributions can be distinguished by analysing the field after a ramp. A characteristic field variation after a ramp is shown in Fig. 7.5).

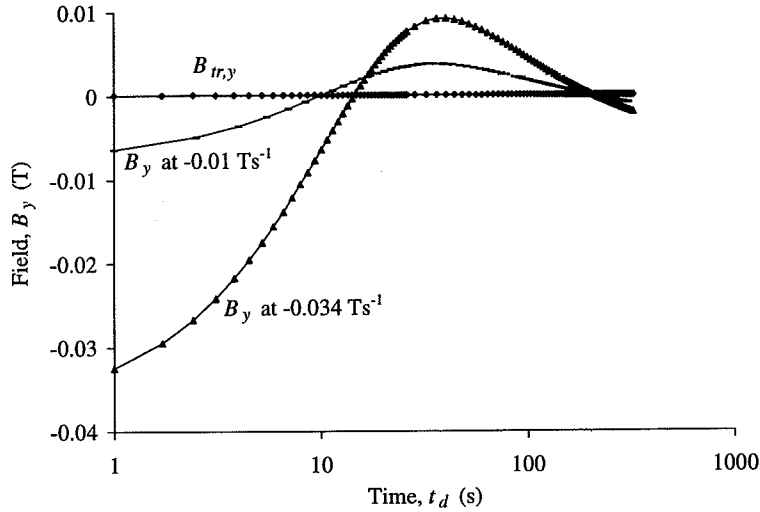


**Figure 7.5.** The field in the  $y$ -direction (see Fig. 2.2a) measured using a Hall probe located at  $x=0$ ,  $y=23$  mm in aperture 1 of the CE1 magnet after a ramp from 3 T to 0 T with  $\dot{B}_{ce}$  equal to  $-0.01$   $\text{T s}^{-1}$  and  $-0.034$   $\text{T s}^{-1}$ . The time  $t_d=0$  corresponds to the end of the ramp. The field produced by the transport current is smaller than 0.1 mT after the field sweep.

Note that the total field still varies, although the cable transport current is 0 (so that also  $B_{y,tr}$  is 0 and fields  $B_{y,m}$  and  $B_{y,geo}$  are constant). Assuming that field  $B_{y,nucd}$  remains constant after the ramp, the decay of the field, for all field-sweep rates, can be written as:

$$B_y(t_r, t_d) = C + B_{is,0}(1 - e^{-t_r/\tau_{is}})e^{-t_d/\tau_{is}} + B_{bi,0}(1 - e^{-t_r/\tau_{bi}})e^{-t_d/\tau_{bi}} \quad [\text{T}], \quad (7.14)$$

with  $C$  a constant,  $t_r = (B_{ce,2} - B_{ce,1})/\dot{B}_{ce}$  the total time of the field sweep and  $t_d$  the time after the field sweep. For all sweep rates the time constants  $\tau_{is}$  and  $\tau_{bi}$  are deduced to be 10 s and  $1.0 \cdot 10^2$  s respectively.

Fields  $B_{is,0}$  and  $B_{bi,0}$ , which are depicted in Fig 7.6, are proportional to  $\dot{B}_{ce}$  and have opposite sign. Both the local field  $B_{is,0}$  and the local time constant  $\tau_{is}$  are a factor of about 3 larger than the calculated mean values, assuming a uniform  $R_c$  of  $1.3 \mu\Omega$  as deduced from the AC-loss measurements (see Table 6.3). The difference implies that locally near the Hall probe  $R_c$  is smaller, which can be expected since the last turn of block 6 of this particular magnet is soldered and shunted by a copper strip. The calculated field for  $R_c=0.5 \mu\Omega$  is shown in Fig. 7.6 as well.

This result shows that fields  $\mathbf{B}_{is}$  and  $\mathbf{B}_{bi}$  can be distinguished by analysis of the time dependence of the total field after (but also during) a field sweep. Since the field is only measured at one longitudinal position, the amplitude of  $\mathbf{B}_{bi}$  remains unknown.

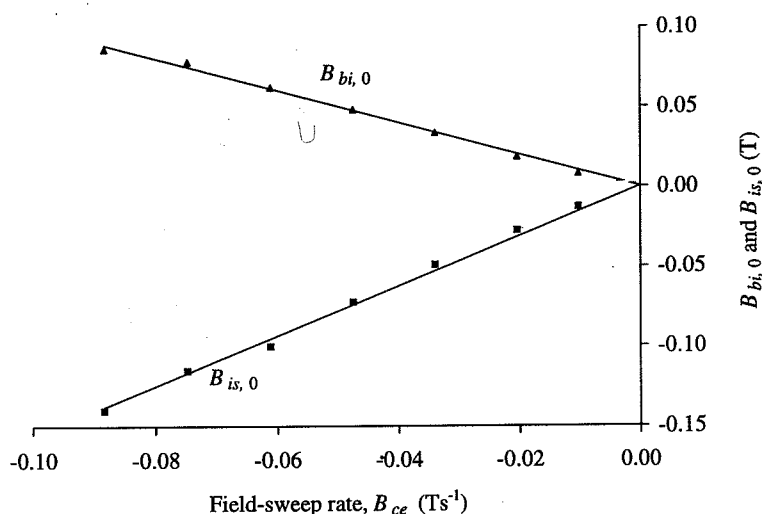


**Figure 7.6.** The field errors  $B_{is,0}$  and  $B_{bi,0}$  as functions of the field-sweep rate for the CE1 model, using a Hall probe located at  $x=0$ ,  $y=23$  mm. The line through the measured points  $B_{bi,0}$  is a best linear fit. The line through the measured points  $B_{is,0}$  is the calculated field error for  $R_c=0.5 \mu\Omega$ .

The FPCs are used to obtain a global value of  $B_{cc,y}$  in aperture 1 of the CE1 magnet (during the fourth cool-down). Field  $B_y$  is determined with the coils H12, H3, H4, H5 and H67 for field cycles between 2 and 5.4 T at five sweep rates between 0.027 and 0.082  $\text{Ts}^{-1}$ . The field error  $B_{cc,y}$  at a certain field during the ramp is deduced from the  $B_y - \dot{B}_{ce}$  curve (see Fig. 7.4) and depicted in Fig. 7.7.

Field  $B_{bi,y}$  is very small compared to field  $B_{is,y}$  (so that  $B_{cc,y}=B_{is,y}$ ) because:

- Field  $B_{cc,y}$  decays exponentially to 0 after the ramp with a time constant of about 6 s. There is no field contribution present that decays with the expected characteristic time of the BICCs of the order of  $10^2$  s.
- Field  $B_{cc,y}$  is proportional to  $\dot{B}_{ce}$ , also for small ramp times of only 40 s. According to Fig. 7.4 this implies that field  $B_{cc,y}$  is dominated by the field contribution caused by the ISCCs.

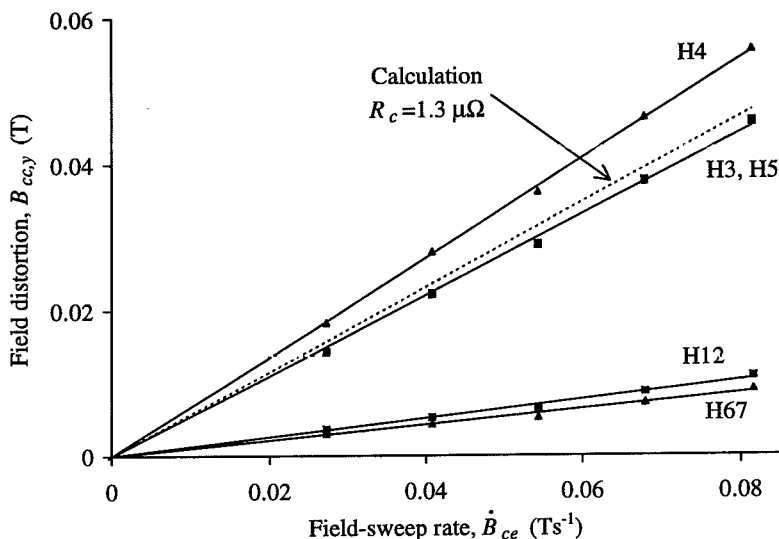


**Figure 7.7.** The field error  $B_{cc,y}$  in aperture 1 of the CE1 magnet as a function of the field-sweep rate, determined by means of FPCs located at five  $z$ -positions. The fields deduced using coils H3 and H5 correspond to within 1% of each other. The calculated field distortions for  $R_c = 1.3 \mu\Omega$  are shown by a dotted line.

Field  $B_{cc,y}$ , and hence  $R_c$ , are field-independent (between 2 and 5.4 T), which is expected according to the loss measurements (see Table 6.3). Field  $B_{cc,y}$  is small in the coil ends because the field component perpendicular to the cable width is small in the ends.

The calculated field distortion  $B_{is,y}$  (using Table 7.1 with  $R_c = 1.3 \mu\Omega$  as given by Table 6.3) agrees very well with the average field  $B_{cc,y}$  in the straight part of the magnet (that is the average of the fields determined using coils H3, H4, H5). An important conclusion is therefore that the field error  $B_{is,y}$  can be well calculated from the average  $R_c$  and conversely.

The higher harmonics of  $\mathbf{B}_{cc}$  are determined by means of RPCs for field cycles between 0.4 and 8.2 T at five field-sweep rates between 0.0068 and 0.034  $\text{Ts}^{-1}$ . A characteristic series of measurements is shown in Fig. 7.8 where the skew-quadrupole field  $a_2$  (normalised to the central field) is depicted during the ramp-up and ramp-down for several field-sweep rates. The  $a_2$  component increases with decreasing field since the ISCCs (and hence the skew-quadrupole field  $A_2$ ) are field-independent. Note that  $a_2$  for  $\dot{B}_{ce} = 0.0066 \text{ Ts}^{-1}$  (as anticipated for the operation of LHC) is larger than  $10^{-3}$  at small fields and therefore about one order of magnitude larger than the value that is usually regarded as being acceptable.

The magnitudes of the harmonic components of  $\mathbf{B}_{cc}$  are deduced from the  $B_n - \dot{B}_{ce}$  and  $A_n - \dot{B}_{ce}$  curves, as illustrated in Fig. 7.4. The multipole components for  $n=2, 3, 4$  and 5 are shown in Fig. 7.9, scaled to a field-sweep rate of 0.01  $\text{Ts}^{-1}$ .

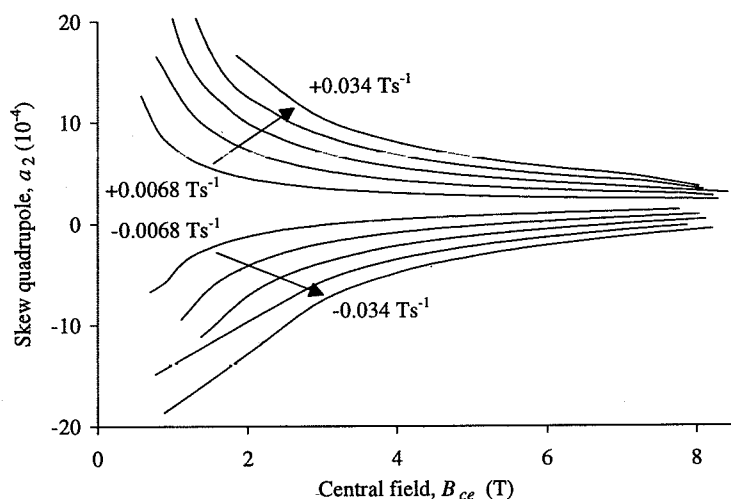


**Figure 7.8.** The normalised skew-quadrupole component of the CE1 magnet at  $x_0=10$  mm,  $y_0=0$  during field cycles between 0.4 and 8.2 T with  $\dot{B}_{ce}=0.0068, 0.014, 0.020, 0.027$  and  $0.034$   $\text{Ts}^{-1}$ . The field is measured using the RPCs H3 and H4 in series.

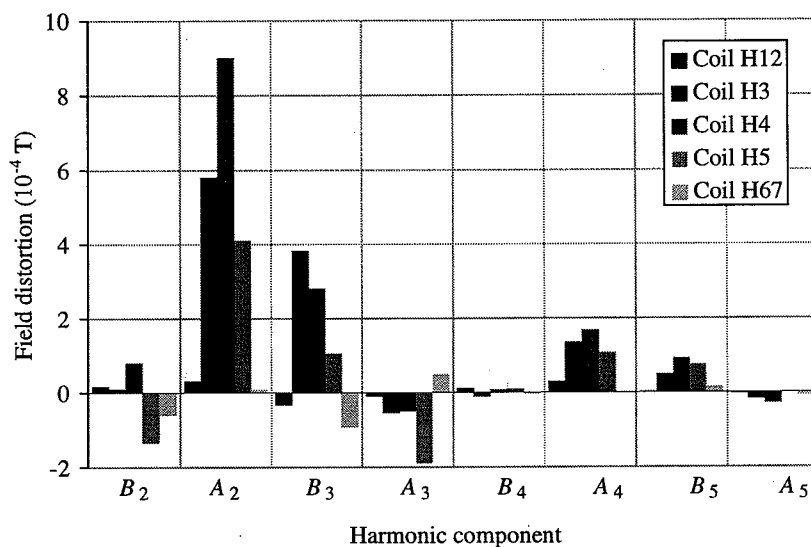


**Figure 7.9.** The field errors  $B_{ce}$  in aperture 1 of the CE1 magnet at  $x_0=10$  mm,  $y_0=0$  and  $\dot{B}_{ce}=0.01$   $\text{Ts}^{-1}$ , measured by means of the rotating pick-up coils H12, H3, H4, H5 and H67.

Coils H12 and H67 cover the coil ends where the field normal to the cable width is small. Hence, field  $B_{is}$  is small as already observed for the total field (see Fig. 7.7). Coils H3, H4 and H5 cover the straight part of the magnet. Fig. 7.9 shows clearly that most of the multipole components vary considerably over the straight part, which is caused by:

- variations of the  $R_c$ -distribution over the cross-section of the coil,
- the contribution from the BICCs, since  $l_{coil} \neq kL_{p,s}$ , so that a certain part of the sinusoidally varying field  $B_{bi}$  is measured.

Evaluation of the time constants of  $B_{cc}$  after the field sweep (in a similar way as is carried out for the measurements with the Hall probe) shows that most of the variations are due to the BICCs while small differences can be attributed to a varying spatial  $R_c$ -distribution along the magnet length. A very rough estimate of fields  $B_{is}$  and  $B_{bi}$  is obtained by assuming that both  $B_{is}$  and the amplitude  $B_{bi,max}$  are constant along the magnet length. Field  $B_{cc}$  for a given  $\dot{B}_{ce}$  can then be written as:

$$B_{cc}(z) = B_{is} + B_{bi,max} \sin\left(2\pi(z - z_0)/L_{p,s}\right) \quad [T]. \quad (7.15)$$

For each component the field contributions caused by the ISCCs and the BICCs as well as the phase  $2\pi z_0/L_{p,s}$  can be deduced by fitting eq. 7.15 to the measured field distortions. The errors in the fields can be large, especially for the higher harmonics, since  $B_{is}$  and  $B_{bi,max}$  are assumed to be  $z$ -independent. The results of the fits are given in section 7.7.5.

### 7.7.2 1 m long EL2 magnet

Only the higher harmonics are measured for this magnet. Field  $B_{cc}$  is determined by means of the RPCs H3, H4 and H5, for field cycles between 2 and 7.5 T at field-sweep rates of 0.0082, 0.016 and 0.033 Ts<sup>-1</sup>. Coils H12 and H67 are not used to measure the field since the evaluation of the  $B_{cc}$  is too difficult due to the complex geometry of the coil ends.

The multipole components for  $n=2, 3, 4$  and 5 of  $B_{cc}$  at  $x_0=10$  mm,  $y_0=0$  are shown in Fig. 7.10 scaled to  $\dot{B}_{ce}=0.01$  Ts<sup>-1</sup>.

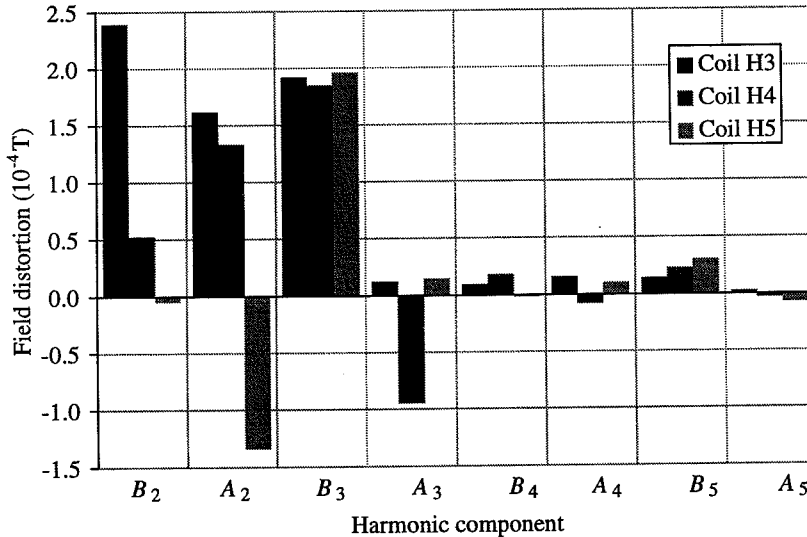


Figure 7.10. The coupling-current induced field  $B_{cc}$  of the EL2 magnet at  $x_0=10$  mm,  $y_0=0$  and  $\dot{B}_{ce}=0.01$  Ts<sup>-1</sup>, measured by means of the rotating pick-up coils H3, H4 and H5.

The field distortions are of the same order as those observed in the CE1 magnet except for the  $A_2$  component which is about one order of magnitude smaller. This implies that the difference  $|1/R_{c,P1} - 1/R_{c,P2}|$  in the EL2 magnet is smaller than in the CE1 magnet.

Analysis of the time dependence of the harmonics shows that the components  $B_2$ ,  $A_2$  and  $A_3$  are dominated by the fields caused by the BICCs while the fast decay of the  $B_3$  component after a ramp implies that this multipole is mainly caused by ISCCs. The almost constant  $B_3$  implies that  $R_c$  is almost  $z$ -independent. The octupole and decapole components are small compared to the lower harmonics and are not further discussed. Fields  $B_{is}$  and  $B_{bi}$  are estimated by fitting eq. 7.15 to each multipole component, and presented in section 7.7.5.

### 7.7.3 10 m long AN2 magnet

In the case of the AN2 magnet, field  $B_{cc,y}$  is determined using the 750 mm long FPC (so that  $l_{coil} = 5.8L_{p,s}$ ) located near the axial centre of the magnet. By using such a long pick-up coil the measured field  $B_{cc,y}$  is likely to be dominated by  $B_{is,y}$ , since the enclosed flux caused by the BICCs is relatively small. Field  $B_{cc,y}$  is measured during four field cycles between 0 and 4.1 T at four different field-sweep rates and shown in Fig. 7.11.

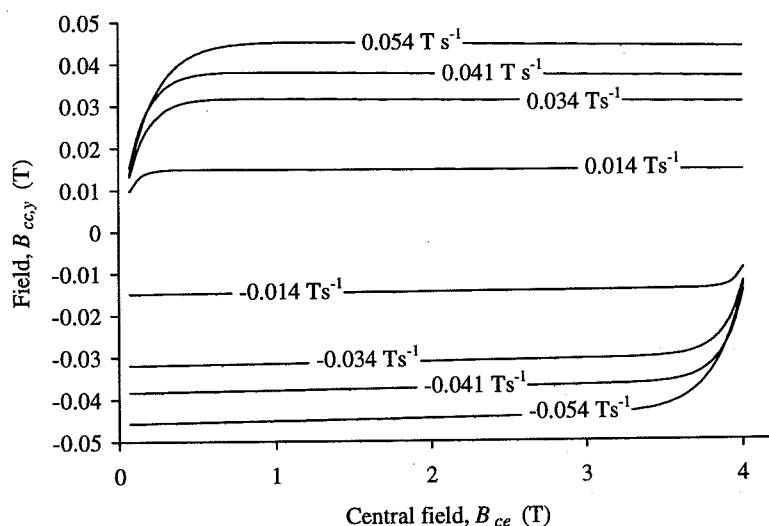
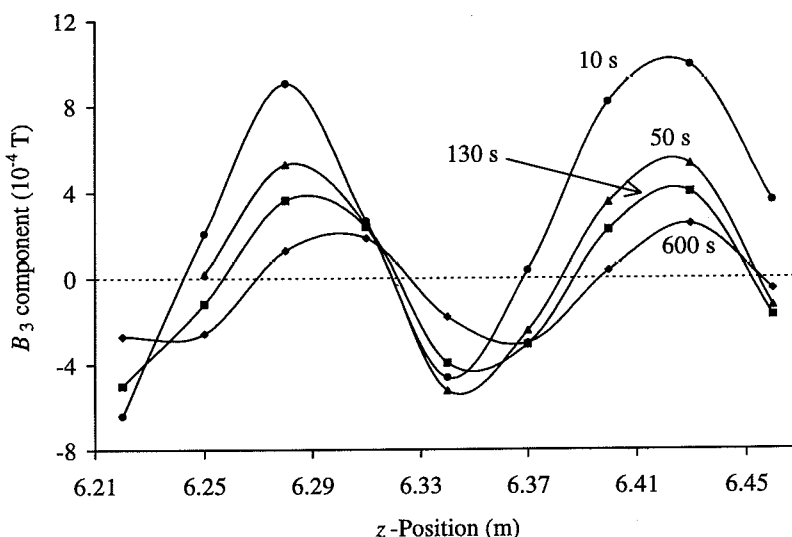


Figure 7.11. The field error  $B_{cc,y}$  in aperture 1 of the AN2 magnet as a function of the central field during field cycles between 0 and 4.1 T at four field-sweep rates.

Field  $B_{cc,y}$  is field-independent and exhibits a time constant of about 4 s, which is about twice as large as the time constant  $\tau_{is,M}$  deduced from the loss measurements during ramping (see Table 6.3). The absence of large characteristic times shows that  $B_{cc,y}$  is mainly caused by the ISCCs, as expected from the large coil length. The field error is about 10% more than the value calculated using Table 7.1 with an average  $R_c$  of  $1.3 \mu\Omega$  in aperture 1 (see Fig. 6.6 and the text below this figure).

An important conclusion is therefore that a measurement by means of a long FPC of field  $B_{cc,y}$  as a function of  $\dot{B}_{ce}$  results in a good estimate of  $R_c$ . At the same time it is possible to investigate the field dependence of  $R_c$ .

In the rest of this section field  $B_{bi}$  is investigated by means of the 30 mm long RPC. The decay of the higher field harmonics is measured at nine  $z$ -positions after a field sweep from 7.5 T to 0.4 T at  $-0.034 \text{ Ts}^{-1}$ . As an example the decay of the  $B_3$  component is depicted in Fig. 7.12.



**Figure 7.12.** Decay of the  $B_3$  component in aperture 1 of the AN2 magnet at  $x_0=10 \text{ mm}$ ,  $y_0=0$  after a ramp down from 7.5 T to 0.4 T at  $\dot{B}_{ce}=-0.034 \text{ Ts}^{-1}$ . The field is measured by means of the 30 mm long RPC at nine  $z$ -positions spaced 30 mm apart.

During the decay the *average*  $B_3$ -value decreases from about  $2 \cdot 10^{-4} \text{ T}$  to 0 in the first seconds due to the decay of the ISCCs. What is left after a few seconds is a sinusoidally varying field which can be regarded as a superposition of fields  $B_{bi}$  and  $B_{nucd}$ . The former decays with a characteristic time  $\tau_{bi}$  of about  $10^2 \text{ s}$ . The latter remains constant in time until the measurement ends after 600-1000 s. An important conclusion is that  $\tau_{bi}$  is about the same as the  $\tau_{bi}$  of the 1 m long CE1 and EL2 magnets. Therefore, the characteristic time  $\tau_{bi}$  seems to be independent of the length of the magnet.

Note, that not only the amplitude but also the phase of the sinusoidal pattern changes during the decay since  $B_{bi}$  and  $B_{nucd}$  have a different phase. Most of the multipoles show a similar decay with characteristic times:

- of several seconds related to the decay of the ISCCs,
- of about  $10^2 \text{ s}$  related to the decay of the BICCs,
- much larger than  $10^3 \text{ s}$  attributed to a NUCD.

In order to investigate whether the remaining field pattern is really independent of  $\dot{B}_{ce}$ , as expected from Table 7.4 in the case of a NUCD, field  $B_{cc}$  is determined at three different field-sweep rates ( $\dot{B}_{ce}=0.014, 0.024$  and  $0.034 \text{ Ts}^{-1}$ ). The central field is cycled between 0.6 and 7.5 T and the field is measured at five  $z$ -positions. Fig. 7.13 depicts the characteristic decay of the normal quadrupole after a ramp up with  $\dot{B}_{ce}=0.014$  and  $0.034 \text{ Ts}^{-1}$ .

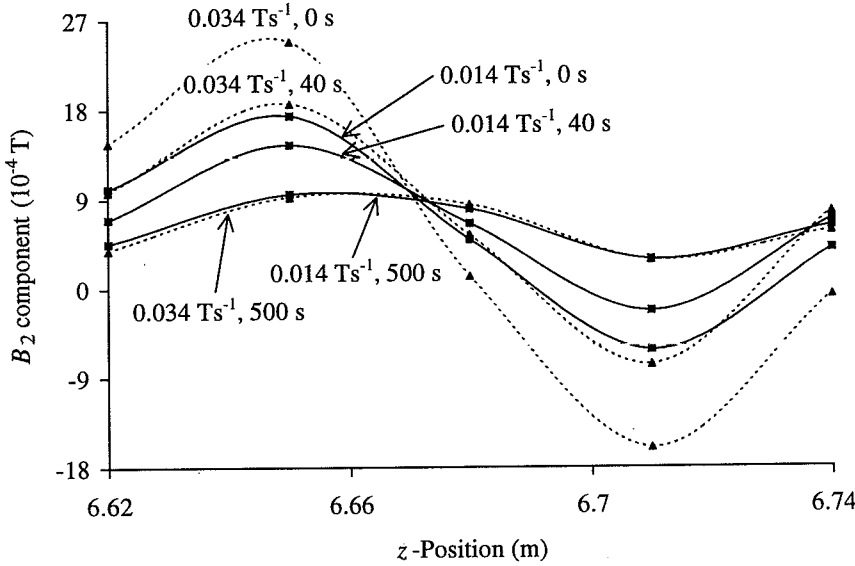


Figure 7.13. Decay of the  $B_2$  component in aperture 1 of the AN2 magnet at  $x_0=10 \text{ mm}$ ,  $y_0=0$  after a ramp up from 0.6 T to 7.5 T. The field is measured using the 30 mm long RPC at five  $z$ -positions. The labels indicate the field-sweep rate and the time after the end of the ramp.

The field caused by the ISCCs is very small, since the average  $B_2$ -value remains constant during the decay. The amplitude of the  $B_2$  component, caused by the BICCs, increases with increasing field-sweep rate and decays with a characteristic time  $\tau_{bi}$  of about  $10^2 \text{ s}$ . After a time  $t_d \gg \tau_{bi}$  the field pattern becomes constant and *independent of the field-sweep rate* of the preceding ramp. The remaining field pattern is therefore caused by a non-uniform current distribution among the strands exhibiting very large characteristic times.

The harmonic coefficients of  $\mathbf{B}_{cc}$  are determined from the slope of the  $\mathbf{B}-\dot{B}_{ce}$  curve in the same way as for the CE1 and EL2 magnets. The results, scaled to  $\dot{B}_{ce}=0.01 \text{ Ts}^{-1}$ , at five  $z$ -positions are shown in Fig. 7.14.

Note the very strong variations of especially the  $B_2$ ,  $A_2$  and  $B_3$  components caused by the BICCs. The magnitudes of the multipole coefficients of  $\mathbf{B}_{is}$  and  $\mathbf{B}_{bi}$  individually, are estimated by fitting eq. 7.15 to the values of each component of  $\mathbf{B}_{cc}$  at the five  $z$ -positions. The results of the fits and the conclusions are presented in section 7.7.5.



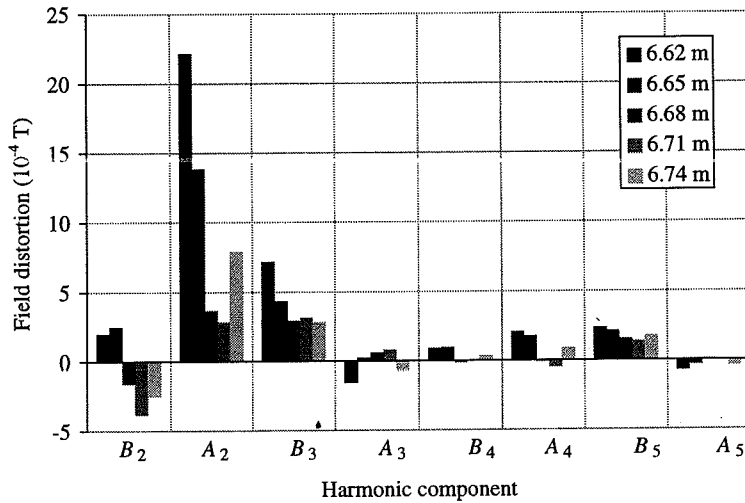


Figure 7.14. The field  $B_{cc}$  in aperture 1 of the AN2 magnet at  $x_0=10$  mm,  $y_0=0$  and  $\dot{B}_{ce}=0.01$  Ts<sup>-1</sup>, measured by means of the 30 mm long RPC, located at five  $z$  positions spaced 30 mm apart.

#### 7.7.4 10 m long AN3 magnet

The coupling-current induced field  $B_{cc}$  of the AN3 magnet is evaluated from the field determined by the 750 mm long RPC using cycles between 0.6 and 8.2 T at  $\dot{B}_{ce}=0.0068$ , 0.014, 0.024 and 0.034 Ts<sup>-1</sup>. Note that the enclosed flux due to the BICCs is probably small compared to that caused by the ISCCs since the coil length is 6.25 times the cable pitch. The field determined in both apertures at two different  $z$ -positions is shown in Fig. 7.15.

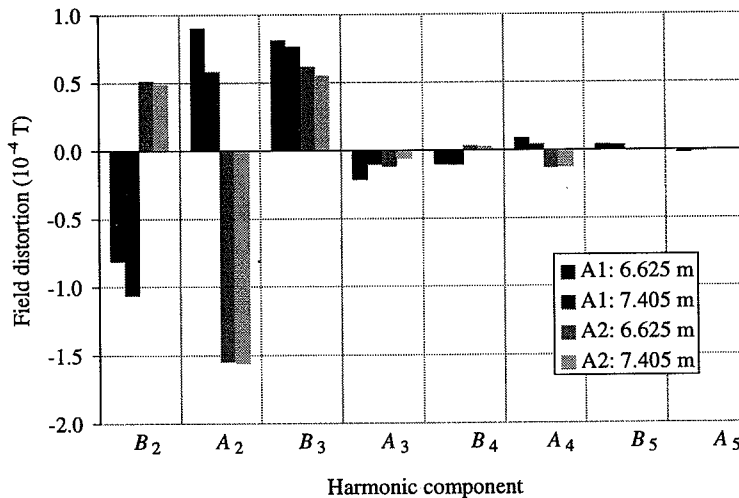


Figure 7.15. The field  $B_{cc}$  of the AN3 magnet at  $x_0=10$  mm,  $y_0=0$  and  $\dot{B}_{ce}=0.01$  Ts<sup>-1</sup> determined by means of the 750 mm long RPC located at two  $z$ -positions in the apertures A1 and A2.

The signs of the fields are relative to the sign of the main field in that aperture. This implies that, according to Table 7.1, the  $B_3$  and  $B_5$  components are positive. Note that the much smaller  $B_3$  component compared to the AN2 magnet, is inherent to the much larger  $R_c$  of the AN3 magnet (see Table 6.4).

The opposite sign of the  $A_2$  and  $A_4$  multipoles in both apertures indicates that the  $R_c$ -values in the poles A11 and A21 are larger than in the poles A12 and A22 respectively (see Fig. 6.4b).

The difference in the magnitude of the  $A_2$  and  $A_4$  components in the two apertures shows that the difference between  $R_c$  in the two poles of aperture 1 is smaller than that in the two poles of aperture 2.

### 7.7.5 Evaluation of fields $B_{is}$ and $B_{bi}$

In Table 7.6 a survey is given of the coupling current induced field errors  $B_{is}$  and  $B_{bi}$  which are determined by fitting eq. 7.15 to the measured field errors  $B_{cc}$ . The fit is only made for the CE1, EL2 and AN2 magnets.

**Table 7.6.** Survey of the harmonic distortions  $B_{is}$  and  $B_{bi}$  (in  $10^{-4}$  T) at  $x_0=10$  mm,  $y_0=0$  in four LHC dipole model magnets at  $\dot{B}_{ce}=0.01$  Ts $^{-1}$ . The  $B_y$ -value is determined by means of the FPCs while the higher harmonics  $B_2$ - $A_5$  are determined by means of the RPCs.

	1 m long CE1, Aperture 1 $R_{c,P1}=1.6 \mu\Omega$ $R_{c,P2}=2.0 \mu\Omega$			1 m long EL2 $R_{c,P1}=2.8 \mu\Omega$ $R_{c,P2}=3.0 \mu\Omega$		
	$B_{is,exp}$	$B_{bi,exp}$	$B_{is,calc}$	$B_{is,exp}$	$B_{bi,exp}$	$B_{is,calc}$
$B_y$	+64	-	+67	-	-	+30
$B_2$	+0.047	8.5	-	+0.87	13	-
$A_2$	+6.9	14	+2.6	+0.70	16	+0.61
$B_3$	+2.6	15	+1.52	+1.9	0.31	+0.94
$A_3$	-0.88	7.3	-	-0.37	2.8	-
$B_4$	+0.032	1.1	-	+0.10	0.69	-
$A_4$	+1.4	1.9	-0.29	+0.033	0.60	+0.068
$B_5$	+0.76	1.6	-0.15	+0.22	0.84	-0.094
$A_5$	-0.18	1.1	-	-0.028	0.51	-

	10 m long AN2, Aperture 1 $R_{c,P1}=1.2 \mu\Omega$ $R_{c,P2}=1.4 \mu\Omega$			10 m long AN3, Aperture 1 $R_{c,P1}=6.2 \mu\Omega$ $R_{c,P2}=6.0 \mu\Omega$		10 m long AN3, Aperture 2 $R_{c,P1}=6.8 \mu\Omega$ $R_{c,P2}=5.7 \mu\Omega$	
	$B_{is,exp}$	$B_{bi,exp}$	$B_{is,calc}$	$B_{cc,exp}$	$B_{is,calc}$	$B_{cc,exp}$	$B_{is,calc}$
$B_y$	+75	-	+68	-	+13	+9.1	+13
$B_2$	-0.17	3.5	-	-0.94	-	+0.50	-
$A_2$	+12	9.9	+3.8	+0.74	+0.12	-1.6	-0.61
$B_3$	+4.5	2.4	+2.1	+0.79	+0.41	+0.58	+0.41
$A_3$	-0.30	1.0	-	-0.16	-	-0.088	-
$B_4$	+0.49	0.58	-	-0.11	-	+0.030	-
$A_4$	+1.0	1.2	+0.42	-0.067	+0.013	-0.13	-0.068
$B_5$	+1.9	0.46	-0.21	+0.037	-0.041	-0.0026	-0.041
$A_5$	-0.35	0.37	-	-0.016	-	+0.00051	-

The error in the presented values is about 10% for  $B_y$ , and about 20-40% for the higher harmonics. In the case of the AN3 magnet, field  $\mathbf{B}_{is}$  is deduced from the average field  $\mathbf{B}_{cc}$  measured by means of the 750 mm long RPC at the two  $z$ -positions. Field  $\mathbf{B}_{bi}$  is disregarded since the total length of 1.5 m is about  $11.5L_{p,s}$ .

The normal-odd harmonics of  $\mathbf{B}_{is}$  are calculated using Table 7.1 with an average  $R_c$  based on the results of the loss measurements. The skew-even harmonics of  $\mathbf{B}_{is}$  are calculated using Table 7.3 with contact resistances  $R_{c,p1}$  and  $R_{c,p2}$  in the two poles of an aperture estimated from the loss measurements on the separate poles.

Table 7.6 shows that the calculated and experimentally determined values of  $B_{is,y}$  correspond well, while for the  $B_3$  component differences of about a factor 2 are observed. In order to meet the field accuracy, it is therefore preferable to have an  $R_c$ -value of the cable which is about a factor 2 larger than the calculated minimum value (see section 7.4).

Large  $A_2$  components are observed for the magnets with large differences between  $R_c$  of the two poles of the same aperture. Because the resistances  $R_{c,p1}$  and  $R_{c,p2}$  are estimated values, the skew-even harmonics cannot be calculated exactly. However, the measurements on the AN3 show that for  $R_c > 10 \mu\Omega$  (as stated in section 7.4) the  $A_2$  and  $A_4$  multipole components will probably be smaller than  $10^{-4}$  T.

In the case of the higher multipoles the discrepancy between the measurements and the calculations becomes larger due to the stronger sensitivity of the multipoles to local  $R_c$  variations.

No direct correlation is present between  $R_c$  and the estimated field  $\mathbf{B}_{bi}$ . Especially the amplitude of the quadrupole and sextupole components (both the skew and the normal) are well above  $10^{-4}$  T at  $x_0 = 10$  mm,  $y_0 = 0$ .

The results of these incidental measurements on the four magnets show that the time constant of about  $10^2$  s seems to be independent of  $R_c$  and the length of the magnet. This implies, according to eqs. 5.13 and 5.14, that the BICCs should be classified in regime A, and hence flow over an average characteristic length which is much smaller than the length of the cable. The effective strand resistivity and the characteristic length can be roughly estimated by using the formulas for a straight cable (eqs. 5.13 and 5.8):

$$\rho_s = 2 \cdot 10^{-8} \frac{N_s \pi d_s^2}{\tau_{bi}} = 2.8 \cdot 10^{-14} \quad [\Omega\text{m}], \quad (7.16)$$

and:

$$\xi = 0.50 \sqrt{\frac{R_c L_{p,s} \pi d_s^2}{2 \rho_s N_s}} = 3.5 \cdot 10^2 \sqrt{R_c} \quad [\text{m}]. \quad (7.17)$$

Since the various turns probably cause a reduction of the average time constant compared to a straight cable,  $\rho_s$  can decrease to about  $10^{-14} \Omega\text{m}$  and  $\xi$  can increase by about a factor 2. This leads to a characteristic length of about 0.5 to 2 m for  $1 < R_c < 7 \mu\Omega$ .

The origin of the large effective strand resistivity that the BICCs 'see' is not well-known. It is certain that it cannot be attributed to the dynamic resistivity, which is linear to the field change  $\dot{B}_{Lx}$  (see eq. 3.6), since  $\tau_{bi}$  and hence  $\rho_s$  are independent of the field-sweep rate.

According to the treatment of BICCs in chapter 5, BICCs can only decay exponentially along the cable length if a certain voltage is present over the strand sections between two nodes of the network model. In the network model, this implies that the strand sections have to be resistive since the voltages over the resistances  $R_c$  are assumed to have no  $x$ - or  $z$ -components. However, a current through  $R_c$  has to flow from the filaments of one strand to the filaments of the other strand and in this process will pass through the copper outer shell of the strands (see Fig. 2.9a) and through part of the matrix. This transfer causes not only a voltage in the  $y$ -direction but locally also a voltage in the axial direction (as well as in the  $x$ -direction). It has to be investigated in detail whether the large effective strand resistivity can be attributed to the small axial resistive voltage caused by the currents through  $R_c$ .

## 7.8 Conclusions

In a magnet made of a multistrand superconductor three field components are present which depend linearly on the central-field-sweep rate  $\dot{B}_{ce}$ , namely:

- the field  $B_{if}$  produced by the IFCCs,
- the field  $B_{is}$  produced by the ISCCs,
- the field  $B_{bi}$  produced by the BICCs.

Field  $B_{if}$  can be calculated by representing the screening-current density in the strands by two currents of opposite sign located at the centre of gravity of half a strand. The field  $B_{if}$  in the aperture of an LHC dipole is smaller than  $0.1 \cdot 10^{-4}$  T at  $x_0=10$  mm,  $y_0=0$  for all multipole components (assuming the characteristic values  $\tau_{if}=0.025$  s and  $\dot{B}_{ce}=0.01$  Ts<sup>-1</sup>), and is negligible compared to the field produced by the filament magnetisation and the field distortions caused by fabrication tolerances.

Field  $B_{is}$  is calculated by representing all the zigzag ISCCs as infinitely long straight line currents. Field  $B_{is}$  is inversely proportional to the cross-contact resistance  $R_c$  and increases strongly for increasing cable width. Since the ISCCs follow the symmetry of the field generated by the transport current, only the normal-odd harmonics are affected if the  $R_c$ -distribution is uniform over the cross-section of the magnet. Calculations and measurements of various LHC dipole magnets are in good agreement and show that mainly the  $B_1$  and  $B_3$  components are large. Characteristic values are about  $24 \cdot 10^{-4}$  T and  $0.7 \cdot 10^{-4}$  T respectively (at  $x_0=10$  mm,  $y_0=0$ ) for  $R_c=3 \mu\Omega$  and  $\dot{B}_{ce}=0.01$  Ts<sup>-1</sup>. The measurements have shown that  $R_c$  varies by less than 10-20% along the length of the straight part of a coil and that  $R_c$  is independent of the current and field levels.

In the case of non-uniform  $R_c$ -distributions the other field harmonics are also affected. Especially the skew-quadrupole component can be large due to a difference in  $R_c$  between the two poles of an aperture. In the LHC dipole model magnets  $A_2$ -values of up to  $10 \cdot 10^{-4}$  T (at  $x_0=10$  mm,  $y_0=0$ ) at  $\dot{B}_{ce}=0.01$  Ts<sup>-1</sup> are observed. The measured fields are in fair

agreement with calculated values based on the average  $R_c$ -values as deduced from the loss measurements. While the  $B_1$  and  $B_3$  components have the same direction in all the coils, the sign of the skew-even harmonics is probably non-systematic.

Reduction of  $B_{is}$  is possible by a decrease of the field-sweep rate and by an increase of  $R_c$ . An  $R_c$ -value of  $10 \mu\Omega$  would limit the field errors in LHC dipole magnets to acceptable values while the total ramp time from injection field to operation field remains below 30 minutes.

An important conclusion is that the contact resistance between the strands of a cable has to be increased for dipole magnets (with a 'two-shell' geometry) having a larger central field in order to meet a field homogeneity of the order of  $10^{-4}$ .

Field  $B_{bi}$  can be determined by calculating the BICCs taking into account the exact spatial field distribution in the coil. The pattern of  $B_{bi}$  along the magnet axis is always (quasi-)sinusoidal with an amplitude proportional to  $\dot{B}_{ce}$  and a period equal to the transposition length. The amplitude of  $B_{bi}$  is difficult to calculate since the magnitude of the BICCs depends strongly on the exact geometry of the magnet and on spatial variations of the contact resistance and the strand resistivity. Simulations show that especially the quadrupole and sextupole components (both normal and skew) can attain large values. Experimental results on LHC dipole magnets show that the amplitude of these multipoles can be as large as  $20 \cdot 10^{-4}$  T (at  $x_0=10$  mm,  $y_0=0$  and  $\dot{B}_{ce}=0.01$  Ts $^{-1}$ ). In the absence of sufficient measurements it is not sure what causes the differences in  $B_{bi}$  between the four magnets that are measured.

The BICCs of the 1 m as well as the 10 m long LHC dipole model magnets exhibit characteristic times of about  $10^2$  s. These times seem to be not only independent of the magnet length but also of  $R_c$ . This implies that the BICCs decay with a characteristic length  $\xi$  which is much smaller than the length of the cable. For the four investigated magnets the characteristic length is estimated to be about 0.5-2 m. Calculations demonstrate that, in this case, the BICCs cause a voltage over the strands which would correspond to an effective strand resistivity  $\rho_s$  of about  $10^{-14}$   $\Omega$ m. This resistivity can be related to the diffusion process of the coupling currents from the contacts into the filaments, but a more detailed investigation of this process is required in order to support this explanation.

In coils made of multistrand conductors a third additional field  $B_{nucd}$  is present, besides fields  $B_{is}$  and  $B_{bi}$ , caused by a non-uniform distribution of the transport current among the strands. This field varies sinusoidally along the magnet length with a period equal to the cable pitch and exhibits a characteristic time which is much larger than  $10^3$  s. The value of the field is independent of the field-sweep rate of the preceding ramp.

Sinusoidal variations of the field along the magnet axis as observed in superconducting magnets are a superposition of fields  $B_{bi}$  and  $B_{nucd}$ . Which of these fields is dominant depends mainly on the excitation level, the field-sweep rate, the spatial  $R_c$ - and  $\rho_s$ -distributions and the uniformity of the soldered cable-to-cable connections. In general, field  $B_{bi}$  becomes relatively more important when the size of the cable increases and the contact resistances between strands decrease.

## Chapter 8

# Ramp-rate limitation of dipole magnets

*In this chapter the effect of interfilament-, interstrand- and boundary-induced coupling currents on the ramp-rate limitation (RRL) of the quench current in dipole magnets is investigated.*

*A significant reduction of the quench current as a function of the field-sweep rate can be observed in magnets with a large as well as a small contact resistance between crossing strands.*

*The RRL in magnets with small contact resistances is shown to be mainly related to the power loss, generated in the contact resistances, especially in coils with poorly cooled conductors. In this case, the RRL of the magnet can be used to estimate the thermal conductivity of the cable insulation.*

*The RRL in magnets with large contact resistances is shown to be mainly attributed to the presence of boundary-induced coupling currents. The magnitude of these coupling currents can be influenced by performing field precycles (before the actual ramp to quench).*

*The results of the RRL of a few 1 and 10 m long LHC dipole model magnets are evaluated. The temperature of the cable is calculated as a function of the average coupling power loss assuming a uniform contact resistance over the cross-section of the coils and uniform temperature within each turn of the magnet. It is shown that the temperature increase in the coil due to beam losses can be well estimated by a detailed analysis of the RRL.*

## 8.1 Introduction

Accelerator dipole magnets are normally operated at a low central-field-sweep rate of the order of  $10^{-2} \text{ Ts}^{-1}$ . Higher field-sweep rates of up to  $10^{-1} \text{ Ts}^{-1}$  occur during a fast de-excitation in the case of a quench in one of the series-connected magnets. During a field sweep the temperature increase in the cable and the induced coupling currents should be as small as possible in order to ensure a good stability of the superconductor.

The effect of the coupling currents on the electromagnetic stability is investigated by means of the *Ramp-Rate Limitation (RRL)* of the quench current. Three types of coupling currents are dealt with in sections 8.2.1-8.2.3:

- The *Interfilament Coupling Currents (IFCCs)* which are induced within a strand subject to a varying magnetic field  $\dot{B}$  (see section 3.4).
- The *Interstrand Coupling Currents (ISCCs)* which are induced in and between the strands of a cable subject to a varying magnetic field  $\dot{B}$  (see chapter 4).
- The *Boundary-Induced Coupling Currents (BICCs)* which are generated due to spatial variations of  $\dot{B}$  (and, to a smaller extent, the cross-contact resistance  $R_c$ ) along the cable length (see chapter 5). The BICCs strongly influence the current distribution among the strands of the cable and therefore the maximum transport current.

The temperature increase in the cable (during a field sweep) is investigated in section 8.2.4. It is assumed that the heat is generated by the IFCCs and ISCCs. The enhancement of the interstrand coupling power loss (ISCL) due to the BICCs is disregarded as well as the losses in the filaments, wedges, collars and yoke as they all are relatively small compared to the ISCL.

The reduction of the quench current as a function of the field-sweep rate is calculated for the PBD magnet as specified in Table 2.1. Experimentally obtained values for the time constants of the IFCCs and the cross-contact resistances of cables are used to obtain a first qualitative estimate of the RRL. It is shown that the main cause of the RRL can be deduced from the shape of the curve relating the quench current and the field-sweep rate.

In sections 8.3-8.5 the RRL is presented which is experimentally observed in several LHC dipole model magnets. The analysis of the RRL is focused on the following questions:

- Do the BICCs affect the temperature margin of the cable and what is the magnitude of the BICCs during ramping of the magnets?
- What is the expected increase of the cable temperature due to beam losses in the coils?
- What is the maximum allowable de-excitation rate of the magnets?

The methods described in this chapter and the experimental results show which possibilities the analysis of the RRL offers with respect to the understanding of the electrodynamics of superconducting magnets. Specific conclusions about the observed RRL in the LHC model magnets are difficult to draw. Firstly, because the RRL of only a few magnets is determined and secondly because the quench current is strongly affected by local variations in the coupling currents and power loss as well as variations of the local critical current density in the cable. Investigation of the RRL is therefore much more complicated than the analysis of the coupling loss (chapter 6) or the coupling-current induced field distortions (chapter 7) which both represent a more *average* effect over the coils.

## 8.2 Calculation of the RRL of magnets

In section 2.4 an empirical scaling law is presented that describes the relation between the critical current  $I_C$  of NbTi superconductors as a function of the applied field  $B$  and the temperature  $T$  [Lubell, '83]:

$$I_C = (C_1 - C_2 |B|) \left( 1 - \frac{T}{T_C(B, I=0)} \right) \quad [\text{A}] \quad \text{for } |B| > B^*, \quad (8.1a)$$

with:

$$T_C(B, I=0) = 9.2(1 - |B|/14.5)^{0.59} \quad [\text{K}], \quad (8.1b)$$

where  $B^*$  is about 3 T. The relation for the critical current for  $B < B^*$  is disregarded here since the treatment of the RRL is focused on high-field magnets with quench fields well above 3 T. Eqs. 8.1a and 8.1b can be rewritten for an arbitrary strand section in the cable of a coil:

$$I_{C, \text{str}} = (C_1 - C_2 |B_{\text{str}}|) \left( 1 - \frac{T_{\text{cab}}}{9.2} (1 - |B_{\text{str}}|/14.5)^{-0.59} \right) \quad [\text{A}] \quad \text{for } |B| > B^*, \quad (8.2)$$

with  $B_{\text{str}}$  the local field at the given strand section and  $T_{\text{cab}}$  the temperature of this strand section. The field  $B_{\text{str}}$  is composed of the field  $\mathbf{B}_{\text{tr}}$  produced by the transport current, and the field  $\mathbf{B}_{\text{cc}}$  caused by the ISCCs and the BICCs:

$$|B_{\text{str}}| = |\mathbf{B}_{\text{tr}} + \mathbf{B}_{\text{cc}}| = \beta_{\text{str}} T_M N_s I_{\text{tr}, \text{str}} + |B_{\text{cc}}| \text{sgn}(\dot{B}_{\text{ce}}) \quad [\text{T}], \quad (8.3)$$

with  $T_M$  the field factor of the magnet and  $\beta_{\text{str}}$  the ratio between the local field (at the given strand position) and the central field (see Fig. 6.1). The vector summation is transformed into a scalar operation since the orientation of the fields  $\mathbf{B}_{\text{tr}}$  and  $\mathbf{B}_{\text{cc}}$  is basically in the  $y$ -direction for the blocks near the midplane where almost all quenches are located (see section 8.3).

The quench current  $I_{q, \text{str}}$  of a strand is here defined by the maximum transport current  $I_{\text{tr}, \text{str}, \text{max}}$  that a section of the strand can carry in the presence of additional coupling currents. Assuming that:

- the weakest strand determines the quench current of the entire magnet,
  - the transport current is uniformly distributed among the strands,
- the quench current of the magnet is defined by:

$$I_q = N_s I_{q, \text{str}} \quad [\text{A}], \quad (8.4)$$

and the quench field by:

$$B_q = T_M I_q \quad [\text{T}]. \quad (8.5)$$

The current  $I_{q,0}$  and the field  $B_{q,0}$  denote the quench current and quench field respectively if the coupling currents are zero.



The following assumptions are made:

- Ramp-rate-induced quenches are not initiated by a conductor movement or a transient energy pulse from the environment.
- The temperature  $T_{cab}$  of the cable does not vary over the cross-section of the cable and along the length of a given turn. The influence of the coil ends on the temperature distribution in the cable is not taken into account.
- The quench starts in the strand section in which the total current becomes equal to the critical current at the given field and temperature.
- A quench that occurs locally in a strand section causes a quench of the whole coil. Recovering of the quench due to, for example, redistribution of the strand currents after a quench is not taken into account.
- The cross-contact resistance  $R_c$  is constant over the whole cross-section of a coil.
- The resistive loss, generated in the cable-to-cable connections, the eddy current loss in the copper wedges and the collars and the magnetisation loss in the filaments and the iron yoke are disregarded. These loss contributions are relatively small at the field and field-sweep rate used in the quench experiments (see sections 8.3-8.5).
- The voltage over a strand is assumed to be 0 up to  $I_{str}=I_{q, str}$ . A variation of the coupling-current distribution at strong excitation (see section 4.5) is therefore disregarded.
- The transport current is uniformly distributed among the strands.

In sections 8.2.1-8.2.4 the influence of the various coupling currents and the coupling power loss on the quench current is presented. The discussion is illustrated by means of calculations of the RRL in a PBD magnet (see Table 2.1) using  $C_1=1.12 \cdot 10^5$  A and  $C_2=7.79 \cdot 10^3$  AT<sup>-1</sup> in eq. 8.2. Other values for the constants  $C_1$  and  $C_2$  give basically the same results if the quench currents are normalised to the maximum values  $I_{q,0}$ . A 26-strand cable is considered with a cross-section of  $17 \times 2.04/2.50$  mm<sup>2</sup> and a cable pitch  $L_{p,s}=0.13$  m. The reduction of the quench current is estimated for the anticipated average field-sweep rate of about  $0.0066$  Ts<sup>-1</sup> and initial field-sweep rate of  $-0.084$  Ts<sup>-1</sup> in the case of a fast exponential de-excitation.

### 8.2.1 Influence of IFCCs on the RRL

In section 3.4 it is shown that the maximum transport current in a strand is affected by the IFCCs flowing in the outer layer of filaments, and can be expressed by:

$$I_{tr, str, max} = I_{C, str} \left( 1 - \frac{(\pi d_s^*)^2 \tau_{if}}{I_{C, str} \mu_0 L_{p, f}} |\dot{B}_{str}| \right)^2 \quad [\text{A}], \quad (8.6)$$

with  $I_{C, str}$  as defined by eq. 8.2 and  $\dot{B}_a = \dot{B}_{str}$ , by which the small twist angle of the cable is disregarded. The quench current is then given by the condition that the transport current is equal to the maximum transport current, so  $I_{q, str} = I_{tr, str} = I_{tr, str, max}$ , and is iteratively calculated by combining eqs. 8.2, 8.3 and 8.6.

As an example, the characteristic relative reduction of the quench current of the PBD magnet is depicted in Fig. 8.1 as a function of  $\dot{B}_{ce}$  for  $L_{p, f}=25$  mm,  $d_s^*=1.2$  mm,  $T_b=1.9$  and  $4.3$  K and  $\tau_{if}=50$  and  $100$  ms. The cable temperature is constant and equal to  $T_b$ .

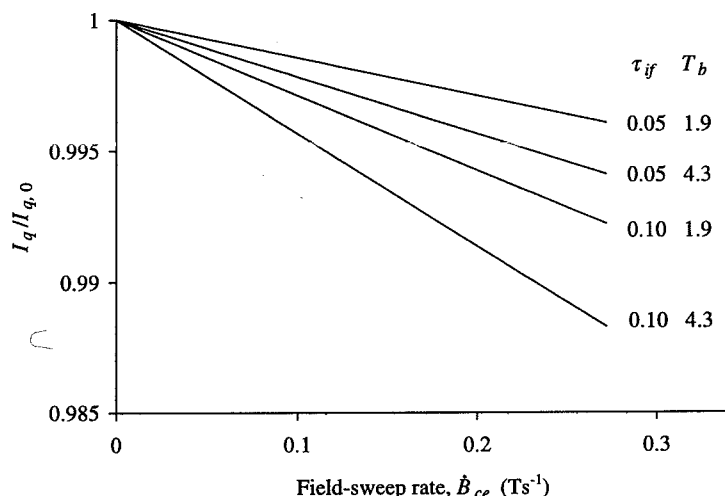


**Figure 8.1.** Calculation of the relative quench current of the PBD magnet caused by the IFCCs as a function of the central-field-sweep rate. Curves for two  $\tau_{if}$ -values (in seconds) are depicted at bath temperatures of 1.9 K and 4.3 K.

The quench origin is located in block 6 near the aperture (at  $r \approx 25$  mm, see Fig. 2.2a) since the local field and therefore also  $\dot{B}_{str}$  ( $=\beta_{str} \dot{B}_{ce}$ , see also Fig. 6.1) are maximum in this part. In the case of dipole magnets with other geometries or cables with other characteristics the reductions are different since parameters such as  $\beta_{str}$ ,  $d_s^*$ ,  $L_{pf}$  and  $\tau_{if}$  are incorporated in eqs. 8.2 and 8.6. The RRL due to the presence of IFCCs can be easily calculated for any magnet geometry if  $\tau_{if}$  is known. Fig. 8.1 shows that the reduction is a factor 1.5 larger at 4.3 K than at 1.9 K.

The reduction of the quench current of the LHC dipoles at  $\dot{B}_{ce}=0.0066$  Ts<sup>-1</sup> will be smaller than 0.01% (for  $\tau_{if}=0.05$  s) whereas at fast de-excitation ( $\dot{B}_{ce}=-0.084$  Ts<sup>-1</sup>) it is still smaller than 0.1%. Only for magnets which are subject to very large field-sweep rates, does the reduction of the quench current due to the IFCCs have to be taken into account.

### 8.2.2 Influence of ISCCs on the RRL

It is shown in section 4.4.1 that the ISCCs in Rutherford-type cables are mainly created by a field change  $\dot{B}_\perp$  normal to the cable width (see Fig. 4.1). Here the case of a positive field-sweep rate is dealt with (see section 8.5 for negative field-sweep rates). The critical part of the coil with respect to the quench current is near the aperture, in the strand sections that bend around the edge of the cable, because:

- fields  $B_{tr}$  and  $B_{cc}$  are maximum,
- the ISCCs flow in the same direction as the transport current and are maximum (see eqs. 7.11 with  $x=w/N_s$ ).

According to eq. 7.11, the maximum ISCC in turn  $i$  at the edge of the cable can be expressed by:

$$I_{s,i,max} = 0.0415 \frac{L_{p,s} w N_s}{R_{c,i}} \beta_{I,i} \dot{B}_{ce} \cos(\pi / N_s) \quad [\text{A}], \quad (8.7)$$

with  $\beta_{I,i}$  the field geometry factor that depends on the magnitude and the shape of the field variation  $\dot{B}_{\perp c}$  across the cable width of turn  $i$  (see Fig. 7.2).

The quench current in a strand section:

$$I_{q,str} = I_{C,str} - I_{s,max} \quad [\text{A}], \quad (8.8)$$

is calculated iteratively using  $I_{tr,str} = I_{q,str}$  in eq. 8.3. The quench origin will depend on  $\dot{B}_{ce}$  since  $I_{q,str}$  depends on  $\beta_{str}$  and  $\beta_I$  which both vary over the cross-section of the coils.

The relative reduction of the quench current of the PBD magnet is depicted in Fig. 8.2 for  $R_c$ -values of 1, 2 and 5  $\mu\Omega$  and bath temperatures of 1.9 K and 4.3 K. If  $\dot{B}_{ce}$  is small then the ISCCs are also small and the quench starts in block 6 where  $\beta_{str}$  is maximum (and hence  $I_{C,str}$  is minimum). The ISCCs become larger for increasing  $\dot{B}_{ce}$  and the quench origin shifts therefore to block 3 where  $\beta_I$  is maximum. Note that the relative quench reduction is a factor 1.5 larger at 4.3 K than at 1.9 K. In the case of cables with a different geometry, the RRL is proportional to  $I_{s,max}$  and hence to  $L_{p,s} w N_s / R_c$ .

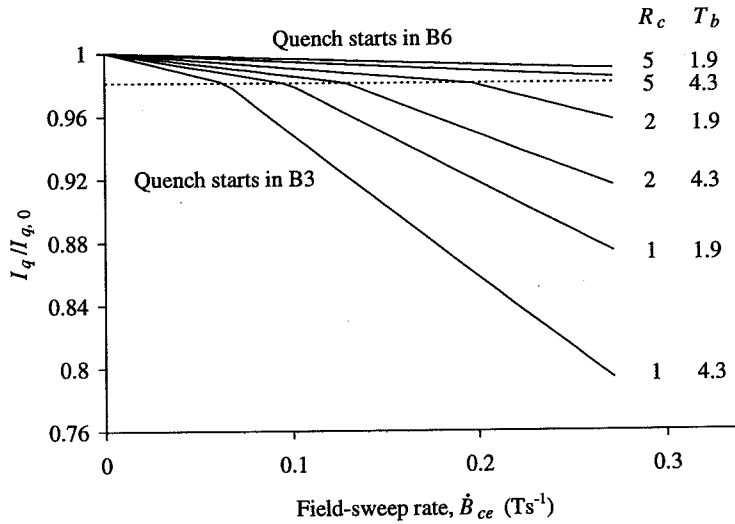


**Figure 8.2.** Calculation of the relative reduction of the quench current of the PBD magnet caused by the ISCCs as a function of the central-field-sweep rate. Curves for three different  $R_c$ -values (in  $\mu\Omega$ ) are depicted at both temperatures of 1.9 K and 4.3 K. The dotted line illustrates the two different quench origins.

The reduction of the quench current of the LHC dipole magnets at  $\dot{B}_{ce} = 0.0066 \text{ Ts}^{-1}$  will be smaller than 0.15% (for  $R_c = 1 \mu\Omega$ ). At fast de-excitation, there is no reduction because the transport current and the ISCC have opposite sign near the aperture where the field is maximum (see section 8.5).

### 8.2.3 Influence of BICCs on the RRL

In chapters 5 and 7 it has been shown that the BICCs exhibit large characteristic times  $\tau_{bi}$  and that their magnitude is proportional to  $\dot{B}_{ce}$ . Therefore, the magnitude of the BICCs at the moment of the quench depends not only on  $\dot{B}_{ce}$  but also on the time  $t_r$  of the ramp. This large characteristic time results in a different evaluation of the RRL caused by the BICCs compared to the ISCCs, for which  $\tau_{is} \ll t_r$ . The BICCs during the ramp can be expressed by (assuming that their magnitude is equal to 0 at  $t=0$ ):

$$I_{bi} = C_{bi} \dot{B}_{ce} (1 - e^{-t/\tau_{bi}}) \quad [\text{A}], \quad (8.9)$$

with  $t$  the time from the beginning of the ramp and  $C_{bi}$  a constant with dimension  $\text{AsT}^{-1}$ . Note that this exponential expression for the BICCs does not describe their real time-dependent behaviour as discussed in sections 5.4.1-5.4.4. It is, however, the most practical approximation by which the effect of the BICCs on the RRL can be investigated. The constant  $C_{bi}$  is rather unpredictable since it is determined by the integral effect of many BICCs induced by the numerous  $\dot{B}_\perp$ -variations along the cable in the coil. The order of magnitude of  $C_{bi}$  can be estimated by calculating the magnitude of the BICCs (using eq. 5.5) due to the variation of  $\dot{B}_\perp$  in one turn of the coil. This would give a  $C_{bi}$  of about  $5 \cdot 10^3 \text{ AsT}^{-1}$  for a PBD magnet with  $\xi=1 \text{ m}$  (as estimated at the end of section 7.7.5) and  $R_c=3 \mu\Omega$ .

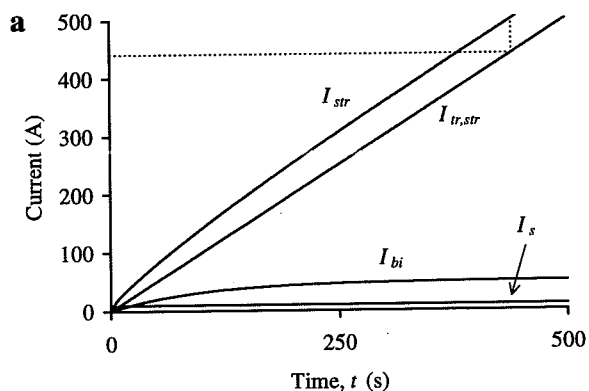
Fig. 8.3 illustrates the calculated current  $I_{bi}$  during a linear ramp from  $I_{tr,str}=0$  to 500 A at small and large ramp rates ( $\dot{I}_{tr,str}=1$  and  $10 \text{ As}^{-1}$ ) with  $\tau_{bi}=100 \text{ s}$  and  $\tau_{is}=4 \text{ s}$ . The steady-state magnitude of the BICC is a factor 5 larger than that of the ISCC. Note that for a large ramp rate the BICC has not yet achieved its steady-state value at the end of the ramp. It is assumed that the strand quenches if the total strand current  $I_{str}$  exceeds 500 A. Comparing both figures it is clear that the reduction of the quench current (i.e. the maximum transport current) will no longer be proportional to the ramp rate as in the case of the IFCCs and the ISCCs.

The quench current in a given strand section in the presence of BICCs:

$$I_{q,str} = I_{C,str} - I_{bi} \quad [\text{A}], \quad (8.10)$$

is iteratively calculated by using  $I_{q,str}=I_{tr,str}$  in eq. 8.3. The typical shape of the  $I_{q,str}-\dot{B}_{ce}$  curve is depicted in Fig. 8.4 in the case of the PBD magnet with  $C_{bi}=5 \cdot 10^3, 1 \cdot 10^4$  and  $2 \cdot 10^4 \text{ AsT}^{-1}$ ,  $\tau_{bi}=100$  and  $200 \text{ s}$  and for an initial transport current of 0 A.

The quench current decreases rapidly for small  $\dot{B}_{ce}$ , whereas the reduction becomes milder for large  $\dot{B}_{ce}$ . The initial slope of the curve is related to  $C_{bi}$  and is independent of  $\tau_{bi}$ . The shape of the curve is related to  $C_{bi}$  as well as  $\tau_{bi}$ . The initial slope is a factor 1.5 larger at 4.3 K than at 1.9 K, which is similar to the case of the reduction due to the IFCCs and the ISCCs.

**Figure 8.3.**

Simulation of the three current contributions  $I_{tr,str}$ ,  $I_s$  and  $I_{bi}$  to the total strand current  $I_{str}$  during a linear ramp with:

- a. a small ramp rate,
- b. a large ramp rate.

The ISCC (with  $\tau_{is}=4$  s) and the BICC (with  $\tau_{bi}=100$  s) are assumed to be 0 at  $t=0$ . The dotted lines show the transport current at which the strand current is equal to 500 A.

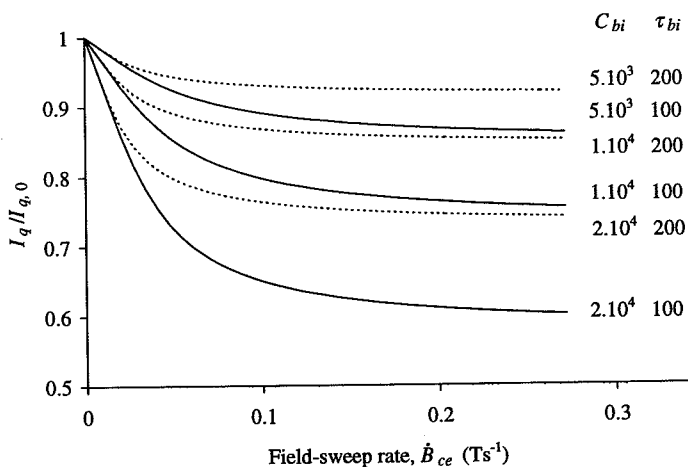
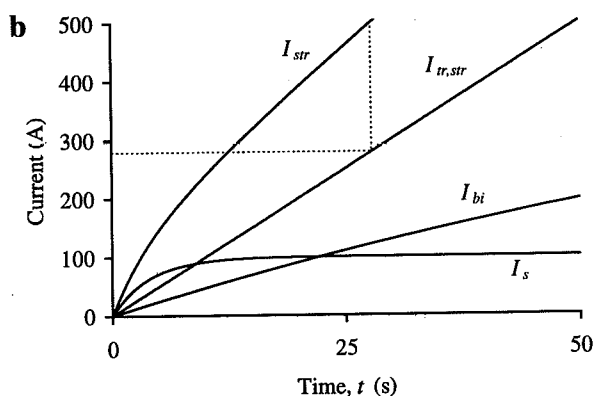


**Figure 8.4.** Calculation of the relative reduction of the quench current of the PBD magnet caused by the BICCs as a function of the central-field-sweep rate. Curves for three different  $C_{bi}$ -values (in  $\text{AsT}^{-1}$ ) are depicted for  $\tau_{bi}=100$  (normal lines) and 200 s (dotted lines),  $T_b=1.9$  K.

The reduction is influenced by the excitation history of the magnet if the BICCs, that are induced during the preceding sweeps, are not yet negligible. As a working rule, any field sweep that is performed in the past and not longer ago than a few times  $\tau_{bi}$  can increase as well as decrease the RRL. In general, preceding field sweeps with a positive (negative) sign increase (reduce) the RRL.

An illustration is given in Fig. 8.5 where the ramps shown in Fig. 8.3 are preceded by a field sweep with negative ramp rate. Comparing Figs. 8.3 and 8.5, it is clear that the quench current is significantly *larger* if the preceding ramp has opposite sign and the time of the final ramp is comparable or smaller than  $\tau_{bi}$ .

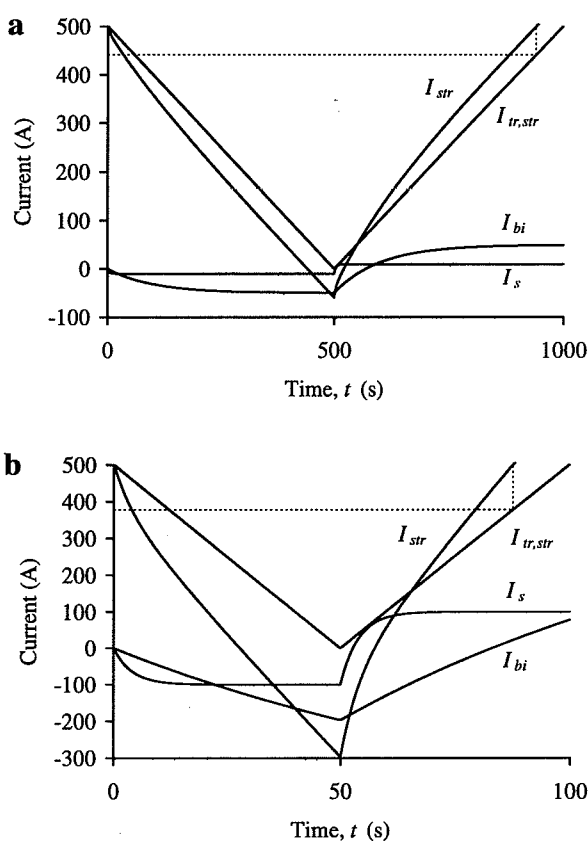


**Figure 8.5.**

Simulation of the three contributions  $I_{tr,str}$ ,  $I_s$  and  $I_{bi}$  to the total strand current  $I_{str}$  during a cycle of  $I_{tr,str}$  of 500-0-500 A, with:

- a: a small ramp rate,
- b: a large ramp rate.

The ISCC (with  $\tau_{is}=4$  s) and the BICC (with  $\tau_{bi}=100$  s) are assumed to be 0 at  $t=0$ . The dotted lines show the transport current at which the strand current is equal to 500 A.

This increase in the quench current due to a partial compensation of the BICCs is further investigated in the case of a PBD magnet for several values of  $\tau_{bi}$  and  $C_{bi}$ . The conditions are the same as used in Fig. 8.4 but now the ramp-to-quench is preceded by a ramp from  $I_{q,0}$  to 0 A (see Fig. 8.6).

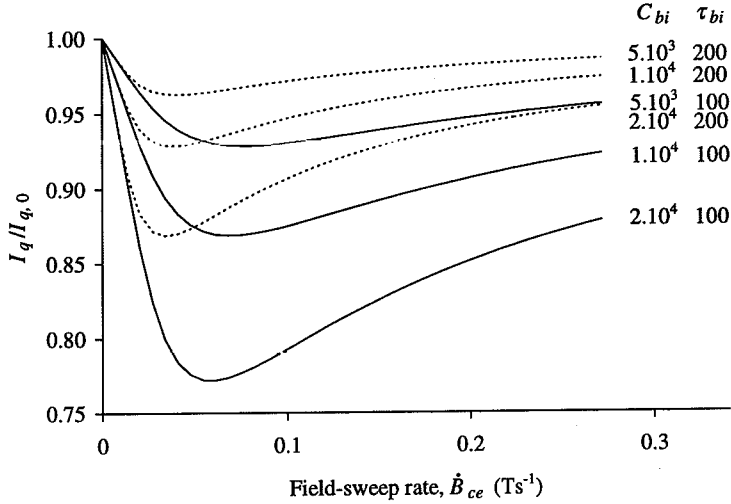


**Figure 8.6.** Calculation of the relative reduction of the quench current of the PBD magnet caused by the BICCs as a function of the central-field-sweep rate. Curves for three different  $C_{bi}$ -values (in  $\text{AsT}^{-1}$ ) are depicted for  $\tau_{bi}=100$  (normal lines) and 200 s (dotted lines),  $T_b=1.9$  K. The ramp to quench is preceded by a ramp from  $I_{q,0}$  to 0.

The ratio  $I_q/I_{q,0}$  attains a minimum which depends on  $C_{bi}$  as well as  $\tau_{bi}$ . The slopes of the curves for  $\dot{B}_{ce} \rightarrow 0$  are independent of  $\tau_{bi}$  and are the same as those of Fig. 8.4 (for quenches without a precycle), because the time of the ramp is much larger than  $\tau_{bi}$  so that the BICCs approach their steady-state values before the end of the ramp. In the case of larger field-sweep rates the difference in the quench currents with and without precycles increases steadily as can be seen easily from Figs. 8.4 and 8.6 (see also section 8.2.5).

#### 8.2.4 Influence of ISCL on the RRL

In section 4.4.1 it is shown that the ISCL in Rutherford-type cables is mainly generated in the contact resistances  $R_c$  caused by a field change normal to the cable width. The ISCL (per metre of cable) depends on the time  $t$  from the start of the ramp, and can be expressed by (for a uniform  $\dot{B}_\perp$ ):

$$P_c = 8.5 \cdot 10^{-3} \frac{L_{p,s} w^2 (N_s^2 - N_s)}{R_c} \dot{B}_\perp^2 (1 - e^{-t/\tau_{is}})^2 \quad [\text{Wm}^{-1}]. \quad (8.11)$$

Eq. 8.11 leads to the power density in turn  $i$  of a coil as a function of  $\dot{B}_{ce}$ :

$$P_{c,i} = 8.5 \cdot 10^{-3} \frac{L_{p,s} w (N_s^2 - N_s)}{h R_{c,i}} \beta_{P,i}^2 \dot{B}_{ce}^2 (1 - e^{-t/\tau_{is,i}})^2 \quad [\text{Wm}^{-3}], \quad (8.12)$$

with  $\beta_p$  the field geometry factor as given in Fig. 6.2. In the following, the  $R_{c,i}$  and  $\tau_{is,i}$  values are assumed to be the same in all the turns of the coil and equal to  $R_c$  and  $\tau_{is}$ .

The enhancement of the ISCL due to the BICCs is disregarded here. The increase is estimated (see also section 5.5) to be much smaller than the ISCL due to the ISCCs. The periodic pattern of the local power loss (see Figs. 5.12 and 5.13) does not cause a significant spatial variation of the cable temperature within a turn because the thermal-conductivity of copper (about  $250 \text{ W m}^{-1} \text{ K}^{-1}$ ) is about four orders of magnitude larger than that of the cable insulation. Due to the good electrical contacts between the strands, also the heat transfer from strand to strand will be much better than that from the strand to the helium outside the cable. Hence, the difference between the average cable temperature and the helium bath temperature is at least one order of magnitude larger than the temperature differences between the strands. In the following all strands in a turn are assumed to have the same temperature, equal to the average cable temperature  $T_{cab}$ .

To what extent the ISCL will heat up the (strand of the) cable depends, besides the parameters used in eq. 8.12, also on the heat transfer from the cable to the helium. The main thermal barrier is formed by the cable insulation (see Fig. 2.8). The heat transfer through the kapton layers and the glass-fibre tape cannot be predicted theoretically but has been determined by the following two experiments carried out by CEA-Saclay and CERN.

1. The temperature  $T_{cab}$  of the cable is determined as a function of the generated heat in the cable. Instead of a NbTi Rutherford-type cable, a stainless steel bar is used in which the heat is uniformly generated by means of resistive dissipation. The temperature increase of the central conductor in a stack of five conductors is depicted in Fig. 8.7 (curve 1) for a bath temperature  $T_b = 1.9 \text{ K}$  [Meuris, '91/'93]. The increase of  $T_{cab}$  vs. the resistive power loss is small up to a power-loss density of about  $7 \text{ mW/cm}^3$ , where  $T_{cab}$  reaches the lambda point  $T_\lambda$ , and increases strongly for larger power losses. It is concluded that a large part of the heat is transferred through the small faces of the conductor [Meuris '91].
2. A certain heat flux is passed transversely through a stack of insulated copper cable pieces of which one side is kept at a constant temperature  $T_0$ . The measurements are performed in vacuum. The effective thermal conductivity  $\lambda_{ins}$  of the total insulation is determined from the temperature difference between both sides of the stack [Dauguet, '92]. The coefficient  $\lambda_{ins}$  increases linearly as a function of the temperature and is equal to about  $0.006$  and  $0.010 \text{ W m}^{-1} \text{ K}^{-1}$  for  $T_0$  equal to  $1.8$  and  $4.2 \text{ K}$  respectively. The relation  $\lambda_{ins}(T_0)$  is used to estimate the increase in the cable temperature due to a uniform heat dissipation in the cable, assuming that the heat transport occurs only through the two small faces of the cable. The results are shown in Fig. 8.7 (curve 2).



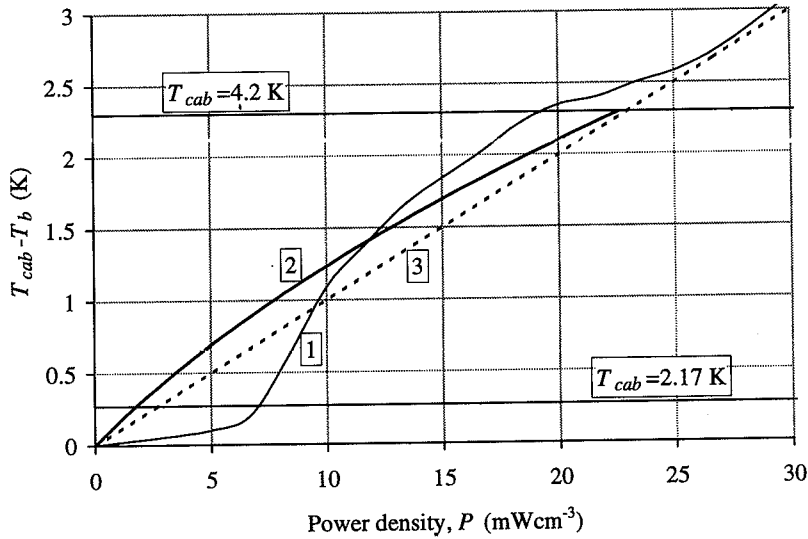


**Figure 8.7.** The temperature increase of a cable (at  $T_b = 1.9$  K) with an insulation as specified in Fig. 2.8 according to:

1. [Meuris, '93],
2. [Dauguet, '92], assuming that the heat is only transferred through the two small faces of the cable,
3. eq. 8.10 with  $q = 10^{-4} \text{ WK}^{-1} \text{ m}^{-3}$ .

Note the initial small temperature increase of curve 1, for  $T_{cab} < T_\lambda$ , due to very high thermal conductivity of superfluid helium. It is beyond the scope of this thesis to treat the thermal behaviour of the cables in detail. However, in order to obtain representative values of the current reduction as a function of the ISCL, a simple linear approximation of the curves 1 and 2 is used, in the range of experimental interest, i.e. for power densities larger than  $0.01 \text{ Wcm}^{-3}$  (see section 8.4). The cooling power is assumed to increase linearly with the temperature difference between the cable and the bath (see curve 3 in Fig. 8.7):

$$P_{cool} = q(T_{cab} - T_b) \quad [\text{Wm}^{-3}], \quad (8.13)$$

with  $q$  the effective thermal-conductivity coefficient per unit volume between the cable and the helium bath. A fit of eq. 8.13 to the experimental curves 1 and 2 shows that  $q$  is about  $10^4 \text{ Wm}^{-3} \text{ K}^{-1}$  under steady-state conditions for  $T_b = 1.9$  K and  $P > 0.01 \text{ Wcm}^{-3}$ . The linear approximation will be used to estimate the reduction of the quench current as a function of the dissipated power.

The temperature  $T_{cab}$  of turn  $i$  under steady-state conditions ( $t \gg \tau_{is}$  and  $P_c = P_{cool}$ ) is calculated by combining eqs. 8.12 and 8.13:

$$T_{cab,i} = T_b + 8.5 \cdot 10^{-3} \frac{L_{p,s} w (N_s^2 - N_s)}{h R_{c,i} q} \beta_{P,i}^2 \dot{B}_{ce}^2 \quad [\text{K}]. \quad (8.14)$$

The quench field is then determined by solving eq. 8.2 with  $T_{cab}$  as defined by eq. 8.14. In Fig. 8.8 the results are given of the calculated relative reduction of the quench current of the PBD magnet due to the ISCL, as a function of  $\dot{B}_{ce}$ , for constant  $q$  and steady-state conditions. Note that the reduction depends on the factor  $(R_c q)$ , so that the reduction for  $R_c = 1 \mu\Omega$  and  $q = 2 \cdot 10^4 \text{ Wm}^{-3}\text{K}^{-1}$  is identical to that for  $R_c = 2 \mu\Omega$  and  $q = 1 \cdot 10^4 \text{ Wm}^{-3}\text{K}^{-1}$ .

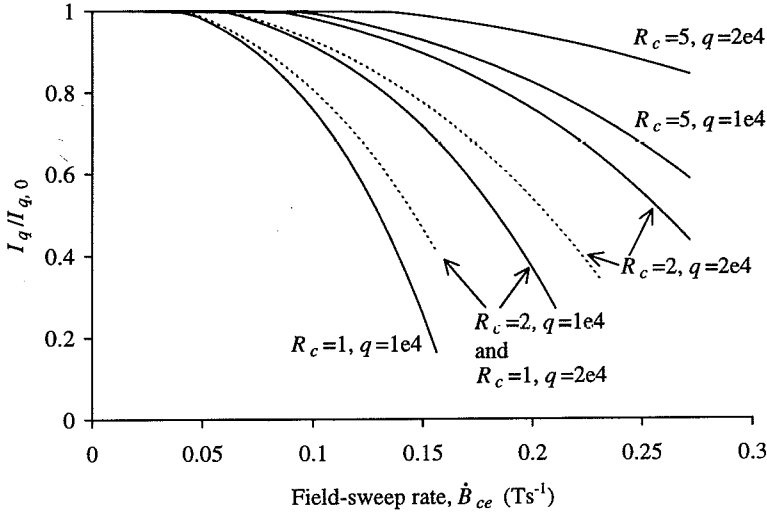


**Figure 8.8.** Calculation of the reduction of the relative quench current of the PBD magnet due to the ISCL as a function of the central-field-sweep rate. Various curves for different  $R_c$  (in  $\mu\Omega$ ) and  $q$  (in  $\text{Wm}^{-3}\text{K}^{-1}$ ) are shown for  $T_b = 1.9 \text{ K}$  and  $4.3 \text{ K}$  (dotted lines).

If  $\dot{B}_{ce}$  is small then the ISCL is also small and the quench starts in block 6 where  $\beta_{str}$  is maximum (and hence  $I_{C, str}$  minimum). Should  $\dot{B}_{ce}$  be large then the ISCL also increases and the quench origin shifts to block 3 where  $\beta_p$  is maximum.

The generated coupling power loss causes a reduction of the quench current which is, in first approximation, linear with  $\dot{B}_{ce}^2/(qR_c)$ , and is larger at  $4.3 \text{ K}$  than at  $1.9 \text{ K}$ . Note that for increasing  $\dot{B}_{ce}$  the reduction of the quench current by temperature, due to the ISCL, is much larger than the reduction by over-current, due to the ISCCs, for the estimated cooling conditions and  $R_c$ -values between  $1$  and  $10 \mu\Omega$ .

### 8.2.5 Discussion

In practical dipole magnets the RRL is mainly caused by a combination of the IFCCs, the ISCCs, the BICCs and the ISCL. In section 8.2.1 it is shown that the reduction of the quench current due to the IFCCs is smaller than  $0.1\%$  for sweep rates up to  $0.1 \text{ Ts}^{-1}$ , and can be disregarded for the operation of accelerator dipole magnets. The quench current is then given by (assuming steady-state conditions):

$$I_{q, str}(B_{str}, \dot{B}_{ce}, T_{cab}) = I_{C, str}(B_{str}, T_{cab}) - I_{is}(\dot{B}_{ce}) - I_{bi}(\dot{B}_{ce}) \quad [\text{A}]. \quad (8.15)$$

The cooling conditions of the magnet, the heat capacity of the cable (and the helium in the voids of the cable), the field-sweep rate, the  $\dot{B}_1$ -distribution and the contact resistance are the main factors that determine which coupling currents or losses are the main cause of the RRL. Another important factor is the time scale of the field sweep as compared to the time constants  $\tau_{is}$  and  $\tau_{bi}$ . Since most of these parameters vary strongly over the cross-section of the coil and even along the length of a turn, it is impossible to calculate the RRL of a magnet accurately.

The dominant cause of the reduction can be deduced from the shape of the experimentally obtained  $I_q$ - $\dot{B}_{ce}$  curve. The ISCCs initially cause a linear decrease (see Fig. 8.2), the BICCs a concave decrease (see Fig. 8.4) and the ISCL a convex decrease (see Fig. 8.8). In practice, however, it is probably a combination of the three causes that determines the RRL of a magnet. An example of a characteristic reduction of the quench current, caused by both the BICCs and the ISCL, is shown in Fig. 8.9 for the PBD magnet with  $R_c = 5 \mu\Omega$ ,  $C_{bi} = 10^4 \text{ AsT}^{-1}$ ,  $q = 10^4 \text{ Wm}^{-3}\text{K}^{-1}$  and  $T_b = 1.9 \text{ K}$ .

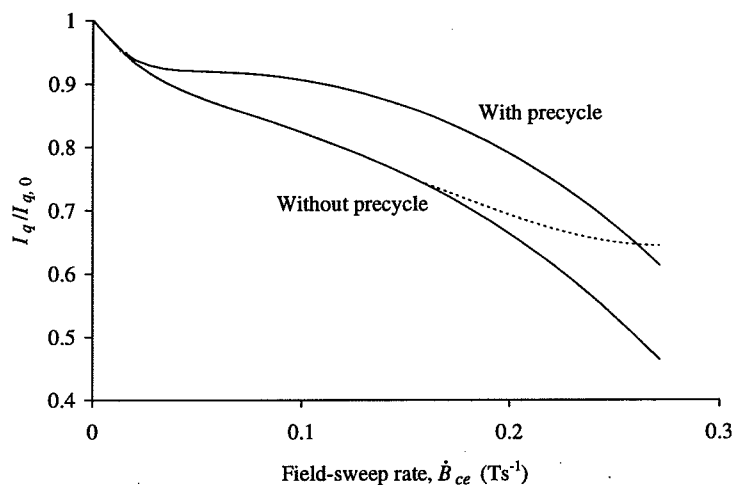


**Figure 8.9.** Calculation of the relative quench current due to a combination of the ISCL and the BICCs as a function of the field-sweep rate. The dotted line shows the milder decrease which occurs if the time of the ramp is too small to attain thermal equilibrium.

If  $\dot{B}_{ce}$  is small the reduction is caused by the BICCs, according to the initial slope of Figs. 8.4 and 8.6, whereas for a larger  $\dot{B}_{ce}$  the reduction is mainly caused by the ISCL. A precycle reduces the RRL for larger field-sweep rates. The shape of the curve changes if the ramp time  $t_r$  becomes too small to reach the steady-state conditions, that is thermal equilibrium. In this case the quench current will increase (see the dotted line) compared to the steady-state value. In the case of ramps with a precycle this increase is less pronounced because the ramp to quench is preceded by a ramp-down so that the total time to reach thermal equilibrium is much larger. For normal excitation of an accelerator magnet the RRL caused by the BICCs can be reduced by decreasing the field-sweep rate toward the end of the sweep (during a period of a few times  $\tau_{bi}$ ).

The difference in quench currents with and without a precycle is shown in Fig. 8.10. By presenting experimental quench results of a coil in this way, it is possible to estimate the magnitude of the BICC, that causes the quench, and its characteristic time. This approach is followed in section 8.3.

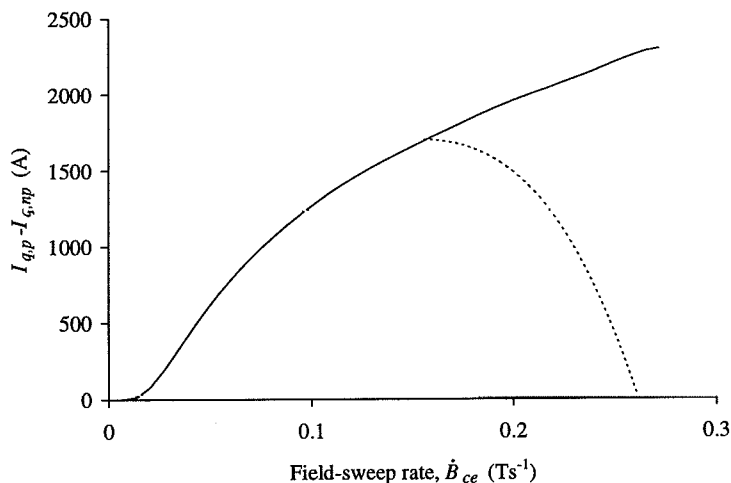


**Figure 8.10.** Calculation of the difference in the quench current between quenches with and without a precycle as a function of the field-sweep rate. The RRL is due to a combination of the ISCL and the BICCs. The dotted line shows the milder decrease which occurs if the time of the ramp is too small to reach thermal equilibrium.

The following points are important with respect to the stability and RRL of superconducting magnets, but a detailed evaluation falls beyond the scope of this thesis:

- In sections 8.2.1-8.2.4 it is assumed that the whole cable cross-section, i.e. all the strands, quenches if locally the current in a single strand exceeds the critical current. However, since the strands are in electrical contact with each other, the strand currents could redistribute as soon as some resistive voltage is built up over the strand. This leads to a decrease of the ISCCs whereas the total power loss remains the same (see section 4.5) so that the RRL could be less severe than calculated. A similar conclusion holds for the BICCs, of which the magnitude can also decrease once the total strand current approaches (or exceeds) the critical strand current. The process of redistribution probably depends strongly on the excitation level, the thermal properties of the cable and the characteristic times and magnitudes of the coupling currents.
- $R_a$  and  $R_c$  also influence the temperature sharing between the strands and the heat transport between the strands and the helium. Hence, it can affect the sensitivity of the coil in the case of small transient heat pulses.
- The presence of coupling currents and ISCL always reduces the temperature margin of the coil for positive  $\dot{B}_{ce}$ . Small transient heat pulses which would not lead to a quench under DC conditions could, therefore, provoke a quench while ramping the magnet. This stability effect should be considered carefully when designing a magnet, by estimating the decrease of the temperature margin caused by the coupling currents and the power

loss, especially of magnets for which the field-sweep rate is fixed. In accelerator magnets the field-sweep rate can be reduced near the end of the excitation where the temperature margin is small. A decrease in the initial field-sweep rate in the case of a fast de-excitation is not possible.

- A non-uniform current distribution due to different joint resistances (see section 5.2) further decreases the temperature margin of the coil.
- The quench current, or the temperature margin, as a function of the field-sweep rate has to be estimated taking the smallest  $R_a$  and  $R_c$  and the worst cooling conditions that are expected to be present in the coil. Variations in the ISCL and the cooling conditions over small lengths (several cm) of the cable do not have to be taken into account since the high thermal conductivity of the cable results in a levelling of the cable temperature. Often these points are closely related and several authors have dealt with these stability effects, recently for example [Amemiya, '94], [Lvovsky, '95], [Ono, '95], [Vysotsky, '95a].

It is clear that the analysis of the RRL of magnets, in terms of the various coupling currents, power losses and cooling conditions, is very complicated. Although it is possible to clarify the mechanisms, it is difficult to extract specific conclusions. However, even rough estimates of the following topics are very interesting in order to optimise the performance of superconducting magnets:

- The influence of BICCs on the RRL, and in particular for the expected field-sweep rates during operation.
- The temperature increase of the cable as a function of the dissipation in the coils. This leads to an estimate of the required temperature margin in the case of beam losses in the coils.
- The RRL in the case of a fast de-excitation of the magnet.

These aspects will be evaluated in the subsequent three sections for the LHC dipole model magnets. The analysis is based on a limited number of quenches, performed on a few magnets. Nevertheless, the experimental results clearly demonstrate the basic mechanisms determining the quench behaviour of magnets during a field sweep.

### 8.3 Influence of BICCs on the RRL in LHC dipole magnets

The RRL of the LHC dipole model magnets is investigated by means of two different current sequences:

**Quenches without a precycle** (see Fig. 8.11a). The transport current is:

- ramped up from 0 to  $I_1$  with a small field-sweep rate,
- kept constant for a time  $t_1$  equal to 600 s,
- ramped up from  $I_1$  to the quench current  $I_{q,np}$  with a constant ramp rate.

**Quenches with a precycle** (see Fig. 8.11b). The transport current is:

- ramped up from 0 to  $I_1$  with a small field-sweep rate,
- kept constant for a time  $t_1$  equal to 600 s,
- ramped down from  $I_1$  to  $I_2$  with a constant ramp rate,
- kept constant for a time  $t_2$ ,
- ramped up from  $I_2$  to the quench current  $I_{q,p}$  with a constant ramp rate.

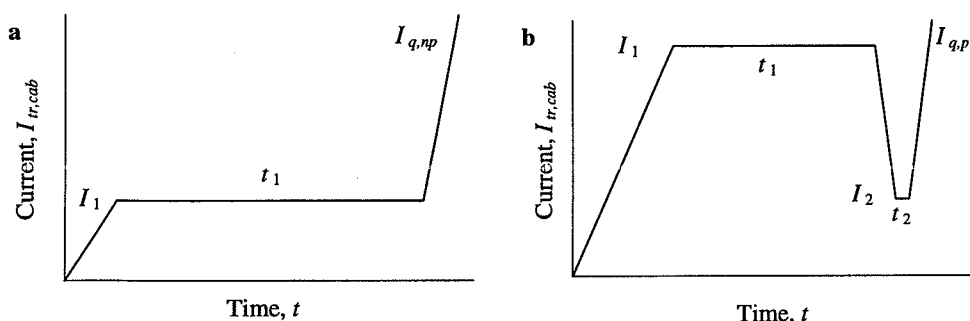


Figure 8.11. Current sequences for performing quenches a. without and b. with a precycle.

The waiting time  $t_1$  of 600 s is chosen in order to stabilise the cable temperature and reduce the magnitude of the BICCs, which are observed to exhibit a characteristic time of about  $10^2$  s (see sections 7.7.1-7.7.5). The influence of the waiting time  $t_2$  on the RRL can reveal the time constant  $\tau_{bi}$ . The quench current will be maximum if  $t_2$  is equal to 0 and will decrease, in first approximation, exponentially to the minimum value  $I_{q,np}$  for  $t_2 \gg \tau_{bi}$ .

In the case of quenches with precycle, the current  $I_1$  is chosen close to the expected quench current  $I_{q,p}$  (usually within 500 A).

The reproducibility of the quench current is about 100 A for identical bath temperature and current history. Figs. 8.12 and 8.13 show the relative quench current as a function of  $\dot{B}_{ce}$  for quenches without precycle at  $T_b=1.8$ -2.0 K and  $T_b=4.3$  K respectively.

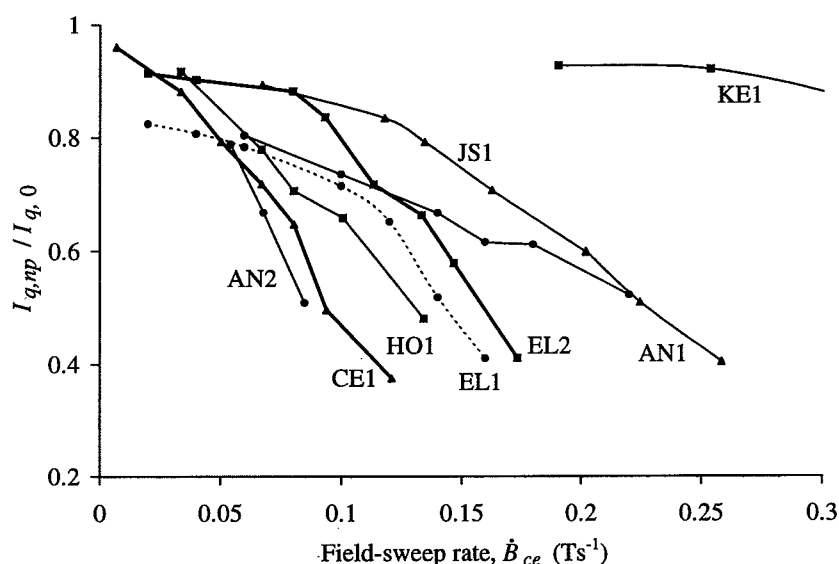


Figure 8.12. The relative quench current as a function of the central-field-sweep rate for quenches without precycle at  $T_b=1.8$ -2.0 K and  $I_1=3$  kA for several magnets as specified in Table 2.3.

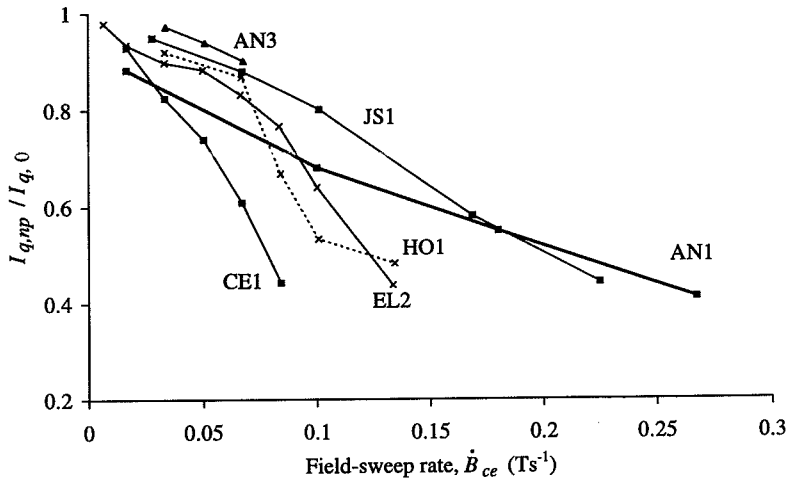


Figure 8.13. The relative quench current as a function of the central-field-sweep rate for quenches without precycle at  $T_b=4.3$  K and  $I_1=3$  kA for several magnets as specified in Table 2.3.

Ramp-rate-induced quenches at  $T_b=1.8$ -2.0 K and  $\dot{B}_{ce}<0.02$  Ts<sup>-1</sup> could often not be performed since the training curve was not completed so that the quench current was not initiated by the coupling currents or the ISCL.

The quench currents are scaled to the measured quench current  $I_{q,0}$  at  $\dot{B}_{ce}=0.001$  Ts<sup>-1</sup>. The average  $I_{q,0}$  for the magnets is about 11500 A at 4.3 K and 15000 A at 1.9 K (N.B.: the  $I_{q,0}$ -values for the KE1 magnet, made from a cable with a smaller cross-section, are about 14% smaller). If the training curve at 1.9 K is not completed, the current  $I_{q,0}$  is estimated from the quench current at 4.3 K multiplied by the empirical factor 1.3 observed on a few magnets [Walckiers, '93]. Due to a possible error in  $I_{q,0}$  it is not certain whether all the curves at 1.9 K are properly scaled. Hence, the strong reduction in the quench current for  $\dot{B}_{ce}<0.05$  Ts<sup>-1</sup>, especially for the EL1 magnet, can be caused by the BICCs (see Fig. 8.9) but can also be inherent to the scaling. At 4.3 K the initial reduction in  $I_{q,np}$  is very likely to be attributed to the BICCs since  $I_{q,0}$  is experimentally well determined.

The origins of almost all ramp-rate-induced quenches are located (by means of pick-up coils in the aperture of the magnets, see [Leroy, '93b], [Siemko, '95]) in the blocks 3 and 4 (see Fig. 2.2b) [Siemko, '94]. However, the quenches of each curve are not always located in the same aperture and the same quadrant.

The reduction of the quench current is about 20-80% larger at 4.3 K than at 1.9 K for large  $\dot{B}_{ce}$ . Since the calculated difference is about 50% (see section 8.2.4), this implies that the heat transfer (or cooling) is about the same at  $T_b=1.9$  K and  $T_b=4.3$  K (for large  $\dot{B}_{ce}$ ). The thermal transfer between the cable and the helium is discussed in more detail in section 8.4.

The shapes of the curves show that the RRL is mainly affected by the ISCL for  $\dot{B}_{ce}>0.05$  Ts<sup>-1</sup>. Due to the apparent sharp reduction at small  $\dot{B}_{ce}$ , the BICCs have probably also a large effect (see Fig. 8.4). However, since the scaling can be quite inaccurate it is preferable to investigate the presence of BICCs by performing quench experiments after a

current precycle. The increase in the quench current if the ramp-up is preceded by a ramp-down (with  $t_2=0$  s, see Fig. 8.11b) is shown in Fig. 8.14 for two magnets at  $T_b=4.3$  K.

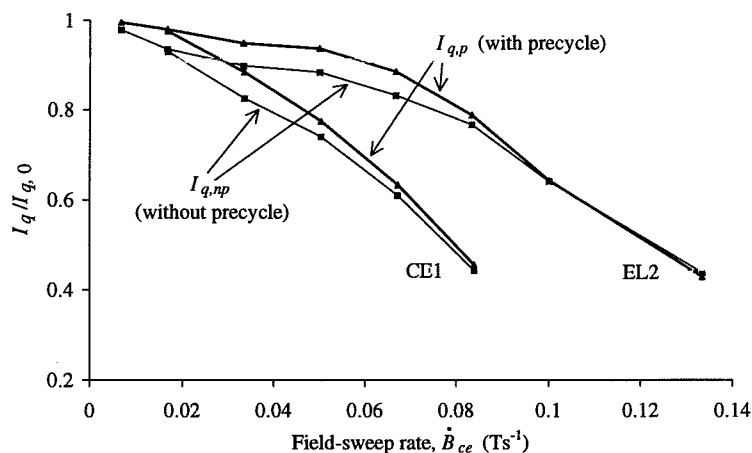


**Figure 8.14.** The quench currents, with and without a precycle, of the CE1 and EL2 magnets as functions of the central-field-sweep rate ( $T_b=4.3$  K,  $I_2=0$ ,  $t_2=0$  s).

It can be clearly seen that the quench current with a precycle is much larger than without, especially for intermediate field-sweep rates, due to the partial compensation of the BICCs. The difference in quench currents ( $I_{q,p}-I_{q,np}$ ) at  $T_b=1.9$  K and 4.3 K is depicted in Figs. 8.15 and 8.16 respectively.

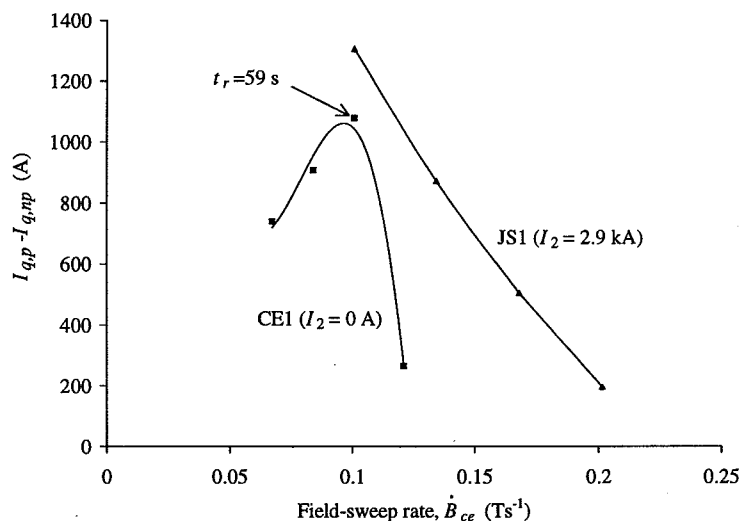


**Figure 8.15.** The difference in quench currents performed with and without a precycle as a function of the central-field-sweep rate at  $T_b=1.8-2.0$  K ( $t_2=0$ ,  $I_{q,0}\approx 15$  kA). The labels indicate the ramp time  $t_r$  for maximum difference ( $I_{q,p}-I_{q,np}$ ).



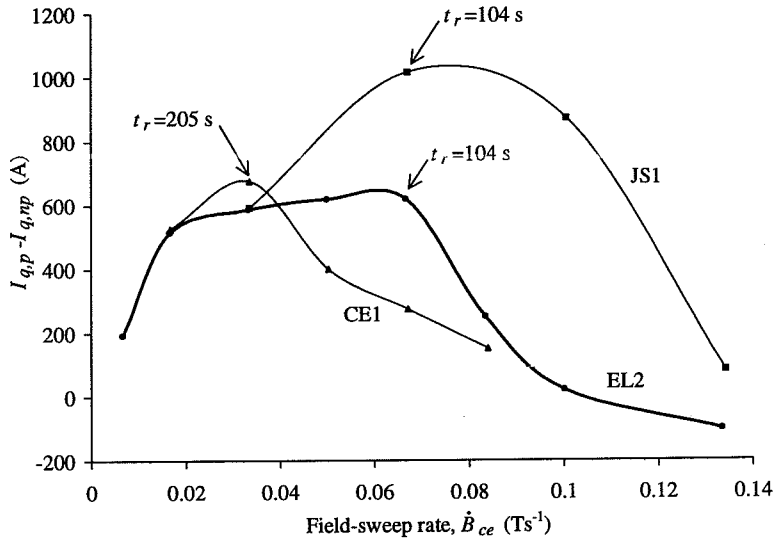


**Figure 8.16.** The difference in quench currents performed with and without a precycle as a function of the central-field-sweep rate at  $T_b = 4.3$  K ( $I_2 = 0$ ,  $t_2 = 0$ ,  $I_{q,0} = 11.5$  kA). The labels indicate the ramp time  $t_r$  for maximum difference ( $I_{q,p} - I_{q,np}$ ).

The figures show that a precycle causes an increase in the quench current up to a maximum of about 1000 A. This corresponds to the expected curves shown in Fig. 8.10 (note that the differences at small  $\dot{B}_{ce}$  could not be determined). The differences become smaller at larger field-sweep rates i.e. at ramp times  $t_r$  smaller than about 50-200 s, and they can even become negative as observed on the EL2 magnet. The most plausible explanation for the shape of the curves is that the temperature of the cable is not yet stabilised for the quenches without a precycle as shown in Fig. 8.10. The maximum of the curves for the CE1 magnet occurs at a smaller ramp time at  $T_b = 1.9$  K than at  $T_b = 4.3$  K, which suggests that the time required for temperature stabilisation is larger for the quenches at 4.3 K, probably caused by the different thermal properties of the helium or the larger heat capacity of the cable at 4.3 K.

The rising parts of the curves are used to estimate the magnitude of the BICCs, by fitting the simulations, which are presented in section 8.2.3, to the curves. Values for  $C_{bi}$  are found between  $2 \cdot 10^3$  to  $5 \cdot 10^3$  AsT $^{-1}$  and correspond well with the rough estimate of  $C_{bi}$  as made at the beginning of section 8.2.3. According to eq. 8.9, this implies that during excitation of the LHC dipoles with  $0.0066$  Ts $^{-1}$ , BICCs will flow in the strands with steady-state values of up to 30 A, which is about as large as the transport current in the strands at injection ( $I_{tr,str} \approx 35$  A) and about 7% of the transport current at nominal field ( $I_{tr,str} \approx 470$  A). At fast de-excitation the BICCs can even attain values of about 400 A. However, due to the large characteristic time, the BICCs at the start of the de-excitation, where the current margin is still small, are much weaker (see also section 8.5).

The enhancement of the quench current due to a precycle will reduce if the time  $t_2$  (see Fig. 8.11) between the precycle and the sweep to quench is large compared to the characteristic time  $\tau_{bi}$  of the BICCs. The difference in quench currents ( $I_{q,p} - I_{q,np}$ ) between quenches with and without a precycle should therefore have a maximum for  $t_2=0$  and decrease towards 0 for  $t_2 \rightarrow \infty$ . The characteristic time of the decrease is, in first approximation, equal to  $\tau_{bi}$ .

The effect of the waiting time  $t_2$  on the quench current at  $T_b=1.9$  and 4.3 K is shown in Figs. 8.17 and 8.18. The quenches have only been incidentally performed on a few magnets. A very systematic analysis of the results is therefore not possible.

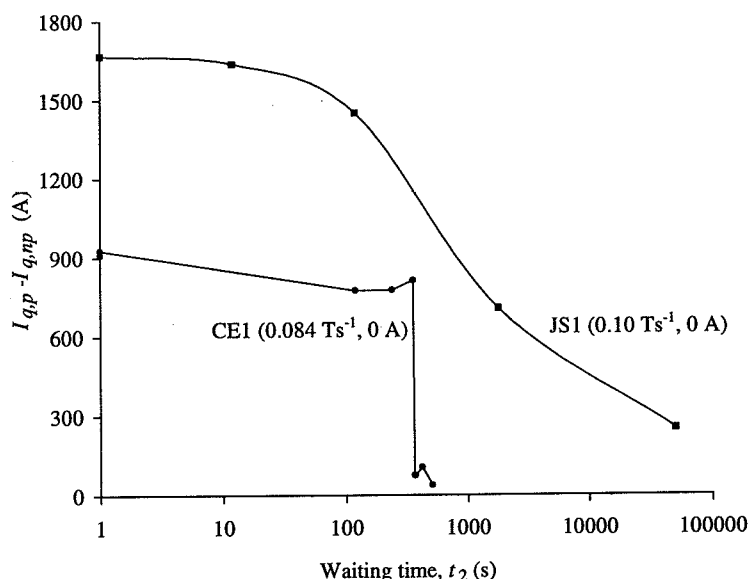
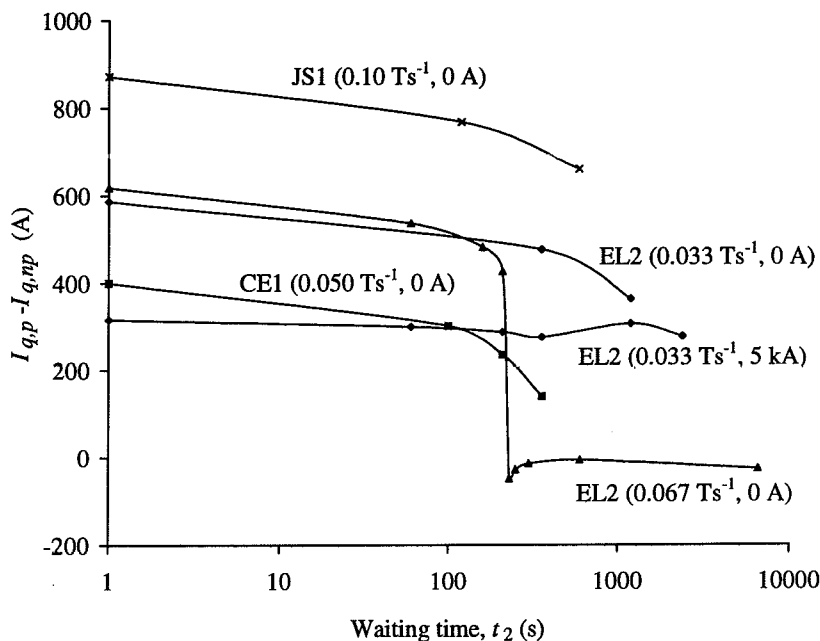


Figure 8.17. The difference in quench currents performed with and without a precycle as a function of the waiting time  $t_2$  at  $T_b=1.9$  K. The labels indicate the central-field-sweep rate and the current  $I_2$ .

The reduction of the quench current for increasing  $t_2$  is clearly visible for all magnets except the EL2 magnet (for  $I_2=5$  kA). Two types of curves are observed:

- curves for which  $I_{q,p}$  gradually decreases with characteristic times of the order of  $10^3$  s,
- curves for which  $I_{q,np}$  shows a peculiar sharp 'step' with a 'width' of less than 10 s.

The gradually decreasing curves correspond to expectations. The large characteristic time is probably caused by the spectrum of characteristic times that is present in a coil. In chapter 5 it is shown that  $\tau_{bi}$  depends not only on the cable geometry but also on the effective strand resistivity and on the contact resistance. In a coil, each BICC exhibits a different characteristic time which usually increases if the average magnitude of the BICCs increases.



**Figure 8.18.** The difference in quench currents performed with and without a precycle as a function of the waiting time  $t_2$  for  $T_b=4.3$  K. The labels indicate the central-field-sweep rate and the current  $I_2$ .

Since the quench is likely to be caused by large BICCs, the characteristic time deduced from Figs. 8.17 and 8.18 could be much larger than the average characteristic time as given in sections 7.7.1 and 7.7.3.

The reason of the peculiar 'step' in two  $I_{q,p}-t_2$  curves is not understood. The quench values on the 'left' and 'right' sides of the step are very reproducible but the origins of the quenches on both sides of the step are different. During the waiting time  $t_2$  there is no anomalous signal on any of the pick-up coils. A sudden current redistribution during  $t_2$  is therefore probably not present. The most plausible explanation is that, during the ramp-up, part of (a strand of) the cable becomes normal which causes a quench on the right side of the step but recovers on the left. Field measurements (with a high sampling rate) during the ramp-up could perhaps reveal the exact reason.

This 'step' phenomenon could be related to the observed ramp-rate sensitivity on a CIC conductor where small sections of the cable seem to quench due to current loops in the cable [Vysotsky, '95b]. In this conductor the quenches recover due to a fast redistribution of the current.

## 8.4 Estimate of the temperature increase of the cable due to power losses in the coil

In order to estimate the temperature of the cable due to the coupling loss, the  $I_q-\dot{B}_{ce}$  curves have to be converted into  $T_{cab}-P_c$  curves.

The field-sweep rate can be replaced by the estimated coupling-power density in the turn or block where the quench starts using eq. 8.12 assuming thermal equilibrium. Average  $R_c$ -values are used for this estimate, which are determined by means of the loss measurements and listed in Table 6.3.

The cable temperature just before the quench can be deduced from the quench current by combining eqs. 8.2, 8.3 and 8.14 assuming that  $I_{bi}=0$ . This assumption causes an error in the calculation of  $T_{cab}$  which is larger for quenches without a precycle than for quenches with a precycle. This is shown clearly in Fig. 8.19 where the  $T_{cab}-P_c$  relation as deduced from the  $I_q-\dot{B}_{ce}$  relation is shown in the case of the JS1 magnet at 1.9 and 4.3 K.

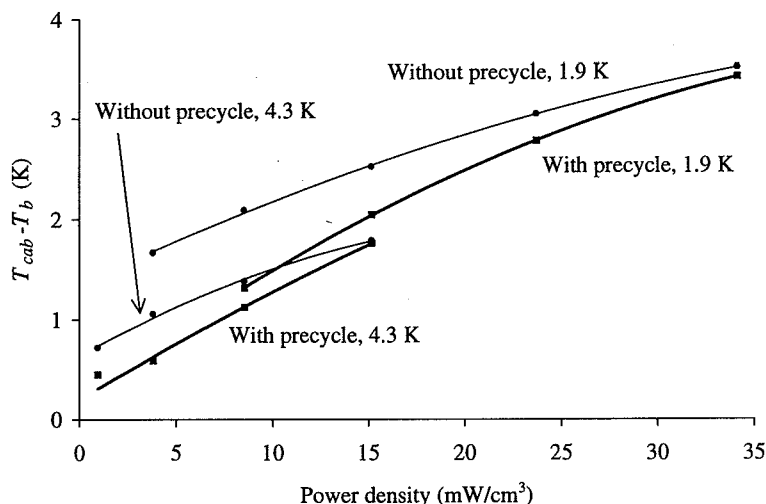


**Figure 8.19.** The estimate of the increase of the cable temperature caused by a steady-state heat dissipation in the cable of the JS1 magnet, deduced from the RRL with and without a precycle at  $T_b=1.9$  and 4.3 K.

At 1.9 K, no quenches could be performed at small  $\dot{B}_{ce}$ , that is small  $P_c$ , because the training curve was not completed. Fig. 8.19 clearly shows that the conversion from a  $I_q-\dot{B}_{ce}$  curve to a  $T_{cab}-P_c$  curve results in relatively large errors if no precycle is performed, because it is obvious that  $T_{cab}(\dot{B}_{ce} \rightarrow 0) = T_b$  if no BICCs are present. Extrapolation of the lower curves (deduced from the  $I_{q,p}$ -values) supports this condition while extrapolation of the upper curves gives offset temperatures of about 1 K. Therefore, only the quenches with a precycle will give representative values for the temperature increase of the cable due to heat dissipation in the coil. The current of quenches performed without precycle can be strongly affected by the BICCs, which subsequently results in an overestimate of  $T_{cab}$ .

Quenches with a precycle have only been performed on a few magnets. Figs. 8.20 and 8.21 show the relations  $T_{cab}-P_c$  as deduced from the quench currents at 1.9 and 4.3 K. A linear approximation according to eq. 8.13 is given as well.

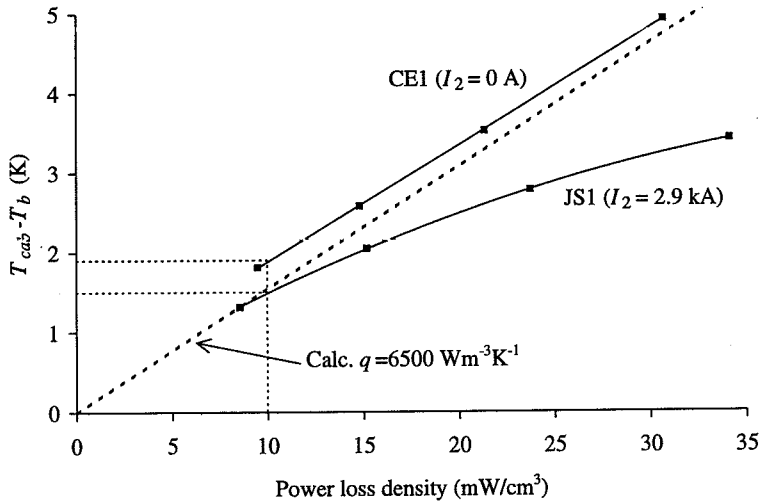


**Figure 8.20.** The estimate of the increase of the cable temperature due to a heat dissipation in the cable of the CE1 and JS1 magnets, deduced from the RRL with a precycle at  $T_b=1.9$  K ( $t_2=0$ ). The linear dotted line shows the calculated relation using eq. 8.13 with  $q=6.5 \cdot 10^3$  Wm<sup>-3</sup>K<sup>-1</sup>.

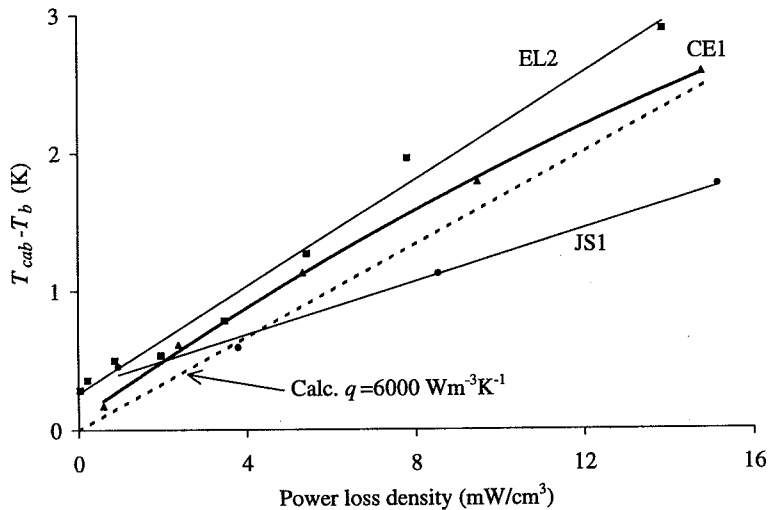


**Figure 8.21.** The estimate of the increase of the cable temperature due to a heat dissipation in the cable of the CE1, EL2 and JS1 magnets, deduced from the RRL with a precycle at  $T_b=4.3$  K ( $I_2=0$ ,  $t_2=0$ ). The linear dotted line shows the calculated relation using eq. 8.13 with  $q=6.0 \cdot 10^3$  Wm<sup>-3</sup>K<sup>-1</sup>.

Fig. 8.20 shows that at  $T_b = 1.9$  K the cable temperature increases by about 1.5 K for a heat dissipation of  $10 \text{ mW/cm}^3$ . The error is estimated to be smaller than 0.5 K and is mainly caused by:

- the use of an average  $R_c$  that is too large or too small compared to the local  $R_c$  in the turn where the quench starts, which results in a decrease, respectively increase, of the calculated power loss,
- additional BICCs in the cable, which results in an increase of the calculated cable temperature.

It is very encouraging that the temperature increase of about 1.5 K at  $P_c = 10 \text{ mW/cm}^3$  corresponds within 0.5 K to that deduced from the two experiments on small stacks of cable pieces (see Fig. 8.7). This proves not only that the temperature increase of a cable can be deduced by combining the electrical loss measurement and RRL of a coil, but also that the main mechanisms determining the RRL of magnets are well evaluated. Furthermore, the quantitative agreement between the various methods shows that the effective cooling surfaces of the cable in the coil itself and in a single stack are about the same (for power losses larger than  $P_c = 10 \text{ mW/cm}^3$ ), although the stress levels in a coil are much higher which could in fact reduce the size of the cooling channels considerably.

The evaluation of the temperature increase can be improved by supplying the turns in the coils, especially those near the midplane where the quenches start, with temperature sensors. The time required for thermal equilibrium of the cable can then be determined as well.

Quenches at a lower level of power losses can be induced at 4.3 K since the training sequence of the magnets is completed. A similar temperature increase is observed as at 1.9 K with a temperature increase between 1.3 and 2.3 K for  $P_c = 10 \text{ mW/cm}^3$ . The difference in temperature increase at 1.9 and 4.3 K may be due to a different thermal conductivity or a different effective cooling surface. In the case of small power-loss densities, the curves deviate slightly from the expected linear decrease towards 0, caused by the BICCs which are not well compensated since the ramp time becomes large.

It is important that the coupling power loss can be directly related to the expected beam losses in the magnets since both types of losses are dissipated in the cables near the midplane of the magnet. Therefore, Fig. 8.20 shows directly the estimated temperature increase of the cable as a function of the beam losses in the coil windings. A precise estimate in the range between 0 and  $10 \text{ mW/cm}^3$ , which is expected in the LHC magnets, is possible if the training sequence of the magnets is completed, which has unfortunately not been the case for the investigated magnets.

The accuracy of the method can be further improved by reducing the magnitude of the BICCs. This can be achieved by slowly increasing the average central field while an additional AC transport current causes a small AC field. The slowly increasing field will not cause significant losses and BICCs. The AC field causes the large  $\dot{B}_{ce}$  required for generating the power loss without provoking large BICCs as long as the period of the AC current is much smaller than the characteristic time of the BICCs.

## 8.5 Negative field-sweep rates

The maximum negative ramp rate in accelerator magnets is important since it determines the maximum possible de-excitation rate of the magnets if there is a quench in one of the series-connected magnets.

In this section the effect of the coupling currents and power loss on the maximum de-excitation rate is discussed. The very few results of quench currents, that are available on several 1 m long LHC dipole model magnets, are presented at the end of this section.

The RRL due to the IFCCs is not significantly influenced by the sign of the field-sweep rate, since the time constant  $\tau_{if}$  is very small and the IFCCs almost immediately reach the steady-state value. The reduction of the quench current, as discussed in section 8.2.1, is about 0.1% (at the expected field-sweep rate  $\dot{B}_{ce} = -0.084 \text{ T s}^{-1}$ ), and is negligible compared to the available margin of at least 10% between operating current and critical current.

The effects of the ISCCs, the BICCs and the ISCL on the RRL is different for negative and positive  $\dot{B}_{ce}$  and are discussed in more detail.

### ISCCs

If  $\dot{B}_{ce}$  is negative the transport current and the ISCCs have opposite sign near the aperture, where the field is maximum. This implies that the ISCCs cause a decrease of the strand current in the parts of the coil with the highest field, and hence they cause an *increase* of the margin of the coil (not taking into account the loss generated by the ISCCs). Only for very large negative  $\dot{B}_{ce}$  in combination with a very small  $R_c$  can the ISCCs cause a significant reduction of the quench current. However, these large field-sweep rates are not attained in accelerator magnets.

### BICCs

The influence of the BICCs on the RRL is much smaller for negative  $\dot{B}_{ce}$  than positive  $\dot{B}_{ce}$  since the characteristic time  $\tau_{bi}$  is large. This means that at the start of the de-excitation, when the field is high, the BICCs are still small. At increasing ramp time, the magnitude of the BICCs increases but the critical current  $I_{C, str}$  also increases because the field decreases. Fig. 8.22 shows an example of the change in the strand currents as a function of the time during a linear de-excitation (in the case of the PBD magnet with  $R_c = 1 \mu\Omega$ ,  $\tau_{is} = 4 \text{ s}$ ,  $C_{bi} = 2 \cdot 10^4 \text{ As T}^{-1}$ ,  $\tau_{bi} = 200 \text{ s}$ , constant  $T_b = 1.9 \text{ K}$ ).

At  $t=0$  the strand current is about 30% smaller than the critical current which corresponds to an operation field of about 85% of  $B_q$ . The strand current increases because the increase of the current  $I_{bi}$  is larger than the decrease of the transport current  $I_{tr, str}$ . However, the strand will not quench since the critical current  $I_{C, str}$  remains larger than  $I_{str}$  during the entire ramp. The magnitude of the BICCs is difficult to evaluate since the BICCs caused by the numerous non-uniformities in a coil partially cancel. This implies that the RRL due to the BICCs is difficult to estimate as well. An increase of  $R_a$  and  $R_c$  of the cable will definitely reduce the magnitude of the BICCs, but could, on the other hand, worsen the stability of the cable (see chapter 9). Hence, a certain optimum of  $R_a$  and  $R_c$  has to be found for which the BICCs are sufficiently small, without affecting the stability of the cable too much.

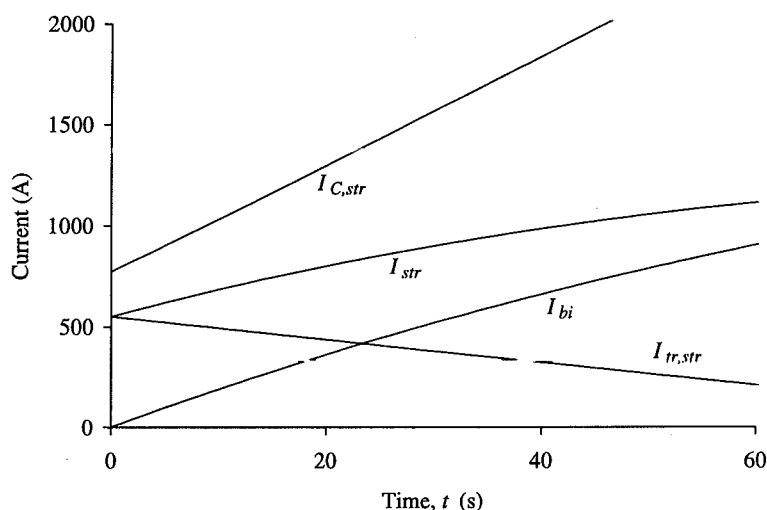


**Figure 8.22.** Simulation of the currents  $I_{tr,str}$ ,  $I_{C,str}$ ,  $I_{str}$  and  $I_{bi}$  during a ramp-down from 550 to 0 A in 100 s (only the first 60 s is shown). The BICC is assumed to be 0 at  $t=0$ . The increase of  $I_{bi}$  is larger than the decrease of the transport current. The critical current, however, increases still faster than the strand current and no quench will occur during the ramp-down.

It is preferable to investigate the effect of the BICCs experimentally by actually measuring the RRL of the magnet. Note that the magnitude of the BICCs could vary significantly among almost identical coils made of the same cable, due to small variations in the cable pitch and local  $R_a$ -,  $R_c$ - and  $\rho_s$ -distributions. The maximum de-excitation rate of a single magnet is therefore not representative for a series of magnets wound from the same cable. Hence, the RRL of several magnets has to be determined in order to be more or less sure that the BICCs will not cause a preliminary quench in any of the magnets of an accelerator ring during a fast de-excitation.

### ISCL

The power loss caused by the coupling currents is independent of the sign of  $\dot{B}_{ce}$ . However, in the case of a negative  $\dot{B}_{ce}$  the time constant  $\tau_{is}$  of the ISCCs implies that the ISCL will be relatively small during the first part of the ramp, where the difference between the currents  $I_{C,str}$  and  $I_{str}$  is still small, and hence the temperature margin. A quench can only occur during the time that the temperature  $T_{cab}$  of the cable is still increasing (assuming constant BICCs). This is illustrated in Fig. 8.23 by means of a simulation of a fast de-excitation of the PBD magnet with  $R_c=1 \mu\Omega$ ,  $\tau_{is}=4$  s,  $q=10^4 \text{ Wm}^{-3}\text{K}^{-1}$ ,  $\dot{B}_{ce}=-0.1 \text{ Ts}^{-1}$ ,  $C_{bi}=0$  and  $T_b=1.9$  K. The temperature increase of the cable causes  $I_{C,str}$  to decrease faster than  $I_{tr,str}$ . After about 6 s a quench occurs when  $I_{tr,str}=I_{C,str}$ .



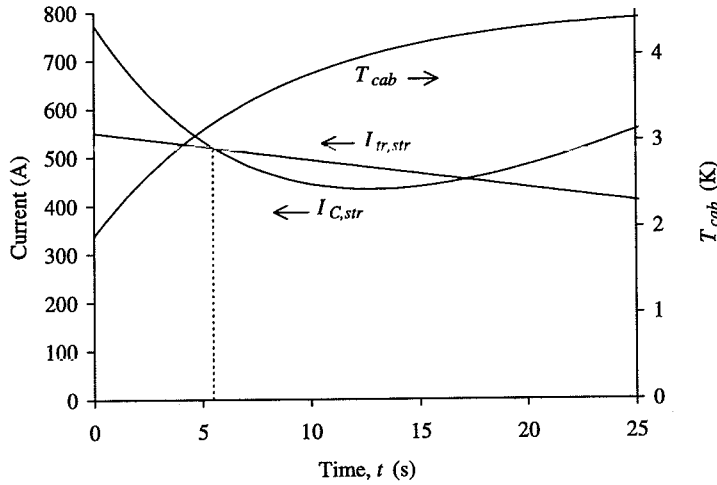


**Figure 8.23.** Simulation of the currents  $I_{tr,str}$  and  $I_{C,str}$  and the temperature  $T_{cab}$  during a linear ramp-down from 550 to 0 A in 100 s. A quench will occur at  $t=6$  s where  $I_{tr,str} = I_{C,str}$ .

In practice, the time required for temperature stabilisation not only depends on the dissipation and the time constant  $\tau_{is}$  but also on:

- the heat capacity of the cable and the helium which is present within the voids of the cable,
- the effective time constant of the heat transfer through the insulation. This time constant is estimated to be about 3–20 s for the LHC dipole model magnets and depends on the energy dissipation in the cable and the bath temperature [AT-MA, '93]. Figs. 8.15 and 8.16 indicate that complete temperature stabilisation takes about 100 s for field-sweep rates comparable to the initial de-excitation rate.

It is beyond the scope of this thesis to investigate the process of temperature stabilisation in a cable. In first approximation, it can be concluded that a quench due to the ISCL is likely to occur in the first 20 s of the de-excitation (for  $R_c > 1 \mu\Omega$  so that  $\tau_{is} < 5$  s). It is, however, possible that, due to a combination of the ISCL and the BICCs, a quench can occur after more than 20 s.

A few results of quenches on 1 m long LHC dipole model magnets are presented in Fig. 8.24, where the smallest (or critical) field-sweep rate  $\dot{B}_{ce,cr}$  is shown at which a quench occurs as a function of the average  $R_c$  of the magnet. In all cases the de-excitation starts at an initial current equal to about  $0.9I_{q,0}$ . The quenches are performed using a constant field-sweep rate, instead of an exponentially decreasing one (with a time constant of about 100 s) as is the case during a fast de-excitation of the dipole magnets in LHC. This does, however, not affect  $\dot{B}_{ce,cr}$ , since all quenches occur during the first 15 s, which is much smaller than the de-excitation time constant.

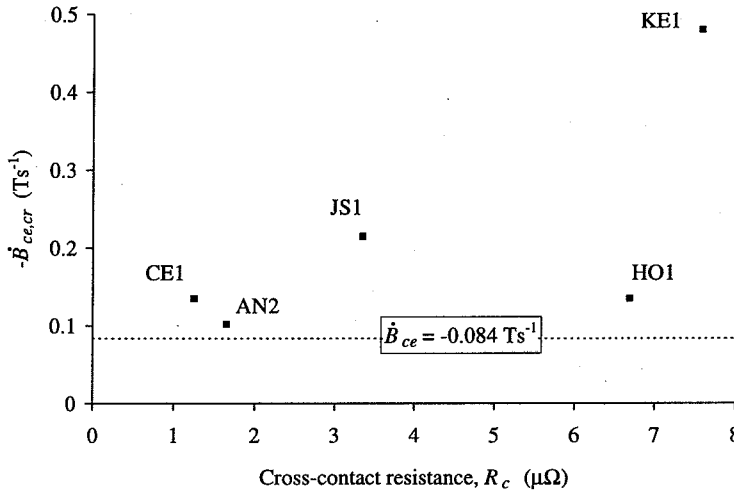


Figure 8.24. The critical de-excitation rate for a few LHC dipole model magnets. The fast de-excitation rate as anticipated for the LHC dipole magnets is shown by a dotted line.

The critical de-excitation rate of each magnet is larger than the anticipated fast de-excitation rate of LHC of about  $-0.084 \text{ Ts}^{-1}$ . It is interesting to see that a correlation exists between the RRL for positive and negative  $\dot{B}_{ce}$  (see Figs. 8.12 and 8.24). This implies that probably also the AN1, EL1 and EL2 magnets, which exhibit a smaller RRL than the CE1 magnet can withstand negative field-sweep rates of at least  $-0.15 \text{ Ts}^{-1}$  without quenching.

The number of magnets, of which  $\dot{B}_{ce,cr}$  is measured, is still too small to draw a conclusion about the correlation between  $\dot{B}_{ce,cr}$  and  $R_c$ . If  $\dot{B}_{ce,cr}$  is only determined by the ISCL, a linear increase of  $\dot{B}_{ce,cr}$  as a function of  $R_c$  is expected. In this case  $\dot{B}_{ce,cr}$  of the HO1 magnet is much too small, which could be due to large BICCs or a small  $R_c$  locally in one of the turns. The fact that no clear correlation exists between  $\dot{B}_{ce,cr}$  and  $R_c$  shows that a certain variation in  $\dot{B}_{ce,cr}$  can be present for magnets with the same average  $R_c$ .

## 8.6 Conclusions

The ramp-rate limitation (RRL) of dipole magnets, and in particular LHC dipole magnets, is investigated as a function of the coupling currents and coupling loss in the cables. The presence of coupling currents and coupling loss always reduces the temperature margin of the coil during a ramp with positive field-sweep rate. Small transient heat pulses which would not lead to a quench under DC conditions could, therefore, provoke a quench while ramping the magnet. This stability effect is especially important in magnets for which the field-sweep rate is fixed. In accelerator magnets the field-sweep rate can often be reduced near the end of the excitation where the temperature margin is small.

The reduction of the quench current as a function of the ramp rate is very difficult to calculate since it is strongly dependent on the local variations in the heat dissipation and

cooling conditions. In addition, the process of current redistribution is unknown in case the strand currents locally exceed the critical current.

In general, the reduction of the quench current of accelerator magnets is not significantly affected by the interfilament coupling currents.

The shape of the  $I_q - \dot{B}_{ce}$  curve between the quench current and the field-sweep rate shows whether the interstrand coupling currents (ISCCs), the boundary-induced coupling currents (BICCs) or the interstrand coupling loss (ISCL) are the main cause of the quench. The ISCCs result in a linear  $I_q - \dot{B}_{ce}$  curve while the BICCs and the ISCL cause concave and convex shapes respectively.

Ramp-rate-induced quench experiments make it possible to estimate the magnitude of the BICCs and the increase of the cable temperature due to beam losses. For this purpose, the RRL of a few LHC dipole model magnets is evaluated at bath temperatures of 1.9 and 4.3 K.

The reduction of the quench current in the LHC dipole models at high ramp rates is mainly attributed to the interstrand coupling loss. The relative reduction of the quench current as a function of the ramp rate is about 50% larger at 4.3 K than at 1.9 K. All the quenches start in the inner coil near the midplane. At lower ramp rates, the reduction of the quench current caused by the BICCs can be significant. In the model magnets the magnitude of the BICCs is estimated to be about 30 A at  $0.0066 \text{ Ts}^{-1}$  (section 8.3) which corresponds to about the transport current in the strands at injection ( $I_{tr,str} \approx 35 \text{ A}$ ) and about 7% of the transport current at nominal field ( $I_{tr,str} \approx 470 \text{ A}$ ).

The temperature increase of the cable of the inner coil is estimated to be about  $1.5 (\pm 0.5) \text{ K}$  for a heat dissipation of  $10 \text{ mW/cm}^3$  (section 8.4). The cable temperature at smaller levels of dissipation could not be deduced. In the LHC magnets, beam losses will be present up to  $10 \text{ mW/cm}^3$ . The temperature increase will then be too large to ensure a proper performance of the magnets. A temperature increase smaller than  $0.25 \text{ K}$  is required in order to keep the coils at a temperature below the lambda temperature and benefit from the good thermal properties of superfluid helium. Hence, either the porosity of the cable insulation or the beam shield has to be improved.

The maximum de-excitation rate of a magnet has to be determined experimentally since calculations are too speculative. Several magnets have to be investigated to be sure that variations in the cooling, heat dissipation and BICCs, which are likely to be present, even in identical magnets made of the same cable, will not cause a preliminary quench during a fast de-excitation. The RRL of the LHC dipole model magnets for positive and negative field-sweep rates  $\dot{B}_{ce}$  seem to be correlated. A large RRL for positive  $\dot{B}_{ce}$  implies a large RRL for negative  $\dot{B}_{ce}$ . All the model magnets can probably be discharged with a field-sweep rate of  $-0.084 \text{ Ts}^{-1}$  (as anticipated for a fast de-excitation of the LHC magnets) without quenching. Quench experiments on more model magnets are required to draw specific conclusions concerning the correlation between the maximum de-excitation rate and  $R_c$ . A good understanding of this correlation is necessary to specify the contact resistance for accelerator magnets.

## Chapter 9

# General conclusions and recommendations

*The main issue of this thesis has been the influence of especially the interstrand- and boundary-induced coupling currents on the power loss, field homogeneity and stability of accelerator dipole magnets. The main conclusions of the thesis are presented in the final sections of each chapter.*

*In chapters 4 and 5 the coupling currents have been dealt with by means of a network model in which the strands are connected by contact resistances. General conclusions concerning the modelling of coupling currents are reviewed here and possible extensions and further improvements discussed.*

*It has been shown in chapters 6, 7 and 8 that most of the electrodynamic effects in a magnet, caused by the coupling currents, can be directly related to the contact resistance. In this chapter it is discussed how an optimum can be found for the contact resistances in order to limit undesired time-dependent effects without affecting the electromagnetic stability of the cable too much.*

*The contact resistances are determined by several parameters during the process from cable winding to excitation of the magnet. Recommendations are given for controlling the contact resistances and for measuring them on a single cable piece, in order to obtain accurate and representative values of the resistances in the coil itself.*

*Finally, it is briefly discussed how the results of the thesis can be applied to other types of cables and magnets.*

## 9.1 Modelling of coupling currents in multistrand cables

Coupling currents in and between the strands of a superconducting Rutherford-type cable can be well calculated when the cable is modelled as a 3-dimensional network of nodes interconnected by strand sections and contact resistances. Two types of contact resistances are present in a cable: contact resistances  $R_a$  between adjacent strands and contact resistances  $R_c$  between crossing strands. Several network models have been developed in the past 20 years. Using these models it turned out that one type of current, called the interstrand coupling current (ISCC), is induced if the cable is subject to a varying field.

An improved model is described in detail in chapter 4 of which the main improvements are the possibilities to calculate the time-dependent behaviour of the coupling currents and to include many types of non-uniformities which are likely to be present in the cable of a coil. Calculations as a function of time can be performed since the mutual- and self-inductances between all strand sections are incorporated in the network model. The non-uniformities can be classified in four types, shown in Table 9.1.

**Table 9.1.** Survey of the causes of various types of non-uniformities in the contact resistances and the field-sweep rate which are present in a coil.

	Variations across the cable width	Variations over the cable length
Non-uniformities in the contact resistances	Variation in the transverse pressure on the cable Keystone of the cable Manufacturing tolerances	Soldered connections Strong variations of the transverse pressure in the coil ends Weak variations of the transverse pressure over the entire cable Manufacturing tolerances
Non-uniformities in the field sweep rate	Inherent to the magnet design, and present everywhere in the coil	Strong variations in the coil ends and the terminals Weak variations over the entire cable

All these non-uniformities are inherent to the cable and magnet geometries except for the manufacturing tolerances. These might lead to variations across the cable width as well as over the cable length. Especially local spots in the cable with smaller electrical contacts between the strands could strongly increase the coupling currents.

A detailed evaluation of the various non-uniformities in a cable has shown that besides the well-known ISCC a second type of coupling current is generated. These currents are induced during a field sweep due to the variations (or boundaries) in contact resistance and field-sweep rate along the cable length and are named '*Boundary-Induced Coupling Currents (BICCs)*'. Variations across the cable width do not cause BICCs but only change the ISCC-distribution.

Both types of induced currents differ with respect to the effective loop length, the characteristic time and the magnitude. The effective loop length of the ISCCs is equal to the cable pitch, whereas the BICCs can flow through large sections of the cable. The large loop length also leads to a characteristic time which can be one or more orders of magnitude larger than that of the ISCCs.

The magnitudes of the ISCCs and the BICCs in Rutherford-type cables are:

- proportional to the field-sweep rate  $\dot{B}$  and especially its component  $\dot{B}_\perp$  normal to the cable width,
- inversely proportional to the contact resistances  $R_a$  and  $R_c$  (or the root of the contact resistances in the case of BICCs with a small loop length).

The magnitudes of the BICCs usually increase for increasing *gradients*  $d\dot{B}/dz$  (and especially the component  $d\dot{B}_\perp/dz$ ), and  $d(R_c^{-1})/dz$ , with  $z$  the coordinate along the cable axis. This implies that in accelerator magnets the BICCs are mainly caused by the coil ends, where the cable bends around the beam pipe, which leads to a locally very small  $\dot{B}_\perp$  over a length of the order of one cable pitch. Also the cable-to-cable connections between the two layers of a coil and the coil terminals, where the electrical contact between the strands is locally very small, will lead to large BICCs.

Both types of induced currents increase strongly for increasing cable width and twist length of the strands. In accelerator magnets, the cable width is restricted within a factor of about 2 in order to limit the inductance of the magnet. This implies that the cable width increases with increasing design operating field. Once the cable width is set, the cable pitch is also more or less fixed since the cable has to be mechanically stable. Hence, the coupling currents and consequently the time-dependent effects in the magnets become more pronounced with an increasing operating field of accelerator magnets. The main parameter by which the magnitudes of the ISCCs and the BICCs can be significantly changed is the contact resistance because the width and cable pitch are strongly correlated to the design field of the magnet. The magnitudes of the ISCCs and BICCs are especially influenced by  $R_c$  whereas  $R_a$  will only be relatively important if  $R_a \ll R_c$  or if the field is applied parallel to the cable width.

It is shown in chapter 5 that the magnitudes of the BICCs and their characteristic times are also related to the effective strand resistivity that the BICCs 'see'. In the 1 m long LHC dipole model magnets the effective resistivity is deduced to be of the order of  $10^{-14}$ – $10^{-15} \Omega\text{m}$ . The diffusion of the coupling currents from the contact points into the filaments of the strands as well as the exact current pattern of the coupling currents over the cross-section of a strand have to be investigated in order to understand this effective resistivity.

Modelling BICCs by means of a network model is much more time-consuming than modelling ISCCs. The reason for this is that the distribution of the ISCCs can be calculated for a given field change assuming that it will not vary in the  $z$ -direction. The actual ISCC distribution in the cable along the length can then be calculated by scaling the currents to the local field change.

Steady-state calculations of the ISCCs in single cables take just a few seconds CPU time on a 10 MFlops machine (for cables having 10-60 strands) and it takes still less than a few minutes for stacks of cable pieces or coils. The computing time required to calculate the time constants of the ISCCs depends strongly on the number of mutual inductances that are involved and hence on the number of strands in the cable and the number of cables in the stack or coil. The CPU time can be significantly reduced by decreasing the number of time steps and disregarding the mutual inductances between strands that are located at a

relatively large distance from each other. The calculation of time constants, with an accuracy of about 10%, then takes usually less than a minute CPU time for a 40-strand cable and up to half an hour for an entire coil with about 40 turns wound from a cable having 30 strands.

In order to calculate the BICCs it is necessary to model the entire cable, which means that an array with about  $5N_s^2$  variables per twist length has to be solved. In the case of practical coils, made of cables having typically 20-40 strands and with a length of the order of  $10^2$ - $10^4$  times the cable pitch, this implies that millions of variables have to be solved. Steady-state calculations are possible but take hours of CPU time. Furthermore, the required large array sizes of up to several GByte are difficult to handle and, therefore, have to be split in smaller subarrays which have to be solved subsequently.

Evaluation of time-dependent effects requires large computing times especially for long cables having many strands. Because the characteristic time of the BICCs depends strongly on the longitudinal position in the cable (see section 5.4.3), more time steps have to be taken than in the case of ISCCs. Calculation of the characteristic time  $\tau_{bi}$  of the BICCs in a 14-strand cable with a length of 10 times the cable pitch requires several minutes CPU time, while it already takes about an hour for a 26-strand cable with a length of 20 times the cable pitch. A good estimate of  $\tau_{bi}$  in long cables can be obtained by extrapolating the results obtained on short cable pieces. In this way, the order of magnitude of  $\tau_{bi}$  can be estimated, even for an entire coil, if of course the effective strand resistivity and the  $R_a$ ,  $R_c$ - and  $\dot{B}$ -distributions along the cable length are known.

Further extensions of the network model are possible with respect to the thermal behaviour and electromagnetic stability of the cable. The temperature in each strand section can be calculated in a similar way as the currents are calculated, if the thermal conductivity and the heat capacity of the conductor are known as well as the heat transfer coefficients between the strands and between the strands and the helium (inside and outside the cable).

The effect of the coupling currents on the electromagnetic stability of the cables requires the use of a non-linear  $U$ - $I$  relation of the strands. In section 4.5 it is shown that the ISCCs could redistribute, without generating a larger power loss, as soon as one of the strand sections reaches the critical current. The impact of strand saturation, caused by the BICCs or a non-uniform current distribution, on the current distribution and the dissipated energy has to be investigated in order to improve the actual picture of stability in multistrand cables. The effect of strand saturation can be evaluated with the network model presented in section 4.2 without any further improvements.

The computing times for each simulation will be of the order of hours CPU time, since the currents for each time step have to be calculated iteratively (due to the non-linear  $U$ - $I$  relation of the strands). A qualitative understanding of the influence of  $R_a$  and  $R_c$  on the electromagnetic stability can be obtained by modelling cables with a small number of strands.

The principle of the BICCs in combination with the geometry of the cable force that BICCs will not only occur in and between the strands of a cable but also in and between the filaments of the strands. The BICCs at strand level are not dealt with in this thesis since

their impact on the performance of accelerator magnets is probably very small (like the impact of the interfilament coupling currents is small compared to that of the ISCCs). For other types of magnets, where  $R_a$  and  $R_c$  are large and the cable is exposed to large field-sweep rates, the BICCs within the strands could play a significant role.

## 9.2 Restrictions of the contact resistances

During a field sweep, the ISCCs and the BICCs affect the performance of the coil with respect to the power loss, field distortions and stability. Before winding a coil, the optimum  $R_a$ - and  $R_c$ -values have to be estimated, which lead to sufficiently small coupling currents during (de-)excitation of the coils.

- The effect of  $R_c$  on the interstrand coupling loss is dealt with in chapter 6. The  $R_c$ -value can be well specified if the maximum allowable dissipation is known, since the calculated and measured power losses correspond well.
- The effect of  $R_c$  on the field distortions caused by the coupling currents is dealt with in chapter 7. The main field distortions caused by the ISCCs in an accelerator dipole magnet are the normal-dipole, skew-quadrupole and normal-sextupole components. The minimum  $R_c$  can be calculated if the allowable field errors are specified, since the calculated and measured values of the above-mentioned field errors correspond within a factor 2. The field distortions caused by the BICCs vary sinusoidally along the magnet axis with a period equal to the cable pitch. Their magnitudes are hard to assess (since it is the net result of a superposition of the fields produced by numerous BICCs) but can easily become one order of magnitude larger than the errors caused by the ISCCs. The effect of sinusoidally varying field distortions on the particle motion is not well-known and has to be investigated in order to put constraints on the maximum allowable magnitude of the BICCs. At present it is thought that the influence of the BICCs on the particle motion is much smaller than that caused by the filament magnetisation and the ISCCs, as long as the integral value of the field distortion caused by the BICCs is much smaller than  $10^{-4}$  T.
- Two effects are considered concerning the influence of  $R_c$  on the electromagnetic stability of the cable (see chapter 8):
  - The coupling currents (especially the ISCCs) cause an energy dissipation (or interstrand coupling loss, ISCL) which results in a temperature increase of the cable and, therefore, decrease the temperature margin of the coil. The temperature increase of the cable can be roughly estimated if  $R_c$  and the heat transport through the cable insulation are known.
  - The coupling currents (especially the BICCs) affect the current distribution among the strands which could locally saturate or quench the strands. The magnitude of the BICCs is difficult to predict but can be estimated by testing prototype magnets.

It is clear that the ISCL, the field distortions and the stability problems can be decreased by increasing  $R_a$  and  $R_c$ . This does reduce the coupling currents but, on the other hand, could also reduce the cryogenic stability of the cable against transient heat pulses, since:



- an increase in  $R_c$  can reduce the current redistribution among the strands in the case of a local transition in a strand section from the superconducting to the normal state,
- coatings, resistive barriers, solder and resin affect the thermal conduction and heat transport between the cable and the helium and can change the mechanical behaviour of the cable and could, therefore, change the process of frictional heating and heating in the cable surroundings.

Both effects are not dealt with in this thesis, since a profound treatment would probably take several years, but could play a role in the quench behaviour (i.e. in the training curve) of a coil in the case of small transient heat pulses. A certain optimum in  $R_c$  should be found for which the power loss, field errors and stability during ramping can be tolerated without affecting the cryogenic stability too much.

In the 1 m long LHC dipole model magnets no correlation is observed between the number of training quenches and  $R_c$ . However, the cables used in these magnets are quite similar with respect to the strand coating, and all have  $R_c$ -values between 1 and 6  $\mu\Omega$ . Hence, a correlation can still be present for cables with much smaller or larger  $R_c$ .

The above implies that it is preferable to wind *model and prototype coils* from cables having contact resistances which are just large enough to reduce the undesired effects related to the ISCCs (i.e. the effects which can be well predicted), instead of making them from cables having much smaller or much larger  $R_a$  and  $R_c$ . The testing of several model and prototype coils makes it then possible to estimate the magnitude of the BICCs and their effect on the stability and the field homogeneity of the magnet. Only if in the coming years:

- the effect of the contact resistances on the stability of the coil will be understood,
  - the behaviour and magnitude of the BICCs become more clear and predictable,
- it will be possible to specify  $R_a$  and  $R_c$  even before constructing the first models.

Of course, the coupling currents can also be reduced by decreasing the field-sweep rate during excitation. This implies an increase in the ramp time and therefore a decrease in the effective operating time of the accelerator. It should be investigated whether an increase in the excitation time would have an effect on the final luminosity at operating field.

The excitation procedure can be improved by using a variable field-sweep rate, being small at small fields, in order to limit the relative field errors. At intermediate fields the field-sweep rate can be larger while at large fields it should again be small, in order not to affect the stability too much.

The temperature increase of the cable due to the coupling currents cannot only be reduced by increasing the contact resistances or by reducing the field-sweep rate but, of course, also by improving the heat transfer through the cable insulation. The constraints on this improvement are that the cable insulation has to withstand the voltages that occur during a quench and has to be strong enough to avoid breakage during winding.

Accelerator magnets often have to be de-excited with a high field-sweep rate in the case of a quench in one of the series connected magnets. A quench-back in other magnets during this fast de-excitation has to be avoided but can occur if the ISCL is large and the cooling of the cable is poor. Additionally, large BICCs will further enhance ramp-rate limitation (i.e.

reduce the critical field-sweep rate). The mechanisms that influence the ramp-rate limitation are discussed in chapter 8. The maximum de-excitation rate depends strongly on local variations in the power loss, cooling properties and BICCs and is therefore very difficult to predict and quench experiments on prototype magnets are necessary to determine this value as well as possible variations among the magnets.

### 9.3 Controlling and measuring contact resistances

Once the minimum  $R_a$  and  $R_c$  are specified, it has to be investigated how these values can be obtained. It is important that  $R_a$  and  $R_c$  should not only be limited but, preferably, also be more or less constant over the cross section of the coils in a magnet. During excitation this reduces the unexpected field distortions whereas during de-excitation it reduces the possibility of having locally large energy losses. The  $R_a$ - and  $R_c$ -values should also be reproducible from magnet to magnet in order to facilitate the field-correction methods during excitation.

The contact resistances depend on various parameters (see section 4.3), and in particular on:

- the pressure on the cable,
- the type of coating,
- the strand deformation,
- the surface conditions and level of oxidation of the strands,
- the temperature and pressure cycle during coil manufacturing.

Large differences in  $R_c$  of several orders of magnitude are observed if the above-mentioned parameters are changed. Therefore, the requirement of reproducible  $R_a$  and  $R_c$  among the magnets in an accelerator implies that all the strands and cables have to be produced, stored and processed by identical and well-controlled methods. Furthermore, also the prestress and the curing cycle have to be the same for all the magnets.

In accelerator magnets the Rutherford-type cables are highly compacted and often keystoneed in order to attain a high overall current density and to improve the uniformity of the coils, which is important to reduce training. The high compaction factor causes a large deformation of the strands and hence a large contact area between the strands which reduces the contact resistance. The keystoneing of the cable probably causes a variation of  $R_a$  and  $R_c$  over the cable width, resulting in the smallest resistances near the smallest edge of the cable. The magnitude of the ISCCs and the ISCL is dominated by  $R_a$  and  $R_c$  in the *centre* of the cable, and are, therefore, almost not affected by the keystone angle.

$R_a$  and  $R_c$  can be changed by means of strand coatings or intrastrand barriers. The use of an (additional) resistive barrier between the two layers in the cable enables to vary  $R_a$  and  $R_c$  independently. Thin sheets of, for example, stainless steel or nickel increase  $R_c$  significantly and could make  $R_c$  more predictable and reproducible.

A first estimate of  $R_a$  and  $R_c$  of a cable can be obtained by means of the *UI* method (see section 4.10.3) performed on a short cable piece. The method is cheap and fast but unfortunately quite sensitive to local variations in the contact resistances. Once an idea is

formed about the type of strand and cable, which would lead to the desired  $R_a$  and  $R_c$ , a more accurate determination of the global  $R_a$  and  $R_c$  should be made by means of the calorimetric method (see section 4.10.2) on a short sample with a length at least equal to the cable pitch.

For both methods it is important to determine  $R_c$  on a cable piece which is and has been exposed to the same pressure and temperature cycle as will the cable in the total process from manufacturing, winding, cool-down and operation. Results of measurements have demonstrated that  $R_c$  in a coil is, in first approximation, independent of the temperature (between 1.9 and 4.3 K), the magnetic field and the Lorentz force on the cable during operation.

## 9.4 Effect of coupling currents in other magnets

Detailed knowledge of the electrodynamic properties of the cable are essential for magnets, wound of large-size cables, which need to have a high field homogeneity (such as beam-guiding magnets), or are subject to a large field-sweep rate (such as fusion magnets, pulsed SMES systems and AC generators). The emphasis in this thesis is on Rutherford-type cables as used in accelerator dipole magnets, but a similar analysis of the electrodynamic properties can be made for other types of magnets as well.

For all *coils made of Rutherford-type cables*, the formulas at strand and cable level remain unchanged. The steady-state ISCCs and ISCL in each turn of a coil can be calculated by using the expressions given in section 4.4.1, while the time constants of the ISCCs in a cable and stack cables are given by eqs. 4.31 and 4.39. The total ISCL in the coil is obtained by summation over all the turns. The field errors caused by the ISCCs can be calculated using the approach given in section 7.2. By doing so, both the ISCL and the field caused by the ISCCs can be estimated within about 20% (for given  $R_a$  and  $R_c$ ), which is often smaller than the accuracy by which the contact resistances are determined.

A qualitative estimate of the BICCs can be made according to the expressions given in sections 5.4.2-5.4.4 and the approach given in section 5.4.5. However, since the cause and the magnitude of the effective strand resistivity are both unknown, it remains necessary to test model magnets to quantify the BICCs and their effect on the magnet performance.

For *coils made of other types of cables*, the discussion of the interfilament coupling and filament magnetisation remains unchanged. The different internal configuration of the cable requires a same type of modelling, however with a different cable-specific network, in order to calculate the ISCCs and BICCs. Hence, the network model as discussed in section 4.2 has to be modified accordingly. In general, the expressions for the coupling currents, power losses and time constants will be qualitatively similar but quantitatively different due to the different geometry.

Fig. 1.3 can be well used as a guideline in the design of cables and magnets of which the performance is susceptible to coupling currents, power losses and field distortions, or magnets of which the operation margin is likely to be strongly reduced due to coupling currents and power loss.

# References

- Akhmetov, A.A., and T. Ogitsu, "Periodicity of eddy currents in flat Rutherford-type cables", *SSCL test & analysis note MD-TA-245* (1993a).
- Akhmetov, A.A., A. Devred, R. Schermer, and R. Mints, "Current loop decay in Rutherford cables", *SSCL-Preprint-485* (1993b).
- Akhmetov, A.A., A. Devred, and T. Ogitsu, "Periodicity of crossover currents in a Rutherford-type cable subjected to a time-dependent magnetic field", *J. Appl. Phys.* **75**(6), pp. 3176-3183 (1994).
- Akhmetov, A.A., K. Kuroda, and M. Takeo, "Influence of sample geometry on amplitude of eddy current oscillation in Rutherford-type cables", *IEEE Trans. Appl. SC* **5**, pp. 725-728 (1995).
- Akita, S., et al., "AC loss and quenching characteristics of 500 kVA AC superconducting coil", *KEK proc. 92-14*, K. Tsuchiya, Ed., pp. 40-43 (1992).
- Amemiya, N., K. Ryu, T. Kikuchi, and O. Tsukamoto, "Influence of current re-distribution and thermal diffusion among strands on stability of superconducting cables against local disturbances", *IEEE Trans. Magn.* **30**, pp. 2281-2284 (1994b).
- Anderson, P.W., "Theory of flux creep in hard superconductors", *Phys. Rev. Lett.* **9**, pp. 309-311 (1962).
- Andreyev, N.I. et al., "Study of AC losses in the models of SC magnets for UNK", *Proc. MT-9*, C. Marinucci, and P. Weymuth, Eds, pp. 524-527 (1985).
- Asner, A., R. Perin, S. Wenger, and F. Zerobin, "First Nb<sub>3</sub>Sn, 1 m long superconducting dipole model magnets for LHC break the 10 T field threshold", *Proc. MT-11*, T. Sekiguchi, and S. Shimamoto, Eds, pp. 36-41 (1990).
- AT-MA, '93: Summary of the CERN AT-MA meeting of 11-11-'93 (1993).
- Avest, D. ter, and L.J.M. van de Klundert, "On the interstrand resistances in superconducting cables", *Cryogenics* **30**, p. 694 (1990).
- Avest, D. ter, *Properties of the superconductor in accelerator dipole magnets*, PhD thesis, University of Twente, The Netherlands, 1991.
- Balbekov, V.I., et al., "The IHEP accelerating and storage complex (UNK)", *Proc. IHEP XII* (1983).
- Bona, M. et al., "Design, fabrication variants and results of LHC twin aperture models", *IEEE Trans. Magn.* **28**, pp. 338-341 (1992).
- Brück, H. et al., "Time dependence of persistent current effects in the superconducting HERA magnets", *Proc. MT-11*, T. Sekiguchi, and S. Shimamoto, Eds., pp. 141-146 (1990).
- Brück, H. et al., "Observation of a periodic pattern in the persistent-current fields of the superconducting HERA dipole magnets", *DESY 91-01* (1991a).
- Brück, H. et al., "Observation of a periodic pattern in the persistent-current fields of the superconducting HERA dipole magnets", *Proc. '91 IEEE Part. Acc. Conf.*, pp. 2149-2151 (1991b).

- Burnod, L., and J.B. Jeanneret, "Beam losses in the SPS and the LHC due to beam-gas and beam-beam collisions", *CERN LHC Note 91* (1989).
- Burnod, L., and J.B. Jeanneret, "Beam losses and collimation in the LHC: a quantitative approach", *CERN LHC Note 167* (1991).
- Campbell, A.M., "A general treatment of losses in multifilamentary superconductors", *Cryogenics* **22**, pp. 3-16 (1982).
- Carr, W.J. Jr., "AC loss in a twisted filamentary superconducting wire", *J. Appl. Phys.* **45**(2), pp. 929-934 (1974).
- Carr, W.J. Jr., M.S. Walker, and J.H. Murphy, "Alternating field loss in a multifilamentary superconducting wire for weak ac fields superposed on a constant bias", *J. Appl. Phys.* **46**, pp. 4048-4052 (1975).
- Caspi, S., W.S. Gilbert, and J.B. Rechen, "Ramp rate sensitivities of several superconducting dipole magnets operated in He I and superfluid He II", *IEEE Trans. Magn.* **MAG-19**, pp. 1394-1397 (1983).
- Caspi, S., W.S. Gilbert, M. Helm, and L.J. Laslett, "The effects of filament magnetization in superconducting magnets as calculated by Poisson", *IEEE Trans. Magn.* **MAG-23**, pp. 510-513 (1987).
- Cole, F.T., e.a., "Report on the design of the Fermi National Laboratory superconducting accelerator", *FNAL int. report* (1979).
- Collings, E.W., *Applied superconductivity - metallurgy, and physics of titanium alloys*, Plenum press, New York, 1986.
- Coull, L., et al., "LHC quench protection system", *IEEE Trans. Magn.* **30**, pp. 1742-1745 (1994).
- Courant, E.D., "Eddy currents in superconducting braid", *ISABELLE Technical note 168* (1980).
- Dauguet, P., "Mesure de la conductivite thermique des isolations des aimants du futur accelerateur du CERN: le LHC", *Internal report (in french) CERN* (1992).
- Dell'Orco, D., R.M. Scanlan, and C.E. Taylor, "Design of the Nb<sub>3</sub>Sn dipole D20", *IEEE Trans. Appl. SC* **3**, pp. 82-86 (1993).
- Devred, A., and T. Ogitsu, "Ramp-rate sensitivity of SSC dipole magnet prototypes", *KEK Preprint 94-156* (1994).
- Druyvesteyn, W.F., "The resistivity of hard superconductors subjected to an increasing field", *Phys. Lett.* **25A**, pp. 31-32 (1967).
- Durand, E., *Magnétostatique*, Masson, Paris, 1968.
- Edwards, H.T., "The Superconducting Super Collider", *Proc. 2<sup>nd</sup> EPAC conf.*, P. Marin, and P. Mandrillon, Eds., pp. 356-360 (1990).
- Egorov, S.A., et al., "AC coupling losses in superconducting cables of finite length", *Presented at the ITER Magnet System Technical Meeting, MIT, Boston, ITER-RF-MS/ACL-02-09-94* (1994).
- Faivre, D., and B. Turck, "Current sharing in an insulated multistrand cable in transient and steady state current conditions", *IEEE Trans. Magn.* **MAG-17**, pp. 1048-1051 (1981).
- Finley, D.A., et al., "Time dependent chromaticity changes in the Tevatron", *Proc. IEEE Part. Acc. Conf.*, pp. 151-153 (1987).

- Foner, S., and B.B. Schwartz, Eds., *Superconductor materials science - metallurgy, fabrication, and applications*, Plenum press, New York, 1981.
- Genevey, P., et al., "Cryogenic tests of the first two LHC quadrupole prototypes", *IEEE Trans. Appl. SC* **5**, pp. 202-205 (1995).
- Ghosh, A.K., "Ramp rate effects in superconducting cables and dipole magnets", *Int. note BNL* (1992).
- Ghosh, A.K., K.E. Robins, and W.B. Sampson, "Axial variations in the magnetic field of superconducting dipoles and quadrupoles", *Proc. '93 IEEE Part. Acc. Conf.*, pp. 2742-2744 (1993).
- Ghosh, A.K., K.E. Robins, and W.B. Sampson, "The ramp rate dependence of the sextupole field in superconducting dipoles", *IEEE Trans. Magn.* **30**, pp. 1718-1721 (1994).
- Gilbert, W.S., et al., "Magnetic field decay in model SSC dipoles", *IEEE Trans. Magn.* **25**, pp. 1459-1462 (1989).
- Gömöry, F., and L. Cesnak, "Loss and magnetization measurement of superconducting magnets pulsed at very low ramp rates", *Cryogenics* **25**, pp. 375-380 (1985).
- Green, M.A., LBL report 23823 (1987).
- Groover, F.W., *Inductance calculations - working formulas and tables*, Dover Publications, New York, p. 55, 1946.
- Hague, B., *The principles of electromagnetism*, Dover Publications, New York, 1962.
- Haken, B. ten, *Strain effects on the critical properties of high-field superconductors*, PhD thesis, University of Twente, The Netherlands, 1994.
- Hartmann, R.A., *A contribution to the understanding of AC losses in composite superconductors*, PhD thesis, University of Twente, The Netherlands, 1989.
- Hosono, F., et al., "AC loss of the toroidal model pancake (TMP)", *IEEE Trans. Appl. SC* **3**, pp. 531-534 (1993).
- Kate, H.H.J. ten, "AC losses and magnet research", *Adv. Cryog. Eng.* **40**, pp. 559-568 (1994).
- Kim, Y.B., C.F. Hempstead, and A.R. Strnad, "Critical persistent currents in hard superconductors", *Phys. Rev. Lett.* **9**, pp. 306-309 (1962).
- Kimura, A., et al., "Stabilities of the Rutherford cables with Cu matrix and CuMn barrier", *IEEE Trans. Appl. SC* **5**, pp. 385-388 (1995).
- Klundert, L.J.M. van de, T.A.W. van Elswijk, A. Nijhuis, and G.B.J. Mulder, "Degradation of the maximum transport current in wires and cables caused by coupling currents", *Proc. MT-11*, T. Sekiguchi, and S. Shimamoto, Eds., pp. 1021-1026 (1990).
- Knoopers, H.G., H.H.J. ten Kate, and L.J.M. van de Klundert, "Distribution of currents in a 6-strand superconducting cable", *Proc. MT-9*, C. Marinucci, and P. Weymuth, Eds, pp. 539-542 (1985).
- Kovachev, V.T., et al., "Interstrand resistance of DSA328 inner coil", *SSCL-637* (1993a).
- Kovachev, V.T., et al., "Interstrand resistance of selected sections of DCA312", *SSCL-651* (1993b).
- Kovachev, V.T., et al., "Interstrand resistance of SSC magnets", *Cryogenics* **34**, pp. 813-820 (1994).

- Krempasky, L., "AC losses in flat twisted superconducting cables", *CERN int. note SPS/EA/78-2* (1978).
- Krempasky, L., C. Schmidt, "Influence of a longitudinal variation of  $dB/dt$  on the magnetic field distribution of accelerator magnets", *Appl. Phys. Lett.* **66**(12), pp. 1545-1547 (1995a).
- Krempasky, L., C. Schmidt, "A possible explanation of the problem of ramp rate limitation in large superconducting magnets", *Presented at MT-14, Tampere* (1995b).
- Kwasnitza, K., and B. Bruzzone, "Large AC-losses in superconducting multistage Nb3Sn cables due to low transverse resistance", *Proc. ICEC-11*, G. and I. Klipping, Eds, pp. 741-745 (1986).
- Lei, Y.Z., T. Shintomi, A. Terashima, and H. Hirabayashi, "AC loss measurements of Rutherford type superconducting cables under mechanical stresses", *IEEE Trans. Appl. SC* **3**, p. 747 (1993).
- Leroy, D., et al., "Test results on 10 T I.H.C. superconducting one metre long dipole models", *IEEE Trans. Appl. SC* **3**, p. 614 (1993a).
- Leroy, D., et al., "Quench observation in LHC superconducting one meter long dipole models by field perturbation measurements", *IEEE Trans. Appl. SC* **3**, pp. 781-784 (1993b).
- LHC, '88, From: Specifications *CERN SPS/EMA 88-1* (1988).
- LHC, '91, The LHC Study Group, "Design Study of the Large Hadron Collider", *CERN 91-03* (1991).
- LHC, '93, The LHC Study Group, "LHC, The Large Hadron Collider Accelerator Project", *CERN/AC/93-03/LHC* (1993).
- London, H., "Alternating current losses in superconductors of the second kind", *Phys. Lett.* **6**, pp. 162-165 (1963).
- Lubell, M.S., "Empirical scaling formulas for critical current and critical field for commercial NbTi", *IEEE Trans. Magn.* **19**, pp. 754-757 (1983).
- Lvovsky, Y.M., "Stability against transient disturbances in cable-in-conduit conductors cooled by supercritical helium", *IEEE Trans. Appl. SC* **5**, pp. 584-587 (1995).
- Mallick, G.T. Jr., D. Natelson, W.J. Carr, Jr., G. Snitchler, and V. Kovachev, "Results of AC loss measurements on heat treated SSC cables", *IEEE Trans. Appl. SC* **3**, p. 744 (1993).
- Marken, K.R., M.D. Sumption, E.W. Collings, and R.M. Scanlan, "Magnetization decay of SSC-type strands in various short test sample configurations", *Adv. Cryog. Eng.* **38**, pp. 715-722 (1992).
- Meuris, C., "Heat transport in insulation of cables cooled by superfluid helium", *Cryogenics* **31**, pp. 624-628 (1991).
- Meuris, C., "Comparaison de differentes isolations", *Workshop on LHC technology, Chamonix* (1993).
- Morgan, G.H., "Theoretical behavior of twisted multicore superconducting wire in a time varying uniform magnetic field", *J. Appl. Phys.* **41**, pp. 3673-3679 (1970).
- Morgan, G.H., "Eddy currents in flat metal-filled superconducting braids", *J. Appl. Phys.* **44**, pp. 3319-3322 (1973).
- Mower, T.M., and Y. Iwasa, "AC losses in multifilamentary composite superconducting strands and cables", *Adv. Cryog. Eng.* **32**, pp. 771-778 (1986).

- Niessen, E.M.J., D. ter Avest, and L.J.M. van de Klundert, "Application of the network method to superconducting cables", *Proc. LTEC 90*, p. 5.4 (1990a).
- Niessen, E.M.J., and L.J.M. van de Klundert, "Loss calculations for the 29-strand NET braid", *University of Twente, int. note UTNET90.2* (1990b).
- Niessen, E.M.J., *Continuum electromagnetics of composite superconductors*, PhD thesis, University of Twente, The Netherlands, 1993.
- Nijhuis, A., H.H.J. ten Kate, P. Bruzzone, and L. Bottura, "Parametric study on coupling loss in subsize ITER Nb<sub>3</sub>Sn cables specimen", *Presented at MT-14, Tampere* (1995).
- Oberli, L., CERN Div. AT-MA, CH1211 Geneva 23, unpublished measurements (1995).
- Ogitsu, T., Y. Zhao, A. Akhmetov, and A. Devred, "Influence of cable eddy currents on magnetic field harmonics", *KEK proc. 92-14*, K. Tsuchiya, Ed., pp. 23-27 (1992a).
- Ogitsu, T., et al., "Influence of cable eddy currents on magnetic field harmonics", *SSCL-Preprint-134 Rev A* (1992b).
- Ogitsu, T., "Dependence of AC loss and multipole coefficients on cable eddy currents", *SSCL test & analysis note MD-TA-240* (1993).
- Ogitsu, T., "Influence of cable eddy currents on the magnetic field of superconducting particle accelerator magnets", *SSCL-N-848* (1994).
- Ono, M., et al., "Estimation method of stability for the multi-strand superconducting cables under partial current distribution", *IEEE Trans. Appl. SC 5*, pp. 564-567 (1995).
- Ouden, D. den, et al., "An experimental 11.5 T Nb<sub>3</sub>Sn LHC type of dipole magnet", *IEEE Trans. Magn. 30*, pp. 2320-2323 (1994).
- Ozaki, S., "The Relativistic Heavy Ion Collider RHIC at Brookhaven", *Proc. 2<sup>nd</sup> EPAC conf.*, P. Marin, P. Mandrillon, Eds, pp. 70-73 (1990).
- Ozelis, J.P., et al., "AC loss measurements of model and full size 50 mm SSC collider dipole magnets at Fermilab", *IEEE Trans. Appl. SC 3*, pp. 678-681 (1993).
- Pang, C.Y., *Losses in type-II superconducting wire due to alternating and rotating fields*, PhD thesis, University of Cambridge, 1980.
- Perin, R., "Status of LHC programme and magnet development", *IEEE Trans. Appl. SC 5*, pp. 189-195 (1995).
- Rem, P.C., D. Dijkstra, F.P.H. van Beckum, and L.J.M. van de Klundert, "A numerical analysis of saturation in multifilamentary wires, carrying AC transport current in an AC-transverse field", *Proc. MT-9*, C. Marinucci, and P. Weymuth, Eds, pp. 567-570 (1985).
- Rem, P.C., *Numerical models for AC superconductors*, PhD thesis, University of Twente, The Netherlands, 1986.
- Richter, D., CERN Div. AT-MA, CH1211 Geneva 23, unpublished measurements (1995).
- Ries, G., and S. Takacs, "Coupling losses in finite length of superconducting cables and in long cables partially in magnetic field", *IEEE Trans. Magn. 17*, p. 2281 (1981).
- Roovers, A.J.M., P.C. Rem, and L.J.M. van de Klundert, "AC losses in a mixed matrix multifilamentary superconducting wire", *Proc. ICEC-11*, G. and I. Klipping, Eds, pp. 766-775 (1986).



- Russenschuck, S., Calculations performed by S. Russenschuck using ROXIE as described in "ROXIE - The routine for the optimization of magnet X-sections, inverse problem solving and end region design", *CERN LHC note 238* (1993).
- Sampson, W.B., and A.K. Ghosh, "Induced axial oscillations in superconducting dipole windings", *IEEE Trans. Appl. SC 5*, pp. 1036-1039 (1995).
- Schermer, R.I., and B.P. Turck, "Current sharing between insulated strands in a superconducting cable", *Adv. Cryog. Eng.* **26**, pp. 599-607 (1979).
- Shintomi, T., et al., "AC losses of Rutherford-type superconducting cables", *Adv. Cryog. Eng.* **40**, pp. 501-508 (1994).
- Siemko, A., CERN Div. AT-MA, CH1211 Geneva 23, unpublished results (1994).
- Siemko, A., "Quench localization in the superconducting model magnets for the LHC by means of pick-up coils", *IEEE Trans. Appl. SC 5*, pp. 1028-1031 (1995).
- Spigo, G.-C., CERN Div. AT-MA, CH1211 Geneva 23, unpublished calculations (1994).
- Sumption, M.D., E.W. Collings, H.H.J. ten Kate, R.M. Scanlan, "Calorimetric measurements of the effect of Ni and staybrite coatings on AC losses in accelerator cables", *Presented at the ICMC'95, Columbus* (1995).
- Sytnikov, V.E., G.G. Svalov, S.G. Akopov, and I.B. Peshkov, "Coupling losses in superconducting transposed conductors located in changing magnetic fields", *Cryogenics* **29**, pp. 926-930 (1989a).
- Sytnikov, V.E., et al., "Experimental study of transverse resistance and coupling losses in superconducting transposed cables", *Presented (but not published) at MT-11* (1989b).
- Sytnikov, V.E., et al., "Transport and induced currents distribution in superconducting transposed cables", *Adv. Cryog. Eng.* **38**, pp. 553-558 (1992).
- Sytnikov, V.E., and I.B. Peshkov, "Coupling losses for superconducting cables in pulsed fields", *Adv. Cryog. Eng.* **40**, pp. 537-542 (1994).
- Takács, S., "Coupling losses in cables in spatially changing AC fields", *Cryogenics* **22**, pp. 661-665 (1982).
- Tixador, P., D. Leroy, and L. Oberli, "Coupling losses in a superconducting model magnet for the LHC", *Proc. MT-11*, T. Sekiguchi, and S. Shimamoto, Eds, pp. 54-59 (1990).
- Turck, B., "Influence of a transverse conductance on current sharing in a two-layer superconducting cable", *Cryogenics* **14**, pp. 448-454 (1974).
- Verweij, A.P., and R. Wolf, "Field errors due to eddy currents in the cable of the LHC pinkbook dipole", *CERN int. note AT-MA 92-52* (1992).
- Verweij, A.P., and R. Wolf, "Field errors due to inter-strand coupling currents in the LHC dipole and quadrupole", *CERN int. note AT-MA 94-97* (1994).
- Vysotsky, V.S., et al., "On stability of multistrand cables with insulated or highly resistive matrix strands", *IEEE Trans. Appl. SC 5*, pp. 572-575 (1995a).
- Vysotsky, V.S., et al., "New method of current distribution studies for ramp rate stability of multistrand superconducting cables", *IEEE Trans. Appl. SC 5*, pp. 580-583 (1995b).

- Walckiers, L., "Behaviour of the LHC models with respect to the conductor limit", *CERN int. note AT-MA 93-82* (1993).
- Walckiers, L., "The harmonic-coil method", *CERN accelerator school on magnetic measurement and alignment*, pp. 138-166, CERN 92-05 (1992).
- Walters, C.R., "Magnetization and design of multistrand superconducting conductors", *IEEE Trans. Magn. MAG-11*, pp. 328-331 (1975).
- Wanderer, P., et al., "Magnetic design and field quality measurements for full length 50 mm aperture model dipoles built at BNL", *Int. J. Mod. Phys. A 2B*, pp. 641-643 (1993).
- Wiik, B.H., "Progress in Hera", *IEEE Trans. Nucl. Sc. NS-32*, pp. 1587-1591 (1985).
- Wilson, M.N., "Rate dependent magnetization in flat twisted superconducting cables", *RHEL int. note M-A-26* (1972).
- Wilson, M.N., *Superconducting Magnets*, Clarendon, Oxford, 1983.
- Wolf, R., "Persistent currents in LHC magnets", *IEEE Trans. Magn. 28*, p. 376 (1992).
- Yamamoto, A. et al., "Development of 10 T dipole magnets for the Large Hadron Collider", *IEEE Trans. Appl. SC 3*, pp. 769-772 (1993).
- Zhao, Y. et al., "Current dependence of harmonic field coefficients of 5-cm-aperture, 15-m-long SSC dipole magnet prototypes", *IEEE Trans. Appl. SC 3*, pp. 674-677 (1993).

**This thesis is partially based on the following publications:**

- Verweij, A.P., "Loss measurements on the MTA1 Jeumont-Schneider prototype dipole", *CERN int. note AT-MA 91-29* (1991).
- Verweij, A.P., "Measurements of the stored energy and energy loss of the MTA1 Elin prototype dipole", *CERN int. note AT-MA 91-33* (1991).
- Verweij, A.P., "Measurements of the stored energy and energy loss of the MTA1 Ansaldo prototype dipole", *CERN int. note AT-MA 91-34* (1991).
- Verweij, A.P., "Electrical measurements on prototype twin aperture NbTi dipoles for the CERN LHC", *CERN int. note AT-MA* (1991).
- Verweij, A.P., and R. Wolf, "Fields errors due to eddy currents in the cable of the LHC pinkbook dipole", *CERN int. note AT-MA 92-52* (1992).
- Verweij, A.P., and H.H.J. ten Kate, "Coupling currents in Rutherford cables under time varying conditions", *IEEE Trans. Appl. SC 3*, p. 146 (1993).
- Verweij, A.P., and L. Walckiers, "Loss measurements of the LHC models and prototypes: Goals and relevant means", *CERN int. note AT-MA 93-70* (1993).
- Verweij, A.P., "Overview of the results of the AC measurements on the 1 m long CERN dipole model", *CERN int. note AT-MA 93-87* (1993).
- Verweij, A.P., and H.H.J. ten Kate, "Time constants of inter-strand coupling currents in Rutherford cables for different geometries", *Appl. SC 2*, H.C. Freyhardt, Ed., pp. 1625-1628 (1993).
- Verweij, A.P., L.E. Eriksson, and H.H.J. ten Kate, "Study on the AC magnetization of LHC type of Rutherford cables", *Supercollider 5* (1994).
- Verweij, A.P., B. Sachse, A. den Ouden, and H.H.J. ten Kate, "The effect of transverse pressure on the inter-strand coupling loss of Rutherford cables", *Adv. Cryog. Eng. 40*, pp. 521-527 (1994).
- Verweij, A.P., D. Leroy, L. Walckiers, R. Wolf, and H.H.J. ten Kate, "Analysis of the AC loss measurements on the one-metre dipole model magnets for the CERN LHC", *IEEE Trans. Magn. 30*, pp. 1758-1761 (1994).
- Verweij, A.P., and R. Wolf, "Field errors due to inter-strand coupling currents in the LHC dipole and quadrupole", *CERN int. note AT-MA 94-97* (1994).
- Verweij, A.P., H.H.J. ten Kate, D. Leroy, L. Oberli, and A. Siemko, "Ramp rate induced quenches in the one-metre dipole model magnets for the CERN LHC", *IEEE Trans. Appl. SC 5*, pp. 1020-1023 (1995).
- Verweij, A.P., and H.H.J. ten Kate, "Super coupling currents in Rutherford type of cables due to longitudinal non-homogeneities of  $dB/dt$ ", *IEEE Trans. Appl. SC 5*, pp. 404-407 (1995).

# Nomenclature

$a_n$	$n^{\text{th}}$ relative skew multipole component	-
$A$	enclosed surface	$\text{m}^2$
$A_n$	$n^{\text{th}}$ multipole skew component	T
$A_{str}$	cross-section of a strand	$\text{m}^2$
$b_n$	$n^{\text{th}}$ relative normal multipole component	-
$B, \mathbf{B}$	magnetic field	T
$B_a$	applied magnetic field	T
$B_{bi}$	field caused by the BICCs	T
$B_C$	critical magnetic field	T
$B_{cc}$	field caused by the coupling currents	T
$B_{ce}$	central field in the aperture of a magnet	T
$B_{geo}$	field caused by geometrical deviations	T
$B_i$	induced field	T
$B_{if}$	field caused by the IFCCs	T
$B_{inj}$	injection field	T
$B_{is}$	field caused by the ISCCs	T
$B_m$	field caused by the filament magnetisation	T
$B_n$	$n^{\text{th}}$ multipole normal component	T
$B_{nucd}$	field caused by a NUCD	T
$B_p$	penetration field	T
$B_q$	quench field	T
$B_s$	field in the interior of a strand	T
$B_{tr}$	field caused by the transport current	T
$B_0$	constant in the Kim relation	T
$d_f$	diameter filament	m
$d_s$	diameter strand	m
$d_s^*$	diameter of the outer layer of filaments in a strand	m
$E, \mathbf{E}$	electric field	$\text{Vm}^{-1}$
$E_{dyn}$	electric field caused by the dynamic resistance	$\text{Vm}^{-1}$
$f$	frequency	$\text{s}^{-1}$
$h_1, h_2$	height of a cable (thick edge and thin edge)	m

$I$	current	A
$I_a$	current in resistance $R_a$	A
$I_c$	current in resistance $R_c$	A
$I_C$	critical current	A
$I_f$	surface current density	$\text{Am}^{-1}$
$I_{if}$	net interfilament coupling current	A
$I_q$	quench current	A
$I_{q,np}, I_{q,p}$	quench current obtained without/with a precycle	A
$I_s$	coupling current in a strand	A
$I_{str}$	total strand current	A
$I_{tr}$	transport current	A
$I_{tr,cab}$	transport current in a cable	A
$I_{tr,str}$	transport current in a strand	A
$I_{tr,str,max}$	maximum transport current in a strand	A
$I_0, J_0$	constants in the Kim relation	A, $\text{Am}^{-2}$
$J, \mathbf{J}$	current density	$\text{Am}^{-2}$
$J_C$	critical current density	$\text{Am}^{-2}$
$J_{tr}$	transport current density	$\text{Am}^{-2}$
$l_{cab}$	cable length	m
$l_{coil}$	length of a pick-up coil	m
$l_M$	magnet length	m
$l_s$	length of a strand section between two nodes	m
$L$	inductance	H
$L_{p,f}$	twist pitch of the filaments	m
$L_{p,s}$	twist pitch of the strands (or cable pitch)	m
$M$	magnetisation	$\text{Am}^{-1}$
$M$	mutual inductance	H
$n$	harmonic component	-
$n$	shape factor	-
$n$	$n$ -value of the resistive transition	-
$N_b$	band number	-
$N_B$	total number of bands of a cable	-
$N_c$	number of cable pieces in a stack	-
$N_{MUT}$	number of bands for the calculation of mutual inductances	-
$N_s$	number of strands in a cable	-
$N_T$	number of turns in a coil	-
$p_{cab}$	packing factor of a cable	-
$P$	power loss	W
$P_a$	power loss in the resistances $R_a$	W
$P_c$	power loss in the resistances $R_c$	W
$P_{cool}$	cooling power	W
$P_{if}$	interfilament coupling power loss	W
$P_R$	power loss in the connections	W
$P_s$	power loss in the strands	W

$P_{wed}$	power loss in the wedges	W
$q$	effective thermal-conductivity coefficient	$\text{Wm}^{-3}\text{K}^{-1}$
$Q_{hys}$	hysteresis loss	J
$Q_{if}$	interfilament coupling loss	J
$Q_{is}$	interstrand coupling loss	J
$Q_{tot}$	total loss	J
$r$	radius	m
$r_0$	reference radius	m
$R$	resistance	$\Omega$
$R_a$	contact resistance between adjacent strands	$\Omega$
$R_c$	contact resistance between crossing strands	$\Omega$
$R_{c,UI}$	$R_c$ -value determined by the UI method	$\Omega$
$R_{mat}$	resistance of the matrix	$\Omega$
$R_s$	strand resistance	$\Omega$
$t$	time	s
$t_d$	decay time	s
$t_m$	time at the discrete step $m$	s
$t_r$	ramp time	s
$T$	temperature	K
$T_b$	helium bath temperature	K
$T_{cab}$	cable temperature	K
$T_C$	critical temperature	K
$T_M$	field factor of a magnet	$\text{TA}^{-1}$
$U$	voltage	V
$U_{ee}$	voltage between the strands at both edges of a cable	V
$U_{ind}$	induced or inductive voltage	V
$U_R$	resistive voltage	V
$U_{str}$	voltage over a strand	V
$v_1, v_2, v_3$	volume fractions	-
$V$	volume	$\text{m}^3$
$w$	width of a cable	m
$x, y, z$	cartesian coordinates	m
$x_0, y_0$	reference point	m

## Greek symbols

$\alpha_{cond}$	aspect ratio of a monolithic conductor	-
$\alpha_k$	keystone angle	deg
$\alpha_{cab}$	aspect ratio of a cable	-
$\alpha_0$	aspect ratio of a cable having strands with a round cross-section	-
$\alpha_m$	coefficient of magnetoresistivity	$\text{T}^{-1}$
$\beta_I$	field geometry factor for the ISCCs	-
$\beta_P$	field geometry factor for the ISCL	-

$\beta_{str}$	field geometry factor at a strand position	-
$\eta$	volumetric proportion of superconductor in a composite	-
$\theta$	angle (see Figs. 4.1 and 2.2a)	deg
$\lambda$	copper to superconductor (Cu/SC) ratio	-
$\lambda_{cu}$	thermal conductivity coefficient of copper	$\text{Wm}^{-1}\text{K}^{-1}$
$\lambda_{ins}$	thermal conductivity coefficient of a cable insulation	$\text{Wm}^{-1}\text{K}^{-1}$
$\mu$	permeability	$\text{Hm}^{-1}$
$\mu_{eff}$	effective permeability	$\text{Hm}^{-1}$
$\mu_0$	permeability of vacuum	$\text{Hm}^{-1}$
$\xi$	characteristic length of the BICCs	m
$\rho_{cu}$	resistivity of copper	$\Omega\text{m}$
$\rho_{eff}$	effective transverse resistivity of a strand	$\Omega\text{m}$
$\rho_c$	effective resistivity of a cross contact	$\Omega\text{m}$
$\rho_{mat}$	matrix resistivity	$\Omega\text{m}$
$\rho_s$	effective resistivity of a strand	$\Omega\text{m}$
$\sigma$	stress	Pa
$\tau$	time constant	s
$\tau_{bi}$	characteristic time of the BICCs	s
$\tau_{if}$	time constant of the IFCCs	s
$\tau_{is}$	time constant of the ISCCs	s
$\varphi$	angle (see Figs. 3.5 and 4.1)	deg
$\omega$	angular frequency ( $=2\pi f$ )	$\text{rad s}^{-1}$

### Common subscripts

$\perp$	normal component
$\parallel$	parallel component
$a$	between adjacent strands
$av$	average
$bi$	boundary-induced
$c$	between crossing strands
$cab$	cable
$eff$	effective
$i$	turn number
$if$	interfilament
$is$	interstrand
$M$	magnet
$str$	strand
$st$	stack
$tot$	total
$tr$	transport

**Abbreviations**

A1, A2	Nomenclature of the apertures (see Fig. 6.4)
A11, A12, A21, A22	Nomenclature of the poles (see Fig. 6.4)
B1, B2, ..., B6	Block numbers (see Fig. 2.2b)
BICC	Boundary-Induced Coupling Current
FPC	Fixed Pick-up Coil (see section 7.6)
H12, H3, H4, H5, H67	Pick-up coils (see section 7.7)
IFCC	InterFilament Coupling Current
ISCC	InterStrand Coupling Current
IFCL	InterFilament Coupling Loss
ISCL	InterStrand Coupling Loss
LHC	Large Hadron Collider
NUCD	Non-Uniform Current Distribution
PBD	Pink Book Dipole magnet (see Table 2.1)
PC	Persistent Current
RPC	Rotating Pick-up Coil (see section 7.6)
RRL	Ramp Rate Limitation
SA	Single-Aperture
TA	Twin-Aperture
WBD	White Book Dipole magnet (see Table 2.1)





## Samenvatting (Summary in Dutch)

In circulaire versnellers worden de deeltjesbundels met dipoolmagneten in hun evenwichtsbaan gehouden en met quadropoolmagneten rond deze evenwichtsbaan gefocusseerd. Verhoging van het dipoolveld is essentieel om de botsingsenergie van versnellers te verhogen. Op het CERN is momenteel de Large Hadron Collider (LHC) in de ontwerpfase. De LHC zal ongeveer 1100 supergeleidende dipoolmagneten bevatten met een veldsterkte van 8-9 T en een lengte van 14 m. De platte (of Rutherford) kabels, waarmee de spoelen van deze magneten zijn gewikkeld, bestaan uit getwiste draden (of strands), die zijn opgebouwd uit getwiste supergeleidende filamenten, ingebed in een kopermatrix.

In een versneller worden de dipoolmagneten opgeregeld van het injectieveld, het veld waarbij de deeltjes vanuit een voorversneller worden geïnjecteerd, tot het operatieveld. Als gedurende de werking van de versneller een magneet quencht, d.w.z. zijn supergeleidende eigenschappen verliest, wordt de stroom door deze magneet uitgekoppeld en vervolgens met alle in serie geschakelde magneten snel afgeregeld. Tijdens het op- en afregelen staan de kabels bloot aan een veldvariatie  $\dot{B}$ , waardoor verschillende typen afschermstromen in de kabel worden geïnduceerd. Centraal in dit proefschrift staat de vraag in welke mate deze stromen de werking van supergeleidende magneten beïnvloeden. Hoewel het onderzoek is toegespitst op de dipoolmagneten ten behoeve van LHC, zijn de resultaten ook toepasbaar op andere typen spoelen die van Rutherford kabels zijn gemaakt. De uitgewerkte modellen zijn tevens geldig voor spoelen die gewonden zijn van andere typen kabels.

De verschillende aspecten van de strand, de kabel en de magneet welke in het algemeen van invloed zijn op de elektrodynamika van de kabel worden besproken. Hierbij wordt ingegaan op de structuur, produktiewijze, veld- en krachtverdeling, kabelconnecties en quenchgedrag van de magneten alsmede de structuur van de kabels en de strands. Vervolgens worden de afschermstromen op strandniveau en kabelniveau behandeld die experimenteel zijn onderzocht aan de hand van metingen aan korte stukken geleider.

In de daarop volgende hoofdstukken wordt de invloed van deze stromen op de werking van versnellerdipoolmagneten onderzocht. Drie aspecten komen hierbij aan de orde: het energieverlies, de veldfouten en de stabiliteit. Deze aspecten worden theoretisch behandeld en zijn experimenteel geëvalueerd voor 11 LHC dipool modelmagneten van zowel 1 m als 10 m lengte.

### Stroomverdeling in strands.

- '*Persistent Currents (PCs)*'. De PCs stromen binnenin de filamenten van de strands en schermen het binnenste gedeelte van de filamenten ten dele af tegen een extern veld. Deze stromen blijven bestaan nadat het externe veld constant geworden is.
- '*Interfilament Coupling Currents (IFCCs)*'. De IFCCs stromen in de filamenten van de strands en via de normaal-geleidende matrix. Hierbij schermen zij het binnenste gedeelte van de strand af tegen de externe veldverandering. De IFCCs lopen door de filamenten

over een karakteristieke lengte gelijk aan de twistlengte van de filamenten, en zijn omgekeerd evenredig met de resistiviteit van de matrix.

Om de verliezen, veldfouten en stabiliteit in de magneten ten gevolge van de PCs en de IFCCs te quantificeren, zijn deze twee stromen in een aantal strands bepaald door meting van de magnetisatie in een variërend magneetveld. Tevens is nagegaan of de stromen in aanliggende strands van eenzelfde kabel elkaar onderling beïnvloeden

### Stroomverdeling in kabels.

In kabels waarin de strands onderling elektrisch contact maken zullen stromen in en tussen de strands van de kabel geïnduceerd worden die het binnenste gedeelte van de kabel ten dele afschermen van de externe veldverandering. Met toenemende botsingsenergie van versnellers nemen tevens de afmetingen van de kabels toe, hetgeen grotere afschermstromen op kabelniveau tot gevolg heeft. De PCs en IFCCs zijn daarentegen vrijwel onafhankelijk van de kabelgeometrie.

De stroomverdeling in de strands van een kabel is berekend met behulp van een computerprogramma waarin de kabel is gemodelleerd middels een elektrisch netwerk van knooppunten verbonden door middel van strand-secties en contactweerstand tussen aanliggende en kruisende strands. Belangrijke verbeteringen vergeleken met bestaande modellen zijn de mogelijkheden om tijdafhankelijk gedrag te onderzoeken en om ongelijkmatige ruimtelijke verdelingen in de kabelparameters en externe factoren op te leggen. De stroomverdeling bestaat uit drie bijdragen:

- **'Transport Current'**. Deze verschilt per strand wanneer de strands verschillende serie weerstanden hebben, veroorzaakt door inhomogene soldeerverbindingen tussen kabels onderling of tussen kabels en stroomtoevoerdraden.
- **'Interstrand Coupling Currents (ISCCs)'**. De ISCCs stromen door de contactweerstand en in de strands over een karakteristieke lengte gelijk aan de twistlengte van de strands. Speciale aandacht wordt besteed aan de tijdconstanten van deze koppelstromen voor verschillende kabelconfiguraties, aan lokale verzadiging van de strands en aan de distributies van de ISCCs in geval van variërende contactweerstand en  $\dot{B}$  over de kabelbreedte. Contactweerstand kunnen orden van grootte variëren aangezien ze sterk afhangen van o.a. de temperatuurbehandeling, de druk en de oppervlaktecondities van de strand. Een nieuwe meetopstelling is ontwikkeld waarmee de contactweerstand van verscheidene kabels zijn onderzocht als functie van de transversale druk.
- **'Boundary-induced Coupling Currents (BICCs)'**. Met het netwerk model is het bestaan van dit type koppelstroom aangetoond. BICCs worden geïnduceerd als gevolg van variaties in interne en externe factoren in de lengterichting van de kabel en met name de variaties in de contactweerstand en  $\dot{B}$  in en nabij de kabelconnecties en de spoelkoppen. De BICCs onderscheiden zich van de ISCCs door hun veel grotere karakteristieke (lus)lengte, karakteristieke tijd en grootte. De typische stroomverdeling van de BICCs wordt geïllustreerd en relaties worden gegeven die deze verdeling beschrijven als functie van de plaats en de tijd. Een nieuwe meetopstelling is ontworpen waarin een 1.3 m lange rechte kabel is onderworpen aan een lokale veldverandering en plaatselijk is voorzien van lagere contactweerstand. Hiermee is het bestaan van BICCs in één enkele kabel voor het eerst experimenteel aangetoond.

### Invloed van de stroomverdeling op de werking van magneten.

- **Energieverlies.** In een versneller zal iedere warmte-ontwikkeling in de magneten uiteindelijk gecompenseerd moeten worden door de cryogene installatie. Naast de bundelverliezen, de warmte-inlek en de resistieve verliezen in de kabelconnecties ontstaat een bijkomend verlies gedurende excitatie. Dit verlies bestaat voornamelijk uit het hystereseverlies inherent aan de PCs en het koppelverlies ten gevolge van de IFCCs in de matrix en de ISCCs en BICCs in de contactweerstand. Elektrische verliesmetingen aan 11 LHC magneten zijn uitgevoerd om de verschillende bijdragen te bepalen en om verschillen tussen de magneten en tussen de vier polen van een magneet te onderzoeken.
- **Veldfouten.** In versneller magneten kunnen veldfouten resulteren in een instabiele deeltjesbeweging en dientengevolge in hogere bundelverliezen en een lagere luminositeit. In dit proefschrift gaat de aandacht voornamelijk uit naar de veldfouten die door de koppelstromen veroorzaakt worden. Het veld als gevolg van de IFCCs is verwaarloosbaar is ten opzichte van de velden veroorzaakt door de ISCCs en de BICCs. De ISCCs genereren velden die vrijwel constant zijn over de lengterichting ( $z$ ) van de magneet en waarvan de multipoolcomponenten afhangen van de grootte en de verdeling van  $R_c$  over de dwarsdoorsnede van de spoel. De BICCs resulteren in veldfouten die sinusvormig variëren over de lengte van de magneet. De door de koppelstromen gegenereerde velden zijn in de boring van een viertal LHC magneten gemeten. De verschillende veldcomponenten zijn gescheiden na evaluatie van de tijdconstanten en de  $\dot{B}$ - en  $z$ -afhankelijkheden van de stromen.
- **Stabiliteit van de geleider.** Temperatuurstijgingen van de kabel en lokaal hogere stromen dan gemiddeld resulteren in een kleinere marge tussen de lokale stroom en de kritieke stroom. Dit betekent dat de stabiliteit van de geleider afneemt zodat kortstondige externe warmtepulsen eerder tot een quench kunnen leiden. De afname van de stabiliteit ten gevolge van de koppelstromen is onderzocht aan de hand van de reductie van de quenchstroom als functie van  $\dot{B}$ . In combinatie met de resultaten van de verliesmetingen is de temperatuur van de kabel als functie van het koppelverlies berekend. Tevens is de effectieve warmteoverdracht tussen de kabel en het helium bepaald en is de te verwachten temperatuurstijging van de kabel ten gevolge van bundelverliezen afgeschat.

In het afsluitende hoofdstuk worden de mogelijkheden van het modelleren van stroomverdelingen in kabels met behulp van een netwerk model kort besproken en worden de restricties ten aanzien van de contactweerstand samengevat. Het specificeren van een minimale waarde van de gemiddelde contactweerstand in de kabels is vereist om grote verliezen en veldfouten ten gevolge van de koppelstromen te vermijden. Tevens moeten de contactweerstand zo constant mogelijk zijn over de dwarsdoorsnede van de spoelen en over alle magneten in de versneller om:

- lokale vermindering van de stabiliteit (als gevolg van de ISCCs en BICCs) zo veel mogelijk te voorkomen,
- de veldcorrectie (als gevolg van de ISCCs en BICCs) te vereenvoudigen.